The ATG8 Protein GABARAP in Secretion, Transport, and Autophagy

Inaugural-Dissertation

zur Erlangung des Doktorgrades
der Mathematisch-Naturwissenschaftlichen Fakultät
der Heinrich-Heine-Universität Düsseldorf

vorgelegt von

Julia Luise Sanwald
aus Kiel

Jülich, September 2020

aus dem Institut für Physikalische Biologie
der Heinrich-Heine-Universität Düsseldorf

Gedruckt mit der Genehmigung der
Mathematisch-Naturwissenschaftlichen Fakultät der
Heinrich-Heine-Universität Düsseldorf

Berichterstatter:

1. Prof. Dr. Dieter Willbold

2. Prof. Dr. Björn Stork

Tag der mündlichen Prüfung: 10. November 2020

Eidesstattliche Erklärung

Ich versichere an Eides statt, dass die Dissertation von mir selbstständig und ohne unzulässige fremde Hilfe unter Beachtung der „Grundsätze zur Sicherung guter wissenschaftlicher Praxis an der Heinrich-Heine-Universität Düsseldorf" erstellt worden ist.

Ferner erkläre ich, dass ich in keinem anderen Dissertationsverfahren mit oder ohne Erfolg versucht habe, diese Dissertation einzureichen.

Düsseldorf, den

(Julia Luise Sanwald)

Stude, non ut plus aliquid scias, sed ut melius.

—

Bemühe dich, nicht mehr von etwas zu kennen, sondern es besser zu kennen.

Seneca (∼ 4 v. Chr. – 65 n. Chr.)

VI

Summary

The human ATG8 (autophagy-related 8) protein family is well-known for its fundamental functions during autophagy, a self-degradation process essential for cellular homeostasis. Subdivided into the two highly homologous subfamilies (MAP1)LC3s ((microtubule-associated proteins 1A/1B) light chain 3) and GABARAPs (γ-aminobutyric acid (A) receptor-associated proteins), the distinct roles of the individual family members are not yet entirely clear. The aim of this work was therefore to study GABARAP regarding its specific functions, especially during autophagy-independent processes.

The versatility of GABARAP is illustrated by its participation in diverse cellular processes like transport and secretion pathways besides autophagy. GABARAP mediates not only the plasma membrane (PM)-directed transport of other proteins or vesicular secretion e.g. of insulin. In fact, by immunological detection of GABARAP in extracellular vesicle (EV) lysates this work also demonstrates the secretion of GABARAP itself. To investigate GABARAP's secretion pathway, the APEX2 (engineered ascorbate peroxidase) proximity labelling system was applied for the first time to EVs, proving its applicability to small ($\sim 100\,\mathrm{nm}$) extracellular compartments. Following its activation, APEX2 catalyses the oxidation of biotin-phenol to a short-lived radical which subsequently labels proteins in direct proximity to the APEX2 construct. Tagged to GABARAP, APEX2 has already been used to determine the proxitome inside an autophagosome. Labelled proteins were enriched via Streptavidin and applied to mass spectrometry. By identifying the APEX2-GABARAP proxitome in EVs or its "co-secretome", respectively, not only GABARAP-interacting proteins like Calreticulin and Clathrin heavy chain 1 were detected, but also typical exosomal marker proteins such as Alix and Annexin V. Furthermore, an in-depth analysis of GABARAP's co-secretome revealed an enrichment of mitochondrial proteins and an overlap with an independently determined autophagosomal proxitome, suggesting a non-degradative autophagic pathway for GABARAP's secretion. Alternatively, GABARAP could be secreted via a pathway that, shortly before this work, was uncovered for GABARAP's paralogue LC3B by employing a different, intracellular proximity labelling approach. This LC3-based secretion mechanism involves the ATG8-conjugation machinery which controls the loading

of e.g. RNA-binding proteins (RBPs) into a subpopulation of intraluminal vesicles, followed by multivesicular body (MVB)-mediated secretion. GABARAP and LC3 might be functionally redundant in this process, as several RBPs detected in LC3 proximity were also found in the GABARAP co-secretome. In summary, GABARAP might be secreted by an autophagosome-mediated pathway and/or by an MVB-mediated pathway employing the ATG8-conjugation machinery, or even by a combined mechanism involving a fusion step of an autophagosome with an MVB yielding an amphisome prior to secretion.

As second part of this work, GABARAP and its paralogues GABARAP-like 1 (-L1) and -like 2 (-L2) were studied regarding their functions during transport processes. Initially, GABARAP was discovered as receptor-associated protein which takes part in intracellular trafficking events, a function which was also described for GABARAPL1 and -L2. Although GABARAPL2 was immediately defined as a protein essential for intra-Golgi trafficking and for Golgi restacking, the latter function has not yet been investigated for GABARAP and both functions not yet for GABARAPL1. To study this matter, HEK293 knockout (KO) cell lines lacking one, two, or all three (TKO) of the GABARAPs were applied to staining with markers targeting either the whole Golgi or the *trans*-Golgi network and subsequent (immuno-)fluorescence microscopy. In doing so, a significant influence of not only GABARAPL2, but also GABARAP, on Golgi morphology was observed, the loss of GABARAP and/or GABARAPL2 leading to an increased number of cells containing a dispersed Golgi compared to wild-type (WT) cells predominantly exhibiting a compact Golgi. In a live-cell ceramide chase experiment using NBD-labelled C_6-ceramide, an accumulation of NBD-labelled, vesicular structures and reduced PM staining was observed in TKO cells compared to WT cells. This finding could be mirrored by Monensin which is known to disrupt the *trans*-Golgi. In contrast, incubation of the cells with Brefeldin (A) (BFA) led to a similar staining pattern in WT and TKO cells. Ceramide is known to be transported from the endoplasmic reticulum (ER) to the *cis*-Golgi by the ceramide transfer protein (CERT) in a non-vesicular manner. This mechanism is presumably not affected by BFA as it inhibits vesicular, but not non-vesicular ER-to-Golgi trafficking. Therefore, an involvement of the GABARAPs in *trans*-Golgi-mediated, vesicular trafficking, but not in CERT-mediated, non-vesicular trafficking of ceramide and its metabolites seems likely. Taken together, absence of GABARAPs resulted in a change in Golgi morphology and lipid trafficking, GABARAP and GABARAPL2 possibly being functionally redundant. The exact mechanisms of action are yet to elucidate in future work.

In parallel, contributions were made to a comprehensive analysis of cytoplasmic structures containing GABARAP and LC3B, respectively, by enhanced yellow fluo-

rescent protein (EYFP)-fusion and single-molecule localisation microscopy (SMLM). Thereby, a similar size distribution was revealed. However, EYFP-GABARAP containing structures were mainly circular, while EYFP-LC3B containing structures were predominantly U-shaped. SMLM therefore enabled an assignment of LC3B and GABARAP to different structures, indicating diverse localisations and hence functions of the two ATG8 proteins.

Zusammenfassung

Die humane ATG8 (*autophagy-related* 8)-Proteinfamilie ist am besten bekannt für ihre grundlegenden Funktionen während der Autophagie, eines zellulären Prozesses, der dem Abbau zelleigener und -fremder Bestandteile und damit der Homöostase dient. Unterteilt wird die ATG8-Familie in zwei Subfamilien, die aus den je untereinander hochgradig homologen (MAP1)LC3s ((*microtubule-associated proteins 1A/1B light chain 3*) und GABARAPs (*γ-aminobutyric acid (A) receptor-associated proteins*) bestehen. Aufgrund ihrer hohen Sequenzähnlichkeit sind die genauen Eigenschaften der einzelnen Familienmitglieder noch nicht vollständig bekannt. Ziel dieser Arbeit war es daher, GABARAP auf seine spezifischen Funktionen besonders hinsichtlich Autophagie-unabhängiger Prozesse zu untersuchen.

Die Vielseitigkeit von GABARAP wird besonders durch dessen Beteiligung an den verschiedensten zellulären Prozessen, neben Autophagie auch Transport und Sekretion, verdeutlicht. GABARAP ist nicht nur in den Plasmamembran (PM)-gerichteten Transport anderer Proteine involviert. Auch an der vesikulären Sekretion von beispielsweise Insulin ist GABARAP beteiligt und wird, wie in dieser Arbeit durch immunologischen Nachweis von GABARAP in Lysaten extrazellulärer Vesikel (EVs) gezeigt wurde, auch selbst sekretiert. Um den Sekretionsmechanismus von GABARAP zu untersuchen, wurde die Methode der APEX2 (modifizierte Ascorbat-Peroxidase)-vermittelten Proxitom-Bestimmung angewandt. Diese Methode basiert auf der Oxidation von Biotin-Phenol zu einem kurzlebigen Radikal, das an Proteine in der direkten (proximalen) Umgebung des APEX2-Konstruktes bindet. APEX2-GABARAP wurde bereits für die Bestimmung des Proxitoms in Autophagosomen verwendet. Durch dessen Anwendung in EVs wurde hier zum ersten Mal die Eignung dieser Methode für kleine ($\sim 100\,\text{nm}$) extrazelluläre Kompartimente gezeigt. Mit Biotin-Phenol markierte Proteine wurden mittels Streptavidin angereichert und über Massenspektrometrie analysiert. Das resultierende APEX2-GABARAP EV-Proxitom oder "Co-Sekretom" enthält nicht nur bekannte GABARAP-Interaktoren wie Calreticulin oder Clathrin heavy chain 1, sondern auch typische exosomale Markerproteine wie Alix und Annexin V. Bei einer tiefergehenden Analyse des GABARAP Co-Sekretoms wurden außerdem eine Anreicherung mitochondrialer Proteine und ein Überlapp mit dem Autophagosomen-Proxitom von

APEX2-GABARAP festgestellt. GABARAP könnte daher einerseits über einen unkonventionellen Sekretionsweg, bei dem Autophagosomen nicht degradiert, sondern sekretiert werden, aus der Zelle transportiert werden. Andererseits könnte GABARAP über einen Weg sekretiert werden, der kurz vor dieser Arbeit für sein Paralog LC3B unter Verwendung einer alternativen intrazellulären Biotinylierungsstrategie entdeckt wurde. Bei diesem LC3-basierten Sekretionsmechanismus kontrolliert unter anderem die ATG8-Konjugationsmaschinerie die Beladung einer Subpopulation intraluminaler Vesikel, z.B. mit RNA-bindenden Proteinen (RBPs), und letztlich deren MVB (*multivesicular body*)-vermittelter Sekretion. GABARAP und LC3 könnten in diesem Prozess eine funktionelle Redundanz aufweisen, da etliche RBPs, die im LC3-Proxitom gefunden wurden, auch im GABARAP Co-Sekretom vorhanden sind. Zusammengefasst könnte GABARAP demnach neben einem Autophagosomen-vermittelten Weg auch über einen MVB-vermittelten Weg, der sich nur der ATG8-Konjugationsmaschinerie bedient, sekretiert werden. Auch eine Kombination beider Mechanismen, bei der ein Autophagosom vor der Sekretion mit einem MVB zu einem Amphisom fusioniert, ist denkbar.

Im zweiten Teil dieser Arbeit wurden GABARAP und dessen Paraloge GABARAP-*like* 1 (-L1) und GABARAP-*like* 2 (-L2) im Hinblick auf ihre Funktionen bei Transportmechanismen untersucht. Ursprünglich wurde GABARAP als Rezeptor-assoziiertes Protein identifiziert, das ebenso wie GABARAPL1 und -L2 an intrazellulären Transportvorgängen beteiligt ist. GABARAPL2 wurde zudem als essenzielles Protein für den Proteintransport innerhalb des Golgi-Apparates und die Erhaltung der Golgi-Morphologie beschrieben. Die Beteiligung von GABARAP an letzterem Prozess und von GABARAPL1 an beiden Prozessen wurde hingegen bis jetzt noch nicht untersucht. Zu diesem Zweck wurden in dieser Arbeit in HEK293 *knockout* (KO) Zelllinien, denen ein, zwei, oder alle drei Mitglieder (*triple* KO, TKO) der GABARAP-Subfamilie fehlen, der komplette Golgi oder das trans-Golgi Netzwerk gefärbt und anschließend mittels (Immun-)Fluoreszenz-Mikroskopie untersucht. Dabei wurde ein signifikanter Einfluss von nicht nur GABARAPL2, sondern auch von GABARAP, auf die Golgi-Morphologie festgestellt. Nach Verlust von GABARAP und/oder GABARAPL2 wurde eine erhöhte Anzahl an Zellen ermittelt, die einen zerstreuten Golgi aufwiesen, im Gegensatz zu wildtypischen (WT-)Zellen, bei denen die meisten einen kompakten Golgi enthielten. In einem Lebendzell-Ceramid-*chase*-Experiment mit NBD-markiertem C_6-Ceramid wurde für TKO-Zellen außerdem eine Akkumulation NBD-positiver, vesikulärer Strukturen und eine verringerte NBD-Färbung der PM im Vergleich zu WT-Zellen beobachtet. Dieser Phänotyp konnte mittels Monensin nachgestellt werden, ein Ionophor, das den *trans*-Golgi zerstört. Im Gegensatz dazu führte eine Inkubation der Zellen mit Brefeldin A (BFA) zu einer ähnlichen Verteilung von NBD C_6-Ceramid in WT- und

TKO-Zellen. Es ist bekannt, dass Ceramid non-vesikulär über das Ceramid Transferprotein (CERT) vom endoplasmatischen Retikulum (ER) zum *cis*-Golgi transportiert wird. Dieser Mechanismus ist vermutlich unbeeinflusst von BFA, da dieses vesikuläre, jedoch nicht non-vesikuläre Transportprozesse vom ER zum *cis*-Golgi inhibiert. Eine Beteiligung der GABARAPs im *trans*-Golgi-vermittelten, vesikulären, jedoch nicht am non-vesikulären, CERT-vermittelten Transport von Ceramid und dessen Metaboliten liegt daher nahe. Insgesamt führte die Abwesenheit der GABARAPs zu einer Veränderung der Golgi-Morphologie und des Lipidtransportes, wobei über eine funktionelle Redundanz von GABARAP und GABARAPL2 spekuliert werden kann. Der zugrundeliegende Mechanismus bleibt Gegenstand zukünftiger Studien.

Parallel wurden Beiträge zu einer Studie geleistet, in der cytoplasmatische GABARAP- bzw. LC3B-enthaltende Strukturen, detektiert mittels *enhanced yellow fluorescent protein* (EYFP)-Fusion und Einzelmolekül-Lokalisations-Mikroskopie (*single-molecule localisation microscopy*, SMLM), untersucht wurden. Während eine ähnliche Größenverteilung festgestellt wurde, waren EYFP-GABARAP-gelabelte Strukturen vor allem kreisförmig und EYFP-LC3B-enthaltende Strukturen wiesen eher eine U-Form auf. Durch SMLM konnten somit LC3B und GABARAP unterschiedlichen Strukturen zugeordnet werden und deuten damit auf verschiedene Lokalisationen und folglich Funktionen der beiden ATG8-Proteine hin.

Danksagung

An erster Stelle möchte ich Herrn Prof. Dr. Dieter Willbold für die Möglichkeit danken, meine Doktorarbeit in seinem Institut anzufertigen, für die ununterbrochene Unterstützung während dieser Zeit, und für die großartigen Gelegenheiten, meine Arbeit auf internationalen Konferenzen vorzustellen.

Zudem gebührt mein Dank meinem Mentor Prof. Dr. Thomas Klein für die Begleitung und konstruktiven Gespräche während der Doktorarbeit im Rahmen des SFB 1208.

Herrn Prof. Dr. Björn Stork danke ich herzlich für die freundliche Übernahme des Zweitgutachtens.

Besonderen Dank möchte ich Dr. Silke Hoffmann aussprechen. Mit ihrer Geduld, ihrer oft unendlich wirkenden Vielzahl an Ideen und ihrer Fähigkeit, in jeder Situation einen kühlen Kopf zu bewahren, hat sie maßgeblich zur (Weiter-)Entwicklung des Projekts und zur Entstehung dieser Arbeit beigetragen.

Zudem möchte ich Dr. Oliver Weiergräber, Dr. Thomas Gensch und Dr. Iman Abdollahzadeh für ihre vielfältigen Denkanstöße bei den gemeinsamen Gruppenmeetings bezüglich Autophagie und Mikroskopie meinen Dank aussprechen.

Ich danke herzlich Prof. Dr. Payam Akhyari und Dr. Andreas Weber aus dem Universitätsklinikum Düsseldorf für die Möglichkeit, NTA-Messungen in ihrem Labor durchzuführen, und für die Einarbeitung und Unterstützung während der Messungen.

Weiterhin gilt mein großer Dank Prof. Dr. Kai Stühler, Dr. Gereon Poschmann und Dr. Daniel Waldera-Lupa für die Durchführung massenspektrometrischer Messungen und ihre Hilfsbereitschaft bei der Auswertung der Daten.

Dr. Johan Buitenhuis danke ich für die geduldige und ausführliche Einweisung am Transmissionselektronenmikroskop und für die Hilfe bei der Aufnahme der Bilder.

Im Labor möchte ich mich bei allen Kollegen für ihre Hilfsbereitschaft bedanken, besonders bei meinen Laborplatz-Nachbarn Dr. Karen Hänel und Stefan Freischem für die vielen Diskussionen und dafür, dass sie immer ein offenes Ohr hatten.

Ein großer Dank geht an alle Mit-Doktoranden, natürlich auch an diejenigen, die hier nicht namentlich genannt sind. Danke für die lustigen Momente in Küche, Büro oder Irish Pub.

Dr. Marianne Schulte, dir danke ich für eine schöne gemeinsame Zeit in Jülich, ob im Sommer beim Grillen im Garten oder im Winter bei gemütlichen Filmabenden.

Irina Apanasenko, спасибо für die gemeinsame unterhaltsame Zeit im SFB 1208 und auf der Autobahn während der zahllosen Fahrten nach Düsseldorf. Auch außerhalb der Arbeit konnte ich mich immer auf dich verlassen.

Serife Akgül, du bist mein Vorbild dafür, niemals aufzugeben oder den Mut zu verlieren. Danke für die gemeinsame Zeit in Labor, Gruppenmeetings und im SFB, und natürlich beim Sushi-Essen.

Jochen Dobner, ich habe es sehr genossen, mit dir zusammenzuarbeiten. Ich glaube, ich habe dich nicht einmal schlecht gelaunt gesehen. Danke für die entspannte Atmosphäre.

Karoline Santur, danke für die vielen lebhaften Unterhaltungen in Labor, Büro und Küche, und vor allem dafür, dass man immer zu dir kommen konnte, wenn man Gesprächsbedarf hatte.

Julia Post-Schulz, seit der Masterarbeit habe ich meine Zeit im Institut mit dir zusammen im Büro verbracht. Du hast einen beeindruckenden Ehrgeiz und Fleiß, der einen anspornt, es dir gleichzutun. Danke für diese Motivation und die gemeinsame Zeit.

Dr. Indra Simons, durch dich habe ich gelernt, wie wertvoll es ist, sich mit jemandem gemeinsam ans Ziel zu kämpfen. Danke, dass wir diese Zeit zusammen durchgestanden haben.

Zu guter Letzt gilt mein allergrößter Dank Patrick und meinen Eltern. Patrick, ohne dich hätte ich es wahrscheinlich noch nicht einmal durch das erste Semester geschafft. Danke, dass du immer für mich da bist. Und Mam und Pap, ohne euch wäre ich nicht so weit gekommen. Eure eigenen Leistungen haben mich immer dazu motiviert, weiterzumachen. Danke, dass ihr mich zu der Person gemacht habt, die ich bin.

Contents

List of Abbreviations

ABC	ATP binding cassette
AcbA/1	acyl-CoA-binding protein (*Dictyostelium*/yeast)
AIM	Atg8-interacting motif
ALG-2	apoptosis-linked gene 2
Alix	ALG-2-interacting protein X
APEX2	engineered ascorbate peroxidase
ATG	autophagy-related
ATP	adenosine triphosphate
BFA	Brefeldin A
BODIPY FL C$_5$	*N*-(4,4-Difluoro-5,7-Dimethyl-4-Bora-3a,4a-Diaza-s-Indacene-3-Pentanoyl)
BSA	bovine serum albumin
CD	cluster of differentiation
CERT	ceramide transfer protein
COPI/II	coatomer protein complex-I/-II
CUPS	compartment of unconventional secretion
DKO	double knockout
DMEM	Dulbecco's Modified Eagle's Medium
DNA	deoxyribonucleic acid
EDTA	ethylenediaminetetraacetic acid
(E)GFP	(enhanced) green fluorescent protein
ER	endoplasmic reticulum
ERES	ER-exit site
ERGIC	ER-Golgi intermediate compartment
ESCRT	endosomal sorting complexes required for transport
EV	extracellular vesicle

EYFP	enhanced yellow fluorescent protein
FCS	fetal calf serum
FGF2	fibroblast growth factor 2
GABA$_{\mathbf{A}}$	γ-aminobutyric acid (A)
GABARAP	GABA$_A$ receptor-associated protein
GABARAPL1	GABA$_A$ receptor-associated protein-like 1
GABARAPL2	GABA$_A$ receptor-associated protein-like 2
GIM	GABARAP interaction motif
GM130	130 kDa *cis*-Golgi matrix protein
GO	gene ontology
GRASP55/65	Golgi reassembly-stacking protein of 55/65 kDa
GTP	guanosine triphosphate
HEK293	human embryonic kidney 293
Hsc70	heat shock 70 kDa protein 8
Huh7	human hepatoma 7
IL-1β	interleukin-1β
ILV	intraluminal vesicle
KIF5B	kinesin-1 heavy chain
KO	knockout
LIR	LC3-interacting region
LSM	laser scanning microscopy
(MAP1)LC3	microtubule-associated proteins 1A/1B light chain 3
MHC-I/II	major histocompatibility complex class I/II
mRNA	messenger ribonucleic acid
MS	mass spectrometry
mTORC1	mechanistic target of rapamycin complex 1
MV	microvesicle
MVB	multivesicular body
NBD C$_{\mathbf{6}}$	6-((N-(7-Nitrobenz-2-Oxa-1,3-Diazol-4-yl)amino)-hexanoyl)
NSF	N-ethylmaleimidesensitive factor
P/S	penicillin/streptomycin
PAS	phagophore assembly site

PBS	phosphate-buffered saline
PE	phosphatidylethanolamine
PI$_3$K	phosphatidylinositol-3-kinase
PI(4,5)P$_2$	phosphatidylinositol-4,5-bisphosphate
PI$_3$P	phosphatidylinositol-3-phosphate
PM	plasma membrane
POI	protein of interest
PRIP	phospholipase C-related catalytically inactive protein
RBP	RNA-binding protein
SH-SY5Y	human neuroblastoma
SKO	single knockout
SMLM	single molecule localisation microscopy
SRP	signal recognition particle
Tat	trans-activator of transcription
TBS	Tris-buffered saline
TEM	transmission electron microscopy
TGFβ1	transforming growth factor β 1
TGN	*trans*-Golgi network
TKO	triple knockout
TSG101	tumor susceptibility gene 101 protein
UIM	ubiquitin-interacting motif
ULK1	Unc-51 like autophagy activating kinase 1
Ume6	unscheduled meiotic gene expression protein 6)
Unc-51	uncoordinated protein 51
UPS	unconventional protein secretion
v-SNARE	vesicle synaptosome-associated protein receptor
WT	wild-type

List of Figures

List of Tables

Chapter 1

Introduction

1.1 Autophagy

Maintaining cellular homeostasis is essential for survival across all domains of life. In eukaryotic cells, a conserved process called autophagy plays a crucial role to fulfil this task. Derived from the greek words $\alpha \upsilon \tau o \varsigma$ (autós) and $\varphi \alpha \gamma \epsilon \iota \nu$ (phagein), the term "autophagy" originally defines a self-eating mechanism leading to the degradation of intracellular components, providing metabolites required by the cell.

Since its first description in the 1960s [1–3], more and more details and the from yeast to mammals increasing degree of complexity, including different types of autophagy, were discovered. Macroautophagy, sequestering cytoplasmic cargo and involving the *de novo* synthesis of a double-lipid bilayer membrane [4], microautophagy, meaning the engulfment of cargo by lyso- or endosomal membranes [5], and chaperone-mediated autophagy, selectively targeting cytosolic proteins and transporting them into the lysosomal lumen [6], embody the three major types of autophagy. In the following, the focus shall be placed on macroautophagy, hereafter referred to as autophagy, as this process represents the basis of this work.

In healthy cells and under the condition of full nutrient supply, basal autophagy serves as recycling and quality control mechanism. However, an upregulation of the autophagic process is induced by stress conditions such as nutrient deprivation, infections, hypoxia, or accumulation of protein aggregates [7]. Malfunctions in the autophagic machinery are thus associated with neurodegenerative diseases [8–10], aging [11, 12], and cancer [13, 14]. Moreover, although autophagic proteins can be involved in the clearance from invading pathogens [15, 16], they may also serve viral replication and transmission [17–20]. Therefore, apart from fundamental research, a detailed knowledge of the mechanisms underlying autophagy is crucial for a deepened understanding of these pathologies.

Autophagy is a multi-step process, each of the steps being regulated by proteins encoded by the so-called autophagy-related (ATG) proteins. Yoshinori Ohsumi, awarded with the 2016 Nobel Prize in Physiology or Medicine, discovered the first Atg proteins in yeast [21, 22] and thereby laid the foundation for present-day's knowledge on the autophagic pathway.

Summarised, autophagy begins with an initiation step which leads to the formation of the phagophore, a crescent-shaped membrane compartment which is further extended and eventually closed, forming a double-membrane vesicle. This vesicle is defined as the autophagosome and contains the autophagic cargo, for example cytosolic proteins or even cell organelles like mitochondria. When the autophagosome then fuses with a lysosome, an autolysosome is created in which both the inner membrane and the cargo are degraded by acid hydrolases provided by the lysosome. The thereby obtained metabolites are finally transported back into the cytosol and recycled [23].

As stated above, autophagy can be initiated by cellular stresses such as nutrient deprivation. Under nutrient-rich conditions, mechanistic target of rapamycin complex 1 (mTORC1) is associated with a complex of Uncoordinated protein 51 (Unc-51) like autophagy activating kinase 1 (ULK1), ATG13, focal adhesion kinase family interacting protein of 200 kDa (FIP 200), and ATG101. The serine/threonine kinase mTORC1 phosphorylates ATG13 and ULK1, thereby inhibiting ULK1's kinase activity. Under starvation, however, mTORC1 dissociates from the complex and ATG13 and ULK1 become dephosphorylated. ULK1 can now phosphorylate itself, ATG13, and FIP 200, leading to a change in phosphorylation status and thereby to the initiation of autophagy [24–26] (Figure 1.1A). In yeast, the formation of an autophagosome starts at a single phagophore assembly site (PAS) [27]. In mammals, on the other hand, autophagosomes can form at multiple cellular locations at the same time. Activation of the ULK1 complex precedes the formation and recruitment of the class III phosphatidylinositol-3-kinase (PI$_3$K) complex, consisting of ATG14, Beclin-1, Vps15, and the PI$_3$K Vps34. The latter produces phosphatidylinositol 3-phosphate (PI$_3$P) that supports nucleation and formation of the omegasome [28, 29], a structure which is thought to be the origin of the autophagosome [30]. The lipid source for autophagosome formation is not entirely clear yet, although recent results are pointing towards the endoplasmic reticulum (ER) [31]. In yeast, phagophore-ER contact sites were shown to be established by a complex formed by the transmembrane protein Atg9, Atg2 which promotes phagophore tethering with the ER, and the PI$_3$P binding protein Atg18 [32] (Figure 1.1B).

Following nucleation of the autophagosomal membrane, two ubiquitin-like conjugation systems are responsible for elongation and closure of the autophagosomal membrane. Firstly, the ubiquitin-like protein ATG12 is activated by the E1-like enzyme ATG7, transferred to the E2-like enzyme ATG10, and then conjugated to ATG5 which interacts with ATG16L, leading to the generation of the ATG12-ATG5-ATG16L complex. Secondly, the ubiquitin-like protein ATG8 is cleaved by ATG4 at its C-terminal glycine 116, making it possible to bind to ATG7. ATG8 is then transferred to the E2-like enzyme ATG3 and finally conjugated to a lipid anchor, e.g. phosphatidylethanolamine (PE) [33]. This modification enables lipidated ATG8, hereafter referred to as ATG8-II, to attach to (autophagosomal) membranes, while the unlipidated form of ATG8, from now on called ATG8-I, is present in the cytosol [34]. Here, it has to be noted that mammalian ATG8 forms a protein family, subdivided into the γ-aminobutyric acid (A) (GABA$_\mathrm{A}$) receptor-associated protein (GABARAP) and microtubule-associated proteins 1A/1B light chain 3 (MAP1LC3, hereafter LC3) subfamilies, which is discussed in a more detailed manner in the following section (1.1.1). Both conjugates are localised to the growing phagophore, ATG8-II on both sides of the membrane, while the ATG12-ATG5-ATG16L complex is rather found on the convex side which will become the outer side of the autophagosome [33]. Presence of the ATG12-ATG5-ATG16L complex is essential for the localisation of ATG8-II to the phagophore, which leads to the elongation of the membrane (LC3 subfamily) and finally the closure of the autophagosome (GABARAP subfamily) [35], followed by dissociation of the ATG12-ATG5-ATG16L complex [33, 36] and degradation of autophagic cargo (Figure 1.1C).
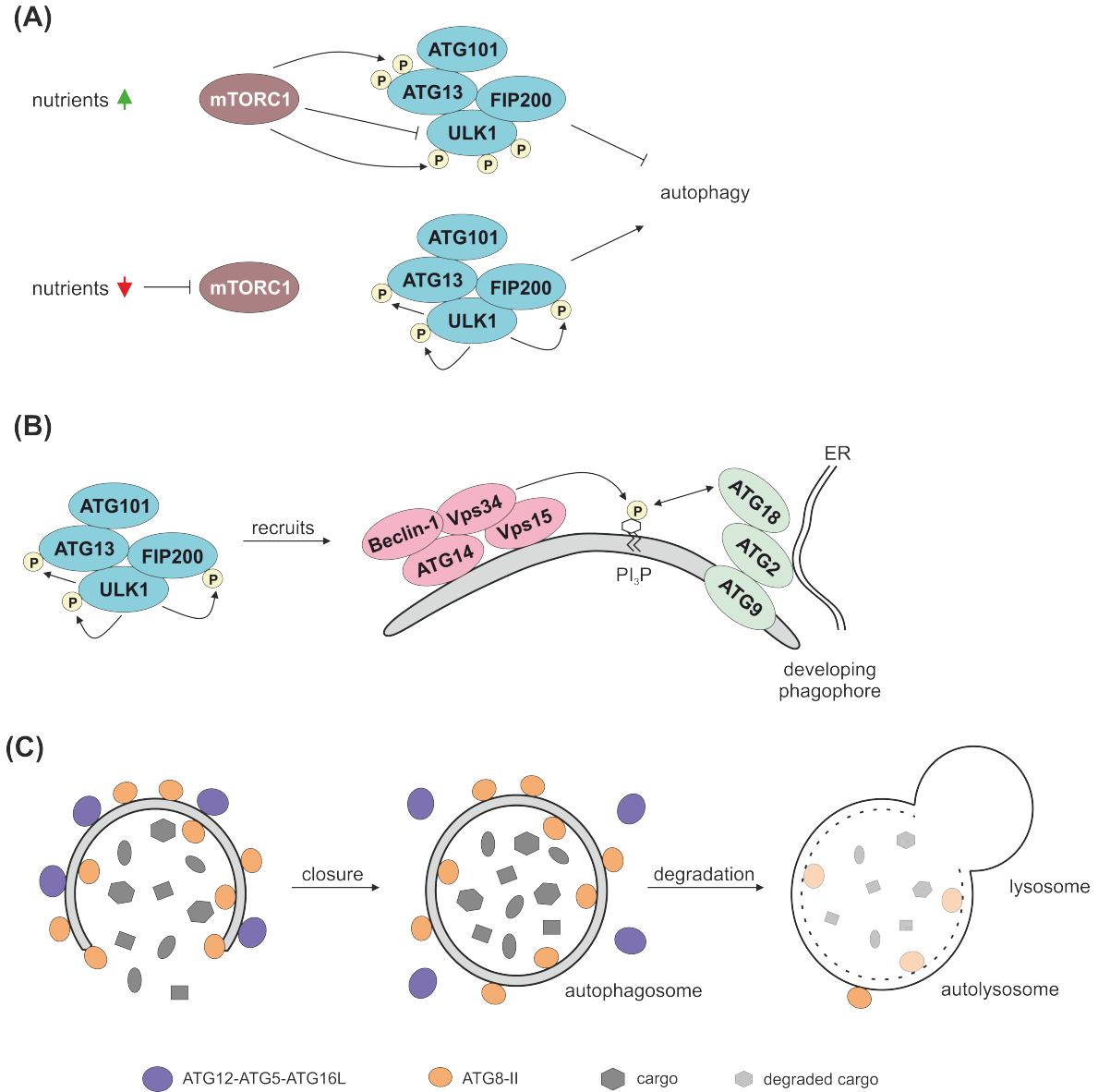
(A)

(B)

(C)

Figure 1.1: Schematic of autophagosome formation and the autophagic process. (A) Under nutrient-rich conditions, mTORC1 associates with the ULK1 complex (light blue). Under nutrient deprivation, mTORC1 dissociates from the ULK1 complex, leading to autophagy initiation. (B) The ULK1 complex recruits the PI$_3$K complex (light red) which facilitates the development of the phagophore together with the ATG9 trafficking system (light green). (C) The ubiquitin-like conjugates ATG12-ATG5-ATG16L (violet) and ATG8-II (orange) localise to the expanding phagophore, eventually closing to form an autophagosome and fusing with a lysosome to complete the degradation process.

1.1.1   The ATG8 Protein Family

Throughout the autophagic process, the highly conserved ATG8 proteins play an essential role. As described above (section 1.1), ATG8 is lipidated by a ubiquitin-like conjugation system, attached to the growing phagophore, and involved in its elongation and closure to finally form an autophagosome. The mammalian ATG8 protein family consists of seven members which are assigned to two subfamilies: On the one hand the GABARAP subfamily ("GABARAPs"), consisting of the three proteins GABARAP, GABARAP-like 1 / glandular epithelial cell 1 (GABARAPL1/GEC1), and GABARAP-like 2 / Golgi-associated ATPase enhancer of 16 kDa (GABARAPL2/ GATE-16), and on the other hand the LC3 subfamily ("LC3s"), consisting of the four proteins LC3A, LC3B, LC3B2, and LC3C [37]. In yeast, however, only one Atg8 protein exists, which was originally identified as homologue of LC3 [38] (Figure 1.2).
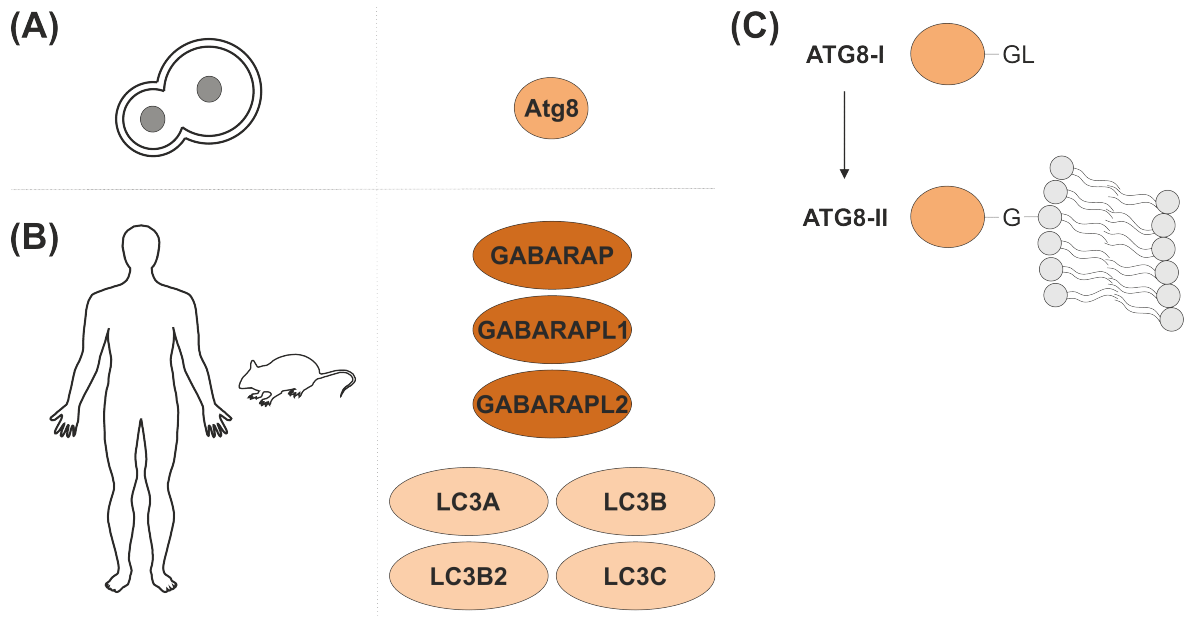

Figure 1.2: The ATG8 protein family. While yeast cells contain only one Atg8 protein (A), there are seven ATG8 orthologues in mammals, subdivided into the GABARAP subfamily and the LC3 subfamily (B). ATG8 proteins may be processed from unlipidated ATG8-I to lipidated ATG8-II; the latter is able to localise to membranes (C) (also compare section 1.1).

Despite their high sequence similarity [39, 40], the GABARAPs and LC3s exhibit different functions during autophagosome biogenesis, the LC3s being engaged at the earlier stage of phagophore elongation and the GABARAPs at the later timepoint of autophagosome closure [35]. Only recently it was observed that by interaction with ULK1, the GABARAPs are even essential for starvation-induced activation of ULK1 and the subsequent initiation of phagophore formation, while the LC3s might rather

negatively affect ULK1 activity [41]. It was furthermore shown that yeast Atg8 levels determine the size rather than the number of autophagosomes [42]. Consistent with these results, it was demonstrated that in a yeast $ume6\Delta$ strain, lacking the transcription factor Ume6 (Unscheduled meiotic gene expression protein 6) which negatively regulates Atg8 transcription [43], larger autophagosomes are formed [44]. Potentially, cells could be able to modulate the size of autophagosomes for example modifying the rate of Atg8 conjugation or its distribution within the cell [45, 46]. On the other hand, loss of Atg8 leads to the formation of smaller autophagosomes in yeast [47] and also in mammalian cells after knockout of all ATG8 family members. Still, the ATG8s were shown to be essential for the autophagosome-lysosome fusion process, with the GABARAPs playing a more prominent role than the LC3s [48].

Although in present ATG8-concerning research the focus is laid predominantly on autophagy, this is not the only function of these proteins. In fact, LC3B, which was the first mammalian ATG8 protein to be discovered, was identified in the context of microtubule-associated proteins [49], although it was not shown to be involved in transport processes itself [37]. GABARAPL2, on the contrary, was immediately identified as intra-Golgi trafficking protein which takes part in Golgi transport processes through $N-$ethylmaleimidesensitive factor (NSF)-dependent interaction with the vesicle synaptosome-associated protein receptor (v-SNARE), and whose activity may be restored by yeast Atg8 *in vitro* [50–52]. Also GABARAP, which was originally described as protein connecting the GABA$_A$ receptor with tubulin, was demonstrated to be localised to transport vesicles and to be involved in the trafficking of the GABA$_A$ receptor to the plasma membrane [39, 53]. In this context, the C-terminal modification of GABARAP was shown to be essential for its trafficking function, as the GABA$_A$ receptor surface expression was reduced after GABARAP(G116A) mutation that prevents cleavage and subsequent lipid conjugation [54]. An investigation of the exact binding capacities of GABARAP revealed the presence of two hydrophobic, tryptophan-binding pockets on the surface of the protein. These pockets were shown to be crucial for binding not only of the $\gamma2$ subunit of the GABA$_A$ receptor [55]. Several further proteins were reported to be ligands of GABARAP, for example ULK1 [56], the human Transferrin receptor [57], Calreticulin [58], and Clathrin heavy chain [40]. Additionally, it was demonstrated that GABARAP functions in a complex together with Phospholipase C-related catalytically inactive protein (PRIP) and the motor protein Kinesin-1 heavy chain (KIF5B) to facilitate vesicle-mediated insulin secretion [59].

Most of these ligands share a common hydrophobic motif, the so-called LC3-interacting region (LIR) [60], in yeast named Atg8-interacting motif (AIM) [61]. Only recently, further motifs were discovered which enable binding to ATG8 proteins: a

GABARAP interaction motif (GIM), which exhibits a higher specificity to GABARAP than to LC3B and might help to identify further specific functions of GABARAP and its ligands [62], and a ubiquitin-interacting motif (UIM), which facilitates high-affinity binding to an alternative ATG8 interaction site [63]. Altogether, the ATG8 proteins exhibit a large variety of functions, of which especially the unique features within the LC3 and GABARAP subfamilies are yet to be uncovered.

1.2 Secretion

After their synthesis at the ribosome, newly produced proteins need to reach their final destination. Proteins which carry out their function at the plasma membrane (PM) or in extracellular space are transported to and across the PM via various transport mechanisms, subdivided into conventional (1.2.1) and (1.2.2) unconventional secretion processes.

1.2.1 Conventional Secretion

In eukaryotes, most secretory proteins are secreted by the highly conserved conventional secretion pathway which involves the translocation of the secretory protein from the endoplasmic reticulum (ER) via the *trans*-Golgi network (TGN) to the PM [64,65] (Figure 1.3). Conventionally secreted proteins share a common feature, an N-terminal signal sequence of about 13-30 hydrophobic amino acids [66]. During protein biosynthesis, the signal sequence and also the translating ribosome are bound co-translationally by the signal recognition particle (SRP), an interaction inhibiting further translation [67, 68]. The complex of SRP, ribosome, and the nascent secretory protein is targeted to the ER by associating with the membrane bound SRP receptor. Here, the SRP and its receptor dissociate from the ribosome-protein complex, while the latter is transferred to the Sec61 complex, termed the translocon [69, 70]. Subsequently, the ribosome resumes its activity, leading to direct translation of the secretory protein into the ER [70]. At this point, quality control occurs via unfolded protein response and ER-associated degradation, a process by which misfolded proteins are translocated back into the cytosol and thereby targeted for proteasomal degradation [71, 72]. Correctly folded proteins leave the ER through the so-called ER-exit site (ERES) via coatomer protein complex-II (COPII)-mediated transport. Assembly of COPII vesicles occurs by recruitment of the GTPase Sar1 (secretion-associated RAS-related 1), which is activated by the guanine nucleotide exchange factor (GEF) Sec12 [73,74] and then binds to the Sec23/Sec24 heterodimer. Together with the Sec13/Sec31 heterotetramer it forms the outer COPII layer [75, 76]. After budding from the ER membrane, the COPII vesicles are transported to an ER-Golgi intermediate compartment (ERGIC) located

between the ER and the *cis*-side of the Golgi apparatus. At the ERGIC, secretory proteins are packed in coatomer protein complex-I (COPI) coated vesicles which are not only involved in anterograde transport to the Golgi and later the PM, but also in retrograde transport back to the ER [77,78]. Then, they are transported through the Golgi cisternae [79] to the PM-facing TGN and during passage post-translationally modified, e.g. glycosylated [80]. Upon arrival at the TGN, the proteins are finally packed in secretory clathrin-coated vesicles and transported to the PM [81].
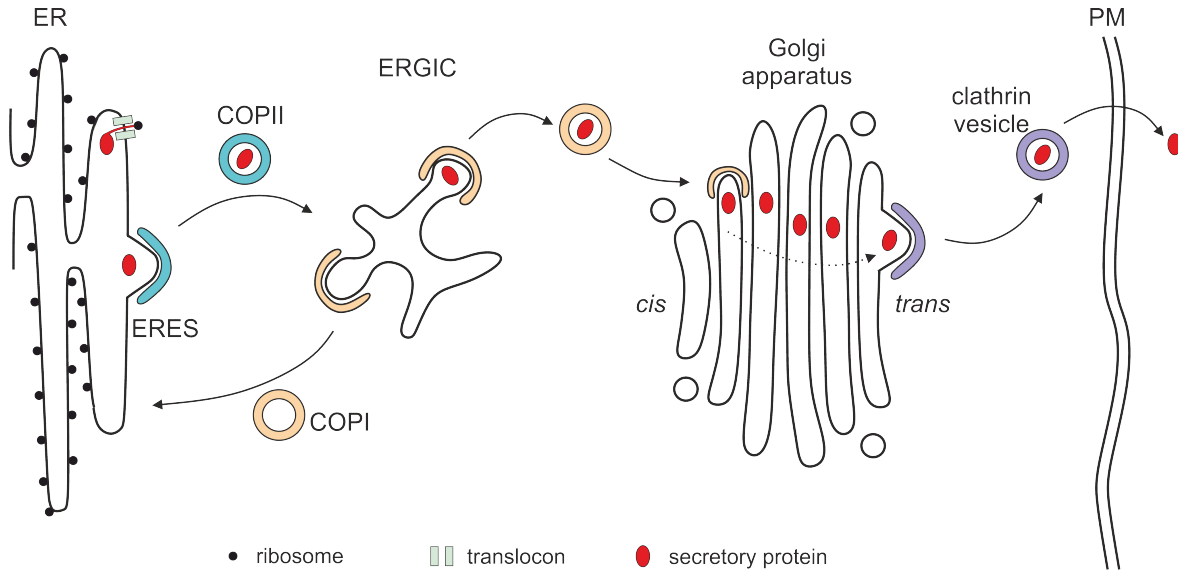

Figure 1.3: Conventional secretion pathway. Secretory proteins are translated through the translocon into the ER. After correct folding of the protein it is packed into a COPII vesicle and leaves the ER at the ERES, from where it is transported to the ERGIC. Further transport to the Golgi apparatus is mediated by COPI vesicles. As soon as the secretory protein reaches the *trans*-Golgi side, the final tranlocation step to the PM is conducted by clathrin coated vesicles.

1.2.2   Unconventional Secretion

A signal sequence is not the only, ultimate trigger for initiating the secretion of a protein. In fact, a rising number of proteins lacking a signal sequence were shown to be secreted independently of the conventional pathway. The first protein which was discovered to be unconventionally secreted was interleukin-1β (IL-1β) almost thirty years ago [82]. Unconventional protein secretion (UPS) may affect both leaderless cytosolic and also transmembrane proteins and, in the most cases, is triggered by stress. Different UPS pathways were uncovered by now and may be characterised into the UPS types I-IV with respect to the involvement of membranes and cellular compartments [83] (Figure 1.4).
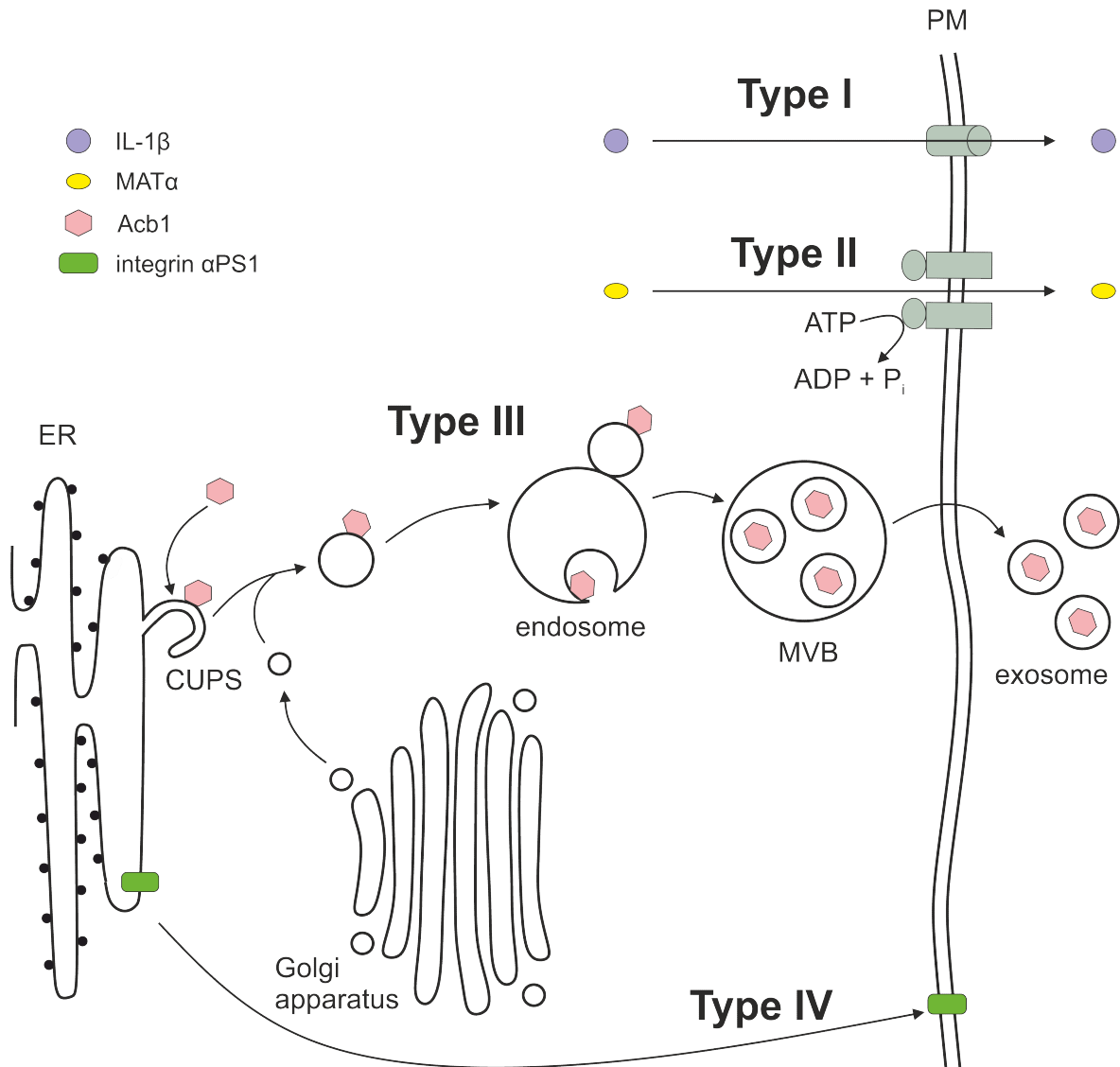
Figure 1.4: Unconventional secretion pathways. Cytosolic proteins lacking a signal sequence may be secreted in a non-vesicular manner through a membrane pore (type I UPS, e.g. IL-1β) or ABC transporters (type II UPS, e.g. MATα), or in a vesicular manner involving endosomal compartments (type III UPS, e.g. Acb1). Transmembrane proteins may furthermore traffic to the PM by Golgi bypass (type IV UPS, e.g. integrin αPS1).

The UPS types I and II are non-vesicular secretion pathways [84]. Type I UPS describes the transport of a folded protein directly across the PM through a pore. Examples for proteins secreted by this mechanism are the fibroblast growth factor 2 (FGF2) [85] and the HIV Trans-activator of transcription (Tat) protein. Through interaction with phosphatidylinositol 4,5-bisphosphate (PI(4,5)P$_2$), FGF2 and HIV Tat are directed to the PM where they oligomerise and form a lipidic membrane pore, thereby enabling translocation to the extracellular side of the PM [86, 87]. Also IL-1β can be secreted by type I UPS, although in this case, IL-1β itself is not involved in

pore formation. Instead, IL-1β secretion was observed in connection to cellular hyper-permeabilisation [88]. Both the IL-1β precursor protein and gasdermin are cleaved by caspase-1. The obtained gasdermin-N, just as FGF2 and HIV Tat, is recruited to the PM by PIP$_2$ where it formes a pore, possibly facilitating IL-1β secretion [89]. Type II UPS is defined as secretion via adenosine triphosphate (ATP) binding cassette (ABC) transporters and is the least studied UPS mechanism [83]. The yeast mating factor MATα, transported by Ste6p, is the best-known example [65,90]. Besides, also acety-lated proteins like hydrophilic acylated surface protein B (HASPB) from *Leishmania* spp. [91] or *Plasmodium falciparum* Ca^{2+}-dependent protein kinase 1 (PfCDPK1) [92] are assigned to type II UPS [84].

Type III and IV UPS are characterised as vesicular secretion pathways [84]. Start-ing with type IV UPS, this pathway is utilised by transmembrane proteins which are synthesised at the ER, just as proteins transported by the conventional secretion path-way. However, type IV UPS does not include a translocation step through the Golgi apparatus and is therefore also referred to as "Golgi bypass" mechanism. This path-way was first described in 1990 for vesicular stomatitis virus G protein (VSV-G) [93] and was also shown to be the cell-surface trafficking mechanism of *Drosophila* inte-grin αPS1 [94] and folding-deficient ΔF508-cystic fibrosis transmembrane conductance regulator (CFTR) [95]. Intriguingly, although these proteins bypass the Golgi, a depen-dency on the Golgi reassembly-stacking proteins (GRASPs) was demonstrated [94,96], Golgi proteins which, too, play a role in type III UPS. The latter mechanism is generally described as secretion pathway for cytoplasmic proteins involving the endosomal sys-tem, originally discovered for *Dictyostelium* acyl-CoA-binding protein AcbA [97,98]. In yeast, its orthologue Acb1 was proven to be secreted not only in a GRASP-dependent manner, but also in dependency on the endosomal sorting complexes required for trans-port (ESCRT) machinery. ESCRT proteins are involved in the formation of multivesicu-lar bodies (MVBs), a cellular compartment generated by inward budding of endosomes and containing intraluminal vesicles (ILVs). Upon fusion with the PM, the ILVs are released as exosomes into the extracellular space (compare 1.2.3), in this case setting free Acb1. The secretion of Acb1 was found to be triggered by starvation, indicating an involvement of the autophagic machinery. And indeed, Atg proteins, but not neces-sarily autophagosomes, were shown to be essential for Acb1 secretion [99,100]. A spe-cific membrane compartment, the compartment of unconventional secretion (CUPS), was proposed to be the origin of secretory membranes. Under starvation, but impor-tantly not by rapamycin-induced autophagy activation, formation of CUPS occurs near ERES and dependent on COPI- and COPII-independent membrane recruitment from the Golgi. Then, acetylated Acb1 is recruited to the CUPS, fuses with endosomes, and is secreted by formation of MVBs and subsequent fusion with the PM [101–103].

Although for yeast Acb1 an involvement of autophagy itself was not proven, there are indications for an autophagosome-mediated secretion mechanism in mammalian cells. For example, the aforementioned IL-1β was demonstrated to be secreted not only by type I, but also type III UPS. Together with caspase 1, IL-1β is found in secretory lysosomes [104]. Induction of autophagy increased IL-1β secretion [105]. Another example is Transforming growth factor β 1 (TGFβ1), the unconventional secretion of which was inhibited by block of autophagy. It was also shown that binding of the ATG8 LC3 proteins to Golgi reassembly-stacking protein of 55 kDa (GRASP55) is required for TGFβ1 secretion [106]. The exact mechanism of secretory autophagy is not yet clear. However, it was proposed that the omegasome, a PI$_3$P-rich structure possibly involved in autophagosome formation (1.1), might be the CUPS equivalent in mammals due to its morphology, ER vicinity, and its inducibility by starvation and may thus play a role in mammalian secretory autophagy. After maturation, the secretory autophagosome may fuse with an MVB, yielding a so-called amphisome, eventually leading to the release of exosomes containing secretory cargo proteins [107–109].

1.2.3 Extracellular Vesicles

Extracellular vesicles (EVs) represent an additional field of UPS and facilitate the secretion of both cytosolic and transmembrane proteins. As a generic term, EVs comprise particles released from cells under natural conditions, which are enveloped by a lipid bilayer, and are not able to replicate. Depending on their size, cellular origin, biochemical characteristics, and molecular markers, EVs may be classified in different subtypes [110]. However, the exact nomenclature is still an issue for discussion [111]. Therefore, in the following the focus is placed on the two most frequently described EV types, microvesicles (MVs) and exosomes.

The so-called MVs, also referred to as ectosomes or microparticles, are defined as PM-derived EVs with a size of 100-1000 nm [112]. The smaller-sized exosomes are characterised by a diameter of 30-100 nm and generated by a more complex pathway than MVs. The biogenesis of exosomes starts with membrane protein internalisation as initially shown in this context for the transferrin receptor [113, 114], thereby forming early endosomes. Inward budding causes the accumulation of ILVs inside the endosome which, from now on, is called MVB. The formation of MVBs is regulated by the ESCRT machinery which is subdivided into four complexes fulfilling distinct functions during MVB biogenesis: ubiquitin-dependent cargo assembly (ESCRT-0), budding (ESCRT-I and -II), and vesicle scission (ESCRT-III). After its formation, an MVB may either enter the degradative pathway by fusing with a lysosome, or it fuses with the PM and in the process releases the ILVs as exosomes. Depletion of certain ESCRT proteins leads to decreased exosome secretion; however, it has to be noted that cells lacking key ESCRT

components are still able to form MVBs. ESCRT-independent MVB generation involves lipid-metabolising enzymes, e.g. phospholipase D2 [115]. The rate of exosome secretion may also be affected by the autophagic machinery. Treatment with Bafilomycin A1, a commonly used compound for inhibiting autophagosomal degradation, lead to an increased release of exosomes [116]. Autophagy induction, on the other hand, resulted in an inhibition of exosome secretion [117]. Moreover, the autophagy proteins ATG5 and ATG16L1 were shown to reduce MVB acidification, thereby reducing MVB degradation and increasing exosome secretion [118]. An overlap of the autophagic and exosomal pathway supposedly occurs in a fusion step of autophagosomes and MVBs, thereby generating amphisomes. Analogously to MVBs, the amphisomes may release their content into the extracellular space upon fusion with the PM [108, 119] (Figure 1.5A).

Being present in various body fluids and tissues, it was shown that EVs facilitate intercellular communication. The HIV-1 Nef protein, for example, utilises EVs for its intercellular transport to bystander cells, thereby increasing HIV-1 pathogenicity [120]. Also exchange of genetic information is promoted through transfer of messenger ribonucleic acid (mRNA) and its subsequent translation by the recipient cell [121, 122]. EVs may furthermore support the spreading of proteins related to neurological pathologies, e.g. Alzheimer's disease [123], and of tumour cells by modifying the cellular physiology of non-tumour cells [124]. On the other hand, EVs can also stimulate anti-tumour immune responses [125]. A therapeutic application seems therefore obvious. Indeed, usage of mainly dendritic cell-derived EVs as anti-tumour vaccines by activating tumour-specific cytotoxic T cells or as vaccines against infectious agents such as *Toxoplasma gondii* by carrying pathogen-specific antigens was implemented. Furthermore, EVs are investigated as systems for drug delivery, e.g. RNA therapeutics due to their natural function as RNA carrier [126].

Implementation of EVs in clinical applications requires optimised protocols for EV isolation and analysis. However, no methodical gold standard has been established yet. In attempt to define a basis for optimising the quality of EV-related studies, a list of requirements was compiled, namely the Minimal Information for Studies of Extracellular Vesicles (MISEV). These requirements relate, amongst others, to EV enrichment, storage, quantification, and downstream analysis [110]. Enrichment methods are generally classified regarding their EV recovery and specificity. High-recovery methods based on polymers or ultracentrifugation might lead to the isolation not only of EVs but also e.g. large protein aggregates, and are hence less specific [127]. Application of filtration steps or density gradients may enhance specificity in the isolation of EV subtypes, but decreases recovery [110]. The properties of an EV sample may be determined by microscopic methods (vesicle integrity, size, count) and by immunoblotting

and/or mass spectrometry to detect marker proteins. As exosomes and MVs share a large overlap in their protein content and a separation of exosomes and MVs is not completely possible yet [115,128], EVs in general are described at this point. Examples for commonly used EV marker proteins are endosome-associated proteins, like Annexins or Rab GTPases, components of the ESCRT machinery, e.g. apoptosis-linked gene 2 (ALG-2)-interacting protein X (Alix) or Tumor susceptibility gene 101 protein (TSG101), tetraspanins, like CD63 and CD81, cytoskeletal constituents, such as actin or tubulin, heat shock proteins, e.g. heat shock 70 kDa protein 8 (Hsc70), integrins, and major histocompatibility complex class I (MHC-I) molecules. EVs were also found to contain lipid rafts and are enriched in cholesterol, sphingomyelin, and ceramides [112,125] (Figure 1.5B). For validation, MISEV recommends confirming the presence of at least three EV marker proteins [110]. Databases specialised on EVs, such as Vesiclepedia [129] or EV-TRACK [130], may support transparent reporting on EV data and methodologies, thus enhancing experimental consistency and reproducibility.
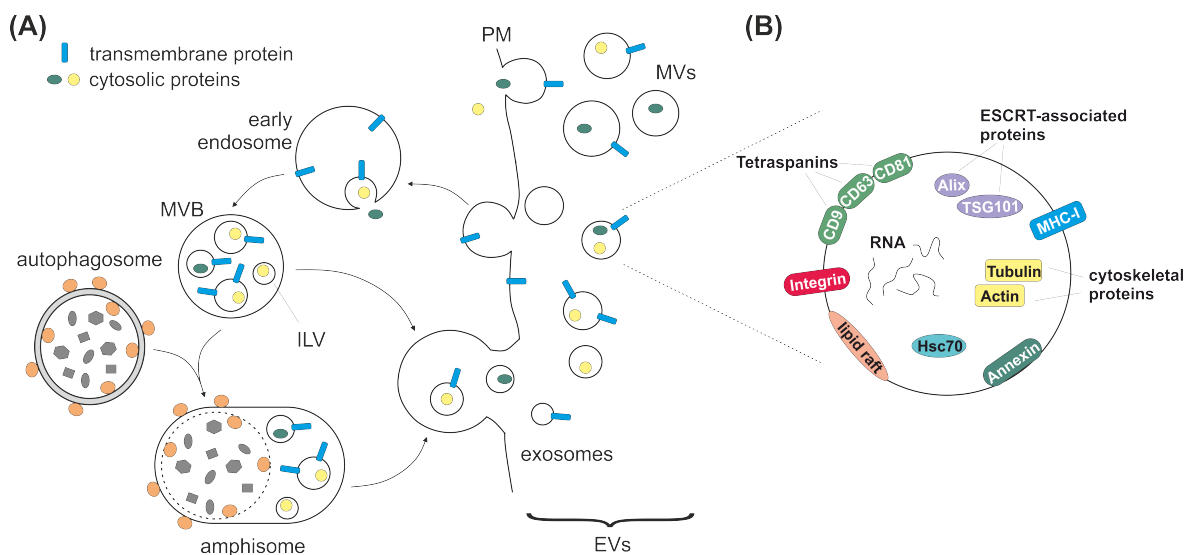

Figure 1.5: Biogenesis and composition of EVs. (A) EVs are generated either by outward budding of the PM, thereby setting free MVs, or via the endosomal pathway. Inward budding of an endosome leads to formation of an MVB which may eventually fuse with the PM and releases ILVs as exosomes. Before fusion with the PM, an MVB might fuse with an autophagosome yielding an amphisome. (B) Typical composition of an EV.

The range of applications and possibilities to modulate the biosynthesis, secretion, and composition of EVs is as large as the variety of EVs themselves. Being able to isolate a specific EV subfraction, to analyse its content, to modify its composition for therapeutic use, or to intervene in the generation of disease promoting EVs, are and will be major topics in current and future EV research.

Chapter 2

Aims

GABARAP, as implied by its classification into the autophagy-related ATG8-protein family, fulfils fundamental roles during autophagy. However, it was initially discovered as a trafficking protein, being essential for the transport of e.g. the $GABA_A$ receptor to the plasma membrane. Therefore, in the frame of this work, GABARAP should be studied regarding not only in the context of autophagy, but rather its involvement in secretion and transport processes independent of autophagy.

2.1 GABARAP's secretion in extracellular vesicles

Although GABARAP was shown to be involved in protein transport and secretion processes and was also detected in extracellular vesicles in various studies, the framework and mechanism of GABARAP's secretion remain unclear. Aiming to decipher the fundamentals of this process, in this work first the extent of GABARAP's secretion should be investigated. For this, EVs isolated from the culture supernatant of different human cell lines and from human and bovine blood plasma shall be analysed for the presence of GABARAP. As GABARAP is known to be lipidated during the autophagic process, the question needs to be clarified whether GABARAP is secreted in its lipidated or unlipidated form. Furthermore, it shall be investigated what kind of vesicles are involved in GABARAP's secretion, and whether GABARAP is secreted by a specific EV subtype, respectively. Recently, for confined intracellular vesicular compartments like autophagosomes, a proximity-based approach delivered promising results regarding the respective proxitome of human Atg8-type proteins. This proximity labelling approach is based on the engineered ascorbate peroxidase APEX2 which labels proteins in its proximity by biotinylation. Whether a similar approach is applicable to determine the co-secretome of a certain protein of interest (POI), in this case GABARAP, in extracellular vesicles is one the main questions covered in this thesis. Therefore, both the activity of APEX2-GABARAP within EVs and the suitability of the resulting pool

of biotinylated proteins for a comprehensive mass spectrometric analysis shall be examined. In case a co-secretome of APEX2-GABARAP can be defined in such a way, respective results shall be subjected to an in-depth gene ontology (GO) analysis and compared with independent data sets. Finally, participating cellular compartments and mechanisms involved in the biogenesis of GABARAP-containing EVs shall be proposed.

2.2   The roles of the GABARAPs in Golgi-mediated transport

Conventional protein transport and secretion processes are based on the Golgi apparatus as central trafficking organelle of the cell. GABARAPL2, a paralogue of GABARAP, was found to modulate intra-Golgi transport and to be required for post-mitotic Golgi reassembly. Although also GABARAP is known to interact with Golgi-localised proteins, a direct involvement of GABARAP in maintaining Golgi integrity was not yet shown. As the GABARAP subfamily is highly homologous and all three members were shown to take part in receptor trafficking, here the GABARAPs shall now be studied with respect to their Golgi-related functions by fluorescence microscopy of labelled ceramide, targeting the whole Golgi complex, and of immunolabelled TGN46 as marker protein for the TGN. In this context, the lipid metabolism in wild-type (WT) compared to GABARAP/L1/L2$^{\text{triple knockout (TKO)}}$ cells is of special interest, because the lipid composition of the Golgi influences vesicle formation at the TGN and consequently protein transport. In a ceramide chase experiment, following intracellular membrane labelling over time, the contributions of the GABARAPs in this matter shall be uncovered. Hence, in this part of the thesis the effect of GABARAPs' triple-knockout not only on the Golgi structure, but also on lipid trafficking shall be examined.

2.3   High-resolution study of ATG8-containing structures

Analysis of autophagic structures is commonly performed by conventional fluorescence microscopy, using common marker proteins for autophagy such as LC3B which is like GABARAP a member of the ATG8 protein family. However, considering the size of autophagy-related compartments of $\sim$50 nm-1.5 µm, it becomes apparent that for a complete characterisation conventional microscopy cannot display the whole information due to the optical diffraction limit. Therefore, contributions shall be made to a comprehensive super-resolution microscopy study investigating the localisation of

EYFP-GABARAP and EYFP-LC3B to differently shaped structures, aiming towards a characterisation of distinct structures labelled by these two proteins.

Chapter 3

Scientific publications

3.1 The GABARAP Co-Secretome Identified by APEX2-GABARAP Proximity Labelling of Extracellular Vesicles.

Authors	J. L. Sanwald, G. Poschmann, K. Stühler, C. Behrends, S. Hoffmann, and D. Willbold.
Journal	Cells (2020), published on 16 June 2020
DOI	10.3390/cells9061468
Impact Factor	4.366 (2019); 5-Year Impact Factor: 5.276 (2019)
Contribution to the manuscript	Planning and performing the experiments
	Data analysis and figure creation
	Writing and editing of the manuscript

Reprint Permission   This section contains a complete reprint of the publication published in Cells (https://www.mdpi.com/journal/cells). Copyright 2020 by the authors. Licensee MDPI, Basel, Switzerland. This article is an open access article distributed under the terms and conditions of the Creative Commons Attribution (CC BY) license (http://creativecommons.org/licenses/by/4.0/).

Article

The GABARAP Co-Secretome Identified by APEX2-GABARAP Proximity Labelling of Extracellular Vesicles

Julia L. Sanwald [1,2] , **Gereon Poschmann** [3] , **Kai Stühler** [3,4] , **Christian Behrends** [5] , **Silke Hoffmann** [2,]* and **Dieter Willbold** [1,2,]*

1. Institut für Physikalische Biologie, Heinrich-Heine-Universität Düsseldorf, Universitätsstraße 1, 40225 Düsseldorf, Germany; julia.sanwald@uni-duesseldorf.de
2. Institute of Biological Information Processing (IBI-7: Structural Biochemistry), Forschungszentrum Jülich, Leo-Brandt-Straße, 52428 Jülich, Germany
3. Institute of Molecular Medicine I, Heinrich-Heine-Universität Düsseldorf, Universitätsstraße 1, 40225 Düsseldorf, Germany; gereon.poschmann@uni-duesseldorf.de (G.P.); kai.stuehler@uni-duesseldorf.de (K.S.)
4. Molecular Proteomics Laboratory, Biologisch-Medizinisches Forschungszentrum (BMFZ), Heinrich-Heine-Universität Düsseldorf, Universitätsstraße 1, 40225 Düsseldorf, Germany
5. Munich Cluster for Systems Neurology (SyNergy), Ludwig-Maximilians-Universität München, Feodor-Lynen-Straße 17, 81377 München, Germany; christian.behrends@mail03.med.uni-muenchen.de
* Correspondence: si.hoffmann@fz-juelich.de (S.H.); d.willbold@fz-juelich.de (D.W.); Tel.: +49-2461-619389 (S.H.); +49-2461-612100 (D.W.)

Abstract: The autophagy-related ATG8 protein GABARAP has not only been shown to be involved in the cellular self-degradation process called autophagy but also fulfils functions in intracellular trafficking processes such as receptor transport to the plasma membrane. Notably, available mass spectrometry data suggest that GABARAP is also secreted into extracellular vesicles (EVs). Here, we confirm this finding by the immunoblotting of EVs isolated from cell culture supernatants and human blood serum using specific anti-GABARAP antibodies. To investigate the mechanism by which GABARAP is secreted, we applied proximity labelling, a method for studying the direct environment of a protein of interest in a confined cellular compartment. By expressing an engineered peroxidase (APEX2)-tagged variant of GABARAP—which, like endogenous GABARAP, was present in EVs prepared from HEK293 cells—we demonstrate the applicability of APEX2-based proximity labelling to EVs. The biotinylated protein pool which contains the APEX2-GABARAP co-secretome contained not only known GABARAP interaction partners but also proteins that were found in APEX2-GABARAP's proximity inside of autophagosomes in an independent study. All in all, we not only introduce a versatile tool for co-secretome analysis in general but also uncover the first details about autophagy-based pathways as possible biogenesis mechanisms of GABARAP-containing EVs.

1. Introduction

In the past few years, the analysis of the direct protein environment of a protein of interest (POI) in a well-defined cellular compartment, so-called proxitome analysis, has grown into an emerging area of research. This has become possible by the development of proximity-based labelling strategies such as biotinylation by an engineered ascorbate peroxidase (APEX). Initially developed for high-resolution electron microscopy [1], APEX was soon applied to living cells for the first time,

determining the proteins inside the mitochondrial matrix and demonstrating that APEX can also be used for proteomic mapping. In order to do so, APEX is tagged to a POI and expressed in a eukaryotic host cell system. When incubating the cells with biotin-phenol and H_2O_2, APEX catalyses the oxidation of biotin-phenol to a short-lived biotin-phenoxyl radical, which is unable to cross biological membranes and labels proteins at electron-rich amino acids in close proximity to POIs (<20 nm) [2].

Shortly afterwards, an improved APEX2 variant exhibiting enhanced catalytic efficiency was generated [3], which since then has been applied to map a variety of protein–protein interactions. Amongst others, APEX2 was tagged to a G-protein coupled receptor (GPCR) to track GPCR signalling [4], to the fibroblast growth factor 1 to identify interaction partners on the cell surface [5], and to Rab proteins to determine new Rab functions [6]. Furthermore, APEX2 was used to define the protein environment in other specific cellular compartments like lipid droplets, organelles regulating lipid storage [7], and autophagosomes. For the latter, the APEX2 system was applied to human orthologues of yeast autophagy-related 8 (Atg8), among them γ-aminobutyric acid type A receptor-associated protein (GABARAP) [8]. However, to our knowledge, the APEX2-mediated proximity labelling technique has yet been most commonly applied to adherent cells, leaving open a big area of interest ranging from eukaryotic cells in suspension over unicellular organisms to extracellular vesicles (EVs). One step in this direction was recently taken by Singer-Kruger et al. by developing an APEX2-labelling strategy for *Saccharomyces cerevisiae* cells [9]. For the next step, the main goal of the here-presented study was therefore to test the applicability of APEX2-mediated proximity labelling to EVs (Supplementary Figure S1).

In this study, we examine EVs in general, as there is often only little information on the EV subtype that is involved in the secretion of the respective POI. The "EV" term includes all kinds of secreted membrane vesicles in the extracellular space, which are highly heterogenous, depending on their cells of origin and their pathways of biogenesis. Commonly, EVs are subdivided into two main groups: microvesicles, which develop by shedding of the plasma membrane, and exosomes, which are formed in an initial step by the invagination of early endosomes. Thereby, multivesicular bodies containing intraluminal vesicles are formed. When fusing with the plasma membrane, the intraluminal vesicles are secreted as exosomes (reviewed by van Niel et al. [10]). Further mechanisms of unconventional protein secretion also involve other vesicle types, for example, secretory lysosomes or even autophagosomes (reviewed by Nickel [11]). Although the content of EVs varies, there are still features that they have in common. For instance, EVs generally contain mRNA, which can be transported to a recipient cell, where the mRNA can be translated and thus serves as intracellular communication [12,13]. Furthermore, it is possible to characterise EVs based on their protein content. Typical EV marker proteins include tetraspanins, e.g., CD81; cytosolic proteins, like members and accessory proteins of the endosomal sorting complexes required for transport (ESCRT) machinery, e.g., ALG-2-interacting protein X (Alix; official gene name: programmed cell death 6-interacting protein (PDCD6IP)); heat shock proteins, e.g., Hsc70; or annexins, e.g., annexin V [14]. Amongst numerous others, these EV marker proteins are usually accessed to determine the quality of an EV sample before conducting a more detailed analysis such as mass spectrometry.

During autophagy, a highly conserved cellular homeostasis mechanism [15], the autophagy-related 8 (ATG8) protein family member GABARAP was shown to be involved in the autophagosome–lysosome fusion process [16] and to be lipidated by a ubiquitin-like system [17,18]. The lipidation does not only support GABARAP's binding to autophagosomal membranes [19,20], enabling the attachment of both autophagic cargo and their receptors as well as regulators of the core autophagic machinery [21,22]. In fact, by connecting to tubulovesicular structures [23], it likely also promotes the initially described function of GABARAP: the trafficking of receptors to the plasma membrane, for example, the $GABA_A$ receptor [24], the human transferrin receptor [25], or the angiotensin II type 1 receptor [26], making it a versatile binding hub. Furthermore, it was shown that GABARAP mediates insulin secretion together with the motor protein kinesin-1 heavy chain (KIF5B) by localising insulin-loaded vesicles at microtubules and enhancing vesicle movement [27]. Despite taking part in all these events, the secretion of GABARAP itself has not yet been studied in detail. However, through a query in Vesiclepedia [28,29],

we realised that GABARAP is already listed as an extracellular vesicle (EV) protein in samples from human [30–33] and mouse [34] cancer cells, and in a recent proteomic study, ATG8-protein family members were detected in EVs from different cell lines [35]. In all the underlying studies linked to the respective entries, GABARAP was found either at the mRNA level or at the protein level by mass spectrometric methods. With our work, we provide further evidence of GABARAP's secretion, as we reveal its presence in EVs of cell culture supernatants from different human cell lines and human blood plasma by immunoblotting. Finally, we investigated the co-secretome of GABARAP in EVs by applying, for the first time, an APEX2-based proximity labelling strategy in EVs. In this context, our goal was to establish a method that solely includes those EVs in the analysis that contain the POI, in our case GABARAP. The APEX2-based approach, by which only EV proteins are labelled that are localised in the same EV as the POI fused to APEX2, might help to cope with this task and to define a co-secretome. Using this technique, we observed an overlap of the EV GABARAP proxitome with that of the autophagosomal GABARAP proxitome [8], suggesting an autophagy-based pathway as one possible biogenesis mechanism of GABARAP-containing EVs.

2. Materials and Methods

2.1. Antibodies

The following primary antibodies were used for immunoblotting at a concentration of 1:1000: Alix (Cat. No. sc-49268, Santa Cruz Biotechnology, Dallas, TX, USA), Annexin V (Cat. No. ab14196, abcam, Cambridge, UK), Calnexin (Cat. No. ab22595, abcam), CD81 (Cat. No. sc-23962, Santa Cruz Biotechnology), c-myc (Cat. No. A190-104A, Bethyl Laboratories, Montgomery, TX, USA), GABARAP (Cat. No. 18723-1-AP, Proteintech, Rosemont, IL, USA) and Hsc70 (Cat. No. ab51052, abcam). Streptavidin-HRP (Cat. No. S911, Invitrogen, Carlsbad, CA, USA) was used at a 0.3 μg/mL concentration. Anti-goat (Cat. No. sc-2354, Santa Cruz Biotechnology), anti-mouse (Cat. No. P026002-2, Agilent Technologies, Santa Clara, CA, USA) and anti-rabbit (Cat. No. 31460, Invitrogen) were used as secondary antibodies at a concentration of 1:10,000. The following primary antibodies were used for immunofluorescence: c-myc (Cat. No. A190-104A, Bethyl Laboratories) at a concentration of 1:200 and GABARAP 8H5 (in-house [36], undiluted). The Goat-488 (Cat. No. ab150133, abcam) and rat-Cy5 (Cat. No. 712-175-150, Jackson ImmunoResearch, Cambridgeshire, UK) secondary antibodies were used at a concentration of 1:250.

2.2. Cloning

The pcDNA5/FRT/TO myc-APEX2-GABARAP vector was obtained from Christian Behrends' lab. The vector pcDNA5/FRT/TO myc-APEX2 was generated by introducing two stop codons in the linker region between APEX2 and GABARAP using the QuikChange II XL Site-Directed Mutagenesis Kit (Cat. No. 200521, Agilent Technologies).

2.3. Cell Culture and Transfection

Human embryonic kidney 293 (HEK293; Leibniz Institute DSMZ—German Collection of Microorganisms and Cell Cultures, Braunschweig, Germany; DSMZ no. ACC 305) cells and hepatocellular carcinoma (Huh7; COSMIC sample ID 907071) cells were cultured at 37 °C in a humidified 5% CO_2 incubator in Dulbecco's Modified Eagle's Medium (DMEM, Cat. No. D5796, Sigma-Aldrich, St. Louis, MO, USA) supplemented with 10% fetal calf serum (FCS, Cat. No. F9665, Sigma-Aldrich). For human neuroblastoma (SH-SY5Y; Leibniz Institute DSMZ; DSMZ no. ACC 209) cells, DMEM supplemented with 20% FCS was used. All the cells were routinely checked for mycoplasma contamination.

For transient transfection with myc-APEX2 and myc-APEX2-GABARAP constructs, 4–6×10^5 cells were seeded on the previous day into an appropriate vessel: the wells of 6-well culture plates (Cat. No. 10062-892, VWR, Randor, PA, USA) were used for immunoblotting (IB) and MS, while for immunofluorescence (IF),

poly D-Lysine coated bottom dishes (Cat. No. P35GC-0-10-C, MatTek Corporation, MA, USA) were used. Transfection was carried out on the next day with 1.0 μg total DNA using PolyFect Transfection Reagent (Cat. No. 301107, Qiagen, Hilden, Germany) according to the manufacturer's instructions.

2.4. Blood Sampling

Human (autologous) blood plasma was donated from J.L.S., a healthy female volunteer, after ≥12 h fasting using a venous cannula. NH_4-Heparin served as an anti-coagulant. The blood sample was centrifuged at 2500× *g* and 12 °C for 15 min. The obtained blood plasma was then allowed to pass through a 0.45 μm filter by gravity flow to eliminate cellular debris before EV isolation.

2.5. Isolation of EVs

For EV preparation from cell culture supernatants, cells were cultured for at least 48 h in DMEM supplemented with exosome-depleted FCS (Cat. No. A25904DG, Life Technologies, Carlsbad, CA, USA). Conditioned cell culture media (CM) were depleted of cellular debris by differential centrifugation for 10 min at 300× *g* and for 20 min at 2000× *g*. After concentrating the media to 1/10th of the original volumes by centrifuging at 2500× *g* and 12 °C in Vivaspin ultrafiltration units (Cat. No. VS2092, Sartorius, Göttingen, Germany), the respective concentrated CM (CCM) samples were used for EV isolation. EVs were either prepared by polymer-based precipitation (ExoQuick-TC, Cat. No. EXOTC10A-1, System Biosciences, Palo Alto, CA, USA) according to the manufacturer's instructions or by differential centrifugation. For differential centrifugation, the respective CCM samples were subjected directly to ultracentrifugation (100,000× *g*, 4 °C, 90 min), twice, with a washing step in between (washing buffer: 100 μL PBS supplemented with protease inhibitor cocktail), if not stated otherwise. Both approaches led to an enrichment of diverse EVs including smaller ones, e.g., exosomes, and larger subtypes, e.g., MVs, since the latter ones were not depleted by a 10,000× *g* centrifugation step.

To obtain highly pure vesicles of smaller sizes, density gradient centrifugation was used. In that case, larger EVs were depleted by an upstream 10,000× *g* centrifugation step prior to ultracentrifugation. Next, the resulting EV pellet was resuspended in washing buffer and applied to an OptiPrep density gradient as described by Lobb et al. [37]. After refractometric determination of the respective densities, the obtained fractions were concentrated by ultracentrifugation as described above and the resulting EVs were analysed by immunoblotting.

2.6. Proximity Labelling

The APEX2-mediated proximity labelling of the cells and streptavidin-based pull-down of biotinylated proteins was conducted as described by Hung et al. [38]. For the biotinylation of EV proteins, two labelling strategies were tested (Figure 3). In strategy "a", the reagents were directly added to the conditioned cell culture media with subsequent EV isolation. In strategy "b", first, the EVs were isolated. The obtained EV pellet was then labelled and quenched like the cells, while great care had to be taken not to disturb the pellet. For both strategies "a" and "b", EVs were prepared using polymer-based precipitation.

2.7. Immunoblotting (IB)

Cells and EVs were lysed in RIPA buffer according to Hung et al. [38]. Proteins were precipitated with methanol/chloroform, dried at room temperature (RT), and resuspended in 2% SDS. The protein concentration was determined using the *DC* Protein Assay (Cat. No. 5000116, Bio-Rad Laboratories, Hercules, CA, USA) according to the manufacturer's instructions. The samples were incubated for 10 min at 45 °C in sample buffer (40% (*v/v*) glycerol, 8% (*v/v*) SDS, 225 mM tris-HCl (pH 6.8), 8% (*v/v*) β-mercaptoethanol, 5 g/L of bromophenol blue sodium salt) and subjected to SDS-PAGE (Any kD Mini-PROTEAN TGX Stain-Free Protein Gels, Cat. No. 4568124 or 4568126, Bio-Rad Laboratories). Per sample and gel lane, 25 μg of total protein were applied. Protein amounts (loading controls) were visualised according to the "stain-free" technique, which enables the direct

visualisation of proteins in gels supplemented with 2,2,2-trichloroethanol (TCE) by an ultraviolet light-induced reaction of tryptophan residues with the trihalo compound that produces fluorescence in the visible range [39]. Following stain-free imaging, the proteins were transferred to a PVDF membrane using Trans-Blot Turbo Mini PVDF Transfer Packs (Cat. No. 1704156, Bio-Rad Laboratories). The membranes were blocked in an appropriate blocking agent (5% (*w/v*) milk powder in TBS-T (0.05% Tween-20 in TBS) or 3% bovine serum albumin (BSA) in TBS-T) at RT for 2 h, incubated with primary antibody overnight at 4 °C, washed in TBS-T, incubated with peroxidase-coupled secondary antibody for 1 h at RT, and washed again in TBS-T. Blots were visualised by chemiluminescence using Clarity Western ECL Substrate (Cat. No. 1705061, Bio-Rad Laboratories) and the ChemiDoc Imaging System (Bio-Rad Laboratories).

2.8. Mass Spectrometric Protein Identification and Quantification

Eluted protein samples were processed for mass spectrometric analysis by in-gel digestion, essentially as described [40]. Briefly, samples were separated (~5 mm running distance) in Bis-Tris buffered 4–12% acrylamide gels (Thermo Fisher Scientific, Waltham, MA, USA). After silver staining and de-staining of the gel, protein-containing bands were washed, reduced by DTT, alkylated by adding iodoacetamide, and digested with 0.1 µg trypsin in 50 mM ammonium hydrogen carbonate overnight at 37 °C. Peptides were extracted from the gel by twice adding 40 µL of 1:1 (*v/v*) acetonitrile and 0.1% trifluoroacetic acid (in water), followed by a 15 min incubation in an ultrasonic bath. Peptides were dried and finally resuspended in 17 µL of 0.1% trifluoroacetic acid.

Next, peptide samples were separated on an Ultimate 3000 rapid separation liquid chromatography system (RSLS, Thermo Fisher Scientific). First, peptides were trapped on a trapping column (Acclaim PepMap100, 3 µm C18 particle size, 100 Å pore size, 75 µm inner diameter, 2 cm length, Thermo Fisher Scientific) using 0.1% (*v/v*) trifluoroacetic acid (in water) as the mobile phase. After 10 min, the peptides were separated at 60 °C on an analytical column (Acclaim PepMapRSLC, 2 µm C18 particle size, 100 Å pore size, 75 µm inner diameter, 25 cm length, Thermo Fisher Scientific) for 2 h (gradient from 4% to 40% solvent (0.1% (*v/v*) formic acid, 84% (*v/v*) acetonitrile in water). The separated peptides were directly analysed by an online coupled QExactive plus quadrupole/orbitrap mass spectrometer (Thermo Fisher Scientific). Peptides were sprayed into the mass spectrometer via an online coupled nano source equipped with distally coated emitters (New Objective) at a spray voltage of 1.4 kV. The mass spectrometer was operated in data dependent positive mode: first survey scans were carried out at a resolution of 70,000 over a scan range of 350 to 2000 *m/z*. Subsequently, up to ten twofold- and threefold-charged precursors were isolated by the build in quadrupole (2 *m/z* isolation window) and fragmented via higher-energy collisional dissociation. Fragment spectra were recorded at a resolution of 17,500 using an available scan range of 200 *m/z* to 2000 *m/z*, and already-fragmented precursors were excluded from fragmentation for the next 100 s.

Raw data were further processed with MaxQuant (version 1.6.3.4) with standard parameters if not indicated otherwise, enabling protein identification and quantification. Searches were carried out with tryptic cleavage specificity considering two potential missed cleavage sites based on 73,112 *Homo sapiens* entries downloaded from UniProtKB (UP000005640) on 18th August 2018 and, additionally, the APEX2-GABARAP sequence. Carbamidomethylation at cysteines was considered as fixed and methionine oxidation as variable modification. Label-free quantification was enabled (LFQ). Only proteins identified with at least two peptides were reported.

For data analysis, normalised (LFQ) intensities were used to determine the enrichment of a protein in one sample type relative to another. Gene Ontology (GO) analyses were conducted by applying protein lists to DAVID Bioinformatics Resources 6.8 [41], using either the *Homo sapiens* database as the default background or Supplementary Table S1A as the background of the total proteins detected in this study.

To generate separate proteins lists for each sample, raw data were processed using the ProteomeDiscoverer 1.4 software environment (Thermo Fisher Scientific). Searches were carried

out using the MSAmanda search engine with tryptic cleavage specificity considering one potential missed cleavage site based on 42,201 *Homo sapiens* SwissProt entries downloaded from UniProtKB on 20th June 2017 and, additionally, the APEX2-GABARAP sequence. Carbamidomethylation at cysteines was considered as fixed, and deamidation at asparagine and glutamine as well as methionine oxidation, as variable modifications. Mass tolerances were 10 ppm both for precursors and fragments. Identifications were validated using the Percolator node and only "high confidence" peptides (FDR <1%) used for further processing. Only proteins identified with at least two peptides were reported.

2.9. Immunofluorescence (IF)

HEK293 cells (4×10^5) were seeded into poly D-Lysine coated bottom dishes (Cat. No. P35GC-0-10-C, MatTek Corporation), incubated in DMEM/10% FCS, and transfected on the following day. After 48 h of further cultivation, the cells were incubated for 2 h at 37 °C in Hank's Balanced Salt Solution (HBSS; Cat. No. 14025050, Thermo Fisher Scientific) and 100 nM Bafilomycin A1 (Cat. No. 196000, Sigma-Aldrich) to induce the accumulation of autophagic structures. Then, the cells were fixed at 37 °C for 10 min with 4% (*w/v*) paraformaldehyde (PFA) in PBS, pH 7.4; washed two times with PBS; and permeabilised by shaking in 0.2% Triton-X-100 for 30 min at RT. After another washing step, the cells were blocked by incubating in 1% BSA overnight at 4 °C. Immunostaining was conducted by adding primary anti-myc antibody, diluted in anti-GABARAP (8H5) antibody, and incubating for 60 min at RT under smooth shaking. Again, the cells were washed three times and then incubated with shaking for 60 min at RT in secondary antibodies under the exclusion of light. After two final washing steps, long storage buffer was added (0.05% sodium azide in PBS) and the cells were subjected to image acquisition.

2.10. Image Acquisition—Laser Scanning Microscopy (LSM)

Images were acquired using an LSM 710 confocal microscope (Zeiss, Oberkochen, Germany) equipped with the ZEN Black 2009 software and a Plan-Apochromat 63x/1.40 Oil DIC M27 objective. Cell nuclei (DAPI) were visualised using the 405 nm channel (MBS-405); GABARAP, using the 488 nm channel (MBS 690+); and myc, using the 543 nm channel (MBS 458/543).

2.11. Transmission Electron Microscopy (TEM)

EVs were prepared for TEM according to Théry et al. [42] with slight alterations. After enriching the EVs using polymer-based precipitation, they were resuspended in 2% (*w/v*) PFA in PBS, pH 7.4. Of this sample, 5 μL were absorbed on a formvar/carbon coated copper grid (Cat. No. S160-4-V, Plano, Wetzlar, Germany) for 20 min. The specimen was fixed with 1% (*v/v*) glutaraldehyde for 5 min, washed eight times with ddH$_2$O, and negative stained with 4% (*v/v*) uranyl acetate for 5 min. Finally, the samples were embedded in a freshly made mixture (4:1) of trehalose (10%, in TBS) and uranyl acetate (2%) for 10 min at RT, and then dried. Images were recorded using a Libra 120 transmission electron microscope (Zeiss, Oberkochen, Germany) at 120 kV.

2.12. Nanoparticle Tracking Analysis (NTA)

HEK293 cells were cultured for 48 h in phenol red-free DMEM (Cat. No. 21063029, Thermo Fisher Scientific) supplemented with exosome-depleted FCS (Cat. No. A25904DG, Life Technologies). Conditioned cell culture media were depleted of cellular debris by differential centrifugation for 10 min at 300× *g* and for 20 min at 2000× *g*. The media were concentrated to 1/10th of the original volumes by centrifuging at 2500× *g* and 12 °C in Vivaspin ultrafiltration units (Cat. No. VS2092, Sartorius), stored overnight at 4 °C, and measured by NTA the day after. Measurement of the samples was conducted with a ZetaView PMX-100 (Particle Metrix, Meerbusch, Germany) using a 1/10 dilution in Ampuwa water (Cat. No. 1088813, Fresenius Kabi, Bad Homburg, Germany). Additionally, the particle size distribution in diluted non-conditioned medium was determined and used for background subtraction. The following acquisition parameters were used: Sensitivity—75%; Shutter—70; Minimum Brightness—20; Minimum Size—20 nm; Maximum Size—500 nm; Polarity—1;

Voltage—0; Particle drift at 0 V—<5 μm/s; Positions—11; Cycles—10; and Multiple acquisitions—2. Each sample was measured in two independent trackings, which were used for the calculation of standard deviations. The measured particle counts per size were corrected by background subtraction.

3. Results

3.1. GABARAP is Secreted in EVs of Different Cell Lines and Sample Types

First, we checked whether GABARAP is secreted in EVs by those cell lines commonly used in cell culture experiments. To this end, we analysed cell culture supernatants from the human cell lines HEK293, Huh7, and SH-SY5Y after inducing the accumulation of autophagic structures by starvation and using an anti-GABARAP antibody, the GABARAP-specificity of which we confirmed before by knockout validation (Supplementary Figure S1 in [36]). For all three cell types, GABARAP was detected in the respective EV sample (Figure 1A). Notably, predominantly the lipidated form of GABARAP, GABARAP-II, was found, according to its migration behaviour [43]. An enrichment of EVs in the respective samples was confirmed by transmission electron microscopy (TEM) and also by nanoparticle tracking analysis (NTA; Supplementary Figure S2), which resulted in particle sizes ranging from approximately 30 to 1000 nm (peak at 200 nm) as expected for EVs derived by differential centrifugation with an omitted run at 10,000× *g*. In addition, we applied EVs isolated both from HEK293 cells and from HEK293 cells stably overexpressing HIV-1 Nef—a protein that is well-known to trigger both its own and EV's secretion in general [44]—to density gradient centrifugation and subsequent immunoblotting. We found that GABARAP co-fractionated with Alix as a well-defined EV marker but also with the Nef protein, when present, at a buoyant density characteristic for exosomes and other EVs [45]. In both cases, GABARAP was not found in fractions of higher density, hinting towards a localisation of GABARAP in EVs rather than in protein aggregate contaminants (Supplementary Figure S3). Next, we wer e curious to see whether GABARAP was also secreted in EVs from "fed" HEK293 cells without inducing the accumulation of autophagic structures and containing predominantly unlipidated GABARAP-I. Interestingly, in the respective EV-enriched samples obtained from CCM of cells cultured under nutrient-rich conditions, we again detected mainly lipidated GABARAP-II (Figure 1B, EVs), suggesting its association with the vesicle membrane. As control, we also analysed unconditioned media (UCM), which were treated just as conditioned media. Unexpectedly, for UCM, a faint signal for unlipidated GABARAP-I was detected, which might have its origin in FCS components remaining in the applied FCS even under exosome depletion. Note that the human and bovine GABARAP and Alix proteins are identical by 100% and 95%, respectively. Consistently, in EVs prepared from FCS without prior exosome depletion, GABARAP-I was again observed (Figure 1C). The reason why in FCS-derived EVs, GABARAP is found in its unlipidated form is unknown; however, this fact supports the idea that GABARAP-II originates from those EVs produced by the cultured cells in all our CCM-derived EV preparations. Finally, we detected GABARAP-II also in EVs isolated from human blood plasma samples (Figure 1D). Altogether, these results demonstrate that secretion of endogenous GABARAP is widespread.

3.2. APEX2-GABARAP Exhibits Different Cellular Localisation Than APEX2's

To get an idea about the distribution of APEX2-tagged GABARAP, cells overexpressing APEX2-GABARAP or APEX2 alone were starved and imaged by confocal laser-scanning microscopy, and their intracellular localisation was compared with that of endogenous GABARAP (Figure 2A). As expected, a broad co-localisation pattern between the anti-myc stain, corresponding to APEX2-GABARAP due to its N-terminal myc tag, and the highly GABARAP-specific antibody 8H5 [36], which detects both endogenous GABARAP and its APEX2-fusion, was observed. By contrast, cells expressing APEX2 alone showed virtually no overlap between the two stains. In agreement with the culture conditions used, APEX2-GABARAP was prominently found in punctate structures,

very likely resembling its lipidated and thus autophagosome-associated fraction. For APEX2 alone, a uniform distribution throughout the cytoplasm was observed as expected for a soluble protein.
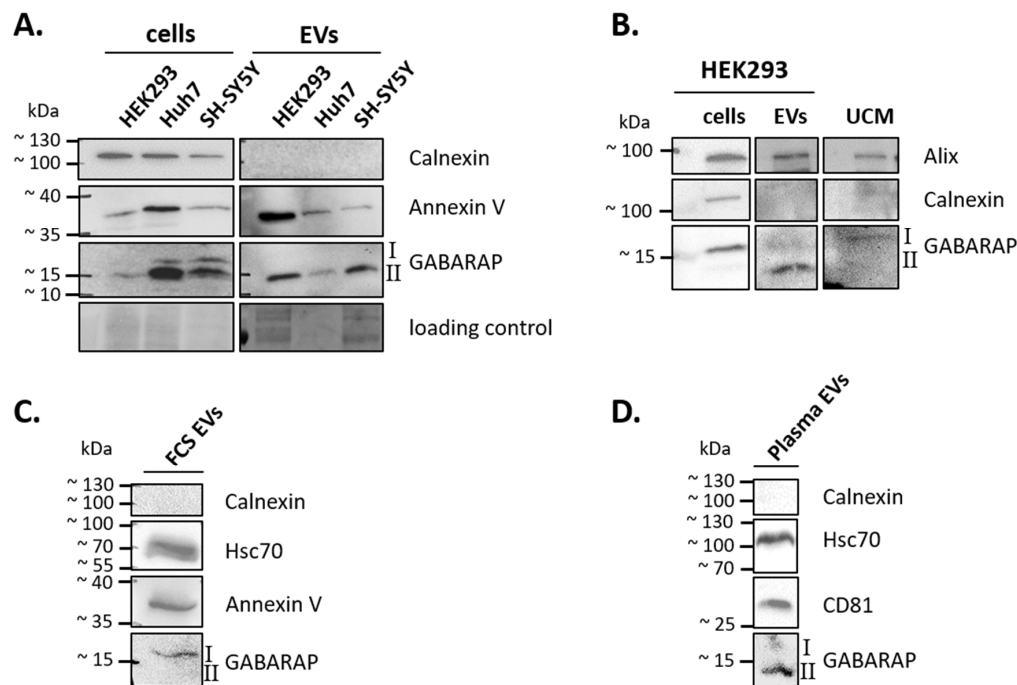

Figure 1. GABARAP is secreted in extracellular vesicles (EVs) and is detectable by immunoblotting. Alix, Annexin V, Hsc70, and CD81 were used as EV marker proteins, and Calnexin, as a marker for cellular impurities in an EV sample. (**A**) GABARAP is detected in EV-enriched samples from the three human cell lines—HEK293, Huh7, and SH-SY5Y—after starvation. One representative blot out of two, each performed with cell lysates from different passage numbers, is shown. EVs were obtained by ultracentrifugation. Cropped images of stain-free gels are presented as loading controls. (**B**) Under fed conditions, predominantly lipidated GABARAP is detectable in HEK293 EVs, while unlipidated GABARAP was detected in unconditioned media (UCM). One representative blot out of two, each performed with cell lysates from different passage numbers, is shown. EVs were enriched using polymer-based precipitation. (**C**) Unlipidated GABARAP is detectable in EVs isolated from bovine blood serum. One representative blot of two analysed EV batches, independently obtained from the same batch of FCS is shown. EVs were enriched by ultracentrifugation. (**D**) GABARAP is detectable in EVs isolated from human blood plasma. One representative blot of two analysed EV batches is shown. Respective EV samples were obtained from independent blood samples of the same donor. EVs were enriched by ultracentrifugation. Cells used in (**A**–**C**) were cultured for at least 48 h in exosome-depleted media before harvest. After lysis, cellular and EV proteins were precipitated by methanol–chloroform precipitation, resuspended in lysis buffer, and used for immunoblotting. Uncropped versions of the blots and their corresponding gels after stain-free imaging are given in Supplementary Figure S4.
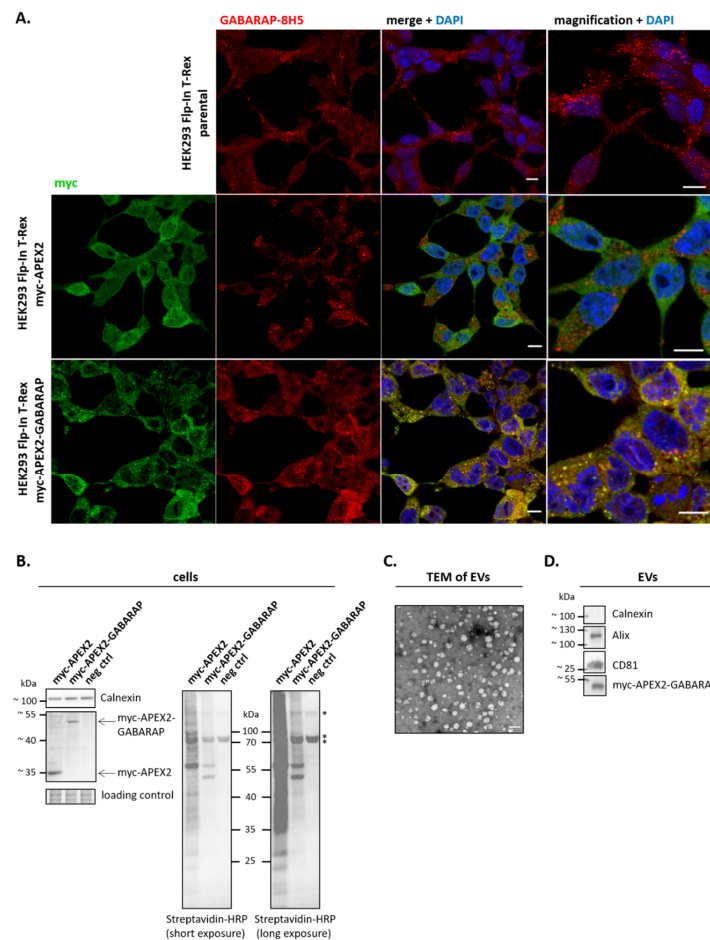
Figure 2. Cellular distribution of APEX2 and APEX2-GABARAP. (**A**) APEX2-GABARAP co-localises with the staining pattern obtained by the paralogue-specific anti-GABARAP (8H5) antibody [36] and shows a distribution pattern as observed for endogenous GABARAP. After a period of 24 h after transfection with APEX2 and APEX2-GABARAP, respectively, the cells were starved by incubating in HBSS + 100 nM BafA1 for 2 h at 37 °C and 5% CO_2, fixed (4% paraformaldehyde, PFA), immunolabelled with goat anti-human c-myc antibody and anti-GABARAP-8H5, and visualised by confocal fluorescence microscopy. Parental, non-transfected cells are shown as control for the distribution of endogenous GABARAP. Nuclei were counterstained with DAPI. For each cell type, one representative image for three different cellular passages, each imaged in at least four frames, is shown. Scale bar, 10 μm. (**B**) Different biotinylation patterns are obtained when expressing APEX2-GABARAP compared to APEX2. HEK293 cells were transfected with APEX2- and APEX2-GABARAP-encoding plasmids, respectively. For the negative control (neg ctrl), no DNA was added. After an incubation period of 48 h, cells were labelled, harvested, and lysed as described by Hung et al. [38]. Cellular lysates were subsequently analysed by immunoblotting using a streptavidin–HRP conjugate. *: Endogenously biotinylated proteins. One representative blot out of four, each performed with cell lysates from different passage numbers, is shown. A crop of a stain-free gel is presented as the loading control. (**C**) Enrichment of EVs was tested by TEM. After preparation, EVs were resuspended in 2% PFA, contrasted in 4% uranyl acetate, embedded in 10% trehalose on formvar/carbon coated grids, and visualised by TEM. One representative image for three different cellular passages, each imaged in at least five frames, is shown. Scale bar, 100 nm. (**D**) EVs were enriched from cell culture supernatant by polymer-based

precipitation after 48 h of cultivation and subjected to immunoblotting. Both the absence of calnexin as a cellular marker protein and the presence of common EV marker proteins (Alix, CD81) and of APEX2-GABARAP itself were confirmed. One representative blot out of three, each performed with cell lysates from different passage numbers, is shown. Uncropped versions of the blots and their corresponding gels after stain-free imaging are given in Supplementary Figure S6.

Next, we confirmed the peroxidase activity of APEX2-GABARAP by adding biotin-phenol and H_2O_2 to the cell cultures, following the protocol as published by Hung et al. [38] and subsequent immunoblotting of the respective cell lysates using a Streptavidin-HRP conjugate. Different biotinylation patterns (Figure 2B) were observed in accordance with the differing intracellular distribution of APEX2 and APEX2-GABARAP. In consistency with its vesicular localisation, a rather distinct biotinylation pattern and thus a restricted pool of proximate proteins was obtained for APEX2-GABARAP, while for APEX2 alone, a very broad biotinylation pattern was observed, reflecting its high mobility and wide variety of putative interacting partners. Furthermore, we prepared EVs from APEX2-GABARAP-expressing cells and confirmed the secretion of overexpressed APEX2-GABARAP (Figure 2D), being consistent with the secretion of endogenous GABARAP (Figure 1). Related to this, by investigating an EGFP knock-in cell line expressing EGFP-GABARAP under the control of the endogenous GABARAP promotor (Supplementary Figure S5, [46]), we could show that EGFP-GABARAP can also be robustly detected by immunoblotting in the respective EV lysates yielded after ultracentrifugation when present at endogenous levels. This indirectly suggests that overexpression is, most likely, not the (sole) explanation for the observed APEX2-GABARAP secretion, which instead should rather reflect the secretion behaviour of GABARAP as documented in Figure 1. The enrichment of EVs from APEX2-GABARAP expressing cells was finally assessed by TEM (Figure 2C) and the immunoblotting of EV lysates against two well-accepted EV marker proteins (Alix, CD81) and calnexin to exclude cellular contaminants (Figure 2D), respectively.

3.3. APEX2-GABARAP Proximity Labelling in EVs

Having demonstrated the functionality of APEX2-GABARAP and also its export in EVs, we subjected EV-enriched samples, containing both EVs positive for APEX2-GABARAP and EVs without APEX2-GABARAP, to proximity labelling followed by streptavidin-pulldown and MS analysis with the aim of defining the GABARAP co-secretome. Since we could detect endogenous GABARAP in EVs both under starvation as well as under basal conditions (Figure 1A,B) and also overexpressed APEX2-GABARAP in EVs prepared under basal conditions (Figure 2D), we cultured the cells without nutrient deprivation to minimise stress-related artefacts. To establish an efficient labelling result, we tested two different strategies, for both of which we proceeded according to the protocol published by Hung et al. [38]. In one approach (simultaneous labelling, Figure 3A, branch a), we added the labelling reagents directly to the conditioned media after cultivating HEK293 cells for 48 h, thereby labelling cellular and EV proteins at the same time and then separating them for analysis. In the other approach (separated labelling, Figure 3A, branch b), cells and EVs were separated from each other in the first step and labelled in the second step. For the EVs, this included an upstream preparation step. The pelleted and concentrated EVs were then labelled in the same procedure as the cells. The total cell lysates and EVs of both approaches were then analysed for biotinylation by immunoblotting using a streptavidin–HRP conjugate. While for the cellular sample, biotinylated proteins were detected in both the cases tested, EV content biotinylation was visible only for EVs that have been labelled separately subsequent to their isolation (Figure 3B). Consistently, under these conditions, the affinity-purification of biotinylated proteins by streptavidin-coated beads could be demonstrated (Figure 3C).
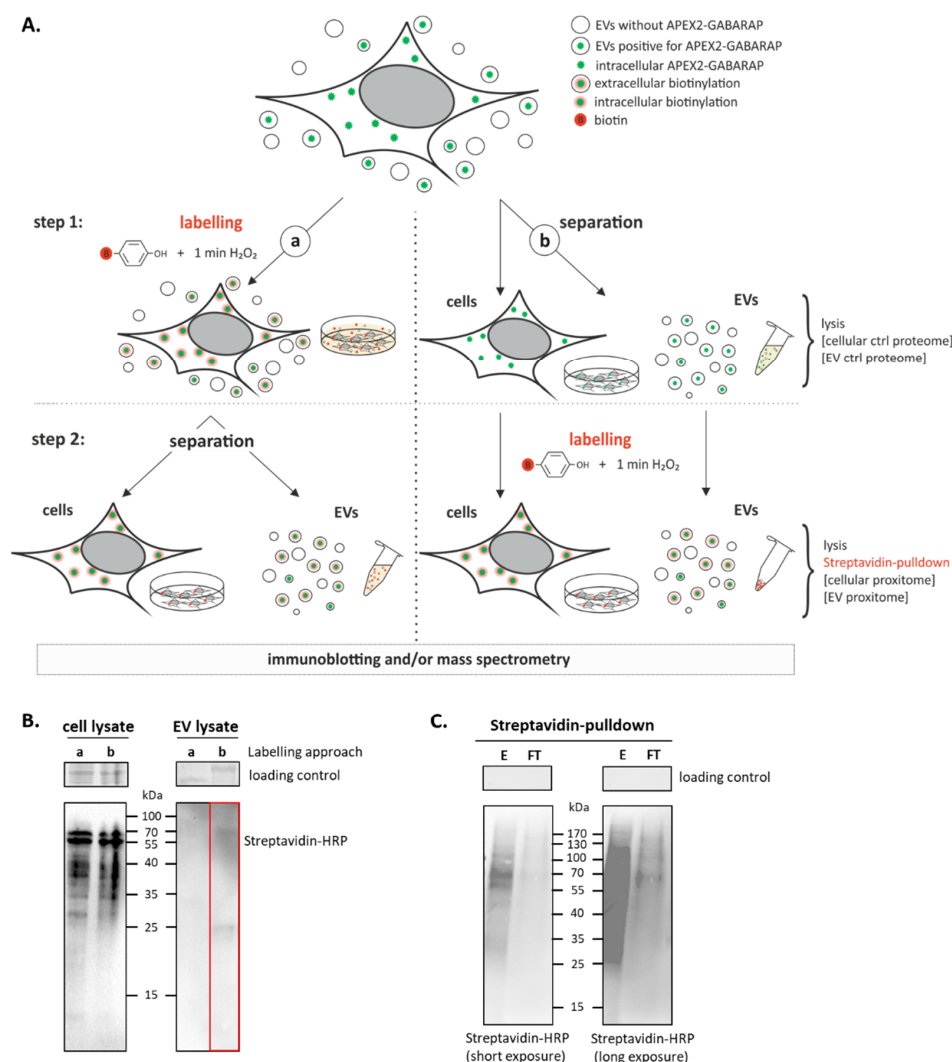
Figure 3. APEX2-mediated proximity labelling in EVs. (**A**) Tested approaches for proximity labelling of EVs. Two labelling strategies for target protein biotinylation within the APEX2-GABARAP-positive EV subfractions were investigated for their efficiency. In branch a, biotin-phenol and H_2O_2 were directly added to the cell culture supernatant in which the cells were cultivated for 48 h after transfection. Afterwards, the cells and EVs were separated from each other by collecting the supernatant. In branch b, cells and EVs were separated in the first step. EVs were pelleted by polymer-based precipitation. Then, cells and EVs were labelled separately. The cells and EVs were lysed and the labelled proteins can be analysed by immunoblotting using a streptavidin-HRP conjugate and/or mass spectrometry. (**B**) Pelleted EVs, but not EVs in solution, may be labelled by APEX2-GABARAP. The labelled EVs were lysed and used for immunoblotting, proving approach "b" suitable for APEX2-mediated labelling in EVs (marked red). One representative blot out of three, each performed with cell lysates from different passage numbers, is shown. (**C**) Biotinylated APEX2-GABARAP EV proteins, obtained using branch b, are enriched by streptavidin. EV lysates were incubated with streptavidin-coated beads. After collecting the flow-through (FT), multiple washing steps were applied, and the eluate (E) was collected. A broad signal was obtained for the eluate, while for the flow-through, only faint signals were obtained, demonstrating the effective capturing of biotinylated EV proteins. One representative blot out of two, each performed with cell lysates from different passage numbers, is shown. Crops of stain-free gels are presented as loading controls. Uncropped versions of the blots and their corresponding gels after stain-free imaging are given in Supplementary Figure S7.

3.4. The GABARAP Co-Secretome as Defined by Proximity Labelling

Finally, we were curious about the identity of those proteins detected in the EVs from APEX2-GABARAP expressing cells after labelling and streptavidin-pulldown, since they define the co-secretome of GABARAP. For this, we cultured the cells under nutrient-rich conditions to obtain the co-secretome of APEX2-GABARAP under basal conditions and subjected the cellular and EV proteins, both labelled and non-labelled, to mass spectrometry (MS) and subsequent analysis using FunRich [47,48]. When examining the cytoplasmic samples (Figure 4A), it becomes apparent that the number of identified proteins in the cellular GABARAP proxitome (total 347) after labelling and streptavidin-pulldown is 64.7% lower than the number identified in the total cellular lysate from untreated control (ctrl) cells (total 983 proteins). Of the cellular proteins, a total of 212 proteins corresponding to 61.1% of the cellular GABARAP proxitome was also identified without labelling and pulldown, and 135 proteins or roughly one-third were detected exclusively after proximity-labelling. While the latter might include false-positive hits, the former consists of more than 50% of the proteins also found in the autophagosomal GABARAP proxitome [8] (Supplementary Figure S8) and therefore probably represents true-positive hits. Altogether, this result met the expectation of a smaller, possibly more specific, number of proteins after labelling and pulldown.

In case of the EV samples (Figure 4B), a slightly elevated number of proteins (584) could be identified from the proximity-labelled sample when compared to the untreated control sample (EV ctrl proteome, 443). This could reflect either a technical-based variance between the samples or, e.g., reflect the enrichment of a multitude of little-abundant proteins by the proximity-labelling procedure raising them just beyond the MS detection limit. Another explanation could be that APEX2-GABARAP shows a ubiquitous distribution through different EV subtypes, which would be consistent with the broad list of identified proteins observed. This could lead to biotinylation and the subsequent detection of proteins that are localised together with APEX2-GABARAP in EVs but are not necessarily in proximity to intracellular APEX2-GABARAP.

In general, the EV GABARAP proxitome contained various proteins commonly found in EVs, like 14-3-3 proteins (YWHAB, YWHAE, YWHAQ, YWHAZ), annexin proteins (ANXA2P2 and ANXA5), cytoskeletal proteins (ACTB, ACTR3, CFL1, PFN1, TUBA1B, TUBA1C, TUBB, TUBB3, and TUBB4B), heat shock proteins (HSP90AA1, HSP90AB1, HSPA6, HSPA8, and HSPD1), metabolic proteins (AHCY, ENO1, FASN, GAPDH, GSTP1, PGK1, PPIA, and UGDH), motor proteins (DYNC1H1, DYNC1I2, MYH10, and MYH9), RNA-binding proteins (RBPs) (e.g., HNRNPK, HNRNPM, HNRNPR, and HNRNPU), small GTPases (ARF3, IQGAP1, RAB1A, RAB1B, RAB10, RAB14, RAB35, RAB7A, RAN, RANGAP1, RANBP1, and RANBP2), transporters and channel proteins (ATP1A1, ATP5B, SLC25A3, SLC25A5, SLC25A6, SLC25A13, VDAC1, VDAC2, and VDAC3), and vesicle trafficking-associated proteins (Alix and VCP). A total of 216 proteins (40.0%) of the EV GABARAP proxitome was also detected in the unlabelled EV control proteome. By calculating the quotient of normalised LFQ intensities, we determined 68 proteins of the EV GABARAP proxitome enriched by a factor of > 2 compared to in the EV ctrl proteome (Supplementary Table S2). Among these enriched proteins, outstanding examples are the sodium/potassium-transporting ATPase subunit alpha-1 ATP1A1, which is required for autophagy induction [49] and is contained in clathrin-coated vesicles and earlier endosomes [50], suggesting an involvement in trafficking processes; Rab GDP dissociation inhibitor beta (GDI2), which was shown to regulate exosome maturation and secretion [51]; L-lactate dehydrogenase B chain (LDHB), a protein taking part in vesicle maturation and necessary for basal autophagy [52]; peroxiredoxin-1 (PRDX1), being released in exosomes [53]; and ubiquitin-like modifier-activating enzyme 1 (UBA1), which is required for Atg7- and Atg3-independent autophagy [54]. Additionally, these proteins are registered in Vesiclepedia [28,29] in the list of the top 100 proteins previously found in EVs. In total, of the EV GABARAP proxitome, more than 95% is registered in Vesiclepedia (Supplementary Figure S9A), and 63 proteins were found in the Vesiclepedia top 100 (Supplementary Figure S9B).
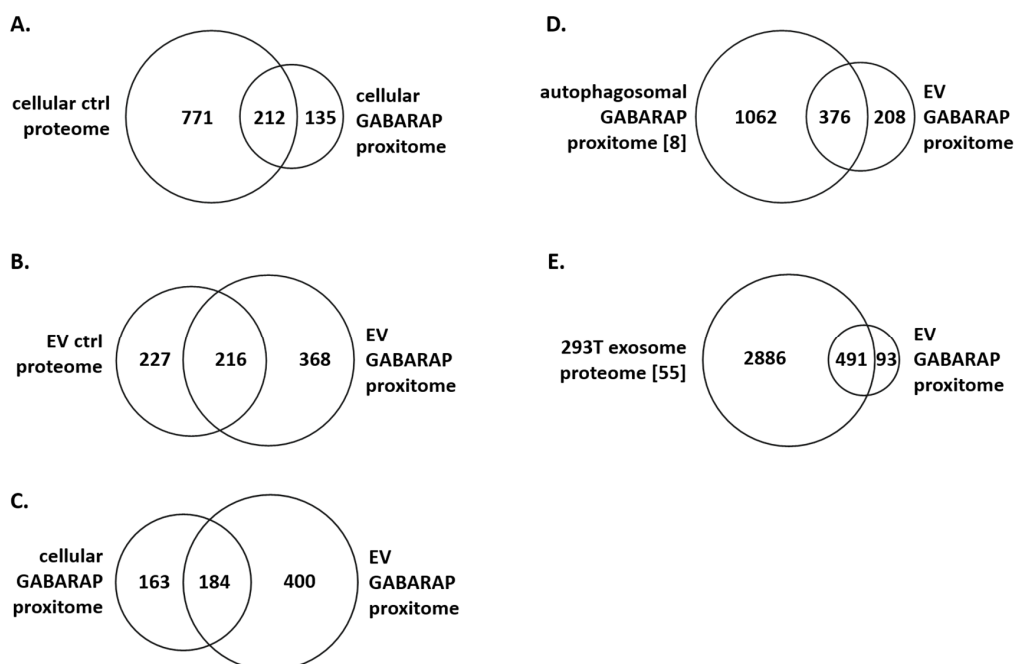
Figure 4. Overview of analysed sample types. Following APEX2-GABARAP expression, one sample type was collected without labelling (cellular (**A**) and EV (**B**) control (ctrl) proteome), while for the other sample type, cells and EVs were labelled and applied to pull-down with streptavidin (cellular (**A**) and EV (**B**) GABARAP proxitome). All samples were lysed and subjected to mass spectrometry. Cellular and EV GABARAP proxitomes were compared as shown in (**C**). The EV GABARAP proxitome was furthermore compared to the autophagosomal GABARAP proxitome as determined by Le Guerroué et al. [8] (**D**) and to the exosomal proteome of 293T cells as determined by Li et al. [55] (**E**). The Venn diagrams were created using FunRich [47,48].

Next, we compared the protein lists obtained from the cellular and EV GABARAP proxitomes (Figure 4C) and noticed that 53.0% of the proteins identified in the cellular GABARAP proxitome were also included in the EV GABARAP proxitome. In addition, when correlating the EV GABARAP proxitome with the autophagosomal GABARAP proxitome as determined by Le Guerroué et al. [8], we found that of the EV GABARAP proxitome, 64.4% (376 proteins) was detected before as proteins in proximity to autophagosomal APEX2-GABARAP (Figure 4D). We also compared the EV GABARAP proxitome with the exosomal proteome of 293T cells as determined by Li et al. [55], showing an overlap of 84.1% (491 proteins) (Figure 4E).

The complete protein hit lists of the EV GABARAP proxitome (Figure 5A,B), the cellular GABARAP proxitome (Figure 5C), the unlabelled cellular ctrl proteome (Figure 5D), the unlabelled EV ctrl proteome (Figure 5E), the 293T exosome proteome [55] (Figure 5F), and the autophagosomal GABARAP proxitome [8] (Figure 5G) were then subjected to an in-depth Gene Ontology (GO) analysis using DAVID Bioinformatics Resources 6.8 [41].
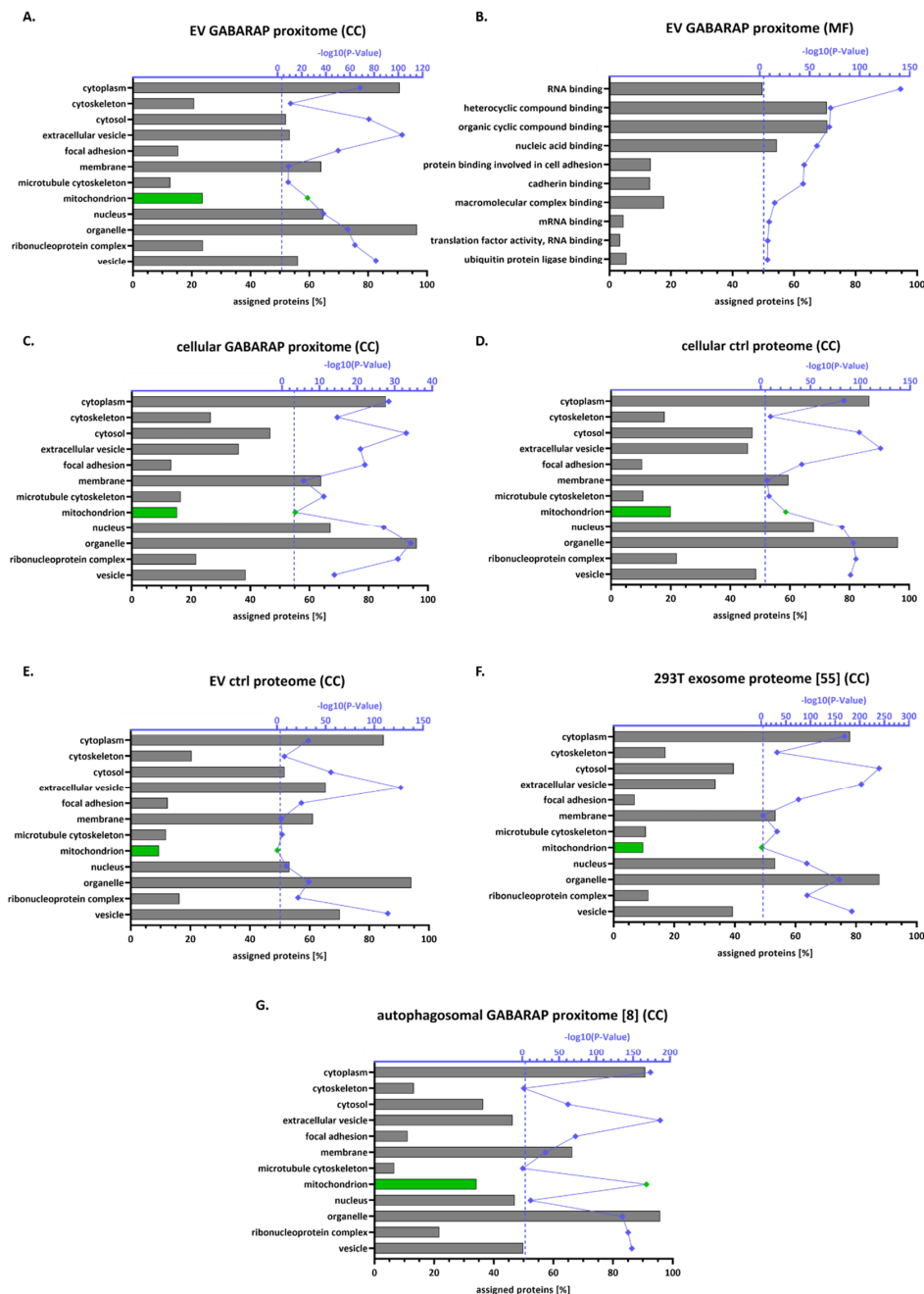
Figure 5. Categorisation of cellular and EV proteins detected by mass spectrometry. The obtained proteins for the EV GABARAP proxitome (**A**,**B**), the cellular GABARAP proxitome (**C**), the cellular ctrl proteome (**D**), the EV ctrl proteome (**E**), the 293T exosome proteome [55] (**F**), and the autophagosomal GABARAP proxitome [8] (**G**) were analysed by Gene Ontology (GO) using DAVID Bioinformatics Resources 6.8 (default background) [41] (CC: cellular compartment; MF: molecular function). The ratio of assigned proteins to the total protein number of the respective sample type is depicted in [%]. In blue, the negative log10 of the *p*-value is shown. Significantly overrepresented cellular compartments exhibiting a *p*-value of ≤0.05% (dashed line) in the EV GABARAP proxitome were selected. Mitochondrion-related bars [%] and -log10 (*p*-Value) data points are highlighted in green. For the complete data, see Supplementary Table S1. A comparative GO CC analysis of the EV GABARAP proxitome using Supplementary Table S1a as background is depicted in Supplementary Figure S10.

As expected, in the GO cellular compartment analysis of the EV GABARAP proxitome (Figure 5A), we found a high percentage of the detected proteins to be assigned to extracellular vesicles (53.5%), while this category was less represented in the cellular GABARAP proxitome (Figure 5C, 36.1%) and in the cellular ctrl proteome (Figure 5D, 45.9%). Furthermore, of all here-analysed protein lists, in the EV GABARAP proxitome the highest percentage of proteins was assigned to focal adhesions (15.3%), in accordance with cell adhesion-related proteins being loaded into EVs [56]. Furthermore, we found, rather unexpectedly, a high percentage of nucleus-assigned proteins in the EV GABARAP proxitome (64.7%). Proteins assigned to extracellular vesicles and focal adhesions also showed a significant overrepresentation when the complete list of proteins identified in this study was set as background; however, this was not the case for nucleus-assigned proteins (Supplementary Figure S10). An additional GO analysis of the EV GABARAP proxitome revealed RBPs as the top term regarding molecular functions (Figure 5B).

Intriguingly, we also detected 23.7% of the EV GABARAP proxitome to be listed and significantly overrepresented as mitochondrion-annotated proteins. Again, mitochondrion-assigned proteins also showed significant overrepresentation against the background protein list of this study (Supplementary Figure S10). By contrast, for both the whole EV ctrl proteome (Figure 5E) and the independent 293T exosome proteome [55] (Figure 5F) less than 10% of the proteins were mitochondrion-annotated and did not show significant enrichment. Interestingly, in the autophagosomal GABARAP proxitome [8] (Figure 5G), 34.2% of the proteins were assigned to mitochondria and significantly enriched in this compartment. With mitochondria being a well-defined cargo of autophagosomes [8], comparative GO analysis of the different data sets therefore hints towards an autophagosomal origin for at least a fraction of those EVs that are positive for (APEX2-)GABARAP.

Next, we analysed the proteins enriched >2-fold in the EV GABARAP proxitome compared to the EV ctrl proteome (Supplementary Table S2). Of the 68 proteins, 56 proteins were also identified in the autophagosomal GABARAP proxitome [8], of which 27 proteins were assigned to the mitochondrion using FunRich [48]. An interesting example for this category is 60 kDa heat shock protein (HSPD1), which is not only mitochondrial but is also trafficked to the cell surface and is released into the extracellular space [57]. Another heat shock protein exhibiting a high affinity for phospholipid membranes, HSP90B1 [58], was identified. Complementary to the mitochondrial proteins, we found the autophagy-involved proteins cofilin-1 (CFL1) [59], interleukin enhancer-binding factor 3 (ILF3) [60], phosphoglycerate kinase 1 (PGK1) [61], poly(rC)-binding protein 1 (PCBP1) [62], and transcription intermediary factor 1-beta (TRIM28) [63]. A role in the modulation of autophagy was also revealed for the heterogeneous nuclear ribonucleoprotein K (HNRNPK) and M (HNRNPM) [61,64]. Further ribosomal proteins—namely RPL5, RPL6, RPL12, RPL18, RPL22, RPS16, and RPS4X—were identified, possibly due to their RNA-binding property or, as recently reported, being present on the surface of exosomes [65].

Furthermore, we had a closer look at those proteins that were discovered specifically within the EV GABARAP proxitome, but neither in the EV ctrl proteome nor in the 293T exosome proteome, and set an intensity threshold of >24, corresponding to 75% of the highest normalised intensity. Of the 36 proteins meeting these requirements, 24 proteins were also found in the autophagosomal GABARAP proxitome, of which, again, many (20 proteins) are assigned to mitochondria by FunRich [48]. Examples of mitochondrial enzymes are the MICOS complex subunit MIC60 (IMMT), solute carrier family 25 member 13 (SLC25A13), and cytochrome b-c1 complex subunit 1 (UQCRC1). IMMT was previously demonstrated to be targeted by LC3C, a human Atg8 orthologue like GABARAP, to deliver mitochondrial proteins to the autophagosome [8]. Furthermore, we detected the acetyl-CoA acetyltransferase (ACAT1) and 7-dehydrocholesterol reductase (DHCR7) lipid metabolism-related proteins, and the trafficking proteins Rab7A (late endosome-to-lysosome traffic), Rab10 (exocytosis), and Rab14 (recycling endosome-to-plasma membrane (PM) traffic (Rab functions reviewed in [66]).

Next, we were curious to see whether proteins found in the intersection of the autophagosome GABARAP proxitome and the EV GABARAP proxitome (Figure 5D) contain an LC3-interacting region-motif (LIR), which can frequently be found in proteins directly interacting with both the LC3s

and the GABARAPs of the Atg8 protein family [67]. For this, we applied a sequence scan for an extended LIR motif (xLIR) [68] using the web-based ScanProsite tool [69]. Of the 376 applied proteins, we found 271 motif hits in 164 sequences (Supplementary Table S3). These hits were compared with the IntAct database, revealing 60 proteins as registered GABARAP interactors (https://www.ebi.ac.uk/intact/interactors/id:O95166*, accessed on 5 July 2019), for example transferrin receptor protein 1 (TFRC) [25], calreticulin (CALR) [70], and cathrin heavy chain 1 (CLTC) [71]. Furthermore, we identified coatomer subunit delta (COPD) as a trafficking protein and secretion-related proteins like Alix; kinesin-1 heavy chain (KIF5B), which is a protein involved in GABARAP-mediated transport [27]; and La-related protein 1 (LARP1), which was shown to take part in autophagy [72]. Future work should include a detailed study on the exact location, accessibility, and context of each potential GABARAP-binding motif identified. Such work is indispensable for each hit to better estimate whether direct binding to GABARAP is just random-based or actually feasible for the respective hit and thus potentially biological meaningful.

4. Discussion

The biological background behind GABARAP's secretion, demonstrated in this study for diverse samples, is unknown. Several scenarios are conceivable including microvesicle shedding or secretion in exosomes via multivesicular bodies or an autophagy-mediated unconventional protein secretion process, so-called autosecretion, leading to the export of autophagosomal content like mitochondria rather than degradation [73]. However, it is unclear whether GABARAP is just secreted as a by-product of the trafficking and secretion of other molecules such as insulin in a cell type-specific manner [27] or whether there exists a not-yet-described GABARAP-involving branch of EV biogenesis and transport. Here, we provide information about the co-secretome of GABARAP in EVs as a basis to unravel GABARAP's secretion mechanism.

Many studies have been conducted to analyse the protein content of EVs by MS (for examples, see [40,41]). Although it is possible to isolate specific EV fractions, e.g., by differential centrifugation, no method had been described to date to identify those proteins contained in the same EV as the POI, in this case GABARAP, and which thus define its co-secretome, which could be helpful in deciphering trafficking and secretion pathways. In principle, APEX2-proximity labelling [35] should be able to overcome this issue as this technique introduces biotin-modifications to those proteins that are localised in a 20 nm distance range surrounding the APEX2-POI-fusion. Because of the restricted sizes of EVs and particularly of exosomes, one can expect that a bulk of the protein content of each APEX2-POI-positive EV will be biotinylated and thus be marked for subsequent streptavidin-pulldown-based enrichment and identification via MS. In this regard, the most challenging task when adapting the APEX2-strategy to EV samples was coping with the small size of the particles, 40–100 nm (exosomes) and 100–1000 nm (microvesicles) [39], which were present in highly diluted form in the conditioned cell culture media. In this study, we were able to achieve the labelling of EV proteins with one of the two approaches tested. We therefore suggest an upstream concentration step for EVs when applying APEX2-mediated proximity labelling to EVs to produce the efficient biotinylation of proteins within APEX2-POI-positive EVs.

In defining the EV GABARAP proxitome, we were able to determine the first parameters in GABARAP's secretion. Proteins taking part in vesicle-mediated transport processes were found, like COPD, as were proteins involved in exosomal secretion such as Alix, GDI2, and PRDX1. Furthermore, we detected known interaction partners of GABARAP such as CALR and CLTC [70,71], and also TFRC and KIF5B, which are involved in PM-directed transport processes together with GABARAP [25,27], possibly enabling the co-secretion of the latter. Comparing the EV GABARAP proxitome with the autophagosomal GABARAP proxitome as defined by Le Guerroué et al. [8], almost two-thirds of the EV GABARAP proxitome was also detected in autophagosomes. An in-depth analysis of proteins enriched in the EV GABARAP proxitome compared to in the EV ctrl proteome and an independent exosome proteome [55] revealed a high percentage of mitochondrion-assigned

proteins in the EV GABARAP proxitome, pointing towards a possible (auto-)secretion mechanism for autophagosomal content specifically in EVs containing APEX2-GABARAP, but not in the bulk of EVs. Additionally, one could also speculate about an amphisome-mediated secretion pathway. Here, autophagosomes may fuse with multivesicular bodies and subsequently release their content into the extracellular space following fusion with the PM [74].

The use of a polymer-based EV isolation method prior to the APEX2-labelling step could be deemed as one limitation of this study. However, we chose this EV isolation technique due to its broad applicability and its ability to produce high yields of EVs regardless of their subtype, e.g., without excluding larger ones like microvesicles. That way we might have co-isolated contaminants such as protein aggregates to some extent [75], but this seems to be acceptable in our eyes, because the vast majority of them should be inaccessible to APEX2-mediated biotinylation and the following streptavidin-based pulldown in the given setup. However, we cannot completely exclude the observation of some "false-positives" within our GABARAP proxitome-derived MS data set due to unspecific co-isolates instead of biotinylated cargo of APEX2-GABARAP positive EVs. Electron microscopic measurements of EVs following the immunogold staining of GABARAP or 3,3′-diaminobenzidine (DAB) staining of APEX2-GABARAP might provide clarity in this respect. Nevertheless, shortly before the submission of our study, an approach based on BirA*-mediated proximity labelling was successfully applied to identify targets of LC3-dependent secretion. This study is interesting, because LC3, like GABARAP, belongs to the highly homologous and partly functionally redundant mammalian ATG8 protein family [21]. By labelling proteins in proximity to BirA*-LC3 intracellularly prior to secretion, Leidal et al. showed that parts of the autophagic machinery, more precisely the LC3-conjugation machinery, are required for the secretion and packaging of diverse RBPs in EVs that are enriched in lipidated LC3 [76]. When comparing our EV GABARAP proxitome, the "co-secretome" of APEX2-GABARAP, with the list of biotinylated proteins significantly enriched in EVs after intracellular BirA*-LC3 tagging, 38.7% of the BirA*-LC3 targeted proteins could also be identified in the EV GABARAP proxitome (Supplementary Figure S11). Among them, as in the Leidal study, we identified the RBPs G3BP1, HNRNPK, LARP1, and SF3A1, which have already been demonstrated to associate with ATG8 family members in pulldown experiments. In this context, a new loading mechanism for RBPs into intraluminal vesicles of multivesicular bodies (MVBs) that relies on the LC3 conjugation machinery, neutral sphingomyelinase 2 (nSMase2), and an LC3-dependent recruitment of its regulator (factor associated with nSMase2 activity (FAN)) has been proposed [76]. Future studies are needed to clarify a putative functional redundancy of both GABARAP and LC3 regarding the underlying molecular mechanisms of "LC3-dependent EV loading and secretion", a newly defined secretory pathway distinct from classical autophagy [76].

Taken together, this study provides the first information about proteins secreted together with GABARAP in EVs, indicating two pathways as possible mechanisms, including a putative autophagosome-mediated mechanism for, e.g., mitochondrial contents as well as an MVB-mediated pathway involving the ATG8-conjugation machinery for RBPs. In a broader context, we show that APEX2-mediated proximity labelling is applicable to secreted and isolated EVs from HEK293 cell culture supernatants and therefore might be a basis for disclosing the secrets of further biologically or medically relevant proteins contained in EVs, e.g., markers for cancer progression or diagnostic markers relevant for diverse neurodegenerative diseases.

Supplementary Materials: The following are available online at http://www.mdpi.com/2073-4409/9/6/1468/s1. Figure S1: APEX2-mediated proximity labelling in intracellular and extracellular compartments of mammalian cells. Figure S2: Enrichment of EV samples from HEK293, Huh7, and SH-SY5Y cells was tested by TEM and NTA. Figure S3: GABARAP is detected in a density gradient. Figure S4: Full images of blots shown in Figure 1A–D. Figure S5: EGFP-GABARAP, expressed at the endogenous level [46], is secreted in EVs. Figure S6: Full images of blots shown in Figure 2B,D. Figure S7: Full images of blots shown in Figure 3B,C. Figure S8: Venn diagram of autophagosomal and cellular proteins. Figure S9: Comparison of the EV GABARAP proxitome with Vesiclepedia entries [28,29]. Figure S10: Categorisation of the EV GABARAP proxitome using proteins of Table S1a as background. Figure S11: Comparison with BirA*-LC3 enriched proteins. Table S1: Mass spectrometric data.

Table S2: Proteins enriched in or exclusive for the EV GABARAP proxitome. Table S3: Proteins containing an xLIR motif.

References

1. Martell, J.D. Engineered ascorbate peroxidase as a genetically encoded reporter for electron microscopy. *Nat. Biotechnol.* **2012**, *30*, 1143–1148. [CrossRef] [PubMed]

2. Rhee, H.-W. Proteomic mapping of mitochondria in living cells via spatially restricted enzymatic tagging. *Science* **2013**, *339*, 1328–1331. [CrossRef] [PubMed]

3. Lam, S.S. Directed evolution of APEX2 for electron microscopy and proximity labeling. *Nat. Methods* **2015**, *12*, 51–54. [CrossRef] [PubMed]

4. Paek, J. Multidimensional tracking of GPCR signaling via peroxidase-catalyzed proximity labeling. *Cell* **2017**, *169*, 338–349. [CrossRef]

5. Zhen, Y. Proximity Labeling by a recombinant APEX2–FGF1 fusion protein reveals interaction of FGF1 with the proteoglycans CD44 and CSPG4. *Biochemistry* **2018**, *57*, 3807–3816. [CrossRef]

6. Del Olmo, T. APEX2-mediated RAB proximity labeling identifies a role for RAB21 in clathrin-independent cargo sorting. *EMBO Rep.* **2019**, *20*, e47192. [CrossRef]

7. Bersuker, K. A Proximity labeling strategy provides insights into the composition and dynamics of lipid droplet proteomes. *Dev. Cell* **2018**, *44*, 97–112. [CrossRef]

8. Le Guerroué, F. Autophagosomal content profiling reveals an LC3C-Dependent piecemeal mitophagy pathway. *Mol. Cell* **2017**, *68*, 786–796. [CrossRef]

9. Singer-Kruger, B. APEX2-mediated proximity labeling resolves protein networks in Saccharomyces cerevisiae cells. *FEBS J.* **2020**, *287*, 325–344. [CrossRef]

10. van Niel, G.; D'Angelo, G.; Raposo, G. Shedding light on the cell biology of extracellular vesicles. *Nat. Rev. Mol. Cell Biol.* **2018**, *19*, 213. [CrossRef]

11. Nickel, W. Pathways of unconventional protein secretion. *Curr. Opin. Biotechnol.* **2010**, *21*, 621–626. [CrossRef] [PubMed]

12. Valadi, H. Exosome-mediated transfer of mRNAs and microRNAs is a novel mechanism of genetic exchange between cells. *Nat Cell Biol.* **2007**, *9*, 654–659. [CrossRef] [PubMed]

13. Kim, K.M. RNA in extracellular vesicles. *Wiley Interdiscip. Rev. RNA* **2017**, *8*, e1413. [CrossRef] [PubMed]

14. Théry, C. Minimal information for studies of extracellular vesicles 2018 (MISEV2018): A position statement of the international society for extracellular vesicles and update of the MISEV2014 guidelines. *J. Extracell. Vesicles* **2018**, *7*, 1535750. [CrossRef]

15. Ohsumi, Y. Historical landmarks of autophagy research. *Cell Res.* **2013**, *24*, 9. [CrossRef]

16. Nguyen, T.N. Atg8 family LC3/GABARAP proteins are crucial for autophagosome–lysosome fusion but not autophagosome formation during PINK1/Parkin mitophagy and starvation. *J. Cell Biol.* **2016**, *215*, 857–874. [CrossRef]

17. Ichimura, Y. A ubiquitin-like system mediates protein lipidation. *Nature* **2000**, *408*, 488–492. [CrossRef]

18. Geng, J.; Klionsky, D.J. The Atg8 and Atg12 ubiquitin-like conjugation systems in macroautophagy. *EMBO Rep.* **2008**, *9*, 859–864. [CrossRef]

19. Tanida, I. GATE-16 and GABARAP are authentic modifiers mediated by Apg7 and Apg3. *Biochem. Biophys. Res. Commun.* **2003**, *300*, 637–644. [CrossRef]

20. Kabeya, Y. LC3, GABARAP and GATE16 localize to autophagosomal membrane depending on form-II formation. *J. Cell Sci.* **2004**, *117*, 2805–2812. [CrossRef]

21. Schaaf, M.B.E. LC3/GABARAP family proteins: Autophagy-(un)related functions. *FASEB J.* **2016**, *30*, 3961–3978. [CrossRef] [PubMed]

22. Weiergräber, O.H.; Mohrlüder, J.; Willbold, D. Atg8 family proteins—Autophagy and beyond. In *Autophagy-A Double-Edged Sword-Cell Survival or Death?* Bailly, Y., Ed.; InTech: Rijeka, Croatia, 2013; pp. 13–45.

23. Chen, Z.-W. C-terminal modification is required for GABARAP-Mediated GABAA receptor trafficking. *J. Neurosci.* **2007**, *27*, 6655–6663. [CrossRef]

24. Wang, H. GABAA-receptor-associated protein links GABAA receptors and the cytoskeleton. *Nature* **1999**, *397*, 69–72. [CrossRef] [PubMed]

25. Green, F. Association of human transferrin receptor with GABARAP. *FEBS Lett.* **2002**, *518*, 101–106. [CrossRef]

26. Cook, J.L. The trafficking protein GABARAP binds to and enhances plasma membrane expression and function of the angiotensin II type 1 receptor. *Circ. Res.* **2008**, *102*, 1539–1547. [CrossRef] [PubMed]

27. Asano, S. Phospholipase C-related catalytically inactive protein (PRIP) controls KIF5B-mediated insulin secretion. *Biol. Open* **2014**, *3*, 463–474. [CrossRef]

28. Kalra, H. Vesiclepedia: A compendium for extracellular vesicles with continuous community annotation. *PLoS Biol.* **2012**, *10*, e1001450. [CrossRef]

29. Pathan, M. Vesiclepedia 2019: A compendium of RNA, proteins, lipids and metabolites in extracellular vesicles. *Nucleic Acids Res.* **2019**, *47*, D516–D519. [CrossRef]

30. Skog, J. Glioblastoma microvesicles transport RNA and proteins that promote tumour growth and provide diagnostic biomarkers. *Nat. Cell Biol.* **2008**, *10*, 1470–1476. [CrossRef]

31. Hong, B.S. Colorectal cancer cell-derived microvesicles are enriched in cell cycle-related mRNAs that promote proliferation of endothelial cells. *BMC Genom.* **2009**, *10*, 556. [CrossRef]

32. Sinha, A. In-depth proteomic analyses of ovarian cancer cell line exosomes reveals differential enrichment of functional categories compared to the NCI 60 proteome. *Biochem. Biophys. Res. Commun.* **2014**, *445*, 694–701. [CrossRef]

33. Hurwitz, S.N. Proteomic profiling of NCI-60 extracellular vesicles uncovers common protein cargo and cancer type-specific biomarkers. *Oncotarget* **2016**, *7*, 86999–87015. [CrossRef] [PubMed]

34. Steenbeek, S.C. Cancer cells copy migratory behavior and exchange signaling networks via extracellular vesicles. *EMBO J.* **2018**, *37*, e98357. [CrossRef] [PubMed]

35. Zhang, H. Identification of distinct nanoparticles and subsets of extracellular vesicles by asymmetric flow field-flow fractionation. *Nat. Cell Biol.* **2018**, *20*, 332–343. [CrossRef]

36. Simons, I.M. The highly GABARAP specific rat monoclonal antibody 8H5 visualizes GABARAP in immunofluorescence imaging at endogenous levels. *Sci. Rep.* **2019**, *9*, 526. [CrossRef] [PubMed]

37. Lobb, R.J. Optimized exosome isolation protocol for cell culture supernatant and human plasma. *J. Extracell. Vesicles* **2015**, *4*, 27031. [CrossRef] [PubMed]

38. Hung, V. Spatially resolved proteomic mapping in living cells with the engineered peroxidase APEX2. *Nat. Protoc.* **2016**, *11*, 456–475. [CrossRef]

39. Ladner, C.L. Visible fluorescent detection of proteins in polyacrylamide gels without staining. *Anal. Biochem.* **2004**, *326*, 13–20. [CrossRef]

40. Grube, L. Mining the secretome of C2C12 muscle cells: Data dependent experimental approach to analyze protein secretion using label-free quantification and peptide based analysis. *J. Proteome Res.* **2018**, *17*, 879–890. [CrossRef]

41. Huang, D.W.; Sherman, B.T.; Lempicki, R.A. Systematic and integrative analysis of large gene lists using DAVID bioinformatics resources. *Nat. Protoc.* **2008**, *4*, 44. [CrossRef]

42. Thery, C. Isolation and characterization of exosomes from cell culture supernatants and biological fluids. *Curr. Protoc. Cell Biol.* **2006**, *30*, 3–22. [CrossRef] [PubMed]

43. Nath, S. Lipidation of the LC3/GABARAP family of autophagy proteins relies on a membrane-curvature-sensing domain in Atg3. *Nat. Cell Biol.* **2014**, *16*, 415–424. [CrossRef] [PubMed]

44. Muratori, C. Massive secretion by T cells is caused by HIV nef in infected cells and by nef transfer to bystander cells. *Cell Host Microbe* **2009**, *6*, 218–230. [CrossRef]

45. Doyle, L.M.; Wang, M.Z. Overview of extracellular vesicles, their origin, composition, purpose, and methods for exosome isolation and analysis. *Cells* **2019**, *8*, 727. [CrossRef]

46. Dobner, J. Deficiency of GABARAP but not its paralogs causes enhanced EGF-induced EGFR degradation. *Cells* **2020**, *9*, 1296. [CrossRef]

47. Pathan, M. FunRich: An open access standalone functional enrichment and interaction network analysis tool. *Proteomics* **2015**, *15*, 2597–2601. [CrossRef] [PubMed]

48. Pathan, M. A novel community driven software for functional enrichment analysis of extracellular vesicles data. *J. Extracell. Vesicles* **2017**, *6*, 1321455. [CrossRef]

49. Mukhopadhyay, R. Digitoxin suppresses human cytomegalovirus replication via Na(+), K(+)/ATPase alpha1 subunit-dependent amp-activated protein kinase and autophagy activation. *J. Virol.* **2018**, *92*, e01861-17. [CrossRef]

50. Massey, K.J. Phosphorylation of rat kidney Na-K pump at Ser938 is required for rapid angiotensin II-dependent stimulation of activity and trafficking in proximal tubule cells. *Am. J. Physiol. Cell Physiol.* **2016**, *310*, C227–C232. [CrossRef]

51. Gu, H. Sorting protein VPS33B regulates exosomal autocrine signaling to mediate hematopoiesis and leukemogenesis. *J. Clin. Investig.* **2016**, *126*, 4537–4553. [CrossRef]

52. Brisson, L. Lactate dehydrogenase B controls lysosome activity and autophagy in cancer. *Cancer Cell* **2016**, *30*, 418–431. [CrossRef] [PubMed]

53. Mullen, L. Cysteine oxidation targets peroxiredoxins 1 and 2 for exosomal release through a novel mechanism of redox-dependent secretion. *Mol. Med.* **2015**, *21*, 98–108. [CrossRef] [PubMed]

54. Chang, T.K. Uba1 functions in Atg7- and Atg3-independent autophagy. *Nat. Cell Biol.* **2013**, *15*, 1067–1078. [CrossRef] [PubMed]

55. Li, J. Identification and characterization of 293T cell-derived exosomes by profiling the protein, mRNA and microrna components. *PLoS ONE* **2016**, *11*, e0163043. [CrossRef]

56. Choi, D.S. Quantitative proteomics of extracellular vesicles derived from human primary and metastatic colorectal cancer cells. *J. Extracell. Vesicles* **2012**, *1*, 18704. [CrossRef]

57. Kim, B.Y. 27-hydroxycholesterol upregulates the production of heat shock protein 60 of monocytic cells. *J. Steroid Biochem. Mol. Biol.* **2017**, *172*, 29–35. [CrossRef] [PubMed]

58. Li, P. Interaction of heat shock protein 90 B1 (Hsp90B1) with liposome reveals its potential role in protection the integrity of lipid membranes. *Int. J. Biol. Macromol.* **2018**, *106*, 1250–1257. [CrossRef]

59. Wang, H.J.; Chen, S.F.; Lo, W.Y. Identification of cofilin-1 induces G0/G1 arrest and autophagy in angiotensin-(1-7)-treated human aortic endothelial cells from itraq quantitative proteomics. *Sci. Rep.* **2016**, *6*, 35372. [CrossRef]

60. Pu, Z. LncRNA MEG3 contributes to adenosine-induced cytotoxicity in hepatoma HepG2 cells by downregulated ILF3 and autophagy inhibition via regulation PI3K-AKT-mTOR and beclin-1 signaling pathway. *J. Cell Biochem.* **2019**, *120*, 18172–18185. [CrossRef]

61. DeJesus, R. Functional CRISPR screening identifies the ufmylation pathway as a regulator of SQSTM1/p62. *Elife* **2016**, *5*, e17290. [CrossRef]

62. Zhang, W. Poly C binding protein 1 represses autophagy through downregulation of LC3B to promote tumor cell apoptosis in starvation. *Int. J. Biochem. Cell Biol.* **2016**, *73*, 127–136. [CrossRef] [PubMed]

63. Peng, Y. TRIM28 activates autophagy and promotes cell proliferation in glioblastoma. *Onco Targets Ther.* **2019**, *12*, 397–404. [CrossRef] [PubMed]

64. Li, Z. HnRNPK modulates selective quality-control autophagy by downregulating the expression of HDAC6 in 293 cells. *Int. J. Oncol.* **2018**, *53*, 2200–2212. [CrossRef] [PubMed]

65. Xu, R. Surfaceome of exosomes secreted from the colorectal cancer cell line SW480: Peripheral and integral membrane proteins analyzed by proteolysis and TX114. *Proteomics* **2019**, *19*, e1700453. [CrossRef]

66. Hutagalung, A.H.; Novick, P.J. Role of rab GTPases in membrane traffic and cell physiology. *Physiol. Rev.* **2011**, *91*, 119–149. [CrossRef] [PubMed]

67. Birgisdottir, A.B.; Lamark, T.; Johansen, T. The LIR motif-crucial for selective autophagy. *J. Cell Sci.* **2013**, *126*, 3237–3247.

68. Kalvari, I. ILIR: A web resource for prediction of Atg8-family interacting proteins. *Autophagy* **2014**, *10*, 913–925. [CrossRef]

69. de Castro, E. ScanProsite: Detection of PROSITE signature matches and ProRule-associated functional and structural residues in proteins. *Nucleic Acids Res.* **2006**, *34*, W362–W365. [CrossRef]

70. Mohrlüder, J. Identification of calreticulin as a ligand of GABARAP by phage display screening of a peptide library. *FEBS J.* **2007**, *274*, 5543–5555. [CrossRef]

71. Mohrlüder, J. Identification of clathrin heavy chain as a direct interaction partner for the γ-Aminobutyric acid type a receptor associated protein. *Biochemistry* **2007**, *46*, 14537–14543. [CrossRef]

72. McKnight, N.C. Genome-wide siRNA screen reveals amino acid starvation-induced autophagy requires SCOC and WAC. *EMBO J.* **2012**, *31*, 1931–1946. [CrossRef] [PubMed]

73. Deretic, V.; Jiang, S.Y.; Dupont, N. Autophagy intersections with conventional and unconventional secretion in tissue development, remodeling and inflammation. *Trends Cell Biol.* **2012**, *22*, 397–406. [CrossRef] [PubMed]

74. Manjithaya, R.; Subramani, S. Autophagy: A broad role in unconventional protein secretion? *Trends Cell Biol.* **2011**, *21*, 67–73. [CrossRef] [PubMed]

75. Tang, Y.T. Comparison of isolation methods of exosomes and exosomal RNA from cell culture medium and serum. *Int. J. Mol. Med.* **2017**, *40*, 834–844. [CrossRef] [PubMed]

76. Leidal, A.M. The LC3-conjugation machinery specifies the loading of RNA-binding proteins into extracellular vesicles. *Nat. Cell Biol.* **2020**, *22*, 1–13. [CrossRef] [PubMed]

1 # Supplementary Figures

2

3 **The GABARAP co-secretome identified by APEX2-GABARAP proximity labelling**

4 **of extracellular vesicles**

5 Julia L. Sanwald [1,2], Gereon Poschmann [3], Kai Stühler [3,4], Christian Behrends [5], Silke Hoffmann [2], Dieter

6 Willbold [1,2]

7 [1] Institut für Physikalische Biologie, Heinrich-Heine-Universität Düsseldorf, Universitätsstraße 1, 40225

8 Düsseldorf, Germany

9 [2] Institute of Biological Information Processing (IBI-7: Structural Biochemistry), Forschungszentrum Jülich,

10 Leo-Brandt-Straße, 52428 Jülich, Germany

11 [3] Institute of Molecular Medicine I, Heinrich-Heine-Universität Düsseldorf, Universitätsstraße 1, 40225

12 Düsseldorf, Germany

13 [4] Molecular Proteomics Laboratory, Biologisch-Medizinisches Forschungszentrum (BMFZ), Heinrich-Heine-

14 Universität Düsseldorf, Universitätsstraße 1, 40225 Düsseldorf, Germany

15 [5] Munich Cluster for Systems Neurology (SyNergy), Ludwig-Maximilians-Universität München, Feodor-

16 Lynen-Straße 17, 81377 München, Germany

17

18

19 Supplementary Figure S1 is related to Introduction

20 Supplementary Figure S2 is related to Figure 1A

21 Supplementary Figure S3 is related to Figure 1

22 Supplementary Figure S4 is related to Figure 1

23 Supplementary Figure S5 is related to Figure 2

24 Supplementary Figure S6 is related to Figure 2B and 2D

25 Supplementary Figure S7 is related to Figure 3B-3C

26 Supplementary Figure S8 is related to Figure 4A

27 Supplementary Figure S9 is related to Figure 4B-4E

28 Supplementary Figure S10 is related to Figure 5A

29 Supplementary Figure S11 is related to Discussion

30

Supplementary Figure S1
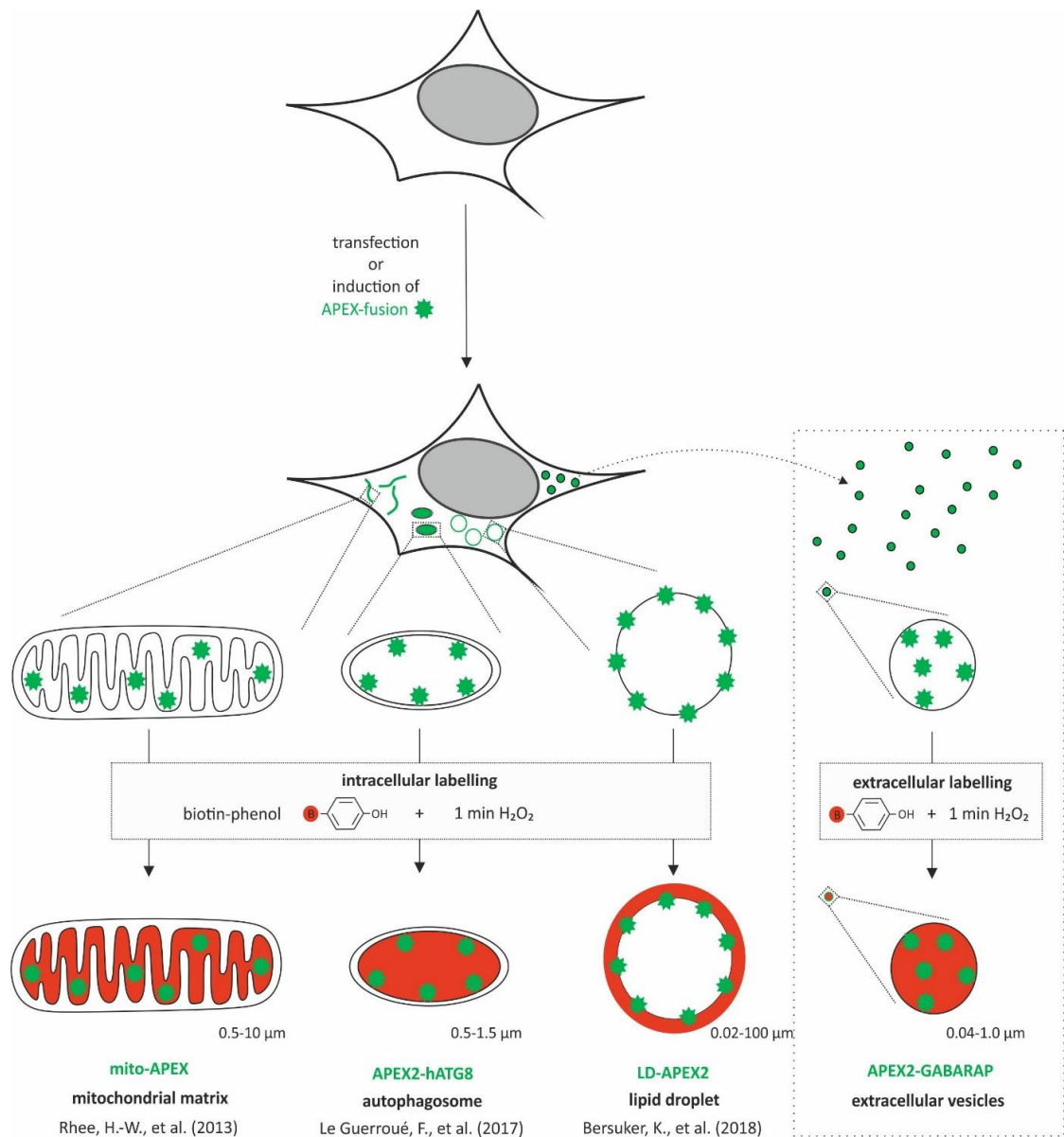
Supplementary Figure S1. APEX2-mediated proximity labelling in intra- and extracellular compartments of mammalian cells. Schematic of cellular compartments in which APEX2-mediated proximity labelling was applied previously (from leftmost to second from right): Mitochondrial matrix, autophagosome, and lipid droplets. For these compartments, labelling was conducted intracellularly. Here, we demonstrate the method's applicability for extracellular compartments, such as extracellular vesicles (rightmost). This schematic does not represent the actual size dimensions and was upscaled for enhanced visibility.
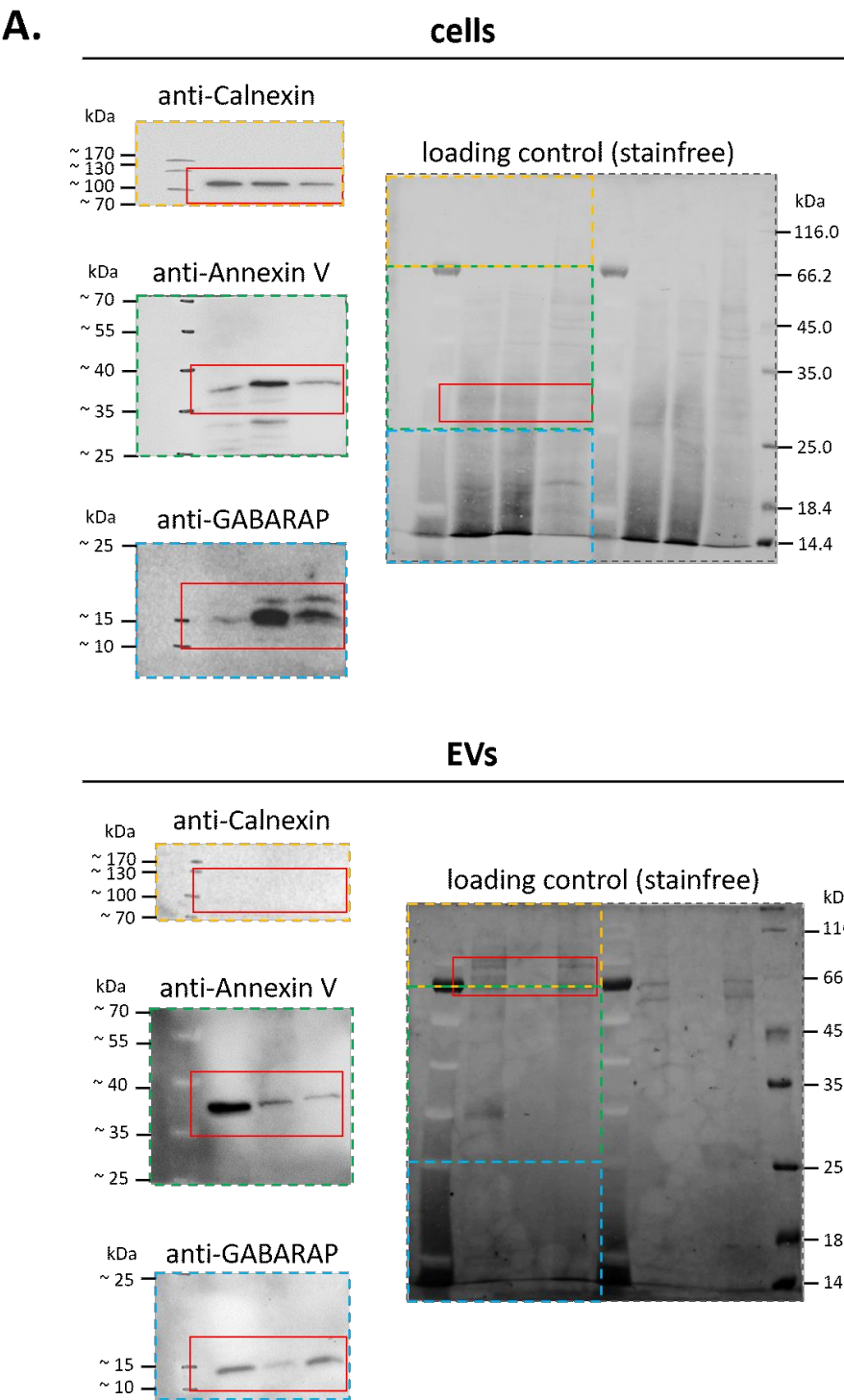
Supplementary Figure S2
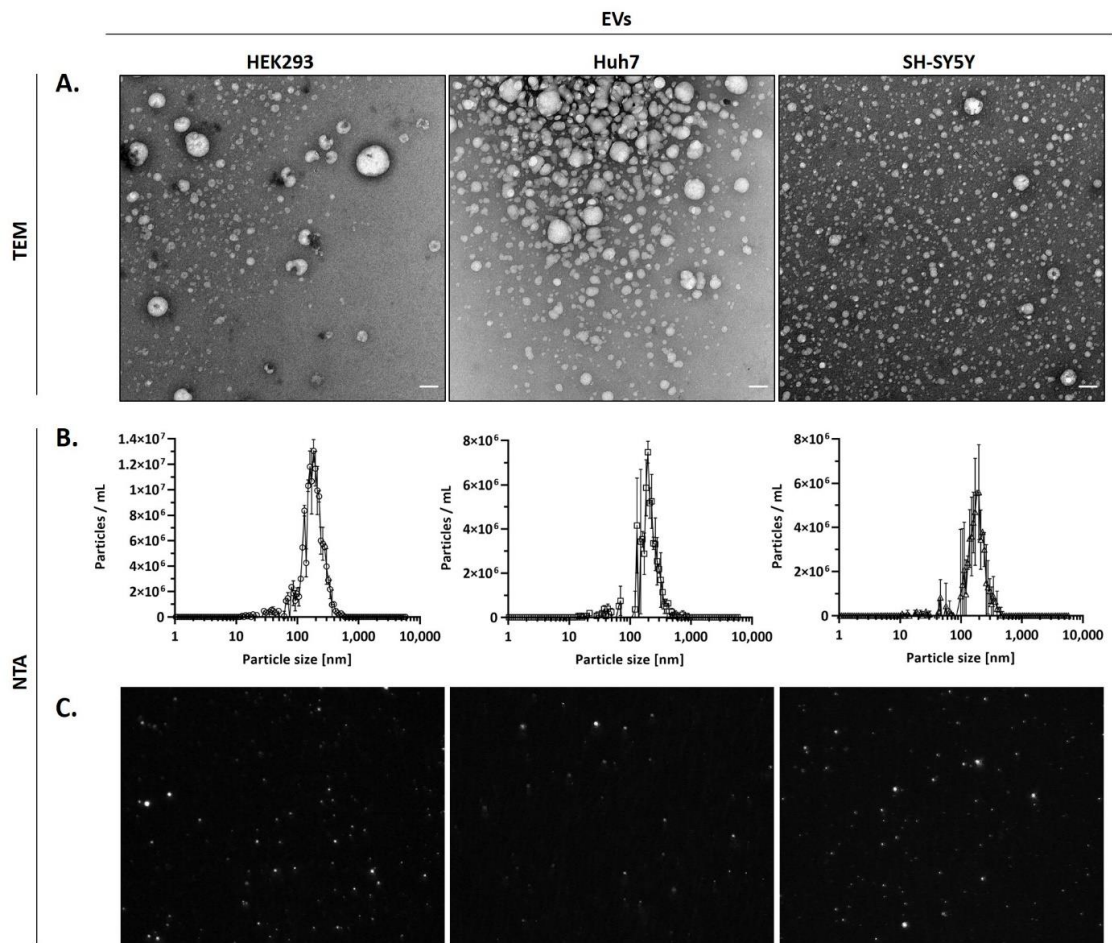
Supplementary Figure S2. Enrichment of EV samples from HEK293, Huh7, and SH-SY5Y cells was tested by TEM and NTA. (A) After ultracentrifugation-based isolation from cell culture supernatants, the EVs were resuspended in 2 % PFA, contrasted in 4 % uranyl acetate, embedded in 10 % trehalose on formvar/carbon coated EM grids, and visualised by TEM. One representative image of at least five technical replicates is shown. Scale bar 100 nm. (B) Nanoparticle tracking analysis (NTA) of the EV samples shown under A. Concentrated cell culture media were subjected to NTA, resulting in a distribution of particle sizes ranging from 10.1 nm to 838.3 nm. Of each sample, two trackings were recorded. Particle counts and standard deviations were calculated after background subtraction. (C) Single frames of NTA measurement videos depicting the particle distribution. Representative data of two technical replicates are shown in (B) and (C).
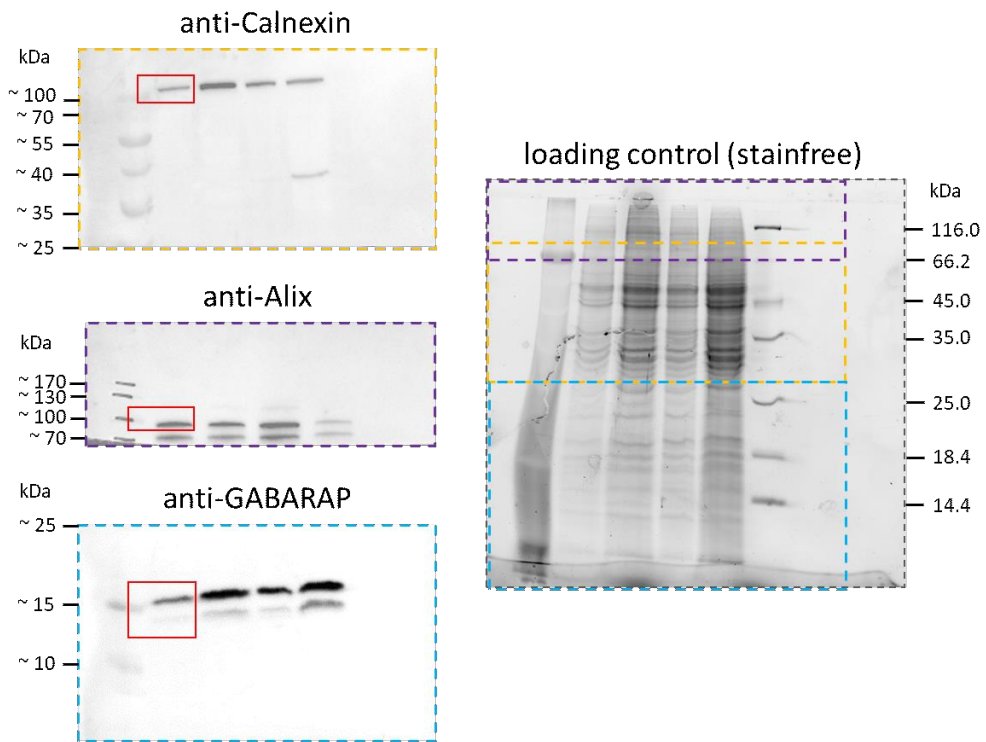
50

53
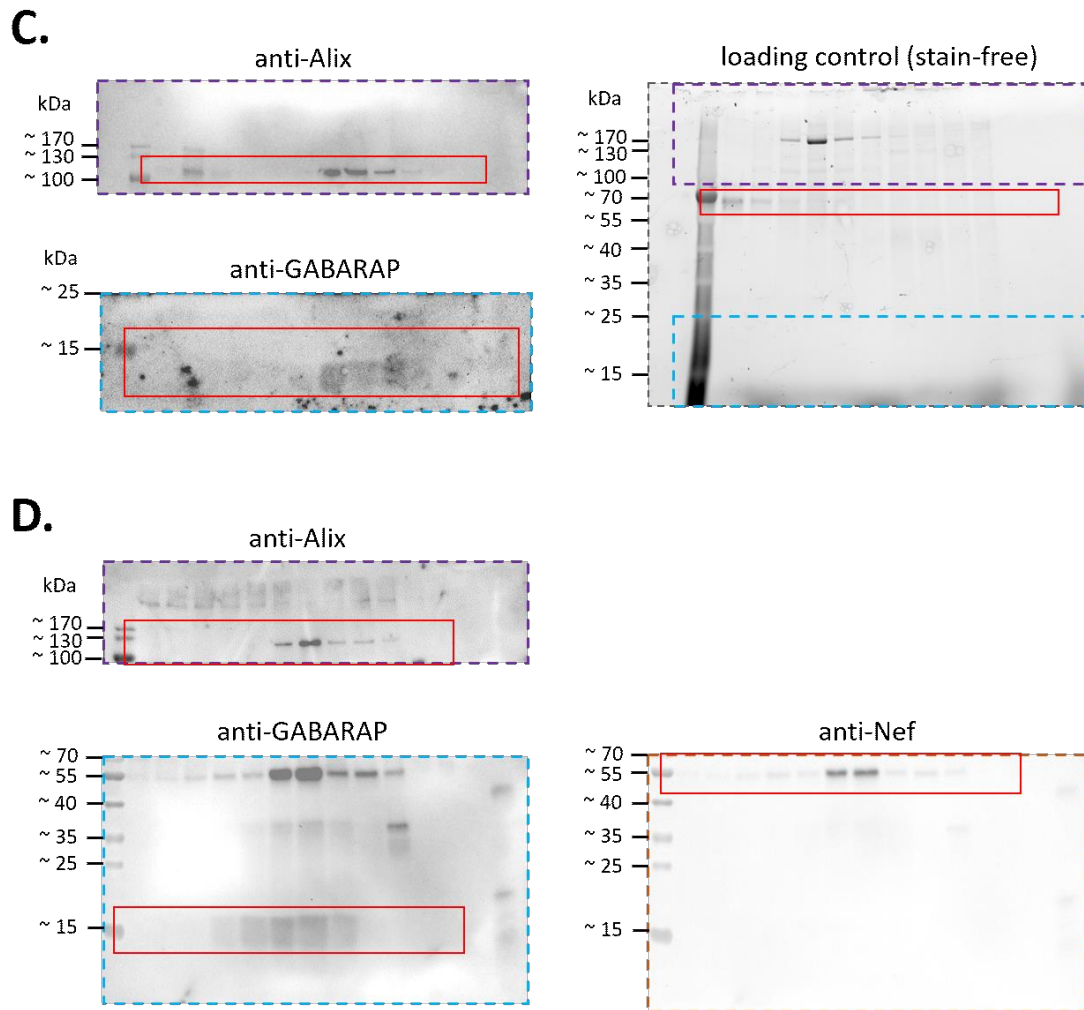
Supplementary Figure S3. GABARAP is detected in a density gradient. GABARAP is detected in density gradient fractions corresponding to the buoyant density of EVs. EVs were isolated (A) from HEK293 WT cells and (B) from HEK293 cells stably overexpressing HIV-1 Nef, a protein known to trigger both its own and EV secretion in general. One representative blot out of three, each performed with cell lysates from different passage numbers, is shown. Before EV isolation by ultracentrifugation, larger vesicles were removed by centrifugation at 10,000 x g. A representative crop of a stain-free gel is shown as loading control. (C) Uncropped immunoblots related to (A). The cropped region is indicated by red box. (D) Uncropped immunoblots related to (B). The cropped region is indicated by red box. Dashed coloured boxes in the stain-free image correspond to the respective areas into which the blot was cut for incubation with different antibodies.

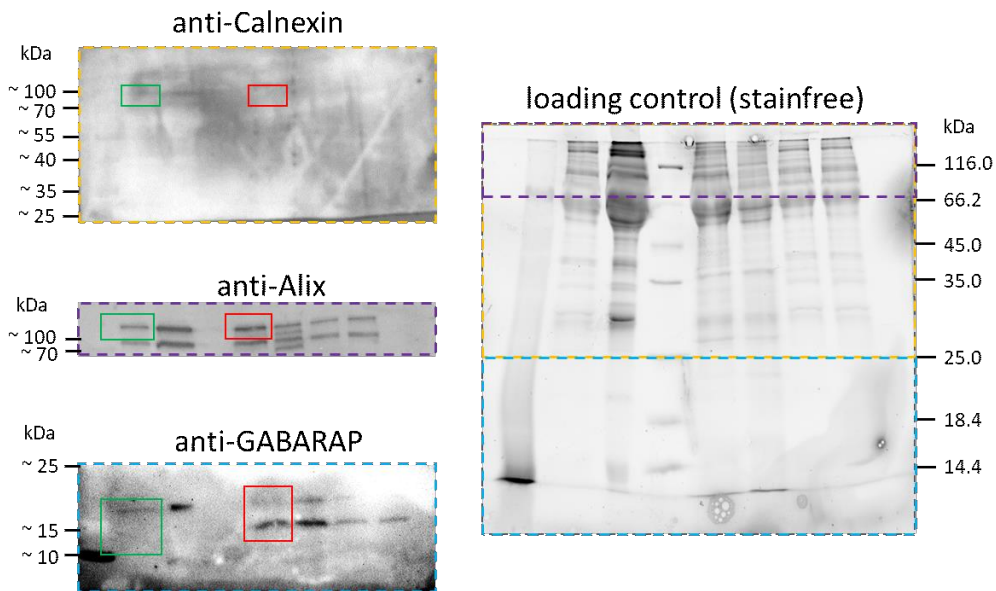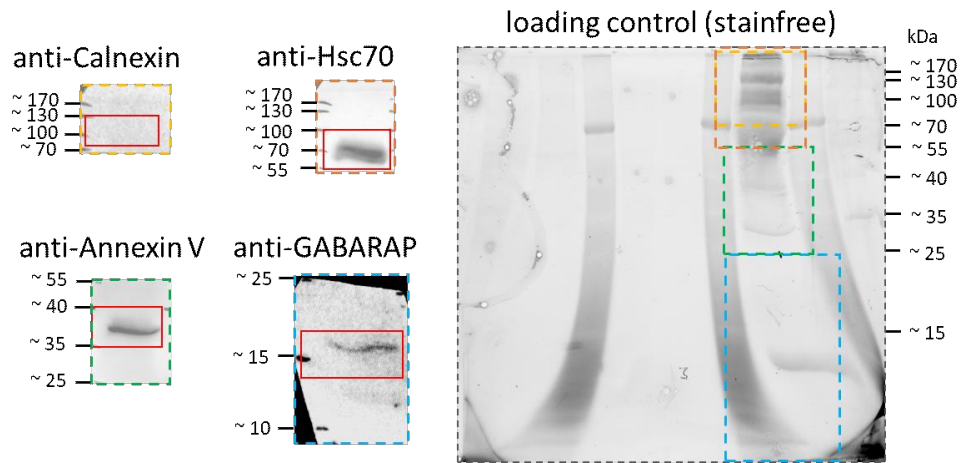**Supplementary Figure S4**

A.

cells

EVs

B.

cells

anti-Calnexin

loading control (stainfree)

anti-Alix

anti-GABARAP

EVs

anti-Calnexin

loading control (stainfree)

anti-Alix

anti-GABARAP

65

C.

anti-Calnexin

anti-Hsc70

loading control (stainfree)

anti-Annexin V

anti-GABARAP

66

D.

anti-Hsc70

anti-Calnexin

* non-specific

loading control (stainfree)

anti-GABARAP

anti-CD81
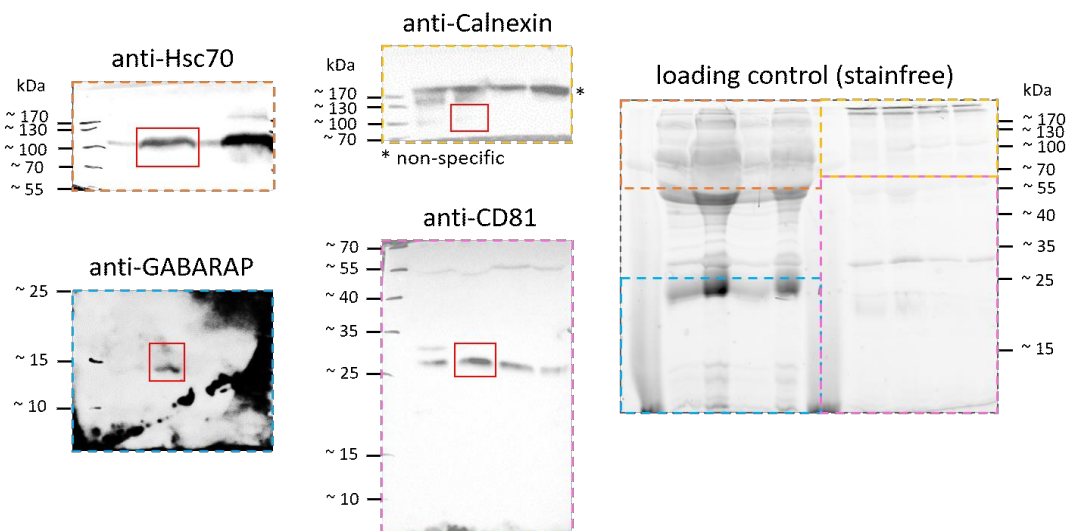
67

Supplementary Figure S4. Full images of blots shown in Figure 1A-1D. The cropped region is indicated by red box. GABARAP (dashed blue box) is secreted in EVs and is detectable by immunoblotting. Alix (dashed purple box), Annexin V (dashed green box), Hsc70 (dashed orange box), and CD81 (dashed magenta box) were used as EV marker proteins, and Calnexin (dashed yellow box) as marker for cellular impurities in an EV sample. (A) Uncropped versions of the blots and the corresponding stain-free gels related to Figure 1A. GABARAP is detected in EVs from the three human cell lines HEK293, Huh7, and SH-SY5Y after starvation. One representative blot of two different cellular passages is shown. EVs were obtained by ultracentrifugation. (B) Uncropped versions of the blots and the corresponding stain-free gels related to Figure 1B. Under fed conditions, predominantly lipidated GABARAP is detectable in HEK293 EVs, while unlipidated GABARAP was detected in unconditioned media (UCM; the cropped regions are indicated by green boxes). One representative blot of two different cellular passages is shown. EVs were prepared using polymer-based precipitation. (C) Uncropped versions of the blots and the corresponding stain-free gel related to Figure 1C. Unlipidated GABARAP is detectable in EVs isolated from bovine blood serum. One representative blot of two analysed EV batches, independently obtained from the same batch of FCS (Cat. No. F9665, Sigma-Aldrich), is shown. EVs were obtained by ultracentrifugation. (D) Uncropped versions of the blots and the corresponding stain-free gel related to Figure 1D. GABARAP is detectable in EVs isolated from human blood plasma. One representative blot of two analysed EV batches is shown. Respective EV samples were obtained from independent blood samples of the same donor. EVs were prepared by ultracentrifugation. Dashed
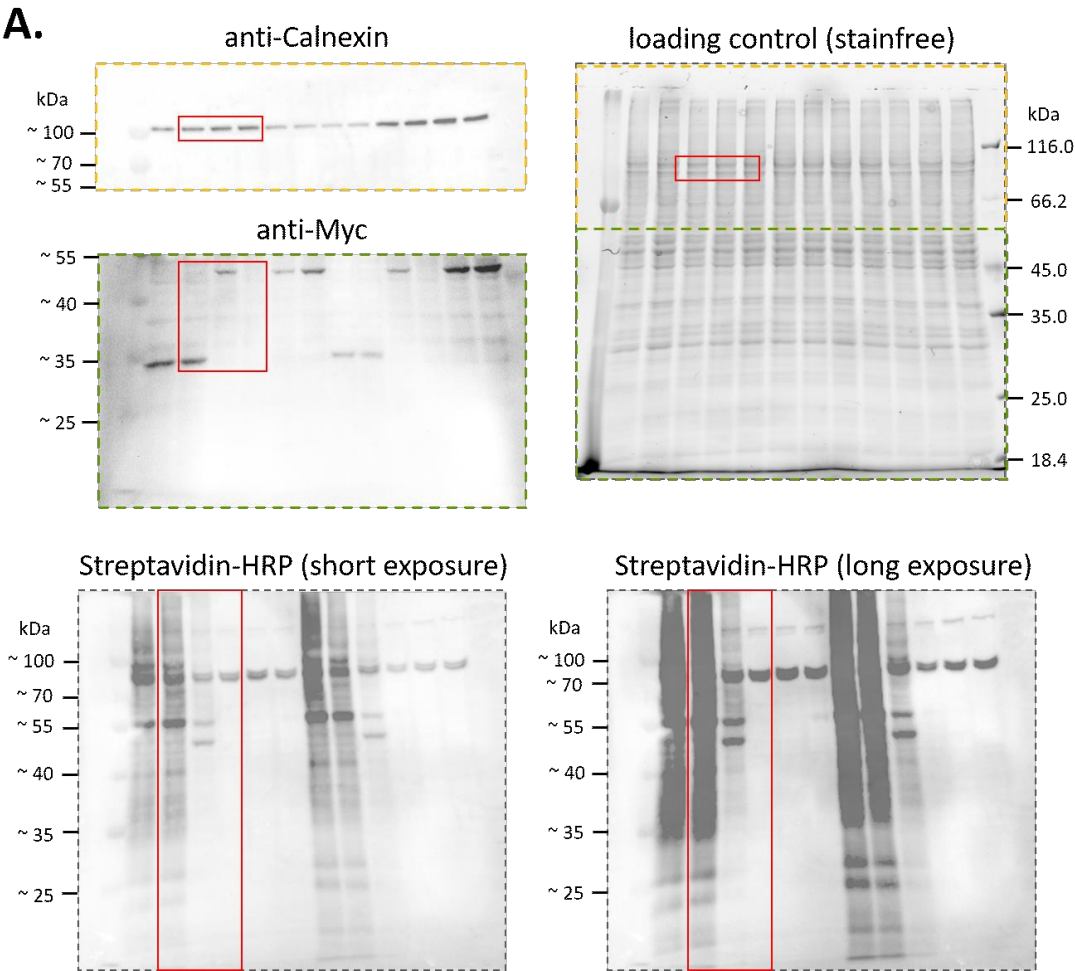
85 coloured boxes in the stain-free image correspond to the respective areas into which the blot was cut for incubation
86 with different antibodies.

Supplementary Figure S5

A.

88

B.
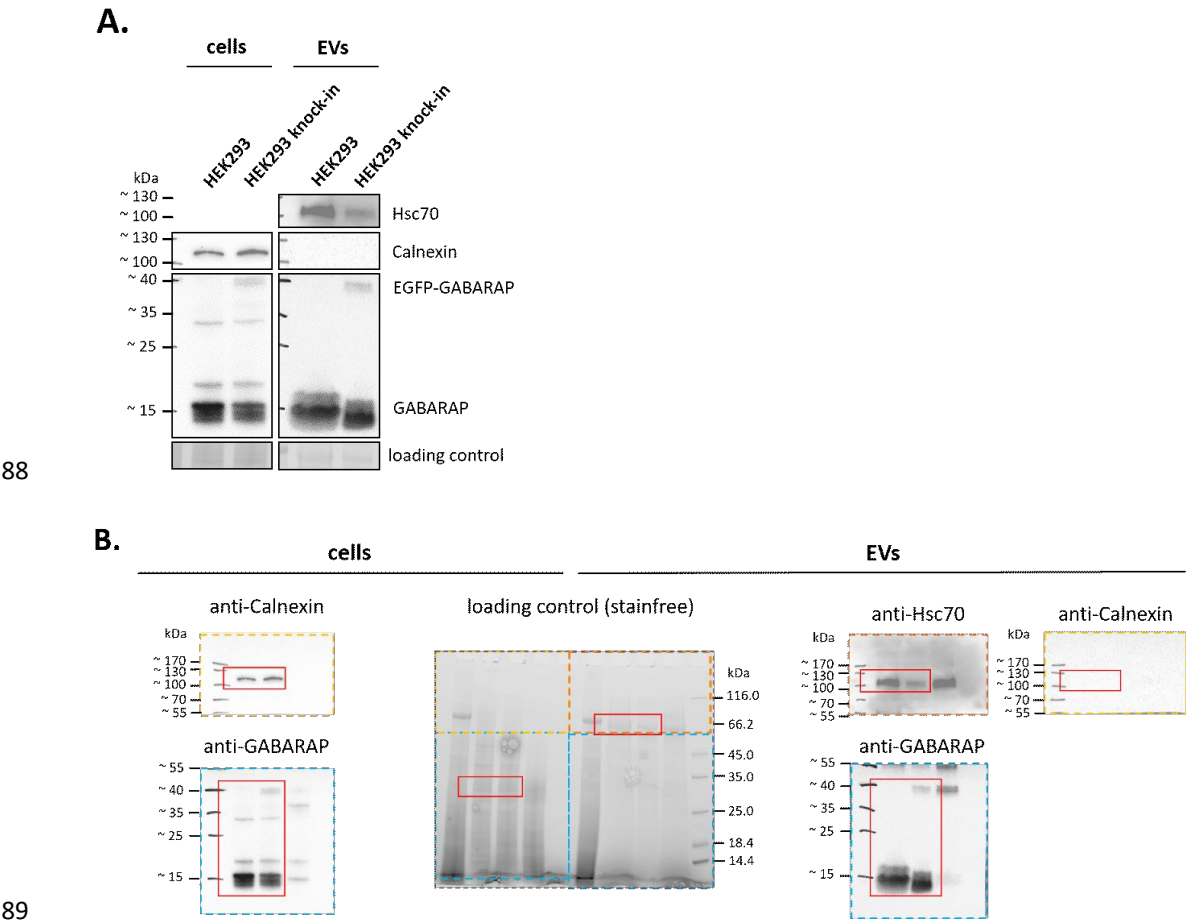
89

90 **Supplementary Figure S5.** EGFP-GABARAP, expressed on endogenous level [46], is secreted in EVs. (A) Wild-
91 type HEK293 cells and knock-in HEK293 cells expressing EGFP-GABARAP on endogenous levels and their
92 supernatants were harvested after an incubation period of 72 h. EVs were prepared by ultracentrifugation. In
93 cellular and EV samples, both wild-type GABARAP and knocked-in EGFP-GABARAP were detected. A
94 representative crop of a stain-free gel is shown as loading control. One representative blot out of two, each
95 performed with lysates from different passage numbers, is shown. (B) Uncropped versions of the blots and the
96 corresponding stain-free gel given in (A). Dashed coloured boxes in the stain-free gel correspond to the respective
97 areas into which the blot was cut for incubation with different antibodies.
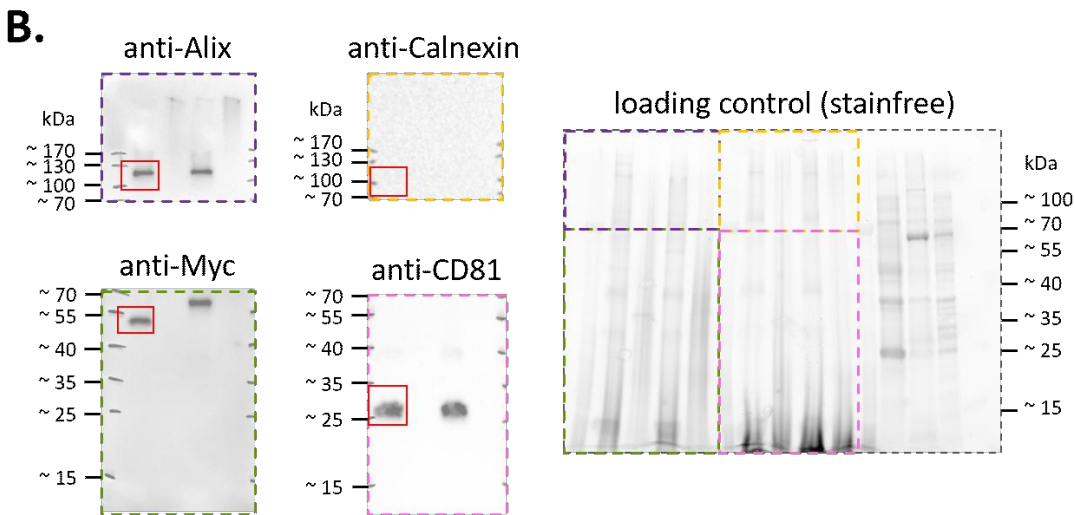
Supplementary Figure S6

A.

anti-Calnexin

loading control (stainfree)

anti-Myc

Streptavidin-HRP (short exposure)

Streptavidin-HRP (long exposure)

99

B.

anti-Alix

anti-Calnexin
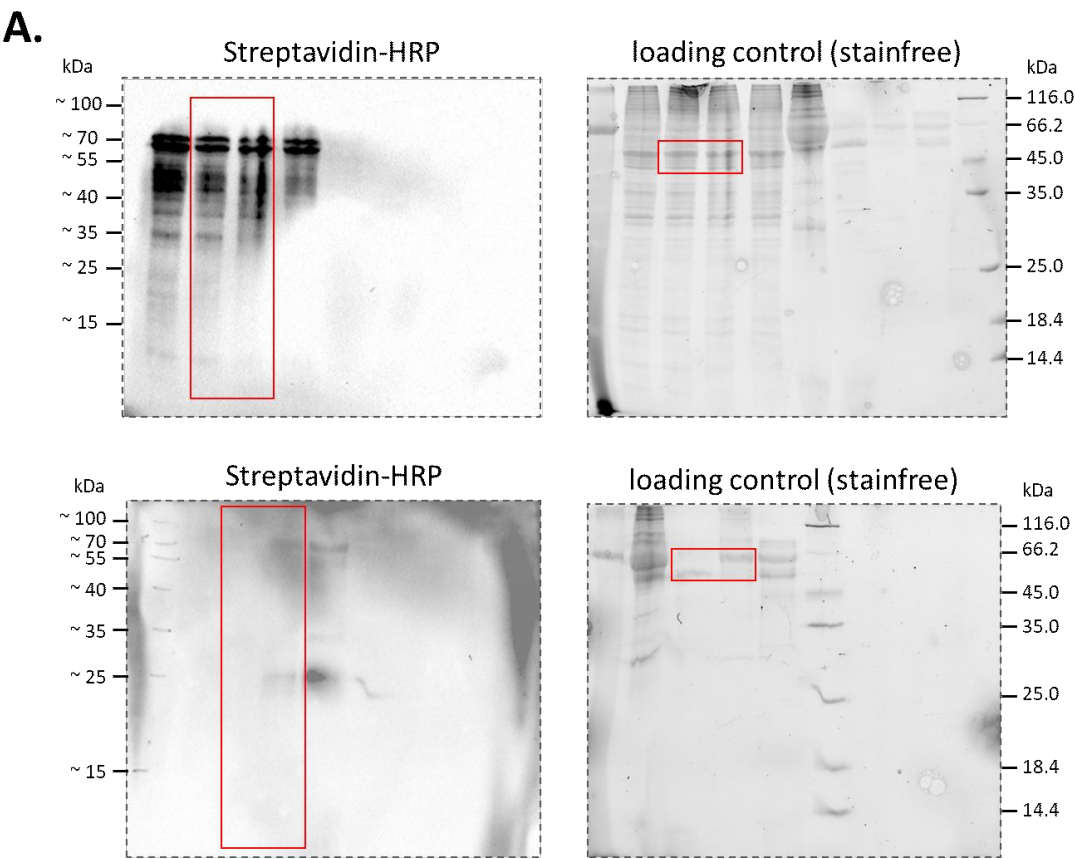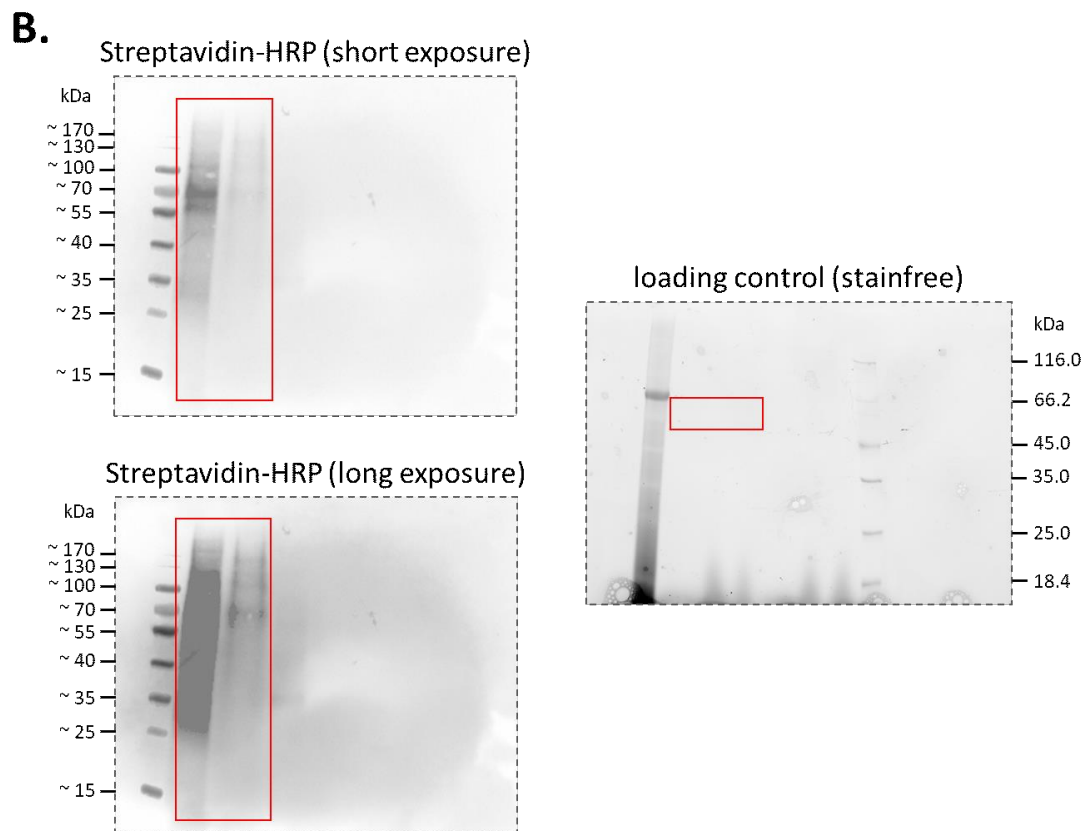
loading control (stainfree)

anti-Myc

anti-CD81

100

101 **Supplementary Figure S6.** Full images of blots shown in Figure 2B and 2D. The cropped region is indicated by red
102 box. Cellular distribution of APEX2 and APEX2-GABARAP. (A) Uncropped versions of the blots and the stain-free
103 gel related to Figure 2B. Different biotinylation patterns are obtained when expressing APEX2-GABARAP

compared to APEX2. HEK293 cells were transfected with APEX2 and APEX2-GABARAP encoding plasmids, resp. For the negative control (neg ctrl), no DNA was added. After an incubation period of 48 h, cells were labelled, harvested, and lysed as described by Hung et al. [38]. Cellular lysates were subsequently analysed by immunoblotting using a Streptavidin-HRP conjugate. One representative blot of four different cellular passages is shown. (B) Uncropped versions of the blots and the stain-free gel related to Figure 2D. EVs were prepared from cell culture supernatant using polymer-based precipitation after 48 h cultivation and applied to immunoblotting. Both the absence of Calnexin (dashed yellow box) as cellular marker protein and the presence of common EV marker proteins (Alix (dashed purple box), CD81 (dashed magenta box)) and of APEX2-GABARAP itself (detected by anti-Myc antibody, dashed light green box) were confirmed. One representative blot of three different cellular passages is shown. Dashed coloured boxes in the stain-free image correspond to the respective areas into which the blot was cut for incubation with different antibodies.

Supplementary Figure S7

A.

B.

Streptavidin-HRP (short exposure)

Streptavidin-HRP (long exposure)

loading control (stainfree)

117

118 **Supplementary Figure S7.** Full images of blots shown in Figure 3B-3C. The cropped region is indicated by red box.
119 APEX2-mediated proximity labelling in EVs. (A) Uncropped versions of the blots and the corresponding stain-free
120 gels related to Figure 3B. Pelleted EVs, but not EVs in solution may be labelled by APEX2-GABARAP. The labelled
121 EVs were lysed and used for immunoblotting, proving approach "b" suitable for APEX2-mediated labelling in EVs.
122 One representative blot of three different cellular passages is shown. (B) Uncropped versions of the blots and the
123 corresponding stain-free gel related to Figure 3C. Biotinylated APEX2-GABARAP EV proteins, obtained using
124 branch b, are enriched by Streptavidin. EV lysates were incubated with Streptavidin-coated beads. After collecting
125 the flow-through (FT), multiple washing steps were applied, and the eluate (E) was collected. A broad signal was
126 obtained for the eluate, while for the flow-through only faint signals were obtained, demonstrating effective
127 capturing of biotinylated EV proteins. One representative blot of two different cellular passages is shown.

128   **Supplementary Figure S8**

129
130   **Supplementary Figure S8.** Venn diagram of autophagosomal and cellular proteins. Comparison of the
131   autophagosomal GABARAP proxitome as determined by Le Guerroué et al. [8] with the intersection between the
132   unlabelled cellular ctrl proteome and the cellular GABARAP proxitome as defined in Figure 4A, consisting of 212
133   proteins (61.1 % of the cellular GABARAP proxitome) probably representing true-positive hits. Venn diagrams
134   were created using FunRich [47, 48].

135

136 **Supplementary Figure S9**

137

A.

B.

138
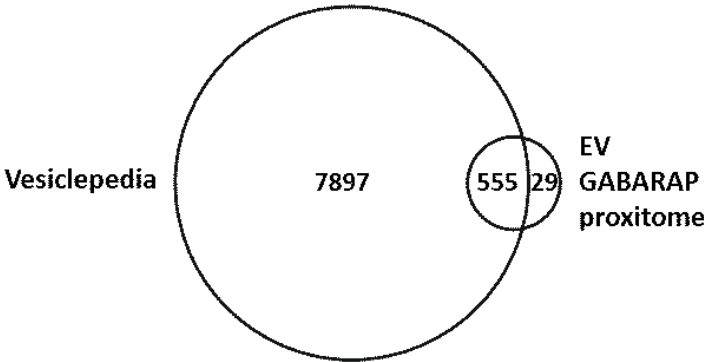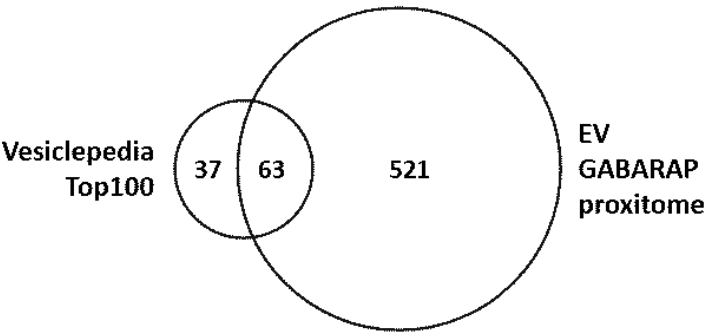
139   **Supplementary Figure S9.** Comparison of the EV GABARAP proxitome with Vesiclepedia entries [28, 29]. Of the
140   EV GABARAP proxitome, more than 95 % are registered in Vesiclepedia (A) and 63 proteins were found in the
141   Vesiclepedia top 100 (B). Either the complete database (A) or the Top100 entries (B) were used as assessed on Nov
142   12th, 2019. Venn diagrams were created using FunRich [47, 48].

143   **Supplementary Figure S10**

EV GABARAP proxitome (CC)
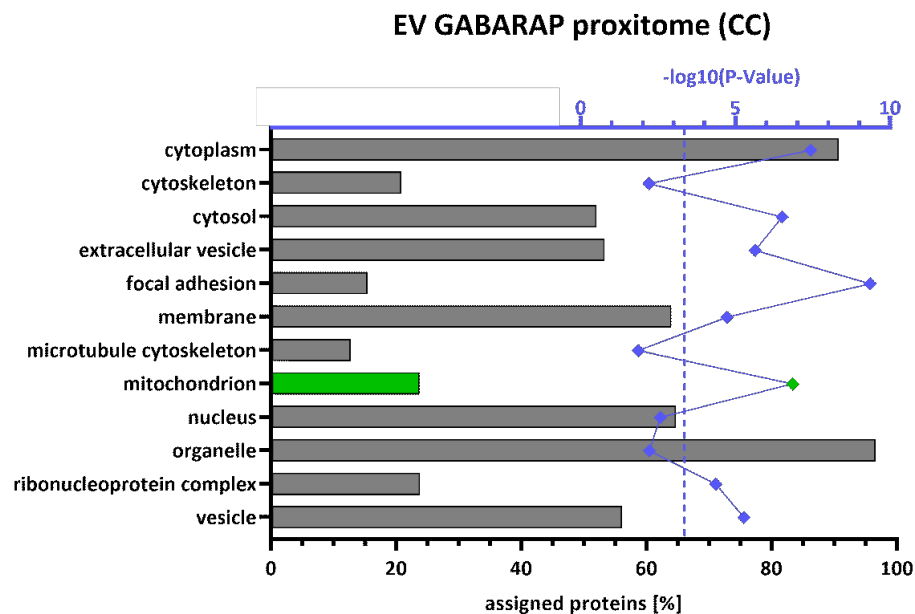
144

145   **Supplementary Figure S10.** Categorisation of the EV GABARAP proxitome using proteins of Table S1A as
146   background. The obtained proteins for the EV GABARAP proxitome were analysed by GO cellular component
147   (CC) using DAVID Bioinformatics Resources 6.8 [41]. Supplementary Table S1A, containing the complete list of
148   proteins detected in this study, was set as background. The ratio of assigned proteins to the total protein number is
149   depicted in [%]. In blue, the negative log10 of the P-Value is shown. Significantly overrepresented cellular
150   compartments are defined by a P-Value of ≤ 0.05 % (dashed line). The mitochondrion-related bar [%] and -log10(P-
151   Value) data point are highlighted in green.

152   **Supplementary Figure S11**
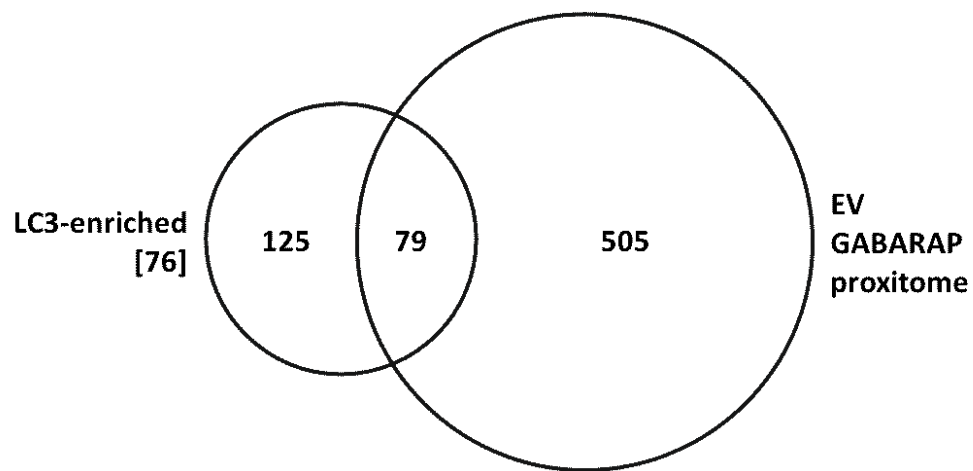
153

154   **Supplementary Figure S11.** Comparison with BirA*-LC3 enriched proteins. Venn diagram of the EV GABARAP
155   proxitome with proteins significantly enriched with extravesicular BirA*-LC3 as defined by Leidal *et al.* [76]. Of the
156   BirA*-LC3-enriched proteins, 38.7 % were also identified in the EV GABARAP proxitome. Venn diagrams were
157   created using FunRich [47, 48].

Supplementary Information

The GABARAP co-secretome identified by APEX2-GABARAP proximity labelling of extracellular vesicles

Julia L. Sanwald [1,2], Gereon Poschmann [3], Kai Stühler [3,4], Christian Behrends [5], Silke Hoffmann [2], Dieter Willbold [1,2]

[1] Institut für Physikalische Biologie, Heinrich-Heine-Universität Düsseldorf, Universitätsstraße 1, 40225 Düsseldorf, Germany

[2] Institute of Biological Information Processing (IBI-7: Structural Biochemistry), Forschungszentrum Jülich, Leo-Brandt-Straße, 52428 Jülich, Germany

[3] Institute of Molecular Medicine I, Heinrich-Heine-Universität Düsseldorf, Universitätsstraße 1, 40225 Düsseldorf, Germany

[4] Molecular Proteomics Laboratory, Biologisch-Medizinisches Forschungszentrum (BMFZ), Heinrich-Heine-Universität Düsseldorf, Universitätsstraße 1, 40225 Düsseldorf, Germany

[5] Munich Cluster for Systems Neurology (SyNergy), Ludwig-Maximilians-Universität München, Feodor-Lynen-Straße 17, 81377 München, Germany

Supplementary Table S1 is related to Figure 4 and Figure 5
Supplementary Table S2 is related to Figure 4B, 4D, and 4E, and Figure 5A, 5B, 5E, 5F, and 5G
Supplementary Table S3 is related to Figure 4D

Supplementary Tables can be found on the enclosed compact disk or on the following website: https://www.mdpi.com/2073-4409/9/6/1468**.**

Supplementary Table S1. Mass spectrometric data. (A) List of proteins detected in the cellular ctrl proteome, cellular proxitome, EV ctrl proteome, and EV proxitome. (B) List of proteins found in the cellular ctrl proteome. (C) List of proteins found in the cellular proxitome. (D) List of proteins found in the EV ctrl proteome. (E) List of proteins found in the EV proxitome. (F) List of proteins found in the intersections of Figure 4A-4E.

Supplementary Table S2. Proteins enriched or exclusive for the EV GABARAP proxitome. List and characterisation of proteins either enriched > 2fold or exclusively detected in the EV GABARAP proxitome compared to the EV ctrl proteome and the 293T exosome proteome [52] (intensity threshold > 24).

Supplementary Table S3. Proteins containing an xLIR motif. Output of the xLIR motif search in proteins found in the intersection EV GABARAP proxitome ∩ autophagosome GABARAP proxitome (376 proteins). In 164 proteins, 271 hits were detected. For the query, the xLIR motif [ADEFGLPRSK]-[DEGMSTV]-[WFY]-[DEILQTV]-[ADEFHIKLMPSTV]-[ILV] was used. The online tool ScanProsite was applied to enable a search in protein lists.

3.2 Lack of GABARAP-Type Proteins is Accompanied by Altered Golgi Morphology and Surfaceome Composition.

Authors

J. L. Sanwald*, J. Dobner*, I. M. Simons, G. Poschmann, K. Stühler, A. Üffing, S. Hoffmann, and D. Willbold.
*contributed equally

Journal

DOI

Impact Factor

Contribution to the manuscript

Cell culture, immunofluorescence experiments, microscopy, individual analysis and characterisation of the cells

Performance of ceramide chase experiments, subsequent live-cell fluorescence microscopy, data curation

Data analysis and figure creation (except MS)

Writing and editing of the manuscript

Reprint Permission

Communication

Lack of GABARAP-Type Proteins is Accompanied by Altered Golgi Morphology and Surfaceome Composition

Julia L. Sanwald [1,2,†] , Jochen Dobner [1,†] , Indra M. Simons [1,2] , Gereon Poschmann [3], Kai Stühler [3,4], Alina Üffing [1,2], Silke Hoffmann [2,*] and Dieter Willbold [1,2,*]

1 Institut für Physikalische Biologie, Heinrich-Heine-Universität Düsseldorf, Universitätsstraße 1, 40225 Düsseldorf, Germany; julia.sanwald@uni-duesseldorf.de (J.L.S.); j.dobner@fz-juelich.de (J.D.); indra.simons@uni-duesseldorf.de (I.M.S.); a.ueffing@fz-juelich.de (A.Ü.)
2 Institute of Biological Information Processing (IBI-7: Structural Biochemistry), Forschungszentrum Jülich, Leo-Brandt-Straße, 52428 Jülich, Germany
3 Institute of Molecular Medicine I, Proteome Research, Heinrich-Heine-Universität Düsseldorf, Universitätsstraße 1, 40225 Düsseldorf, Germany; gereon.poschmann@uni-duesseldorf.de (G.P.); kai.stuehler@uni-duesseldorf.de (K.S.)
4 Molecular Proteomics Laboratory, Biologisch-Medizinisches Forschungszentrum (BMFZ), Heinrich-Heine-Universität Düsseldorf, Universitätsstraße 1, 40225 Düsseldorf, Germany
* Correspondence: si.hoffmann@fz-juelich.de (S.H.); d.willbold@fz-juelich.de (D.W.); Tel.: +49-2461-619389 (S.H.); +49-2461-612100 (D.W.)
† Authors contributed equally to this work.

Abstract: GABARAP (γ-aminobutyric acid type A receptor-associated protein) and its paralogues GABARAPL1 and GABARAPL2 comprise a subfamily of autophagy-related Atg8 proteins. They are studied extensively regarding their roles during autophagy. Originally, however, especially GABARA-PL2 was discovered to be involved in intra-Golgi transport and homotypic fusion of post-mitotic Golgi fragments. Recently, a broader function of mammalian Atg8s on membrane trafficking through interaction with various soluble *N*-ethylmaleimide-sensitive factor-attachment protein receptors (SNAREs) was suggested. By immunostaining and microscopic analysis of the Golgi network, we demonstrate the importance of the presence of individual GABARAP-type proteins on Golgi morphology. Furthermore, triple knockout (TKO) cells lacking the whole GABARAP subfamily showed impaired Golgi-dependent vesicular trafficking as assessed by imaging of fluorescently labelled ceramide. With the Golgi apparatus being central within the secretory pathway, we sought to investigate the role of the GABARAP-type proteins for cell surface protein trafficking. By analysing the surfaceome composition of TKOs, we identified a subset of cell surface proteins with altered plasma membrane localisation. Taken together, we provide novel insights into an underrated aspect of autophagy-independent functions of the GABARAP subfamily and recommend considering the potential impact of GABARAP subfamily proteins on a plethora of processes during experimental analysis of GABARAP-deficient cells not only in the autophagic context.

Keywords: Atg8; GABARAP; Golgi apparatus; surfaceome

1. Introduction

The autophagy-related 8 (Atg8) proteins, consisting of members of the microtubule-associated proteins 1A/1B light chain 3 (MAP1LC3, hereafter LC3) subfamily and the γ-aminobutyric acid type A (GABA$_A$) receptor-associated protein (GABARAP) subfamily, are mainly recognised for their functions during autophagy.

In that context, the GABARAP-type proteins were shown to be involved in the later steps, involving autophagosome closure [1] and autophagosome-lysosome fusion [2], thereby enabling the autophagic degradation and recycling of cellular components. Interdependence of autophagy, endocytosis, and secretion pathways has been reported by a growing number of studies (reviewed in [3]). Notably, the three members of the

GABARAP family, GABARAP, GABARAP-like 1 (GABARAPL1), and GABARAP-like 2 (GABARAPL2), were initially discovered in the context of transport and trafficking processes. Early studies described an association of GABARAP with the eponymous GABA$_A$ receptor [4], and subsequently with other receptors including, e.g., the transferrin receptor (TFRC) [5]. Participation of GABARAP in vesicular transport along microtubules has also been reported [6,7]. Similarly, GABARAPL1 was also found to associate with tubulin [8] and to facilitate, e.g., κ opioid receptor trafficking [9]. The third member of the GABARAP family, GABARAPL2, was identified as an intra-Golgi transport modulator interacting both with the *N*-ethylmaleimide-sensitive factor (NSF) and the Golgi v-SNARE GOS-28 [10,11], and was reported to be required during post-mitotic Golgi reassembly [12]. In both processes, GABARAPL2 is deemed to act as a Golgi-SNARE protector [13]. Consistent with this idea, recent reports show direct interactions of all LC3 and GABARAP proteins with other types of SNARE proteins [14,15].

Furthermore, GABARAP was shown to interact with NSF [16] and 130 kDa *cis*-Golgi matrix protein (GM130), which tethers a certain pool of GABARAP proteins to the Golgi [17]. Other examples for Golgi-associated proteins interacting with GABARAP include PX-RICS, a splicing variant of Rho GTPase-activating protein (RICS) containing a phosphoinositide-binding (PX) domain that by interaction with GABARAP mediates ER-to-Golgi transport [18], and optineurin, that interacts with various human Atg8 paralogues and is involved in various cellular processes, including Golgi maintenance [19,20]

In non-mitotic mammalian cells, the Golgi apparatus consists of interconnected stacks of cisternae [21,22]. During conventional protein transport and secretion, the Golgi serves as a central trafficking organelle. After translation in the endoplasmic reticulum (ER), respective proteins are loaded into coatomer protein complex-II (COPII)-coated vesicles, transported to an ER-Golgi intermediate compartment (ERGIC), and translocated in an anterograde manner by passing the *cis*-, the *medial*-, and the *trans*-Golgi. Once a protein has reached the *trans*-Golgi network (TGN), it is sorted by coat proteins for its destination, for example the plasma membrane (PM) [23]. However, not only the transport of proteins, but also that of lipids is a central Golgi function. One of these lipids is ceramide, which is transported from the ER to the Golgi by ceramide transfer protein (CERT) [24]. Once it has reached the Golgi, ceramide is metabolised by sphingomyelin synthases. Ceramide metabolites are further transported to the PM or other membranes [25].

In this work, we employed various knockout (KO) cell lines to study the role and importance of the GABARAP subfamily in maintaining Golgi morphology and on lipid transport in a ceramide chase experiment. Finally, we comparatively analysed the surfaceomes of wild-type (WT) cells and of cells deficient for the GABARAP subfamily. Taken together, we demonstrate that the GABARAP subfamily, additionally to its well-described roles during autophagy, is involved in Golgi apparatus morphology maintenance, secretory vesicular trafficking of lipids and cell surface proteins. We thus suggest considering these autophagy-independent effects when analysing GABARAP-type protein function.

2. Results

2.1. GABARAP- and/or GABARAPL2-Deficient Cells Display Altered Golgi Morphology

To investigate the impact of individual GABARAP family members on Golgi morphology, we used a panel of human embryonic kidney 293 (HEK293) KO cell lines which exhibit a single KO (SKO), a double KO (DKO) combination, or a triple KO (TKO) of the respective GABARAP-type protein gene locus [26,27]. Golgi morphology was studied via visualisation of both the TGN by anti-TGN46 staining (Figure 1A) and the complete Golgi by BODIPY-FL C5-ceramide staining (Supplementary Figure S1). For both markers, consistent patterns for each of the analysed cell lines were observed, cross validating the observed results. Next, because of its more distinct staining profile, we categorised the signal obtained for TGN46 as compact (I), partly compact (II), and dispersed (III) Golgi pattern (Figure 1B), technically always considering all individual planes of each recorded z-stack during analysis. As summarised in Figure 1C, the vast majority of the stains

from WT cells, expressing all three GABARAP-type proteins, were classified as category I or II. Hence, WT cells had a compact or partly compact Golgi morphology in most of the cases (46% and 39%, respectively), while category III patterns indicating extensive Golgi fragmentation were rare. Cells with a GABARAPL1[SKO] displayed only mild alterations with a slight tendency towards lower Golgi compactness, but overall showed the most WT-like phenotype of all genotypes analysed. In contrast, both GABARAPSKO and GABARAPL2[SKO] cells showed category I patterns in less than 20% of the cases, and more than 60% the fraction of category II was considerably increased compared to WT. However, the percentage of category III was similar between all the three SKO lines and thus also resembled the WT situation. While SKO-like results were obtained for GABARAPL1/L2[DKO] cells, GABARAP/L1[DKO] cells showed a further reduction of category I (to 8%), accompanied with an increase of category II (to 71%). Strikingly, 36% of the GABARAP/L2[DKO] cells exhibited even more category III Golgi structures than GABARAP/L1/L2[TKO] cells (33%) and thus displayed the highest degree of disorganisation among all genotypes (Figure 1C). Overall, there was a significant association between the genotype analysed and Golgi compactness as calculated by Pearson's chi-squared test (χ^2 (14) = 414.62, $p < 0.001$). Based on the obtained standardised residuals (Figure 1D), which represent the standard deviation of the actual from the expected count, lack of GABARAP or GABARAPL2 alone or in combination with a lack of GABARAPL1 was associated with a shift from a compact to a more dispersed Golgi morphology. Strikingly, GABARAP/L1[DKO] cells specifically showed an enrichment of partly compact Golgi morphology, whereas GABARAP/L2[DKO] and GABARAP/L1/L2[TKO] cells showed an enrichment of dispersed Golgi morphology. The representative 3D visualisations of the recorded confocal stacks after TGN46-staining can be found in Supplementary Figure S2. Consistently, also staining of the *cis*-Golgi marker protein GM130 (Figure S3A), followed by the categorization as applied for TGN46 staining (Figure 1), revealed a shift from compact to partly compact and completely dispersed Golgi morphology in GABARAP/L2[DKO] and GABARAP/L1/L2[TKO] cells compared to WT (Figure S3B,C). The same was true for another marker of *cis*-Golgi, Golgi reassembly-stacking protein of 65 kDa (GRASP65), which was analysed accordingly (Figure S3D–F). Taken together, these results indicate that besides GABARAPL2, at least also GABARAP seems to be involved in Golgi maintenance.

2.2. GABARAP-Type Protein Deficiency is Accompanied by Impaired Ceramide Trafficking

As the Golgi plays a fundamental role in conventional protein secretion and PM-directed transport [28], and because of the described transport-related functions of GABARAP and its two paralogues [4,9,10], we hypothesised that a lack of all GABARAP subfamily members at once should considerably impact membrane trafficking from the Golgi to the PM. It is well known that ceramide, after being transported by CERT from the ER to the Golgi apparatus, is converted to sphingomyelin, glucosylceramide, and more complex glycosphingolipids before it reaches the PM, and can therefore be used to study lipid metabolism and vesicle-mediated lipid transport from the Golgi to the PM [29]. Fluorescently labelled probes such as 6-((N-(7-Nitrobenz-2-Oxa-1,3-Diazol-4-yl)amino)hexanoyl)S-phingosine (NBD C_6-ceramide) or BODIPY-FL C_5-ceramide are selective stains for the Golgi in living and fixed cells [30] and therefore are applicable to study both Golgi morphology and Golgi-related lipid transport.
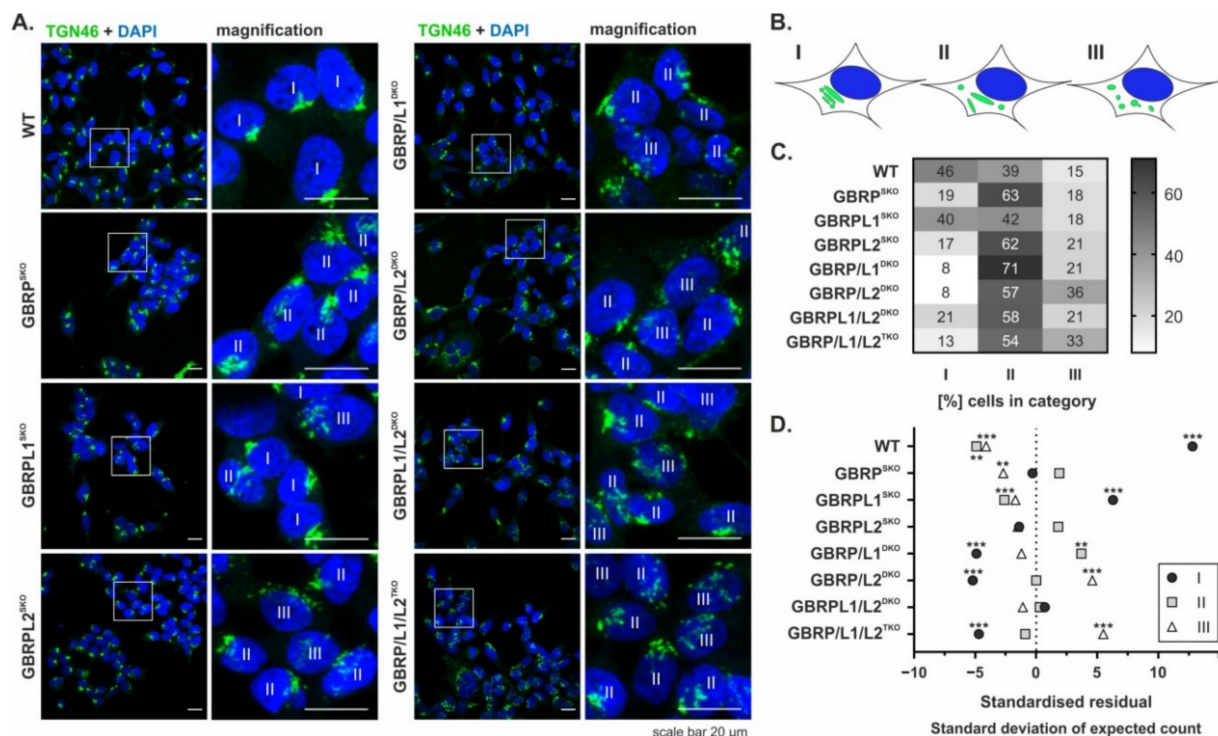
Figure 1. Influence of γ-aminobutyric acid type A (GABA$_A$) receptor-associated protein (GABARAP)-type protein deficiency on *trans*-Golgi morphology. (**A**) Wild type (WT) cells or cells deficient for one (SKO), two (DKO), or all three (TKO) GABARAP-type proteins (GBRPs) were fixed (4% PFA), immunolabelled with anti-human TGN46 antibody, and visualised by confocal fluorescence microscopy. Nuclei were counterstained with DAPI. Scale bar, 20 μm. (**B**) Scheme representing the categorisation of a compact (I), partly compact (II), and dispersed (III) Golgi structure. (**C**) Heatmap of percentage of cells per cell type assigned to Golgi category I, II, and III. Per cell type, in total ≥188 cells from ≥5 individual experiments were analysed. Cells were categorised by visual judgement. (**D**) Standardised residual values. Asterisks indicate significant differences from the mean based on the standardised residual distribution with: |z| ≥ 2.58 ** (*p* ≤ 0.01), |z| ≥ 3.29 *** (*p* ≤ 0.001).

Thus, as schematically depicted in Figure 2A, we followed the subcellular distribution of NBD C$_6$-ceramide over time in WT and GABARAP/L1/L2^{TKO} cells in the presence or absence of inhibitors of Golgi-related vesicular trafficking by live-cell fluorescence microscopy. The respective results are summarised in Figure 2B. While after 30 min a rather diffuse labelling of intracellular membranes was observed, after 90 min we noted an increase in staining intensity in the perinuclear region of WT cells, likely representing the Golgi apparatus. In GABARAP/L1/L2^{TKO} cells, on the other hand, the staining appeared in more punctate or vesicular structures compared to WT cells, a pattern which became even clearer after 24 h. Although WT cells also showed vesicular staining, they additionally exhibited staining at the PM which was only very faint in GABARAP/L1/L2^{TKO} cells. After 48 h, overall staining became less intense. At this timepoint, WT cells exhibited faint PM staining and diffuse intracellular labelling, while in GABARAP/L1/L2^{TKO} cells, still intensely labelled vesicular structures were found. When incubating the cells for 90 min with 10 μM Brefeldin A (BFA), ceramide additionally labelled perinuclear rims probably representing ER staining due to ER-to-Golgi fusion by BFA [31]. Interestingly, the overall staining pattern appeared similar between WT and GABARAP/L1/L2^{TKO} cells in the presence of BFA. Since BFA only inhibits vesicular transport without affecting ER-to-Golgi lipid transport by CERT [31], this indirectly suggests that GABARAP subfamily proteins do not have an impact on non-vesicular ER-to-Golgi transport of ceramide.
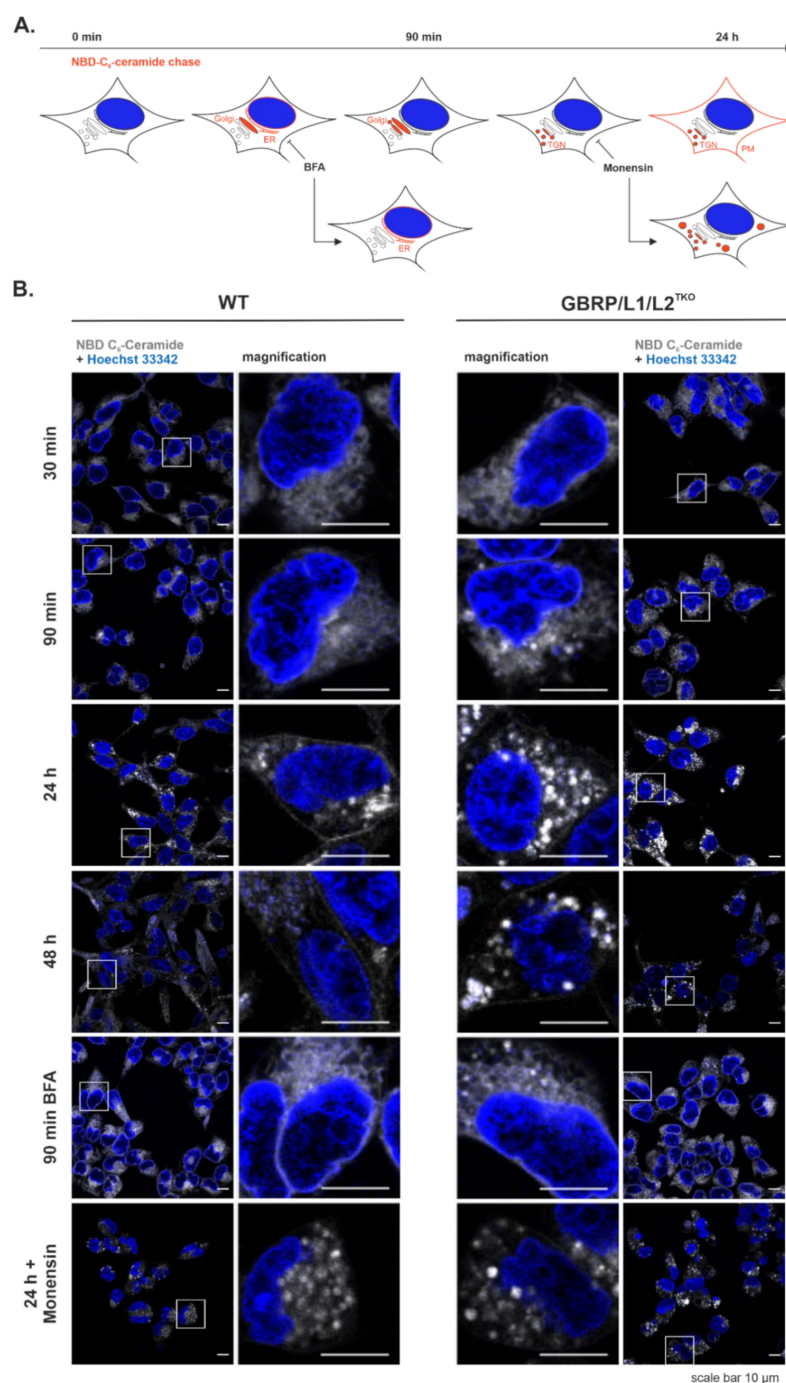
Figure 2. Intracellular ceramide distribution in WT and GABARAP/L1/L2^{TKO} cells. (**A**) Scheme representing the putative intracellular trafficking of NBD C$_6$-ceramide (shown here in red) in WT cells, including sites of action of BFA and Monensin. (**B**) Live cell confocal fluorescence microscopy of WT and GABARAP/L1/L2^{TKO} cells labelled with NBD C$_6$-ceramide (shown here in grey scale). After labelling for 1 h at 4 °C, the cells were further incubated at 37 °C for 30 min, 90 min, 24 h, or 48 h in full medium, or 90 min in full medium containing 10 µM Brefeldin A (BFA), or 24 h in full medium containing 10 µM Monensin. Nuclei were counterstained with Hoechst 33342. For each condition, one representative image from 5 individual experiments is shown. Scale bar, 10 µm.

Finally, incubation for 24 h with 10 μM Monensin, an ionophore known to cause disruption of the *trans*-Golgi apparatus [32], led to a similar phenotype in WT and GABARAP/L1/L2^{TKO} cells, resembling the ceramide distribution in GABARAP/L1/L2^{TKO} cells after 24 h without Monensin. Although, in principle, Monensin treatment can affect cell viability by causing oxidative stress [33], after 24 h of staining, cell nuclei were still intact, indicating that the cells were still viable. Taken together, these results hint towards a role of the GABARAP subfamily at least in *trans*-Golgi-to-PM trafficking of ceramide and its metabolites.

2.3. GABARAP-Type Protein Deficiency is Associated with Altered Surfaceome Composition

To investigate whether compromised Golgi integrity and impaired anterograde ceramide transport in the absence of the GABARAP subfamily is accompanied by altered cell surface protein expression, we finally analysed the surfaceome of GABARAP/L1/L2^{TKO} cells in comparison to WT cells.

To compare their cell surface proteomes, cultures of WT and GABARAP/L1/L2^{TKO} cells were exposed to surface biotinylation, lysed, subjected to streptavidin pull-down, and the protein pools obtained were processed by quantitative proteomics. Data were post-processed (for details refer to material and methods section) and normalised protein levels were analysed. As shown in Figure 3A (for raw data please refer to Supplementary Table S1), a total of 2710 different proteins were identified by this approach. By concentrating on already verified surface-located proteins, 216 of the initially identified hits were found to be surface annotated with high confidence (verified or putative) according to the cell surface protein atlas (CSPA, [34]). Notably, with 58 proteins, more than 25% of them displayed significantly different abundances and were therefore examined in more detail. Remarkably, 36 proteins displayed a significantly higher and 22 proteins displayed a significantly reduced surface abundance in GABARAP/L1/L2^{TKO} compared to WT cells. Figure 3B shows hierarchical clustering of these proteins, thereby demonstrating the high degree of conformity between individual replicates and the identity of the respective associated proteins (for more detailed information please refer to Supplementary Table S2).

Among all differentially abundant surface annotated proteins, a gene ontology (GO)/reactome pathway enrichment analysis revealed, among others, significant over-representation of proteins belonging to the category of sodium ion membrane transport ($-\log 10$ $p = 3.18$, 37.8-fold,) and cell adhesion ($-\log 10$ $p = 1.41$, 6.7-fold) as given in Figure 3C,D, respectively.

Most of the identified annotated surface proteins were single pass type I transmembrane proteins (32/58), but also single pass type II transmembrane proteins (4/58), multi pass transmembrane proteins (13/58), and GPI-anchored membrane proteins (2/58) were identified. Proteins with significantly higher abundance in GABARAP/L1/L2^{TKO} compared to WT cells included those with described or predicted transporter/channel activity or associated proteins thereof (CNNM4, CNNM2, SLC4A7, ASIC1, ABCC1, ANO6, SLC39A14, ATP1B3, ATP1A1, SLC3A2, ITPRIP) as well as receptor or receptor-associated proteins (ITGA7, ADAM15, INSR, PTPRF, TYRO3, M6PR, TFRC), cell adhesion associated proteins (PODXL2, KIRREL, NPTN, ALCAM/CD166, JAM3, CADM1), or proteins with described involvement in immunity (CD59, ALCAM/CD166, NCR3LG1, CD276, CADM1).

Proteins with known ER and/or Golgi association (GGCX, TMED7, SMPDL3B, SEL1L) were also identified within the group of higher surface abundance in GABARAP/L1/L2^{TKO} cells. Proteins with significantly lower abundance at the PM of GABARAP/L1/L2^{TKO} compared to WT cells were functionally more dispersed and included proteins associated with immunity (HLA-A, HLA-C, CD46), autophagy (CAPNS1), Ca^{2+} channel activity (CACHD1), receptor proteins (EPHA4), adhesion (MCAM/CD146, EPCAM, F11R, LGALS3BP), and proteins associated with ER and/or Golgi (RPN1, MIA3, EMC1, TMEM259, STT3A).
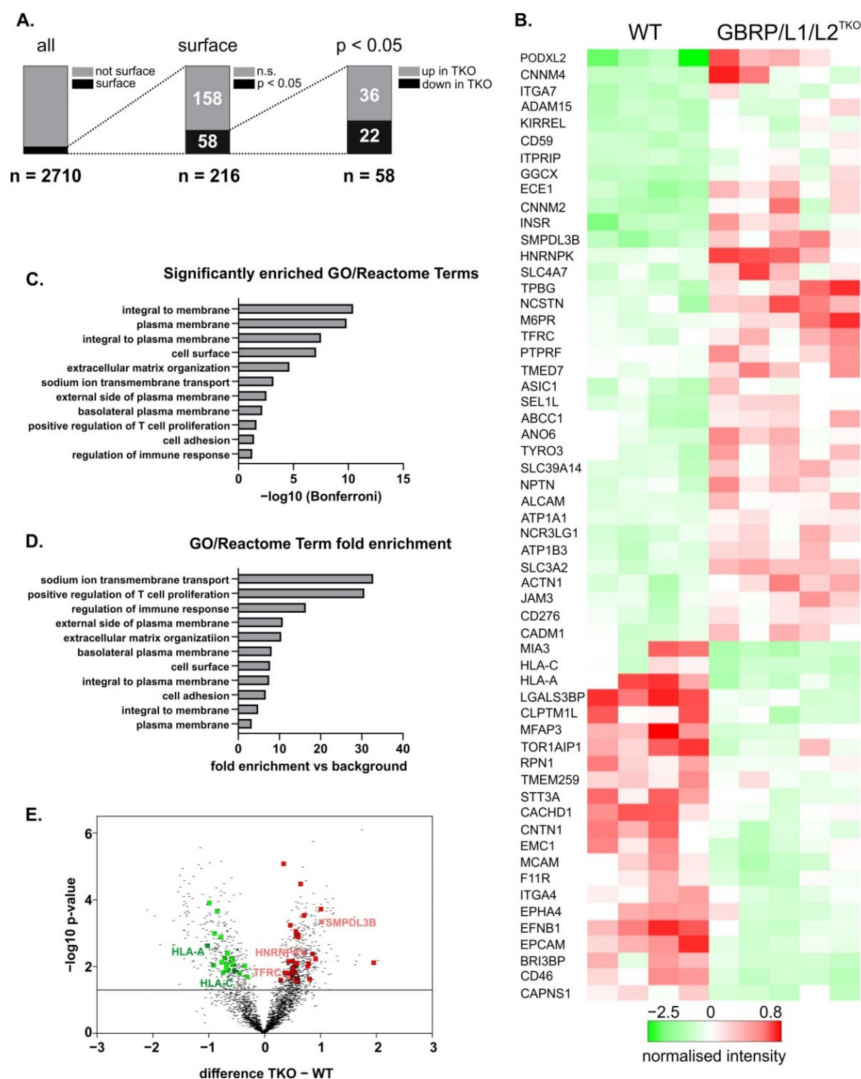
Figure 3. Comparative surfaceome composition analysis between WT and GABARAP/L1/L2^{TKO} cells. (**A**) Representation of filtering and statistical testing workflow. Mass spectrometry of isolated cell surface proteins revealed 2710 proteins of which 216 were surface annotated with high confidence (verified or putative) according to the cell surface protein atlas (CSPA) [34]. Of these 216, 58 showed significantly different abundances between WT and GABARAP/L1/L2^{TKO} cells. (**B**) Heatmap visualising the hierarchical clustering of normalised abundances for the 58 proteins described in (**A**) considering the individual replicates. (**C**,**D**) Relative enrichment of categories of identified proteins as determined by Gene Ontology (GO)/reactome pathway enrichment analysis. (**E**) Scatter plot of independent t-test results of the 2710 proteins. Proteins with significantly higher abundance in GABARAP/L1/L2^{TKO} cells compared to WT cells are marked in red and proteins with significantly lower abundance are marked in green. Proteins further addressed are highlighted. In general, proteins are denoted by their gene names.

Finally, Figure 3E displays a scatter plot of the 2710 protein hits detected in this study. Among those proteins with significantly increased abundance in cells lacking the GABARAP-type proteins (red dots), we identified with TFRC one of the earliest described GABARAP interactors [5]. Although the functional relevance of this association has not been clarified to date, it is tempting to speculate that its surface trafficking and/or correct glycosylation are dependent on any or all GABARAP-type proteins. Importantly, abundance of the major histocompatibility I (MHC-I) subtypes HLA-A and HLA-C was found to be reduced in GABARAP/L1/L2^{TKO} cells. This is intriguing, because macroautophagy

has been implicated in MHC-I antigen presentation to the cell surface [35]. As a proof of concept, we monitored TFRC and HLA-A surface levels by IB of biotinylated and pulled surface-enriched proteins and fluorescence-activated cell sorting (FACS), respectively. Surface levels of TFRC were significantly increased (Figure S4A), while surface HLA-A levels were significantly decreased (Figure S4B) in GABARAP/L1/L2^{TKO} compared to WT cells, which is in agreement with the MS data (Table S2 and related Figure 3B,E).

A further interesting hit is the acid sphingomyelinase-like phosphodiesterase 3b (SMPDL3B) which was described to regulate the levels of ceramide metabolites ceramide-1-phosphate (C1P) and sphingosine-1-phosphate (S1P) [36]. SMPDL3B is a lipid raft associated enzyme and thus involved in regulation of membrane fluidity [37]. Notably, another member of the family of sphingomyelinases, the neutral sphingomyelinase 2 (nS-Mase2), has been linked to LC3, which directly interacts with the nSMase2 regulator FAN (factor associated with nSMase2 activation) to specify cargo loading, e.g., of heterogeneous nuclear ribonucleoprotein K (HNRNPK), into extracellular vesicles (EVs) [38]. Very recently, we detected HNRNPK also in GABARAP-containing EVs [39]. Intriguingly, here we identified increased abundances of both SMPDL3B and HNRNPK in the absence of GABARAP-type proteins. Whether HNRNPK secretion is directly influenced by the GABARAP subfamily will thus be very interesting to determine in the future.

3. Discussion

In this work, we demonstrate that the lack of GABARAP, GABARAPL1, and GABARAPL2, both individually and combined (DKO, TKO), alter Golgi morphology, and that a lack of the whole GABARAP subfamily influences important vesicle-mediated intracellular trafficking events like ceramide distribution and surface protein expression. Our results thus extend the current knowledge regarding GABARAP-type protein functions in Golgi-related processes, which was limited to GABARAPL2 so far [13], to the two closely related paralogues GABARAP and GABARAPL1, which have not been investigated in this context yet.

First, we show that in addition to the expected effect of GABARAPL2 deficiency on Golgi morphology, also a lack of GABARAP significantly impacts the Golgi, shifting it from a compact to a more dispersed phenotype. Based on transcriptional data of HEK293 cells [40], it can be assumed that both proteins are expressed at comparable levels, thus suggesting that GABARAP and GABARAPL2 act in parallel to maintain the Golgi structure. This notion is further supported by the fact that double deficiency for GABARAP and GABARAPL2 drastically increased the Golgi disorganisation observed in this study, which would not be explainable if either protein was the only key player in this regard. The minor effect seen for GABARAPL1-deficient cells in this context might be based on the lower abundance of this paralogue in HEK293 cells, which can also be assumed from available gene expression data [40].

Golgi fragmentation and its functional impairment have been reported to be not necessarily causative, as in many Golgi fragmentation phenotypes cell surface transport processes function at normal kinetics [41–43]. Furthermore, it has been shown that Golgi fragmentation induced by gold nanoparticles, although not compromising the viability of individual cells, negatively affects cellular adhesion [44]. However, recently, DKO of GRASP55 and GRASP65 was reported to result in Golgi fragmentation accompanied by functional impairment [45]. Increased Golgi fragmentation has also been reported in the context of, e.g., cancer and neurodegenerative diseases such as Parkinson's disease or amyotrophic lateral sclerosis (ALS) as reviewed in [46]. Notably, also a KO of the GABARAP interactor GM130 led to a disruption of the Golgi, causing trafficking defects in mice [47]. Therefore, it is conceivable that alterations in Golgi morphology caused by a GABARAP-type protein deficiency as shown in this study might also have functional implications.

In line with this notion, by studying fluorescently labelled ceramide as a well-characterised example for Golgi-mediated vesicular trafficking, we discovered impaired PM-directed

transport of fluorescently labelled ceramide and its metabolites in cells deficient for all three GABARAP-type proteins.

BFA treatment, which is known to inhibit vesicular ER-to-Golgi trafficking by fusion of ER with Golgi, had no additional effect on TKO cells, indicating that non-vesicular transport of ceramide by CERT seems to be unaffected in the absence of the GABARAP subfamily.

Strikingly, treatment of WT cells with the ionophore Monensin, which is known to cause a disruption of the *trans*-Golgi apparatus [32], mimicked the effect of GABARAP/L1/L2^{TKO} on ceramide trafficking, indicating that GABARAP subfamily proteins play a role during vesicular transport of ceramide and its reaction products. Furthermore, in GABARAP/L1/L2^{TKO} cells we observed a dispersed fluorescence signal when staining not only the TGN marker TGN46, but also with the pan-Golgi marker BODIPY-FL C$_5$-ceramide. We thus speculate that further Golgi compartments rely on the presence of at least one GABARAP paralogue to maintain compactness. An obvious explanation for these results is provided by a Golgi-SNARE protector function already suggested for GABARAPL2 [13] which prevents uncontrolled (re-)fusion of Golgi-associated membranes, and which may be redundant for GABARAP and/or GABARAPL1.

Another explanation might be given by the reported interaction of GABARAP with the phosphatidylinositol 4-kinase IIα (PI4KIIα) [48]. PI4KIIα produces the messenger lipid phosphatidylinositol-4-phosphate (PI4P) which is, e.g., implicated in endosomal trafficking [49,50]. Locally increased PI4P levels furthermore lead to an accumulation of Golgi-derived endosomes [51]. GABARAP-type proteins might be involved in subcellular targeting of PI4P by PI4KIIα and thus influence local lipid homeostasis. Absence of GABARAP-type proteins might lead to PI4KIIα mislocalisation which could explain the accumulation of intensely NBD C$_6$-ceramide-labelled structures observed in this work.

Consistent with the hypothesis that Golgi fragmentation is linked with disturbed membrane transport, our comparative analysis of the surfaceomes of WT and GABARAP/L1/L2^{TKO} cells revealed a substantial number of proteins with significantly different surface abundance. This suggests that the trafficking of surface proteins is influenced by the GABARAP subfamily in a far more general manner than supposed to date. The fact that some of the surface-located proteins identified during our proteomics study were up-regulated, while others were downregulated, is particularly interesting and most likely reflects the plethora of cellular processes that GABARAP-type proteins participate in, mainly as providing interaction platforms for protein complexes [52–55]. It must thus be considered that GABARAP-type protein deficiency provokes a pleiotropy of potentially counteracting effects. For example, a reduction of overall degradation kinetics due to the function of the GABARAP-type proteins during lysosomal fusion events [2,56] might be counteracted by non-redundant roles of single paralogues, as, e.g., shown by the enhanced degradation of EGFR in the absence of GABARAP [26]. This adds further complexity to the picture and illustrates how several opposing effects might be evoked simultaneously. Accordingly, altered Golgi dynamics, probably in concert with inputs of further processes, likely determine the actual degree of the surface abundance of an individual protein. It is also conceivable that the diverse processes vary in their impact depending on the nature of each surface protein affected and the respective metabolic status of the cell system investigated. In parallel, deficiency of the GABARAP-type subfamily may additionally directly disturb the intracellular distribution of surface proteins, especially those containing functional interaction motifs [52]. Interestingly, recent results from a yet unpublished study show altered surfaceome composition of *Atg5*$^{-/-}$ mouse embryonic fibroblasts [57]. ATG5 is a key component of the LC3/GABARAP lipidation machinery which is essential for their integration into autophagy-related and unrelated membranes [53]. The effect of GABARAP subfamily protein lipidation on cell surface protein trafficking will be interesting to determine in future studies.

However, it has to be kept in mind that many surface proteins have been described to bypass the canonical Golgi secretion pathway [28]. Particularly, autophagy-dependent secretion [58] is likely influenced by a lack of GABARAP subfamily proteins. Deficiency of

GABARAP-type proteins might furthermore result in Golgi bypass of proteins which are usually secreted conventionally. This would lead to a subset of dysfunctional PM-associated proteins due to altered glycosylation patterns [59].

In summary, the presented work demonstrates a significant impact of GABARAP subfamily proteins on Golgi morphology, ceramide trafficking and surfaceome composition in cultured cells. The variety of proteins in terms of molecular function with altered surface abundance is broad and illustrates how many processes are potentially affected by the absence of all GABARAP-type proteins. We therefore conclude that the lack of the GABARAP subfamily is associated with impairment of a multitude of processes on a cellular and likely also organismal level. Hence, we suggest consideration of general cellular integrity which might be compromised on several levels. Attention should not be limited to autophagy, but also be given to phenotypical Golgi morphology and, if applicable, also to the extent of surface expression and functionality of selected proteins when working with GABARAP subfamily-deficient systems.

4. Materials and Methods

4.1. Antibodies

For immunofluorescence, primary TGN46 antibody (Cat. No. AHP500GT, Bio-Rad Laboratories, Hercules, CA, USA) was used at a concentration of 1:250. Goat anti-GRASP65 antibody (Cat. No. sc-19481, Santa Cruz Biotechnology, Dallas, TX, USA) and goat anti-GM130 antibody (Cat. No. sc-16268, Santa Cruz Biotechnology, Dallas, TX, USA) were used at a concentration of 1:50. Sheep-488 (Cat. No. A-11015, Thermo Fisher Scientific, Waltham, MA, USA) and Donkey Anti-Goat IgG H&L Alexa Fluor 647 (Cat. No. ab150131, abcam, Cambridge, UK) were used as a secondary antibody at a concentration of 1:200 and 1:250, respectively.

4.2. Eukaryotic Plasmids

KO plasmids are based on plasmid pSpCas9(BB)-2A-GFP (PX458) which was a gift from Feng Zhang (Addgene plasmid # 48138) [60].

4.3. Cell Culture

Human embryonic kidney 293 Flp-In T-REx (HEK293 Flp-In T-REx; Cat. No. R78007, Thermo Fisher Scientific, Waltham, MA, USA) cells were cultured at 37 °C and 5% CO_2 in Dulbecco's Modified Eagle's Medium (DMEM, Cat. No. D5796, Sigma-Aldrich, St. Louis, MO, USA) supplemented with 10% Foetal Calf Serum (FCS, Cat. No. F9665, Sigma-Aldrich, St. Louis, MO, USA). Cells were routinely checked for mycoplasma contamination.

4.4. CRISPR/Cas9 Mediated KO Generation

KO cell lines were generated and validated as described previously [26,27]. In brief, HEK293 Flp-In T-REx cells were transfected with KO plasmids based on pSpCas9(BB)-2A-GFP (PX458) [60] and single sorted for fluorescence protein (FP) positive signals via fluorescence-activated cell-sorting (FACS) in wells of 96 well plates. Clonal lines were recovered, and occurrence of genome editing was verified via amplification of a 400 bp product flanking the target site and sanger sequencing as well as on a protein level with specific antibodies.

4.5. Ceramide Chase

The ceramide chase experiment was conducted according to [29]. Briefly, HEK293 Flp-In T-REx cells (3×10^5) were seeded into fibronectin-coated 35 mm imaging dishes (Cat. No. 81158, ibidi, Gräfelfing, Germany) and cultured for 24 h in phenol red-free DMEM (Cat. No. 21063029, Thermo Fisher Scientific) supplemented with 10% FCS. Fluorescent NBD C_6-Ceramide, Cat. No. N1154, Thermo Fisher Scientific, Waltham, MA, USA) was dissolved in 95% ethanol to a stock concentration of 1 mM. Cells were labelled with 10 nmol/mL NBD C_6-Ceramide in Hanks' Balanced Salt Solution (Cat. No. 14025050, Thermo Fisher Scientific,

Waltham, MA, USA) containing 0.68 mg/mL bovine serum albumin (BSA) for 1 h at 4 °C in the dark. After labelling, the medium was aspirated, and the cells were rinsed two times with HBSS and further incubated at 37 °C and 5% CO_2 for 30 min, 90 min, 24 h, and 48 h. As inhibitors of Golgi function, Brefeldin A (Cat. No. 00-4506-51, Life Technologies, Carlsbad, CA, USA) and Monensin (Cat. No. 00-4505-51, Life Technologies, Carlsbad, CA, USA) were used at a concentration of 10 μM each. Cells were incubated with Hoechst 33342 (Cat. No. R37605, Invitrogen, Carlsbad, CA, USA) according to the manufacturer's instructions for nuclei staining.

4.6. Immunofluorescence (IF)

HEK293 Flp-In T-REx cells (3×10^5) were seeded in the presence of 1% penicillin/streptomycin (Cat. No. P0781, Sigma-Aldrich, St. Louis, MO, USA) into fibronectin-coated 35 mm imaging dishes (Cat. No. 81158, ibidi, Gräfelfing, Germany) and cultured for 24 h in DMEM supplemented with 10% FCS. For immunostaining with anti-TGN46 antibody, Flp-In T-REx 293 cells (Cat. No. R78007, Invitrogen, Carlsbad, CA, USA) (WT and as GABARAP(s) SKO, DKO, or TKO) were fixed at 37 °C for 10 min with 4% (*w/v*) paraformaldehyde (PFA; pH 6.5), washed two times with PBS, pH 7.4, and permeabilised by shaking in 0.2% Triton-X-100 for 30 min at RT. Cells were blocked by incubation in 1% BSA over night at 4 °C and incubated on the following day first with primary antibody for 1 h shaking at RT, washed three times with PBS, and then incubated with secondary antibody for 1 h shaking at RT under exclusion of light. Again, the cells were washed two times, stored in long storage buffer (0.05% sodium azide in PBS), and applied to image acquisition.

4.7. Image Acquisition–Laser Scanning Microscopy (LSM)

For image acquisition, an LSM 710 confocal microscope (Zeiss, Oberkochen Germany) equipped with ZEN black 2009 software (Zeiss, Oberkochen, Germany) and a Plan-Apochromat 63x/1.40 Oil DIC M27 objective was used. Nuclei (DAPI or Hoechst 33342) were visualised using the 405 nm channel (MBS -405), TGN46 using the 488 nm channel (MBS 488) and NBD C_6-Ceramide using the 458 nm channel (MBS 458). The number of focal planes (z-frames) with a z-distance of 0.4 μm was set between 11 and 18 or 11 and 34 for the recording of TGN46- or BODIPY-stained cells, respectively.

4.8. Image Evaluation

Image analysis was done using ImageJ/Fiji [61,62]. All individual planes of the z-stacks recorded were combined in ImageJ by applying the function „SUMSLICES". Morphology of *trans*-Golgi was qualitatively judged for each cell visually by categorizing the obtained TGN46-staining patterns according to Figure 1B. The 3D visualisations of the recorded confocal stacks from the TGN46-stains were obtained by using ZEN 2.3 SP1 FP1 (black edition). All images have been arranged using CorelDRAW 2017 (version 20, Corel Corporation, Ottawa, Canada). Data analysis and visualisation were done using GraphPad Prism (version 8, GraphPad Software, San Diego, CA, USA). Pearson's chi-square test statistic and standardised residuals representing z-scores were calculated using the statistical analysis software package (SPSS, version 22, SPSS Inc., Chicago, IL, USA).

4.9. Isolation, Identification, Quantification and Analysis of Surfaceomes

PM-based proteins were isolated as described before using the Pierce Cell Surface Protein Isolation Kit according to the manufacturer's instructions (89881, Thermo Fisher Scientific, Waltham, MA, USA) [26].

Briefly, for each individual experiment, four T75 flasks were prepared, pooled and further processed at >80% confluency. On the day of surface protein isolation, flasks were labelled with Sulfo-NHS-SS Biotin at 4 °C on a shaker. After quenching, cells were pelleted and lysed with periodical sonication and vortexing steps. Biotinylated surface proteins were bound to NeutrAvidin beads, eluted and prepared for mass spectrometric measure-

ments by in-gel digestion essentially as described [63]. Briefly, proteins were separated over a short distance (about 5 mm) in a polyacrylamide gel, stained, reduced with dithiothreitol, alkylated with iodoacetamide and digested with trypsin overnight. Peptides were extracted from the gel and reconstituted in 0.1% (v/v) trifluoroacetic acid in water. Liquid chromatography coupled with mass spectrometry were essentially carried out as described [63]. Then, 500 ng peptides per sample were separated using a 2 h gradient on C18 material using an Ultimate 3000 Rapid Separation Liquid Chromatography system (Thermo Fisher Scientific, Waltham, MA, USA) online coupled via a nano-source electrospray interface to a QExactive plus (Thermo Fisher Scientific, Waltham, MA, USA) mass spectrometer operated in positive data dependent mode. First, survey scans were recorded at a resolution of 70,000 and subsequently, up to 10 two- and three-fold charged precursors were selected by the quadrupole of the instrument (2 m/z isolation window), fragmented by higher-energy collisional dissociation and analysed at a resolution of 17,500.

Recorded mass spectra were further analysed by MaxQuant (version 1.6.2.10, Max Planck institute for biochemistry, Planegg, Germany) enabling peptide and protein identification and label-free quantification (LFQ). Searches were carried out with standard parameters if not indicated otherwise and were based on 73,112 protein entries from the homo sapiens reference proteome (UP000005640, downloaded on 18 August 2018 from the UniProt Knowledgebase). Label-free quantification was enabled as well as the 'match between runs' option. Peptides and proteins were identified at a false discovery rate of 1% and only proteins considered for further analysis showing at least 2 different peptides.

Positive hits were inferred when at least three valid values were detected in at least one group (WT or GABARAP/L1/L2^{TKO}). Log$_2$ transformed intensities were normalised by subtracting the median from every value. Afterwards, missing values were imputed by replacing them with random values from the normal distribution (downshift 1.8 SD, width 0.3 SD). One n (WT) was removed, because principle component analysis revealed lack of similarity to the other WT samples. Two-tailed two-sample Student's T-test was calculated (S0: 0, FDR: 5%) for a surface-annotated subset according to the CSPA [34]. Hierarchical clustering was calculated (Euclidean distance, pre-processed with κ-means, average linkage) for differentially expressed annotated surface proteins. High confidence surface proteins (CSPA annotated) with significantly different abundances between WT and GABARAP/L1/L2^{TKO} analysed for relative enrichment of gene ontology (GO)/reactome terms where all identified proteins during mass spectrometry were set as a background database.

References

1. Weidberg, H.; Shvets, E.; Shpilka, T.; Shimron, F.; Shinder, V.; Elazar, Z. LC3 and GATE-16/GABARAP subfamilies are both essential yet act differently in autophagosome biogenesis. *EMBO J.* **2010**, *29*, 1792–1802. [CrossRef] [PubMed]
2. Nguyen, T.N.; Padman, B.S.; Usher, J.; Oorschot, V.; Ramm, G.; Lazarou, M. Atg8 family LC3/GABARAP proteins are crucial for autophagosome-lysosome fusion but not autophagosome formation during PINK1/Parkin mitophagy and starvation. *J. Cell Biol.* **2016**, *215*, 857–874. [CrossRef] [PubMed]
3. Birgisdottir, Å.B.; Johansen, T. Autophagy and endocytosis—Interconnections and interdependencies. *J. Cell Sci.* **2020**, *133*, jcs228114. [CrossRef] [PubMed]
4. Wang, H.; Bedford, F.K.; Brandon, N.J.; Moss, S.J.; Olsen, R.W. GABAA-receptor-associated protein links GABAA receptors and the cytoskeleton. *Nature* **1999**, *397*, 69–72. [CrossRef]
5. Green, F.; O'Hare, T.; Blackwell, A.; Enns, C.A. Association of human transferrin receptor with GABARAP. *FEBS Lett.* **2002**, *518*, 101–106. [CrossRef]
6. Asano, S.; Nemoto, T.; Kitayama, T.; Harada, K.; Zhang, J.; Harada, K.; Tanida, I.; Hirata, M.; Kanematsu, T. Phospholipase C-related catalytically inactive protein (PRIP) controls KIF5B-mediated insulin secretion. *Biol. Open* **2014**, *3*, 463–474. [CrossRef]
7. Nakajima, K.; Yin, X.; Takei, Y.; Seog, D.-H.; Homma, N.; Hirokawa, N. Molecular Motor KIF5A Is Essential for GABAA Receptor Transport, and KIF5A Deletion Causes Epilepsy. *Neuron* **2012**, *76*, 945–961. [CrossRef]
8. Mansuy, V.; Boireau, W.; Fraichard, A.; Schlick, J.-L.; Jouvenot, M.; Delage-Mourroux, R. GEC1, a protein related to GABARAP, interacts with tubulin and GABAA receptor. *Biochem. Biophys. Res. Commun.* **2004**, *325*, 639–648. [CrossRef]
9. Chen, C.; Li, J.G.; Chen, Y.; Huang, P.; Wang, Y.; Liu-Chen, L.Y. GEC1 interacts with the kappa opioid receptor and enhances expression of the receptor. *J. Biol. Chem.* **2006**, *281*, 7983–7993. [CrossRef]
10. Legesse-Miller, A.; Sagiv, Y.; Porat, A.; Elazar, Z. Isolation and characterization of a novel low molecular weight protein involved in intra-Golgi traffic. *J. Biol. Chem.* **1998**, *273*, 3105–3109. [CrossRef]
11. Sagiv, Y.; Legesse-Miller, A.; Porat, A.; Elazar, Z. GATE-16, a membrane transport modulator, interacts with NSF and the Golgi v-SNARE GOS-28. *EMBO J.* **2000**, *19*, 1494–1504. [CrossRef] [PubMed]
12. Müller, J.M.M.; Shorter, J.; Newman, R.; Deinhardt, K.; Sagiv, Y.; Elazar, Z.; Warren, G.; Shima, D.T. Sequential SNARE disassembly and GATE-16-GOS-28 complex assembly mediated by distinct NSF activities drives Golgi membrane fusion. *J. Cell Biol.* **2002**, *157*, 1161–1173. [CrossRef] [PubMed]
13. Elazar, Z.R.; Shouval, S.; Shorer, H. Involvement of LMA1 and GATE-16 family members in intracellular membrane dynamics. *Biochim. Biophys. Acta Mol. Cell Res.* **2003**, *1641*, 145–156. [CrossRef]
14. Kumar, S.; Jain, A.; Farzam, F.; Jia, J.; Gu, Y.; Choi, S.W.; Mudd, M.H.; Claude-Taupin, A.; Wester, M.J.; Lidke, K.A.; et al. Mechanism of Stx17 recruitment to autophagosomes via IRGM and mammalian Atg8 proteins. *J. Cell Biol.* **2018**, *217*, 997–1013. [CrossRef] [PubMed]
15. Gu, Y.; Princely Abudu, Y.; Kumar, S.; Bissa, B.; Choi, S.W.; Jia, J.; Lazarou, M.; Eskelinen, E.-L.; Johansen, T.; Deretic, V. Mammalian Atg8 proteins regulate lysosome and autolysosome biogenesis through SNAREs. *EMBO J.* **2019**, *38*, e101994. [CrossRef] [PubMed]
16. Kittler, J.T.; Rostaing, P.; Schiavo, G.; Fritschy, J.M.; Olsen, R.; Triller, A.; Moss, S.J. The subcellular distribution of GABARAP and its ability to interact with NSF suggest a role for this protein in the intracellular transport of GABA(A) receptors. *Mol. Cell. Neurosci.* **2001**, *18*, 13–25. [CrossRef]
17. Joachim, J.; Jefferies, H.B.J.; Razi, M.; Frith, D.; Snijders, A.P.; Chakravarty, P.; Judith, D.; Tooze, S.A. Activation of ULK Kinase and Autophagy by GABARAP Trafficking from the Centrosome Is Regulated by WAC and GM130. *Mol. Cell* **2015**, *60*, 899–913. [CrossRef]
18. Nakamura, T.; Hayashi, T.; Nasu-Nishimura, Y.; Sakaue, F.; Morishita, Y.; Okabe, T.; Ohwada, S.; Matsuura, K.; Akiyama, T. PX-RICS mediates ER-to-Golgi transport of the N-cadherin/beta-catenin complex. *Genes Dev.* **2008**, *22*, 1244–1256. [CrossRef]
19. Ryan, T.A.; Tumbarello, D.A. Optineurin: A Coordinator of Membrane-Associated Cargo Trafficking and Autophagy. *Front. Immunol.* **2018**, *9*, 1024. [CrossRef]
20. Toth, R.P.; Atkin, J.D. Dysfunction of Optineurin in Amyotrophic Lateral Sclerosis and Glaucoma. *Front. Immunol.* **2018**, *9*, 1017. [CrossRef]
21. Farquhar, M.G.; Palade, G.E. The Golgi apparatus (complex)-(1954-1981)-from artifact to center stage. *J. Cell Biol.* **1981**, *91 Pt 2*, 77s–103s. [CrossRef]
22. Ladinsky, M.S.; Mastronarde, D.N.; McIntosh, J.R.; Howell, K.E.; Staehelin, L.A. Golgi structure in three dimensions: Functional insights from the normal rat kidney cell. *J. Cell Biol.* **1999**, *144*, 1135–1149. [CrossRef] [PubMed]
23. Szul, T.; Sztul, E. COPII and COPI traffic at the ER-Golgi interface. *Physiology* **2011**, *26*, 348–364. [CrossRef] [PubMed]
24. Kumagai, K.; Hanada, K. Structure, functions and regulation of CERT, a lipid-transfer protein for the delivery of ceramide at the ER-Golgi membrane contact sites. *FEBS Lett.* **2019**, *593*, 2366–2377. [CrossRef] [PubMed]
25. Liu, Y.-Y.; Li, Y.-T. Ceramide glycosylation catalyzed by glucosylceramide synthase and cancer drug resistance. *Adv. Cancer Res.* **2013**, *117*, 59–89.
26. Dobner, J.; Simons, I.M.; Rufinatscha, K.; Hansch, S.; Schwarten, M.; Weiergraber, O.H.; Abdollahzadeh, I.; Gensch, T.; Bode, J.G.; Hoffmann, S.; et al. Deficiency of GABARAP but not its Paralogs Causes Enhanced EGF-induced EGFR Degradation. *Cells* **2020**, *9*, 1296. [CrossRef]

27. Simons, I.M.; Mohrlüder, J.; Feederle, R.; Kremmer, E.; Zobel, T.; Dobner, J.; Bleffert, N.; Hoffmann, S.; Willbold, D. The highly GABARAP specific rat monoclonal antibody 8H5 visualizes GABARAP in immunofluorescence imaging at endogenous levels. *Sci. Rep.* **2019**, *9*, 526. [CrossRef]

28. Grieve, A.G.; Rabouille, C. Golgi bypass: Skirting around the heart of classical secretion. *Cold Spring Harb Perspect Biol.* **2011**, *3*, a005298. [CrossRef]

29. Madison, K.C.; Howard, E.J. Ceramides are transported through the Golgi apparatus in human keratinocytes in vitro. *J. Invest. Dermatol.* **1996**, *106*, 1030–1035. [CrossRef]

30. Pagano, R.E.; Martin, O.C.; Kang, H.C.; Haugland, R.P. A novel fluorescent ceramide analogue for studying membrane traffic in animal cells: Accumulation at the Golgi apparatus results in altered spectral properties of the sphingolipid precursor. *J. Cell Biol.* **1991**, *113*, 1267–1279. [CrossRef]

31. Hanada, K. Intracellular trafficking of ceramide by ceramide transfer protein. Proceedings of the Japan Academy. *Ser. B Phys. Biol. Sci.* **2010**, *86*, 426–437.

32. Mollenhauer, H.H.; Morré, D.J.; Rowe, L.D. Alteration of intracellular traffic by monensin; mechanism, specificity and relationship to toxicity. *Biochim. Biophys. Acta* **1990**, *1031*, 225–246. [CrossRef]

33. Ketola, K.; Vainio, P.; Fey, V.; Kallioniemi, O.; Iljin, K. Monensin is a potent inducer of oxidative stress and inhibitor of androgen signaling leading to apoptosis in prostate cancer cells. *Mol. Cancer Ther.* **2010**, *9*, 3175–3185. [CrossRef] [PubMed]

34. Bausch-Fluck, D.; Hofmann, A.; Bock, T.; Frei, A.P.; Cerciello, F.; Jacobs, A.; Moest, H.; Omasits, U.; Gundry, R.L.; Yoon, C.; et al. A Mass Spectrometric-Derived Cell Surface Protein Atlas. *PLoS ONE* **2015**, *10*, e0121314. [CrossRef]

35. Crotzer, V.L.; Blum, J.S. Autophagy and its role in MHC-mediated antigen presentation. *J. Immunol.* **2009**, *182*, 3335–3341. [CrossRef]

36. Mitrofanova, A.; Mallela, S.K.; Ducasa, G.M.; Yoo, T.H.; Rosenfeld-Gur, E.; Zelnik, I.D.; Molina, J.; Varona Santos, J.; Ge, M.; Sloan, A.; et al. SMPDL3b modulates insulin receptor signaling in diabetic kidney disease. *Nat. Commun.* **2019**, *10*, 2692. [CrossRef]

37. Heinz, L.X.; Baumann, C.L.; Koberlin, M.S.; Snijder, B.; Gawish, R.; Shui, G.; Sharif, O.; Aspalter, I.M.; Muller, A.C.; Kandasamy, R.K.; et al. The Lipid-Modifying Enzyme SMPDL3B Negatively Regulates Innate Immunity. *Cell Rep.* **2015**, *11*, 1919–1928. [CrossRef]

38. Leidal, A.M.; Huang, H.H.; Marsh, T.; Solvik, T.; Zhang, D.; Ye, J.; Kai, F.; Goldsmith, J.; Liu, J.Y.; Huang, Y.-H.; et al. The LC3-conjugation machinery specifies the loading of RNA-binding proteins into extracellular vesicles. *Nat. Cell Biol.* **2020**, *22*, 187–199. [CrossRef]

39. Sanwald, J.L.; Poschmann, G.; Stuhler, K.; Behrends, C.; Hoffmann, S.; Willbold, D. The GABARAP Co-Secretome Identified by APEX2-GABARAP Proximity Labelling of Extracellular Vesicles. *Cells* **2020**, *9*, 1468. [CrossRef]

40. Thul, P.J.; Åkesson, L.; Wiking, M.; Mahdessian, D.; Geladaki, A.; Ait Blal, H.; Alm, T.; Asplund, A.; Björk, L.; Breckels, L.M.; et al. A subcellular map of the human proteome. *Science* **2017**, *356*, eaal3321. [CrossRef]

41. Cole, N.B.; Sciaky, N.; Marotta, A.; Song, J.; Lippincott-Schwartz, J. Golgi dispersal during microtubule disruption: Regeneration of Golgi stacks at peripheral endoplasmic reticulum exit sites. *Mol. Biol. Cell* **1996**, *7*, 631–650. [CrossRef] [PubMed]

42. Bexiga, M.G.; Simpson, J.C. Human diseases associated with form and function of the Golgi complex. *Int. J. Mol. Sci.* **2013**, *14*, 18670–18681. [CrossRef] [PubMed]

43. Gosavi, P.; Gleeson, P.A. The Function of the Golgi Ribbon Structure—An Enduring Mystery Unfolds! *BioEssays* **2017**, *39*, 1700063. [CrossRef] [PubMed]

44. Ma, X.; Sun, J.; Zhong, L.; Wang, Y.; Huang, Q.; Liu, X.; Jin, S.; Zhang, J.; Liang, X.-J. Evaluation of Turning-Sized Gold Nanoparticles on Cellular Adhesion by Golgi Disruption in Vitro and in Vivo. *Nano Lett.* **2019**, *19*, 8476–8487. [CrossRef] [PubMed]

45. Bekier, M.E.; Wang, L.; Li, J.; Huang, H.; Tang, D.; Zhang, X.; Wang, Y. Knockout of the Golgi stacking proteins GRASP55 and GRASP65 impairs Golgi structure and function. *Mol. Biol. Cell* **2017**, *28*, 2833–2842. [CrossRef]

46. Makhoul, C.; Gosavi, P.; Gleeson, P.A. Golgi Dynamics: The Morphology of the Mammalian Golgi Apparatus in Health and Disease. *Front. Cell Dev. Biol.* **2019**, *7*, 112. [CrossRef]

47. Liu, C.; Mei, M.; Li, Q.; Roboti, P.; Pang, Q.; Ying, Z.; Gao, F.; Lowe, M.; Bao, S. Loss of the golgin GM130 causes Golgi disruption, Purkinje neuron loss, and ataxia in mice. *Proc. Natl. Acad. Sci. USA* **2017**, *114*, 346–351. [CrossRef]

48. Wang, H.; Sun, H.-Q.; Zhu, X.; Zhang, L.; Albanesi, J.; Levine, B.; Yin, H. GABARAPs regulate PI4P-dependent autophagosome:lysosome fusion. *Proc. Natl. Acad. Sci. USA* **2015**, *112*, 7015–7020. [CrossRef]

49. Minogue, S.; Waugh, M.G.; De Matteis, M.A.; Stephens, D.J.; Berditchevski, F.; Hsuan, J.J. Phosphatidylinositol 4-kinase is required for endosomal trafficking and degradation of the EGF receptor. *J. Cell Sci.* **2006**, *119*, 571–581. [CrossRef]

50. Henmi, Y.; Morikawa, Y.; Oe, N.; Ikeda, N.; Fujita, A.; Takei, K.; Minogue, S.; Tanabe, K. PtdIns4KIIα generates endosomal PtdIns(4)P and is required for receptor sorting at early endosomes. *Mol. Biol. Cell* **2016**, *27*, 990–1001. [CrossRef]

51. Mao, D.; Lin, G.; Tepe, B.; Zuo, Z.; Tan, K.L.; Senturk, M.; Zhang, S.; Arenkiel, B.R.; Sardiello, M.; Bellen, H.J. VAMP associated proteins are required for autophagic and lysosomal degradation by promoting a PtdIns4P-mediated endosomal pathway. *Autophagy* **2019**, *15*, 1214–1233. [CrossRef] [PubMed]

52. Johansen, T.; Lamark, T. Selective Autophagy: ATG8 Family Proteins, LIR Motifs and Cargo Receptors. *J. Mol. Biol.* **2020**, *432*, 80–103. [CrossRef]

53. Martens, S.; Fracchiolla, D. Activation and targeting of ATG8 protein lipidation. *Cell Discov.* **2020**, *6*, 23. [CrossRef] [PubMed]
54. Schaaf, M.B.; Keulers, T.G.; Vooijs, M.A.; Rouschop, K.M. LC3/GABARAP family proteins: Autophagy-(un)related functions. *FASEB J.* **2016**, *30*, 3961–3978. [CrossRef] [PubMed]
55. Wesch, N.; Kirkin, V.; Rogov, V.V. Atg8-Family Proteins-Structural Features and Molecular Interactions in Autophagy and Beyond. *Cells* **2020**, *9*, 2008. [CrossRef]
56. Vaites, L.P.; Paulo, J.A.; Huttlin, E.L.; Harper, J.W. Systematic Analysis of Human Cells Lacking ATG8 Proteins Uncovers Roles for GABARAPs and the CCZ1/MON1 Regulator C18orf8/RMC1 in Macroautophagic and Selective Autophagic Flux. *Mol. Cell Biol.* **2018**, *38*, e00392-17. [CrossRef] [PubMed]
57. Baines, K.; Lane, J.D. The ATG5 Interactome Links Clathrin Vesicular Trafficking With The ATG8 Lipidation Machinery For Autophagosome Assembly. *bioRxiv* **2019**, 769059. [CrossRef]
58. Keulers, T.; Schaaf, M.; Rouschop, K. Autophagy-Dependent Secretion: Contribution to Tumor Progression. *Front. Oncol.* **2016**, *6*, 251. [CrossRef]
59. Chang, I.J.; He, M.; Lam, C.T. Congenital disorders of glycosylation. *Ann. Transl. Med.* **2018**, *6*, 477. [CrossRef]
60. Ran, F.A.; Hsu, P.D.; Wright, J.; Agarwala, V.; Scott, D.A.; Zhang, F. Genome engineering using the CRISPR-Cas9 system. *Nat. Protoc.* **2013**, *8*, 2281–2308. [CrossRef]
61. Schindelin, J.; Arganda-Carreras, I.; Frise, E.; Kaynig, V.; Longair, M.; Pietzsch, T.; Preibisch, S.; Rueden, C.; Saalfeld, S.; Schmid, B. Fiji: An open-source platform for biological-image analysis. *Nat. Methods* **2012**, *9*, 676–682. [CrossRef] [PubMed]
62. Schneider, C.A.; Rasband, W.S.; Eliceiri, K.W. NIH Image to ImageJ: 25 years of image analysis. *Nat. Methods* **2012**, *9*, 671–675. [CrossRef] [PubMed]
63. Grube, L.; Dellen, R.; Kruse, F.; Schwender, H.; Stuhler, K.; Poschmann, G. Mining the Secretome of C2C12 Muscle Cells: Data Dependent Experimental Approach to Analyze Protein Secretion Using Label-Free Quantification and Peptide Based Analysis. *J. Proteome Res.* **2018**, *17*, 879–890. [CrossRef] [PubMed]

Lack of GABARAP-type proteins is accompanied by altered Golgi morphology and surfaceome composition

Julia L. Sanwald [1,2 †], Jochen Dobner [1 †], Indra M. Simons [1,2], Gereon Poschmann [3], Kai Stühler [3,4], Alina Üffing [1,2], Silke Hoffmann [2], Dieter Willbold [1,2]

[1] Institut für Physikalische Biologie, Heinrich-Heine-Universität Düsseldorf, Universitätsstraße 1, 40225 Düsseldorf, Germany

[2] Institute of Biological Information Processing (IBI-7: Structural Biochemistry), Forschungszentrum Jülich, Leo-Brandt-Straße, 52428 Jülich, Germany

[3] Institute of Molecular Medicine I, Proteome Research, Heinrich-Heine-Universität Düsseldorf, Universitätsstraße 1, 40225 Düsseldorf, Germany; gereon.poschmann@uni-duesseldorf.de (G.P.); kai.stuehler@uni-duesseldorf.de (K.S.)

[4] Molecular Proteomics Laboratory, Biologisch-Medizinisches Forschungszentrum (BMFZ), Heinrich-Heine-Universität Düsseldorf, Universitätsstraße 1, 40225 Düsseldorf, Germany

[†] Authors contributed equally to this work

Supplementary Methods are related to Figures S1, S4

Supplementary Figure S1 is related to Figure 1

Supplementary Figure S2 is related to Figure 1

Supplementary Figure S3 is related to Figure 1

Supplementary Figure S4 is related to Figure 3

Supplementary Figure S5 is related to Figure S4

Supplementary Table S1 is related to Figure 3B

Supplementary Methods

Live-cell imaging with fluorescently labelled ceramide

HEK293 Flp-In T-REx cells (3×10^5) were seeded into fibronectin coated 35 mm imaging dishes (Cat. No. 81158, ibidi) and cultured for 24 h in DMEM supplemented with 10 % FCS. Staining of the cells (WT and as GABARAP(s) SKO, DKO, or TKO) with BODIPY-FL C5-ceramide (Cat. No. B-22650, Life Technologies) was conducted according to the manufacturer's instructions. Briefly, cells were rinsed in HBSS and incubated for 30 min at 4 °C with 5 μM BODIPY-FL C5-ceramide. Then, the cells were rinsed three times in ice-cold HBSS and incubated 30 min in phenol red-free DMEM supplemented with 10 % FCS. Finally, the cells were rinsed once in HBSS and stored in phenol red-free DMEM supplemented with 10 % FCS. Cells were incubated with Hoechst 33342 (Cat. No. R37605, Invitrogen, Carlsbad, CA, USA) according to the manufacturer's instructions for nuclei staining. BODIPY-FL C5-ceramide was visualised by LSM using the 488 nm channel (MBS 488).

Fluorescence-activated cell sorting

Surface levels of HLA-A were analysed under steady-state conditions in HEK293 WT and GABARAP/L1/L2^{TKO} cells. In brief, $1 * 10^6$ cells of 90 % confluent cells were washed twice with ice-cold PBS and resuspended in 100 μl ice-cold FACS buffer (2 mM EGTA, 1 %FBS, 25 mM HEPES in PBS) containing 1:20 diluted HLA-A3 antibody conjugated to PE (ThermoFisher Scientific, 12-5754-42) or APC (ThermoFisher Scientific, 17-5754-42). Isotype controls (ThermoFisher Scientific, PE: Mouse IgG2a K, 12-4724-81, APC: Mouse IgG2a K, 17-4724-81) After 30 min incubation on ice in the dark, cells were washed thrice with ice-cold FACS buffer, resuspended in 0.5 ml FACS buffer and analysed by flow cytometry (Aria III, BD Bioscience, Franklin Lakes, USA). Cells were gated according to their size (SSC-A x FSC-A) and being single cells (FSC-A x FSC-H). Median fluorescence intensity of GABARAP/L1/L2^{TKO} cells was calculated relative to HEK293 WT intensity. Statistical significance was inferred as calculated by Welch's t-test using GraphPad Prism (version 8).

Immunoblotting

For proof-of-method immunoblotting, 10 μg of surface-enriched proteins were diluted with 4 x Lämmli's buffer (250 mM Tris-HCl pH 6.8, 40 % glycerol, 5 % SDS, 0.005 % bromophenol blue) containing 8 % fresh 2-mercaptoethanol. After samples were boiled for 5 min at 95 °C, surface fraction lysates were applied on 8 % SDS-PAA gel. After gel electrophoresis, semi-dry blotting of proteins onto 0.4 μm μm polyvinyliden fluoride membrane was performed for 1 h 30 min at 77 mA constant current. Unspecific binding sites were blocked for 1 h at RT with 5 % BSA in TBS-T (TBS, 0.1 % Tween-20) and membrane incubated with primary antibody for TFRC (#13208, Cell Signaling Technologies, Danvers, USA) at 1:1000 dilution overnight at 4 °C. After washing (three times with TBS-T) and incubation with 1:5000 diluted fluorescently labelled secondary antibody (ab150083, abcam) for 1 h at RT, target protein was

visualised using BioRad Imager. Statistical significance was inferred as calculated by Student's t-test using GraphPad Prism (version 8).
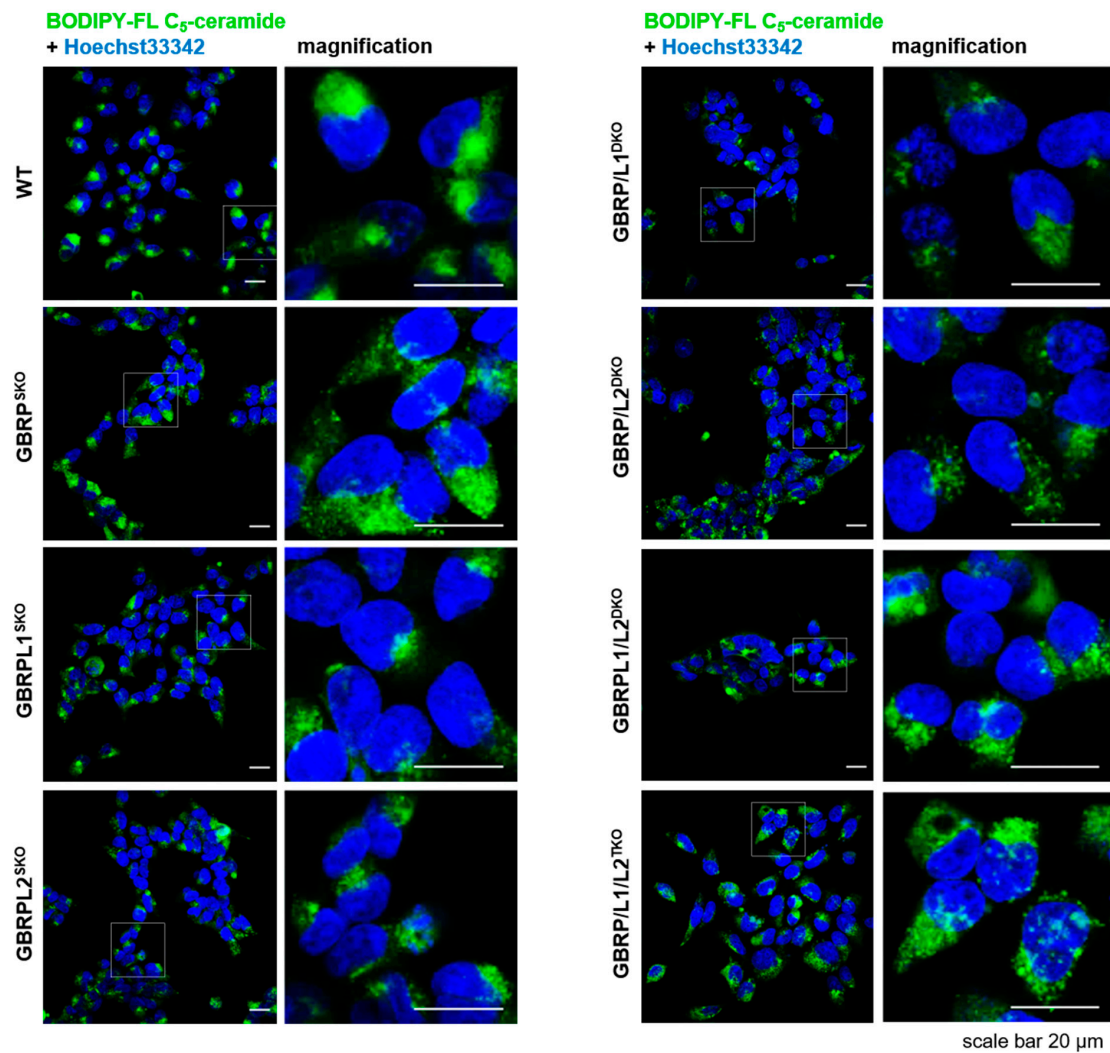
Supplementary Figure S1. Loss of GABARAP leads to a redistribution of Golgi-localised ceramide. HEK^{WT} (WT) or HEK cells with deficiency for one (SKO), two (DKO), or all three (TKO) of the GABARAPs (GBRPs) were cultured for 24 h at 37 °C and 5 % CO_2 in fibronectin coated 35 mm imaging dishes, stained with BODIPY-FL C$_5$-ceramide according to the manufacturer's instructions (Cat. No. B-22650, Life Technologies), and visualised by confocal fluorescence microscopy. Nuclei were counterstained with Hoechst 33342. Cells were recorded as z-stacks and the slices of each stack were combined in ImageJ by applying the function „SUMSLICES". For each condition, a representative image of five frames is shown. Scale bar, 20 μm.
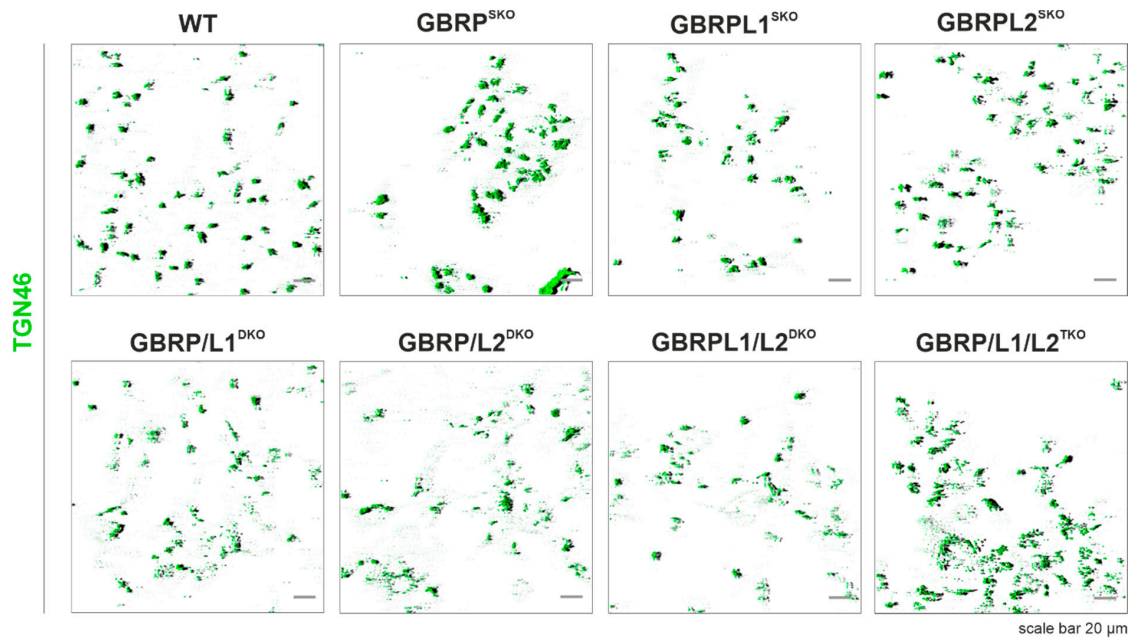
Supplementary Figure S2. 3D visualisation of the *trans*-Golgi morphology in HEK293 WT cells and under various GABARAP-type protein deficiencies. Individual planes of each stack were displayed as 3D image in ZEN 2.3 SP1 FP1 (black edition). The reconstructions relate to the respective images in Figure 1A. Scale bar, 20 μm.
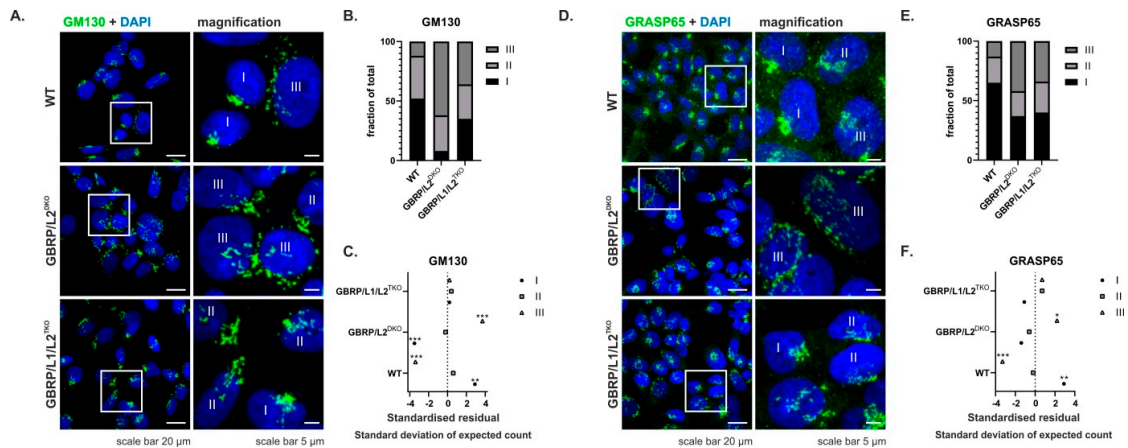
Supplementary Figure S3. Influence of GABARAP-type protein deficiency on *cis*-Golgi morphology. (A) WT, GABARAP/L2[DKO] or GABARAP/L1/L2[TKO] cells were fixed (4 % PFA), immunolabelled with anti-human GM130 antibody, and visualised by confocal fluorescence microscopy. Nuclei were counterstained with DAPI. Scale bar total = 20 μm, scale bar zoom-in = 5 μm. (B) Distribution of percentage of cells per cell type assigned to Golgi structure category I (compact), II (partly compact), and III (dispersed) according to GM130 staining. (C) Standardised residual distribution of analysed genotypes. Per cell type, in total ≥ 63 cells from three individual experiments were analysed and categorised by visual judgement. Asterisks indicate significant differences from the mean based on the standardised residual distribution with: |z| ≥ 2.58 ** (p ≤ 0.01), |z| ≥ 3.29 *** (p ≤ 0.001). (D) WT, GABARAP/L2[DKO] or GABARAP/L1/L2[TKO] cells were fixed (4 % PFA), immunolabelled with anti-human GRASP65 antibody, and visualised by confocal fluorescence microscopy. Nuclei were counterstained with DAPI. Scale bar total = 20 μm, scale bar zoom-in = 5 μm. (B) Distribution of percentage of cells per cell type assigned to Golgi structure category I (compact), II (partly compact), and III (dispersed) according to GRASP65 staining. (C) Standardised residual distribution of analysed genotypes. Per cell type, in total ≥ 103 cells were analysed and categorised by visual judgement. Asterisks indicate

significant differences from the mean based on the standardised residual distribution with: $|z| \geq 1.96$ * ($p \leq$ 0.05), $|z| \geq 2.58$ ** ($p \leq 0.01$), $|z| \geq 3.29$ *** ($p \leq 0.001$).
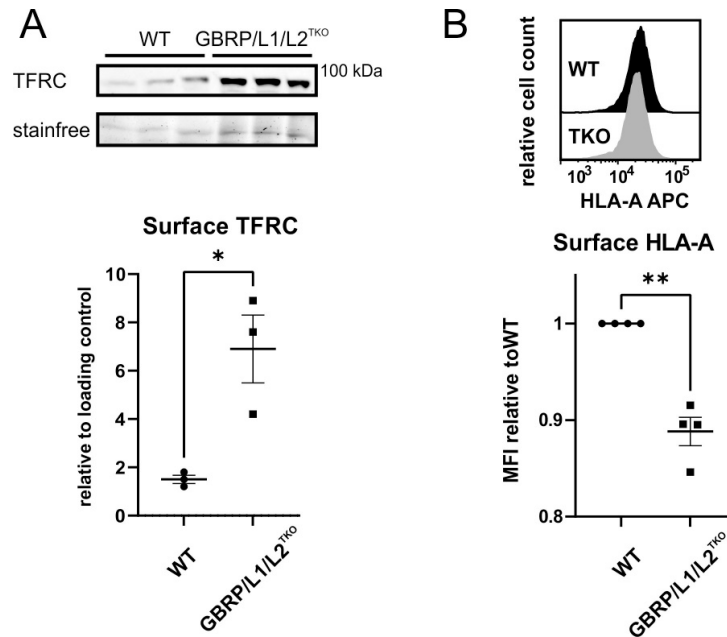
Supplementary Figure S4. Validation of surface proteome mass-spectrometry analysis by two independent methods. (A) Cell surface protein-enriched fractions were analysed by immunoblot. Surface levels of TFRC are shown for three independent experiments. Asterisk marks significant differences between GABARAP/L1/L2[TKO] and WT cells as calculated using independent t-test. $p \leq 0.05$ = *. (B) Surface levels of MHC-I subtype HLA-A were analysed by fluorescence-activated cell sorting. Representative histograms of four independent experiments of single cells stained with HLA-A antibody are shown. Significant differences of median fluorescence intensities (MFI) between WT and GABARAP/L1/L2[TKO] cells are marked by asterisk as calculated by Welch's t-test. $p \leq 0.01$ = **. GBRP = GABARAP. APC = Allophycocyanin.
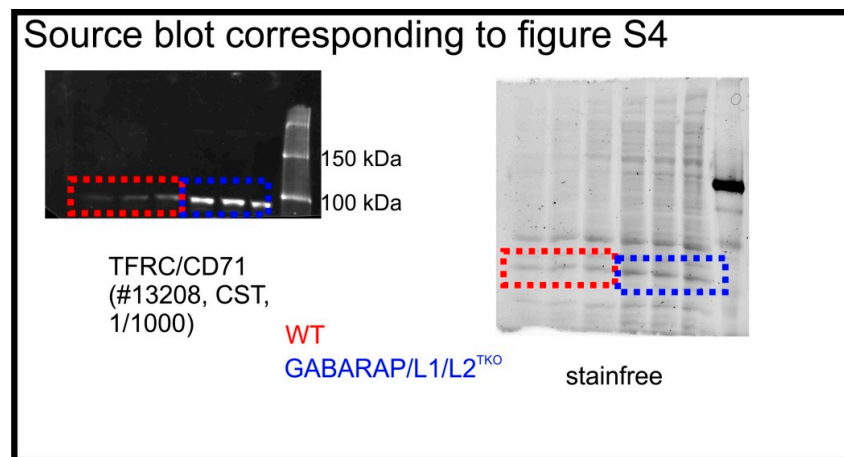
Supplementary Figure S5. Source blot corresponding to Figure S4. Regions used for display and analysis are indicated.

1 **Supplementary Table S1.** Raw data of mass-spectrometry analysis of surface-enriched proteomes of HEK293 WT
2 and GABARAP/L1/L2^{TKO} cells can be found in the attached excel file Table S1 Mass-spectrometry data set.

7

Supplementary Table S2. Significantly different expressed surface-annotated proteins. For consistency, proteins are sorted as depicted in Figure 3B. Respective raw data are given in Supplementary Table S1.

GENE SYMBOL	GENE NAME	GENE ID	UNIPROT	CSPA CONFIDENCE LEVEL	DIFFERENCE TKO-WT
PODXL2	podocalyxin like 2	50512	Q9NZ53	1	1.95089
CNNM4	cyclin and CBS domain divalent metal cation transport mediator 4	26504	Q6P4Q7	1	0.801802
ITGA7	integrin subunit alpha 7	3679	Q13683	1	0.516933
ADAM15	ADAM metallopeptidase domain 15	8751	Q13444	1	0.575086
KIRREL	Kin of IRRE-like protein 1	55243	Q96J84	1	0.514684
CD59	CD59 molecule (CD59 blood group)	966	P13987	1	0.559599
ITPRIP	inositol 1,4,5-trisphosphate receptor interacting protein	85450	Q8IWB1	1	0.417335
GGCX	gamma-glutamyl carboxylase	2677	P38435	2	0.703851
ECE1	endothelin converting enzyme 1	1889	P42892	1	1.0075
CNNM2	cyclin and CBS domain divalent metal cation transport mediator 2	54805	Q9H8M5	1	0.859415
INSR	Insulin receptor	3643	P06213	1	0.912155
SMPDL3B	sphingomyelin phosphodiesterase acid like 3B	27293	Q92485	1	1.01647
HNRNPK	heterogeneous nuclear ribonucleoprotein K	3190	P61978	1	0.694312
SLC4A7	solute carrier family 4 member 7	9497	Q9Y6M7	1	0.592821
TPBG	trophoblast glycoprotein	7162	Q13641	1	0.787366
NCSTN	nicastrin	23385	Q92542	1	0.772031
M6PR	mannose-6-phosphate receptor, cation dependent	4074	P20645	1	0.557621
TFRC	transferrin receptor	7037	P02786	1	0.422732
PTPRF	protein tyrosine phosphatase receptor type F	5792	P10586	1	0.287566
TMED7	transmembrane p24 trafficking protein 7	51014	Q9Y3B3	1	0.367156
ASIC1	acid sensing ion channel subunit 1	41	P78348	1	0.541489
SEL1L	SEL1L adaptor subunit of ERAD E3 ubiquitin ligase	6400	Q9UBV2	1	0.604953
ABCC1	ATP binding cassette subfamily C member 1	4363	P33527	1	0.578134
ANO6	anoctamin 6	196527	Q4KMQ2	1	0.478563
TYRO3	TYRO3 protein tyrosine kinase	7301	Q06418	1	0.544295
SLC39A14	solute carrier family 39 member 14	23516	Q15043	1	0.594535
NPTN	neuroplastin	27020	Q9Y639	1	0.499769

ALCAM	activated leukocyte cell adhesion molecule	214	Q13740	1	0.458814
ATP1A1	ATPase Na+/K+ transporting subunit alpha 1	476	P05023	1	0.340416
NCR3LG1	natural killer cell cytotoxicity receptor 3 ligand 1	374383	Q68D85	1	0.578246
ATP1B3	ATPase Na+/K+ transporting subunit beta3	483	P54709	1	0.570178
SLC3A2	solute carrier family 3 member 2	6520	P08195	1	0.643518
ACTN1	actinin alpha 1	87	P12814	1	0.712156
JAM3	junctional adhesion molecule 3	83700	Q9BX67	1	0.468754
CD276	CD276 molecule	80381	Q5ZPR3	1	0.428201
CADM1	cell adhesion molecule 1	23705	Q9BY67	1	0.497293
MIA3	MIA SH3 domain ER export factor 3	375056	5JRA6	1	-0.909785
HLA-C	major histocompatibility complex, class I, C	3107	P10321	1	-0.539395
HLA-A	major histocompatibility complex, class I, A	3105	P04439	1	-1.0196
LGALS3BP	galectin 3 binding protein	3959	Q08380	1	-0.991107
CLPTM1L	cleft palate transmembrane protein 1-like	81037	Q96KA5	2	-0.741051
MFAP3	microfibril associated protein 3	4238	P55082	1	-0.768297
TOR1AIP1	torsin 1A interacting protein 1	26092	Q5JTV8	2	-0.685934
RPN1	ribophorin 1	6184	P04843	1	-0.358063
TMEM259	transmembrane protein 259	91304	Q4ZIN3	2	-0.314032
STT3A	STT3 oligosaccharyltransferase complex catalytic subunit A	3703	P46977	2	-0.59739
CACHD1	cache domain containing 1	57685	Q5VU97	1	-0.580828
CNTN1	contactin 1	1272	Q12860	1	-0.711767
EMC1	ER membrane protein complex subunit 1	23065	Q8N766	1	-0.646965
MCAM	melanoma cell adhesion molecule	4162	P43121	1	-0.682648
F11R	F11 receptor	50848	Q9Y624	1	-0.478582
ITGA4	integrin subunit alpha 4	3676	P13612	1	-0.446824
EPHA4	EPH receptor A4	2043	P54764	1	-0.57585
EFNB1	ephrin B1	1947	P98172	1	-0.896389
EPCAM	epithelial cell adhesion molecule	4072	P16422	1	-0.78135
BRI3BP	BRI3 binding protein	140707	Q8WY22	2	-0.665538
CD46	CD46 molecule	4179	P15529	1	-0.848529
CAPNS1	calpain small subunit 1	826	P04632	1	-0.562122

Supplementary Information

Lack of GABARAP-type proteins is accompanied by altered Golgi morphology and surfaceome composition

Julia L. Sanwald [1,2 †], Jochen Dobner [1 †], Indra M. Simons [1,2], Gereon Poschmann [3], Kai Stühler [3,4], Alina Üffing [1,2], Silke Hoffmann [2], Dieter Willbold [1,2]

[1] Institut für Physikalische Biologie, Heinrich-Heine-Universität Düsseldorf, Universitätsstraße 1, 40225 Düsseldorf, Germany
[2] Institute of Biological Information Processing (IBI-7: Structural Biochemistry), Forschungszentrum Jülich, Leo-Brandt-Straße, 52428 Jülich, Germany
[3] Institute of Molecular Medicine I, Proteome Research, Heinrich-Heine-Universität Düsseldorf, Universitätsstraße 1, 40225 Düsseldorf, Germany; gereon.poschmann@uni-duesseldorf.de (G.P.); kai.stuehler@uni-duesseldorf.de (K.S.)
[4] Molecular Proteomics Laboratory, Biologisch-Medizinisches Forschungszentrum (BMFZ), Heinrich-Heine-Universität Düsseldorf, Universitätsstraße 1, 40225 Düsseldorf, Germany
† Authors contributed equally to this work

Supplementary Table S1 is related to Figure 3B

Supplementary Table S1 can be found on the enclosed compact disk or on the following website: https://www.mdpi.com/1422-0067/22/1/85/s1.

Supplementary Table S1. Mass-spectrometry data set.

3.3 Autophagy-Related Proteins GABARAP and LC3B Label Structures of Similar Size but Different Shape in Super-Resolution Imaging.

Authors	I. Abdollahzadeh, J. Hendriks, <u>J. L. Sanwald</u>, I. M. Simons, S. Hoffmann, O. H. Weiergräber, D. Willbold, and T. Gensch.
Journal	Molecules (2019), published on 13 May 2019
DOI	10.3390/molecules24091833
Impact Factor	3.267 (2019); 5-Year Impact Factor: 3.589 (2019)
Contribution to the manuscript	Support with cell culture experiments Cloning of peYFP-C1/LC3B Editing of the manuscript
Reprint Permission	This section contains a complete reprint of the publication published in Molecules (https://www.mdpi.com/journal/molecules). Copyright 2019 by the authors. Licensee MDPI, Basel, Switzerland. This article is an open access article distributed under the terms and conditions of the Creative Commons Attribution (CC BY) license (http://creativecommons.org/licenses/by/4.0/).

Autophagy-Related Proteins GABARAP and LC3B Label Structures of Similar Size but Different Shape in Super-Resolution Imaging

Iman Abdollahzadeh [1,2], Johnny Hendriks [1], Julia L. Sanwald [3], Indra M. Simons [3], Silke Hoffmann [2], Oliver H. Weiergräber [2,*], Dieter Willbold [2,3] and Thomas Gensch [1,*]

[1] Institute of Complex Systems 4 (ICS-4, Cellular Biophysics), Forschungszentrum Jülich GmbH, Wilhelm-Johnen-Straße, 52428 Jülich, Germany; i.abdollahzadeh@fz-juelich.de (I.A.); jhendriks@upcmail.nl (J.H.)

[2] Institute of Complex Systems 6 (ICS-6, Structural Biochemistry), Forschungszentrum Jülich GmbH, Wilhelm-Johnen-Straße, 52428 Jülich, Germany; si.hoffmann@fz-juelich.de (S.H.); d.willbold@fz-juelich.de (D.W.)

[3] Institut für Physikalische Biologie, Heinrich-Heine-Universität Düsseldorf, Universitätsstraße 1, 40225 Düsseldorf, Germany; julia.sanwald@uni-duesseldorf.de (J.L.S.); indra.simons@uni-duesseldorf.de (I.M.S.)

[*] Correspondence: o.h.weiergraeber@fz-juelich.de (O.H.W.); t.gensch@fz-juelich.de (T.G.); Tel.: +49-2461-612028 (O.H.W.); +49-2461-618068 (T.G.)

Abstract: Subcellular structures containing autophagy-related proteins of the Atg8 protein family have been investigated with conventional wide-field fluorescence and single molecule localisation microscopy. Fusion proteins of GABARAP and LC3B, respectively, with EYFP were overexpressed in HEK293 cells. While size distributions of structures labelled by the two proteins were found to be similar, shape distributions appeared quite disparate, with EYFP-GABARAP favouring circular structures and elliptical structures being dominant for EYFP-LC3B. The latter also featured a nearly doubled fraction of U-shape structures. The experimental results point towards highly differential localisation of the two proteins, which appear to label structures representing distinct stages or even specific channels of vesicular trafficking pathways. Our data also demonstrate that the application of super-resolution techniques expands the possibilities of fluorescence-based methods in autophagy studies and in some cases can rectify conclusions obtained from conventional fluorescence microscopy with diffraction-limited resolution.

Keywords: Atg8; autophagy; EYFP blinking; GABARAP; LC3B; shape distribution; single molecule localisation microscopy; SMLM; super-resolution

1. Introduction

Macroautophagy (hereafter autophagy) enables cells to replenish resources for energy metabolism and for anabolic reactions during periods of starvation, and to specifically dispose of large structures that are not amenable to proteasomal degradation. Correspondingly, autophagic cargo ranges from bulk cytosol to protein aggregates, damaged organelles, and even intracellular pathogens [1,2]. A hallmark of autophagy is the formation of double-membrane structures termed phagophores, which engulf cytoplasmic cargo and finally close to yield autophagosomes. The mature autophagosomes (several hundred nanometres in diameter) subsequently fuse with lysosomes, resulting in acidification and degradation of their contents by acid hydrolases. Genetic screening in yeast has led to the identification of more than 30 Atg genes, most of which are conserved in mammalian cells [3]. Among the corresponding

proteins, Atg8 homologs serve different functionalities in autophagosome biogenesis and cargo recruitment. While in yeast only a single Atg8 is expressed, in mammalian cells the family has expanded into a number of paralogs assigned to either the GABA type A receptor-associated protein (GABARAP) or the microtubule associated protein 1 light chain 3 (MAP1LC3, hereafter LC3) subfamily [4].

Numerous studies have shown that proteins of both subfamilies are crucial for mammalian autophagy, and that they exert individual as well as subfamily- and family-specific functions [5,6]. Many of these activities relate to covalent attachment of Atg8 proteins to membrane lipids via their C-termini, enabling them to attract other components to autophagic membranes. These interactions are usually mediated by short linear motifs termed LIRs (LC3 interacting regions) in the target proteins, which bind to conserved hydrophobic pockets on the Atg8 protein surface [7]. For instance, Atg8 family members are well-known to participate in the recruitment of cargo to the concave face of expanding phagophores, exhibiting different specificities for so-called cargo receptors or the cargo molecules themselves [8]. Moreover, data from knockdown experiments and interaction studies point to a mechanistic role of GABARAP-type proteins in both early and late stages of autophagosome formation, involving interactions with components of the autophagy-initiating ULK complex and of the lysosome fusion machinery, respectively [9–11]. Members of the LC3 subfamily, on the other hand, appear to mostly support expansion of phagophores [9], but the respective molecular interactions are poorly defined and may involve lipids rather than proteins. Indeed, similar to their yeast ortholog, mammalian Atg8 proteins have been implicated in the regulation of membrane curvature and in vesicle adhesion and (hemi)fusion [12,13]; the mechanisms underlying these activities and their biological relevance, however, are only beginning to be unravelled. It is worth noting that autophagosome biogenesis has recently been observed to occur even in the absence of Atg8 proteins, albeit with reduced efficiency [14]. While this finding indicates substantial redundancy in the autophagy pathway, supporting fall-back operation even after loss of important components, it does not compromise the utility of proteins belonging to the Atg8 family—to the extent they are expressed—as markers of autophagic structures. Indeed, they are among the first proteins to be found on emerging phagophores shortly after nucleation, and continue to be present on the outer (convex) face at least until autophagosome closure (possibly longer), while on the inner (concave) face they are delivered for degradation together with cargo material [15].

Given the limited size of autophagy-related membrane structures ($\approx$50 nm–1.5 μm), the spatial distribution of associated proteins can only imperfectly be resolved by conventional fluorescence microscopy. This method is subject to the diffraction limit of optical microscopy, which is represented by the Abbe criterion as $d_{x,y} = \lambda/2NA$, where $d_{x,y}$ is the lateral resolution of the microscope, λ is the wavelength of the light, and NA is the numerical aperture of the optics. Hence, for a conventional microscope with NA $\approx$ 1, the Abbe limit for green light ($\lambda \approx$ 500 nm) is roughly 250 nm. The resolution improvement of fluorescence microscopy achieved with the development of super-resolution techniques enables the precise distribution of proteins of interest to be investigated [16]. One of the new methods is single-molecule localisation microscopy (SMLM), which relies on the accurate localisation ($d_{x,y}$ on the order of 10–30 nm) of single fluorescent proteins based on the point spread function of their emitted photons, requiring fluorescence events to be recorded individually [17].

In the current study, we have used SMLM to investigate the spatial distribution of Atg8 proteins in mammalian cells, under autophagy-inducing conditions, using GABARAP and LC3B as representatives of the two subfamilies. At the same time, we aimed to evaluate the impact of the improved lateral resolution in SMLM, compared to conventional fluorescence microscopy, on the results of morphometric analysis. The geometry of fluorophore distribution is of key importance for the interpretation of results in a biological context because it directly relates to the type and stage of the underlying membranous structures. As a first step, we therefore focussed on the development of categories appropriate for systematic investigation of geometrical parameters (such as shape and size) of Atg8-positive structures. Statistical data analysis of SMLM images acquired from cells expressing enhanced yellow fluorescent protein (EYFP) fusion proteins revealed striking differences in shape distribution between GABARAP and LC3B. Moreover, the SMLM-based shape classification is at variance with the one obtained from

conventional wide-field fluorescence microscopy, in particular if small- to medium-sized structures are considered.

2. Results

The shape and size distributions of EYFP-GABARAP and EYFP-LC3B containing structures, respectively, were investigated in fixed HEK293 cells, which were subjected to a standard protocol for enrichment of autophagic structures (starvation and block of autophagosome-lysosome fusion by application of bafilomycin A1) for 2 h right before fixation. For each overexpression, ten cells were selected for detailed evaluation. It was taken care that the selected cells were typical by not preferring cells with certain features, e.g., high (or low) number of fluorescent structures.

First, a fluorescence wide-field image (with diffraction-limited resolution) of the cell of interest was recorded using low excitation power. Subsequently, a pre-acquisition illumination (with 20- to 75-fold higher excitation power) of 20 to 120 s was performed, in which most of the EYFP molecules were photo-converted to metastable, non-fluorescent dark states. SMLM pictures of the EYFP-containing structures with super-resolution (i.e., resolution better than the diffraction limit) were obtained from a wide-field image series keeping the high excitation power mode and utilizing the enduring blinking behaviour of EYFP [18–21]. Measurement of this image series (typically 4000 frames with 50 ms observation time each) was started at the end of the pre-acquisition illumination period, when the remaining EYFP molecules in the fluorescent state were well separated and the maximum intensity in single frames equalled that known for our setup from other single molecule studies on EYFP. A computer program developed in our lab (SNSMIL; Shot Noise based Single Molecule Identification and Localisation [22]) was used to calculate a super-resolution SMLM picture from the image series.

Representative examples of fixed HEK293 cells (starved and bafilomycin A1-treated) expressing EYFP-GABARAP and EYFP-LC3B, respectively, are given in Figure 1. The super-resolved SMLM images (Figure 1B,D) reveal a much higher total number of EYFP-GABARAP containing structures (75 times more) and EYFP-LC3B containing structures (89 and 78 times more for the left and right cell, respectively), compared to the corresponding wide-field images. A similar increase is found for all cells expressing one or the other fluorescent Atg8 construct. The number of EYFP-LC3B containing structures per cell (2898 ± 844) is significantly larger compared to the number of EYFP-GABARAP containing structures (1777 ± 356).

Notably, the subcellular distributions of the two overexpressed Atg8 proteins fused to EYFP are quite different: While EYFP-GABARAP is found mainly in the cytoplasm, EYFP-LC3B shows a higher concentration in the nucleus than in the cytoplasm. The larger labelled structures, however, are exclusively found in the cytoplasm for both proteins. These findings are in good agreement with data reported in literature [1–6]. Indeed, LC3B is thought to reside in the cell nucleus in an inactive acetylated form, which serves as a reservoir to be mobilised upon autophagy stimulation [23]; a different LC3 fraction associated with nuclear insulin receptor substrate 1 (IRS-1) has been suggested to attenuate autophagy in certain tumour cells [24]. GABARAP reservoirs, by contrast, have been identified on the ER and in the pericentriolar matrix [25], but not in the nucleus. Since the entire process of autophagosome biogenesis, maturation and degradation is known to take place outside the nucleus, we decided to focus on the cytoplasmic fraction of the fluorescently labelled objects for further analysis. Re-examination of the SMLM images under this premise yields much more similar values of 1550 ± 286 cytoplasmic EYFP-GABARAP containing structures (CS-EYFP-GABARAP) and 1813 ± 233 cytoplasmic EYFP-LC3B containing structures (CS-EYFP-LC3B), respectively (see Table 1). Thus, the before determined larger number of fluorescently labelled structures in EYFP-LC3B expressing cells, compared to EYFP-GABARAP expressing cells, is caused to a large extent by the nuclear protein fraction in the former case. One last remark to Figure 1C,D, i.e., wide-field and SMLM fluorescence images of EYFP-LC3B expressing cells, needs to be made. The fluorescence intensity contrast between nucleus and cytoplasm in Figure 1C is considerably larger when compared to the difference in numbers of fluorescent structures in those two areas of the cell. This can be explained by properties of the two detection methods, e.g., the larger

focal depth of fluorescence wide-field imaging vs. single molecule detection or possible losses of single molecule detection when two many molecules emit in the same image.
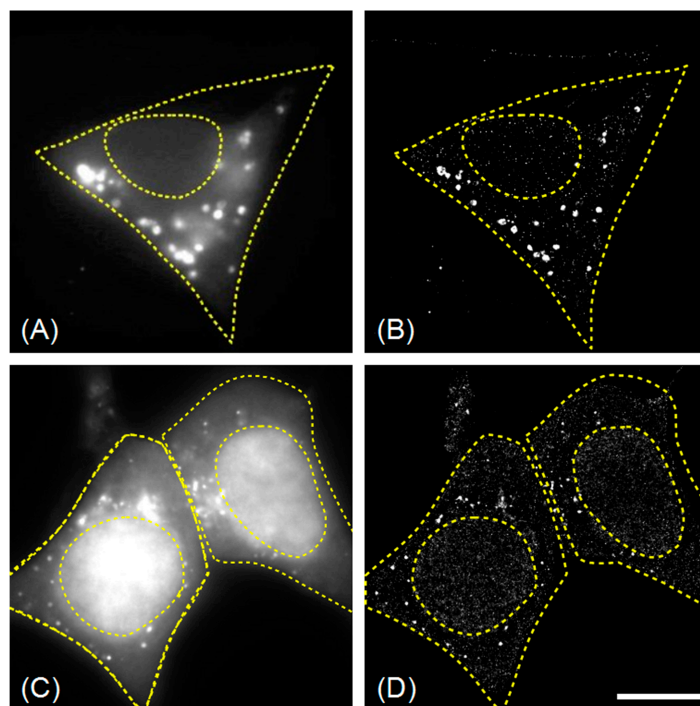
Figure 1. Wide-field (**A,C**) and SMLM (**B,D**) images of fixed HEK293 cells (starved and bafilomycin A1-treated) expressing EYFP-GABARAP (**A,B**), and EYFP-LC3B (**C,D**). In the wide-field fluorescence images only a few labelled structures are found (**A**: 22; **C**: 35 and 20 in the left and right cell, respectively), while in the corresponding super-resolution images (**B,D**) the numbers of EYFP-GABARAP containing structures (1640) and EYFP-LC3B containing structures (3100 and 1564) are almost two orders of magnitude larger. Scale bar (valid for **A–D**): 10 μm.

2.1. Size Distributions of Cytoplasmic EYFP-GABARAP and EYFP-LC3B Containing Structures

The size distributions of all CS-EYFP-GABARAP and CS-EYFP-LC3B are depicted in Figure 2. In general, they are very similar with mean and median slightly above and below 100 nm, respectively. The total number of CS-EYFP-LC3B per cell is only slightly larger than that of CS-EYFP-GABARAP. Notably, the vast majority of structures are smaller than the diffraction limit (ca. 200 nm for fluorescence imaging of EYFP).
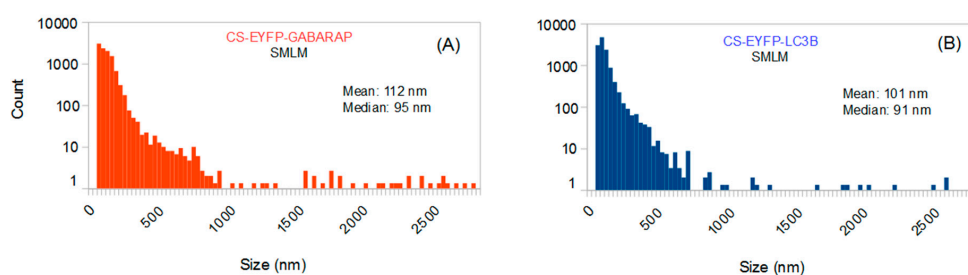
Figure 2. Size distributions (binning 32 nm) of all cytoplasmic, fluorescently labelled structures identified in the SMLM images of ten EYFP-GABARAP expressing (**A**) and ten EYFP-LC3B expressing HEK293 cells (**B**) under starvation and bafilomycin A1 treatment.

For a more appropriate and meaningful comparison of the shape distributions of CS-EYFP-GABARAP and CS-EYFP-LC3B (Section 2.2), we considered it useful to divide the fluorescently labelled structures into two groups with respect to their size, namely small and large structures, for two reasons. First, there might exist a bias towards identifying circular shapes for small fluorescently labelled structures because of limited resolution and pixel size (16 nm in SMLM images). Second, large and small fluorescently labelled structures might well have different origins or functions and, as a consequence, also different shape distributions. We applied two different splitting values, 100 nm and 300 nm. The portion of fluorescently labelled structures larger than 300 nm will contain basically all structures whose shapes could be also classified with conventional fluorescence microscopy techniques like laser-scanning confocal or wide-field fluorescence microscopy. On the other hand, 100 nm is the upper size limit for most common intracellular vesicles in endocytic and secretory pathways. Table 1 reveals that the value of 100 nm splits the CS-EYFP-GABARAP in almost equally large groups, while splitting at 300 nm sees only 2% of the CS-EYFP-GABARAP in the group of the large structures and 98% belong to the small structures. For CS-EYFP-LC3B we find almost the same behaviour with about 40% and 3% of the structures larger than 100 nm and 300 nm, respectively.

Application of single molecule fluorescence imaging techniques might lead to differences with respect to conventional fluorescence microscopy for two reasons: (1) the different resolution, affecting the apparent shapes of visible objects, and (2) the different detection probability for structures as a function of their size. For a meaningful comparison of the information provided by the two methods, we generated sets of CS-EYFP-GABARAP and CS-EYFP-LC3B identifiable on wide-field fluorescence images of the cells (see Table 1).

Table 1. Number of cytoplasmic structures containing EYFP-GABARAP and EYFP-LC3B identified in SMLM images. Counts are given for the entire size range considered (50 nm–2.8 µm) as well as for two sub-ranges (split alternatively at 100 nm or at 300 nm). For comparison, the numbers of cytoplasmic EYFP-GABARAP and EYFP-LC3B containing structures identified in the corresponding wide-field fluorescence images (named "conventional selection") are also given.

Overexpressed Protein	Size Category	Number of Structures	Fraction of Structures (%)
EYFP-GABARAP	50 nm–2.8 µm	15,501	100
	50 nm–100 nm	8009	51.66
	100 nm–2.8 µm	7492	48.33
	50 nm–300 nm	15,153	97.75
	300 nm–2.8 µm	348	2.25
	Conventional selection	348	
EYFP-LC3B	50 nm–2.8 µm	18,129	100
	50 nm–100 nm	11,579	63.87
	100 nm–2.8 µm	6550	36.13
	50 nm–300 nm	17,643	97.32
	300 nm–2.8 µm	486	2.68
	Conventional selection	486	

The size distributions of these "conventionally selected" CS-EYFP-GABARAP and CS-EYFP-LC3B are given in Figure 3. As expected, the results of SMLM-based size analysis differ from those obtained when all structures found in the SMLM images are considered (compare Figure 2A with Figures 3B and 2B with Figure 3D, respectively): No small structures (<300 nm) are found in the conventionally selected set, and mean and median are shifted towards higher values (between 455 and 533 nm). Interestingly, the size distributions of the conventionally selected CS-EYFP-GABARAP and CS-EYFP-LC3B, when determined in the conventional wide-field fluorescence images, were different from those using the respective super-resolution images (compare Figure 3A with Figures 3B and 3C with Figure 3D): There

is an increased number of structures smaller than 500 nm in the SMLM evaluation, although mean and median did not change dramatically.
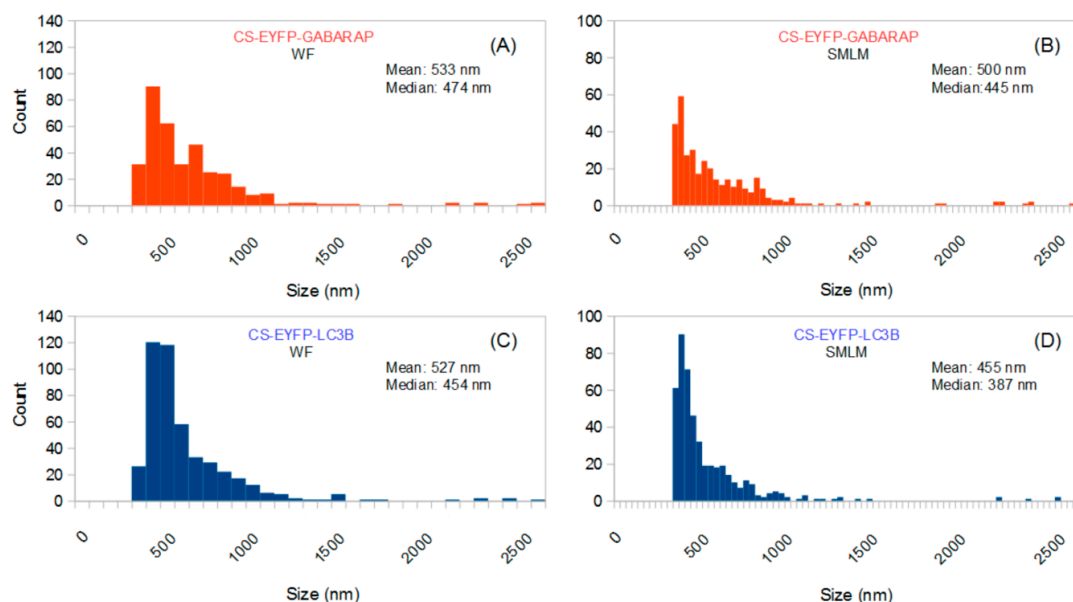
Figure 3. Size distributions of all conventionally selected fluorescently labelled structures (identified in wide-field images) of ten EYFP-GABARAP expressing (**A**,**B**) and ten EYFP-LC3B expressing fixed HEK293 cells (**C**,**D**) under starvation and bafilomycin A1 treatment, where size was determined in the wide-field fluorescence (**A**,**C**) and the SMLM images (**B**,**D**), respectively. Note the different binning used in **A/C** (80 nm) and **B/D** (32 nm), respectively, caused by the lower resolution in wide-field fluorescence compared to super-resolution microscopy.

2.2. Shape Classification

In the next step, we decided to group all fluorescently labelled cytoplasmic structures (within the size ranges defined above) according to their shapes. The shape classification used in this study has been limited to three geometrical categories, namely U-shape, circles and ellipses (abbreviated: u, c and e, respectively). This classification is based on the well-established mechanism of autophagosome formation (Figure 4G and [6,26,27]), where these three shape categories reflect all possible autophagic structures. In the beginning of autophagosome formation, a small double bilayer (i.e., a phagophore) grows around the cargo and may appear as a U-shape structure (when viewed from the side) or as a relatively small circular (when viewed along is longitudinal axis) or elliptical object (when viewed at intermediate angles) in the two-dimensional SMLM imaging mode. During the elongation phase, the phagophore geometry is approaching a half-moon or elliptical shape. Once the autophagosome is mature, its shape will be very similar to a sphere, i.e., a circle in our 2D-projection SMLM imaging mode, except for very large and asymmetrical cargo. In Figure 4, typical examples for the three categories of EYFP-GABARAP and EYFP-LC3B containing structures, respectively, from SMLM images of fixed HEK293 cells are depicted.
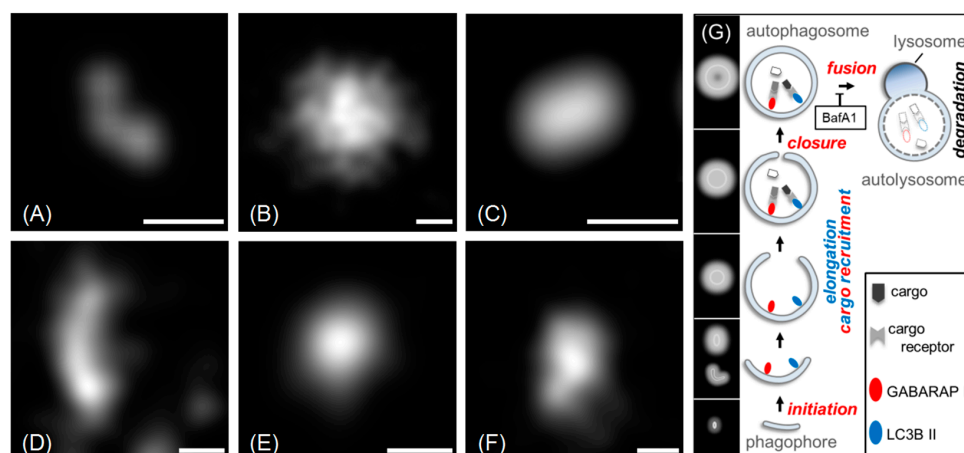
Figure 4. Examples for the three shape categories (**A**,**D**: U-shape; **B**,**E**: circle; **C**,**F**: ellipse). Structures in **A**, **B**, and **C** are from EYFP-GABARAP expressing cells, structures in **D**,**E**, and **F** are from EYFP-LC3B expressing cells (scale bars: 100 nm). In **G**, the presumed roles of GABARAP and LC3B at distinct stages of the autophagy pathway (phagophore initiation, elongation, closure, and fusion of the mature autophagosome with a lysosome to yield an autolysosome) are depicted. Steps that are assumed to require GABARAP and LC3B on the convex face of the isolation membrane (not drawn for clarity reasons) are highlighted in blue and red, respectively. As shown, GABARAP and LC3B can both link cargo materials to the concave face of the isolation membrane during selective autophagy in a cargo receptor-mediated manner. The various autophagic structures drawn as cross-sections are assigned to the respective 2D projections as anticipated in SMLM reconstructions (with a marked direction-dependence in the case of an early phagophore). Note, however, that SMLM cannot strictly distinguish between these membrane-bound autophagic organelles and other (vesicular or non-vesicular) structures populated by Atg8 proteins (see Discussion).

2.2.1. Shape Distributions of Cytoplasmic EYFP-GABARAP and EYFP-LC3B Containing Structures Selected in Super-Resolution Fluorescence Microscopy Images

Classification of all CS-EYFP-GABARAP in the SMLM images led to a unique shape distribution similarly found in all ten fixed HEK293 cells analysed (Figure 5). The number of CS-EYFP-GABARAP per cell varied between 350 and 2300 with a total number of 15501 in all ten cells (Table 1). To better compare the shape distributions of CS-EYFP-GABARAP, we considered it useful to divide the CS-EYFP-GABARAP in two groups, small and large structures, with two different splitting values, 100 and 300 nm, respectively (see paragraph 2.1). The shape distributions in the five size cases (all structures, and structures smaller/larger than 100 nm/300 nm) can be generally described as follows: The majority of CS-EYFP-GABARAP appear as circles, fewer structures as ellipses and a minor fraction shows U-shape (only for CS-EYFP-GABARAP larger than 300 nm, circles and ellipses have similar occurrence; Figure 5E). U-shape structures show the lowest percentage among CS-EYFP- GABARAP (only 9 to 23%) with the highest value in the group of the largest CS-EYFP-GABARAP (>300 nm).

Classification of all CS-EYFP-LC3B occurred in the same way as described above for CS-EYFP-GABARAP (applying again the separation values of 100 nm and 300 nm, respectively). The total number of CS-EYFP-LC3B in the ten analysed transfected HEK293 cells amounted to 18129 and was hence slightly (ca. 20%) larger compared to the experiments with CS-EYFP-GABARAP. Yet, comparison of the total number of labelled structures in an experiment based on overexpression of proteins is not useful, since a number of experimental parameters may vary in transient transfections (e.g., quality of DNA, efficiency of plasmid uptake, yield of chromophore maturation), preventing the reproducibility of absolute protein numbers. The shape distributions of structures labelled with Atg8-family proteins, on the other hand, will reflect specific properties and biological functions of GABARAP and LC3B, respectively, as long as expression levels are not too high.
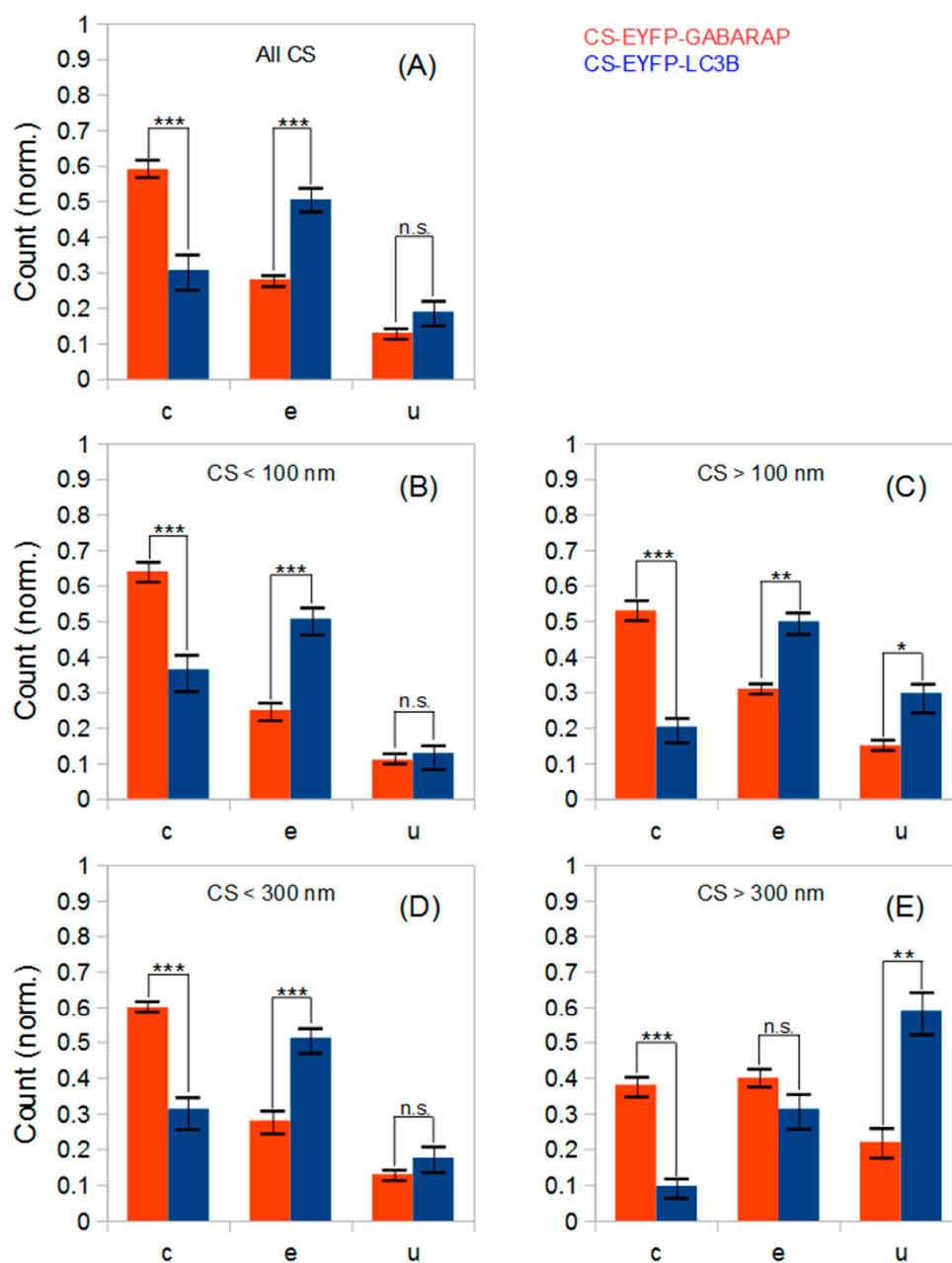
Figure 5. Shape analysis of all cytoplasmic fluorescent structures observed in SMLM images of ten HEK293 cells expressing either EYFP-GABARAP (red) or EYFP-LC3B (blue) under starvation and bafilomycin A1 treatment. (**A**) All CS-EYFP-GABARAP (15501) and CS-EYFP-LC3B (18129); (**B**) CS-EYFP-GABARAP (8009) and CS-EYFP-LC3B (11579) smaller than 100 nm; (**C**) CS-EYFP-GABARAP (7492) nd CS-EYFP-LC3B (6550) larger than 100 nm; (**D**) CS-EYFP-GABARAP (15153) and CS-EYFP-LC3B (17643) smaller than 300 nm; (**E**) CS-EYFP-GABARAP (348) and CS-EYFP-LC3B (486) larger than 300 nm. Error bars represent standard error of the mean. Statistical significance is represented as $P \leq 0.01$ (∗∗∗); $P \leq 0.05$ (∗∗), and $P \leq 0.1$ (∗) from two-tailed t-tests (n.s., not significant). c, e and u stands for circles, ellipses and U-shapes.

The five shape distributions of CS-EYFP-LC3B are plotted in Figure 5 next to the corresponding ones of CS-EYFP-GABARAP, and direct comparison immediately reveals that populations of structures

labelled by EYFP-LC3B and EYFP-GABARAP differ from one another. For all five categories of CS-EYFP-LC3B, ellipses constitute the major fraction (31–51%), while circles—the major fraction for CS-EYFP-GABARAP—were only the second most prevalent for total and the small-size groups of CS-EYFP-LC3B (ca. 30%) and even the minor fraction for the large-size groups of CS-EYFP-LC3B (10–20%). U-shape objects among the CS-EYFP-LC3B were found to be present in higher relative amounts (13–59%) compared to CS-EYFP-GABARAP, being the most abundant shape for CS-EYFP-LC3B larger than 300 nm.

The total number of analysed structures is high and the shape distributions for CS-EYFP-GABARAP and CS-EYFP-LC3B, respectively, appear visually different, especially for the large-size structures. The number of cells analysed (10 for each protein), however, is only moderate. Nevertheless, we performed two-tailed t-tests to survey whether the differences in the relative abundances of circles, ellipses and U-shapes are statistically significant. The results are given in numbers in Table 2, and most of them are also shown graphically in Figure 5.

Table 2. P-values from two-tailed t-tests to assess the statistical significance of differences in the shape distributions (c, circles; e, ellipses; u, U-shapes) of (i) CS-EYFP-GABARAP vs. CS-EYFP-LC3B (various size classes), (ii) different size classes of CS-EYFP-GABARAP, (iii) different size classes of CS-EYFP-LC3B, and (iv) CS-EYFP-GABARAP or CS-EYFP-LC3B structures classified in wide-field vs. SMLM. P-values are indicated by shading and typeface ($\leq$0.01, dark grey and bold face; $\leq$0.05, medium grey and bold face; $\leq$0.1, no shading and regular face) for ease of orientation.

	c	e	u
CS-EYFP-GABARAP vs. CS-EYFP-LC3B (50 nm–2.8 μm)	**0.0026**	**0.00050**	0.21
CS-EYFP-GABARAP vs. CS-EYFP-LC3B (< 100 nm)	**0.010**	**0.0053**	0.66
CS-EYFP-GABARAP vs. CS-EYFP-LC3B (> 100 nm)	**0.000026**	**0.019**	**0.10**
CS-EYFP-GABARAP vs. CS-EYFP-LC3B (< 300 nm)	**0.0024**	**0.00035**	0.29
CS-EYFP-GABARAP vs. CS-EYFP-LC3B (> 300 nm)	**0.000023**	0.49	**0.04**
CS-EYFP-GABARAP: CS < 100 nm vs. CS > 100 nm	0.29	0.54	0.20
CS-EYFP-GABARAP: CS < 300 nm vs. CS > 300 nm	**0.0042**	**0.02**	0.23
CS-EYFP-LC3B: CS < 100 nm vs. CS > 100 nm	**0.09**	0.71	**0.04**
CS-EYFP-LC3B: CS < 300 nm vs. CS > 300 nm	**0.03**	**0.08**	**0.02**
CS-EYFP-GABARAP: WF vs. SMLM	**0.000010**	0.50	**0.0018**
CS-EYFP-LC3B:WF vs. SMLM	**0.000010**	0.70	**0.01**

The five shape distributions of CS-EYFP-GABARAP are all statistically significantly different from the corresponding distributions of CS-EYFP-LC3B with at least one P-value smaller than 0.01 and a second one smaller than 0.05. The higher amount of U-shapes for larger cytoplasmic structures containing EYFP-LC3B compared to those containing EYFP-GABARAP is significant too–albeit at a weaker level. Thus, though the number of investigated cells is only moderately high (due to the time-consuming and elaborate size and shape analysis), the shape differences between the structures labelled by the two proteins are highly relevant.

2.2.2. Shape Distributions of Cytoplasmic EYFP-GABARAP and EYFP-LC3B Containing Structures Selected in Wide-Field Fluorescence Microscopy Images

Most fluorescence microscopy studies using Atg8-family proteins fused to fluorescent proteins until now have been carried out using fluorescence microscopy methods with diffraction-limited resolution. As pointed out in Section 2.1, we performed a "hybrid" analysis of our data set, where we carried out a conventional selection of CS-EYFP-GABARAP and CS-EYFP-LC3B and determined their size distribution via conventional as well as super-resolution imaging (Figure 3). As expected, the number of cytosolic fluorescently labelled structures detected by "conventional selection" was found largely reduced and is well below 50 per cell. The improved spatial resolution in the SMLM compared to wide-field fluorescence images, however, unearthed an even more serious observation. The result of

the shape classification for one and the same structure can be different in a wide-field fluorescence image and its corresponding SMLM image, respectively.

To demonstrate this issue, wide-field and super-resolution fluorescence images of five conventionally selected CS-EYFP-LC3B are depicted in Figure 6 (similar examples can be found for CS-EYFP-GABARAP). The structures in A and C are circles, while B, D and E fall into the ellipse category when judged by the wide-field fluorescence images. This simple picture changes when examining the fluorescent structures in the respective SMLM images. While the structures in A (circle) and B (ellipse) appears to have the same shape in super-resolution (compare with F and G, respectively), the other three structures have a different shape when imaged and analysed with higher spatial resolution. The ellipse in D turns into a U-shape in I, while the circle in C resolves into an inhomogeneous ellipse in H. The ellipse in E even appears to be clearly two objects in J, a U-shape and a circle.
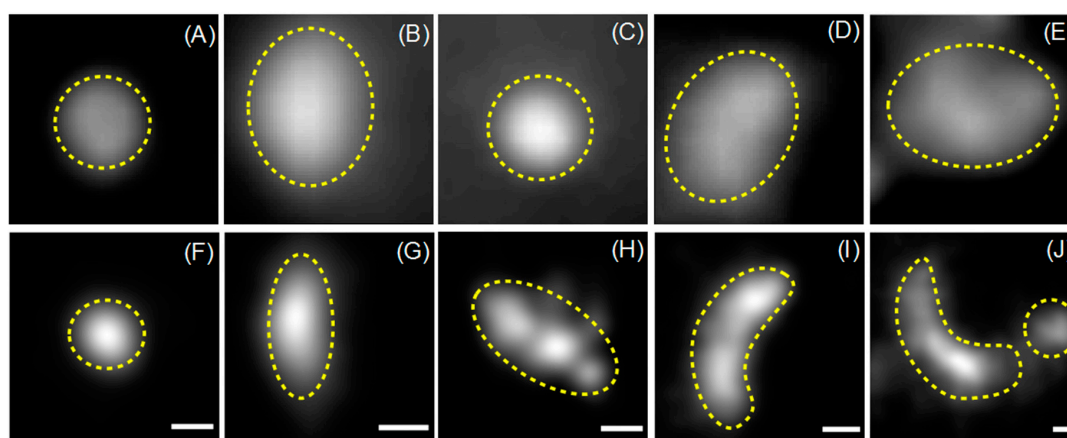
Figure 6. Wide-field fluorescence (**A**–**E**) and SMLM images (**F**–**J**) of five CS-EYFP-LC3B that were identified on the basis of the wide-field image (scale bars: 100 nm).

We analysed the shapes of the "conventionally selected" CS-EYFP-GABARAP and CS-EYFP-LC3B and made a striking observation. For both Atg8 proteins we find a significant difference of the shape distribution dependent on whether the shape was classified in wide-field or super-resolution fluorescence images (Figure 7). U-shapes are very rare (<3%) for CS-EYFP-GABARAP in wide-field fluorescence and grow to ca. 20% in super-resolution images. The relative amount of elliptical shape increases from below 15% to almost 40% on the expense of the circular shape, whose percentage drops from above 80% to 55% (Figure 7A). The change of shape distribution is even more pronounced for CS-EYFP-LC3B when comparing wide-field and super-resolution fluorescence imaging (Figure 7B). Here, circular shapes turn from the dominant fraction (75%) in wide-field fluorescence to the minor fraction (ca. 15%) in super-resolution fluorescence, while the percentage of elliptical shape more than doubles and U-shape grows from less than 5% to almost 40%. For both proteins, the relative abundances for circles and U-shapes are statistically highly significantly different as can be seen in Figure 7 and Table 2.

One more relevant observation of more general nature has to be stated, namely that the shape distributions of the structures containing the two Atg8 proteins appear very similar upon examination in conventional fluorescence microscopy with diffraction-limited resolution (none of the three shape categories has a statistically different relative abundance, see Table 2), but are rather different when shape is judged in super-resolution SMLM fluorescence microscopy. A direct comparison is depicted in Figure 7, since for both proteins the group of cytoplasmic fluorescent structures identified in wide-field images is identical to the group of cytoplasmic fluorescent structures larger than 300 nm identified in SMLM images (fractions of both circles and U-shapes are significantly different). Our data

point towards involvement of GABARAP and LC3B in different stages of autophagosome biogenesis or participation in further, non-autophagy related processes. But this difference would have been overlooked when using conventional fluorescence microscopy methods.

Figure 7. Shape distributions of fluorescently labelled cytoplasmic structures identified in the wide-field images of ten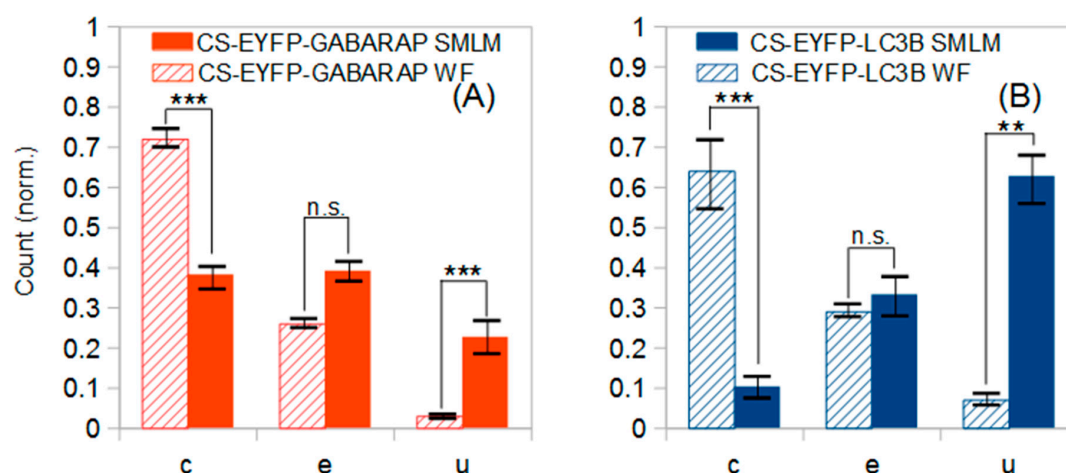 EYFP-GABARAP expressing and ten EYFP-LC3B expressing HEK293 cells, respectively, under starvation and bafilomycin A1 treatment. (**A**) Conventionally selected CS-EYFP-GABARAP (348) classified in wide-field fluorescence (hatched bars) and the same structures classified in the respective SMLM (full bars) images; (**B**) Conventionally selected CS-EYFP-LC3B (486) classified in wide-field fluorescence (hatched bars) and the same structures classified in the respective SMLM (full bars) images. Error bars represent standard error of the mean. Statistical significance is represented as $P \leq 0.01$ (∗∗∗); $P \leq 0.05$ (∗∗), and $P \leq 0.1$ (∗) from two-tailed t-tests (n.s., not significant). c, e and u stands for circles, ellipses and U-shapes.

3. Discussion

The introduction of optical microscopes has marked a revolution in the biological sciences since it enabled the cellular structure of organisms to be directly viewed for the first time [28]. After several centuries, and notwithstanding numerous technical improvements, the basic principle of using lenses to generate magnified views of samples is still widely utilised and continues to provide valuable insight into biological matter. An important complement has been the development of fluorescent tags, which allowed structures of interest to be specifically labelled in both fixed and live cells and which integrated nicely with existing microscopic technology.

It therefore comes as no surprise that fluorescence-enhanced light microscopy has been a major visualisation tool in autophagy research [29]. Autophagic organelles are complex membrane structures undergoing shape transformations during their life cycle, and both morphogenesis and functionality of these membranes are thought to be controlled by associated proteins. Hence, specific microscopic detection of autophagy-related proteins may not only provide hints at their biological functions but can also help to visualise the underlying organelle as a whole, provided that the marker is indeed distributed throughout the structure of interest. Atg8 family proteins are thought to largely meet this requirement; while in-vitro experiments revealed a certain preference for curved membranes [12], enrichment at the edges of expanding phagophores, e.g., has not been demonstrated thus far. Over almost two decades, Atg8 imaging has contributed to a huge body of literature, the vast majority of which, however, has been compromised by the diffraction limit of conventional microscopy. Super-resolution techniques, which basically extract highly precise positional information from microscopic images which per se are diffraction-limited, help to alleviate this shortcoming and are starting to contribute new insight into the autophagy process.

In the current study, we have used SMLM to revisit several intriguing questions in the field: (1) the distribution of sizes and shapes of structures labelled by Atg8 family proteins, resulting from a non-synchronous evolution of numerous individual objects, and (2) the differential localisation of GABARAP and LC3B (representing the two Atg8 subfamilies), which is closely related to their functions on a molecular level.

Our data demonstrate that application of SMLM has the potential to provide superior results in comparison with conventional wide-field microscopy, in terms of both completeness of observations (Figures 1 and 2) and wealth of associated information (Figures 5 and 6). These criteria bear obvious relation with the nominal spatial resolution of the respective images. Observational completeness can be defined as the fraction of the items of interest that can be detected using the method in question. In our hands, SMLM captures about 50 times the number of EYFP-labelled structures found via wide-field microscopy; comprehensive analysis of the size distributions revealed this difference to be mainly due to a vast number of smaller structures (those with diameters < 300 nm) going unnoticed on the wide-field images (Table 1, Figure 3). This is a huge limitation given that a significant portion of autophagy-related structures should fall into this size range, including early isolation membranes and even smaller-sized mature autophagosomes. The advantages of super-resolution microscopy in terms of information content are supported by the observation that even a set of larger structures, which are readily visible on both wide-field and SMLM images, yields quite different data depending on the method used for analysis. In addition to a distortion of size distributions at lower resolution (Figure 3), we find large effects on the assignment of shapes (Figures 6 and 7). The latter illustrates what we consider the most significant corollary of the current study: While structures with dimensions on the order of (or slightly above) the diffraction limit may be readily detectable by conventional microscopy, the information extracted from such images should be treated with caution because sizes and shapes may be biased. Autophagy constitutes an instructive example of a process in which the morphology of organelles directly reflects their functional state, and misinterpretation of, e.g., a U-shape structure (commonly assigned to an early phagophore viewed from the side) as an elliptical object (usually assigned to a late phagophore or autophagosome) may affect biological conclusions drawn from experiments.

Besides these methodological aspects, our SMLM analysis using EYFP fusion proteins revealed important differences between the two Atg8 orthologs investigated. In particular, the shape distributions of the respective labelled structures are quite disparate, indicating differential (but possibly overlapping) localisation: GABARAP and LC3B may appear on phagophores at different stages of their evolution, but could also support distinct autophagic channels or participate in non-autophagy-related pathways. These considerations are well-supported by current evidence. For instance, experiments in which entire Atg8 subfamilies have been knocked down or knocked out in cultured cells suggested that LC3 proteins were mostly required for phagophore expansion, whereas GABARAP proteins acted at a later stage, such as maturation, closure, or autophagosome-lysosome fusion [9,14]. Such a division of tasks would seem consistent with the preponderance of circular and elliptical shapes in our SMLM images after overexpression of GABARAP and LC3B, respectively. It is interesting to note that this correlation can even be replicated in vitro: Vesicles coated with GABARAP tend to fuse into approximately spherical structures whereas LC3B coupling yields more elongated shapes [13]. Regarding their functions in cargo recruitment, members of the Atg8 family are well-established to differ in their affinities towards target structures, often with marked subfamily specificity [7], supporting the idea that the prevalence of different Atg8 orthologs on individual phagophores or autophagosomes may be modulated by the type of substrate. It is also worth noting that enrichment of Atg8 proteins in punctate objects does not necessarily signify phagophores or autophagosomes. The centrosomal pool of GABARAP, e.g., which is thought to play a critical role in autophagosome biogenesis, presumably consists of non-lipidated protein [25], and indeed, neither the centrosomal matrix nor the centriolar satellites shuttling GABARAP along microtubules contain membrane vesicles. Similarly, nuclear association of LC3 with IRS-1 leads to the formation of layered clusters not involving biological membranes [24].

Mammalian Atg8 proteins have also been found to associate with IRGM (immunity-related GTPase M) and the Q_a-SNARE syntaxin-17 (Stx17) in large protein complexes (so-called autophagosome recognition particles, ARPs) which deliver Stx17 to mature autophagosomes, thus enabling fusion with lysosomes. [30]. Again, these structures are assumed to be non-membranous, with IRGM shielding the transmembrane domain of Stx17. Finally, both GABARAP and LC3B participate in cellular processes that are unrelated to autophagy but do involve vesicular structures. Prominent examples include trafficking of vesicles carrying transmembrane receptors towards the plasma membrane, which is typically mediated by GABARAP subfamily proteins [5], and LC3-associated phagocytosis, which is usually engaged if membrane-wrapped extrinsic cargo is to be degraded [31]. A more general function in cellular signalling has emerged for GABARAP-type proteins, which are able to recruit a ubiquitin ligase targeting the RAC1-specific guanine nucleotide exchange factor TIAM1 (T-lymphoma invasion and metastasis-inducing protein 1). This process has been suggested to occur on nonautophagic membranes, although mechanistic connections to autophagy regulation may exist [32]. Based on these considerations, it seems very likely that a certain fraction of the objects labelled by EYFP-fused Atg8 proteins actually constitute non-membranous autophagic or membranous non-autophagic structures, and thus do not represent phagophores or autophagosomes. The abundance of fluorescently labelled particles in the sub-100 nm range, for instance, may be explained to a large part by non-vesicular structures like centriolar satellites or ARPs. While protein complexes of this size are clearly resolved in our SMLM images, they only contribute to a diffuse background in conventional diffraction-limited microscopy, preventing their differentiation from the cytosolic Atg8 pool. Despite the significant gain in spatial information provided by super-resolution fluorescence imaging, unambiguous assignment of structures to specific pathways or even intermediates thereof still requires secondary labelling for a plethora of markers, and will be the subject of future work.

In order to assess the localisation of GABARAP and LC3B, we have resorted to transient overexpression of fluorescent fusion proteins, which is part of the standard toolkit in cell biology research. In comparison to immunolabelling of endogenous protein, this strategy ensures decent signal strength and excellent specificity of detection, but comes with the downside of potentially non-specific localisation of overexpressed protein. The latter might accumulate at sites which are not significantly populated in parent cells, and even at physiological locations pathways may suffer from an overload of protein as well as the presence of the fusion partner. The strength of nuclear staining we observed with EYFP-LC3B even after autophagy stimulation may indicate such an effect of overexpression since it exceeds what has been described previously for endogenous LC3 detected by immunofluorescence. On the other hand, the numbers of cytoplasmic structures populated with EYFP-GABARAP and EYFP-LC3B are quite similar despite the fact that total cytoplasmic fluorescence (representing the abundance of the fusion protein) differs by a factor of five; this suggests that the overall activity of the respective pathways is at most moderately affected by Atg8 protein overexpression, thus supporting the validity of the approach. Development of cell lines stably expressing fluorescent fusion proteins under the control of endogenous promoters will be instrumental to avoid artefacts caused by protein overload while retaining the specificity of detection in both conventional and super-resolution imaging modes.

4. Materials and Methods

4.1. Eukaryotic Plasmids

The gene for GABARAP was subcloned from a GST-GABARAP-fusion plasmid (Addgene plasmid #73948 [33], Addgene, Watertown, MA, USA) by PCR amplification into the XhoI and BamHI sites of peYFP-C1 (Clontech, Mountain View, CA, USA), yielding peYFP-C1/GABARAP [34]. The fluorescent variant of LC3B was generated analogously, starting from a GST-fusion plasmid (Addgene plasmid #73949 [33], Addgene) and yielding peYFP-C1/LC3B.

4.2. Cell Culture and Transfection

Human embryonic kidney 293 (HEK293 [35]; Leibniz-Institute DSMZ–German Collection of Microorganisms and Cell Cultures, Braunschweig, Germany) cells were cultivated at 37 °C in a humidified incubator at 5% CO_2 in Dulbecco's Modified Eagle's Medium (DMEM, Cat. No. D5796, Sigma-Aldrich, Munich, Germany) supplemented with 1% penicillin/streptomycin (P/S, Sigma-Aldrich) and 10% Fetal Calf Serum (FCS, Sigma-Aldrich). For transient transfection with EYFP-GABARAP or EYFP-LC3B constructs, 6×10^5 HEK293 cells were seeded into a 6-well culture plate (Cat. No. 10062-892, VWR, Randor, PA, USA) containing DMEM with 10% FCS and 1% P/S. On the next day, transfection with 1.2 μg total DNA was performed using Polyfect (Cat. No. 301107, QIAGEN, Hilden, Germany) according to the manufacturer's instructions. The following day, $4–5 \times 10^4$ of the transfected cells were seeded into a fibronectin (Sigma-Aldrich) coated μ-dish (Cat. No. 81158, ibidi, Martinsried, Germany) containing DMEM with 10% FCS and 1% P/S and were cultivated for another day in the incubator.

4.3. Starvation

Transfected cells were starved with Hank's Balanced Salt Solution (HBSS, Cat. No. 14025050, Thermo Fisher Scientific, Waltham, MA, USA). For accumulation of autophagic structures in cells, 100 nM bafilomycin A1 (CAS No. 0088899552, Merck KGaA, Darmstadt, Germany) was used as an autophagosome-lysosome fusion blocking agent along with HBSS. Incubation took place at 37 °C and 5% CO_2 for 2 h.

4.4. Fixation

Since autophagic structures are supposed to be connected to cytoskeleton elements, a fixation procedure was used that minimises alterations to cytoskeleton components [36]. The cells were incubated in cytoskeleton buffer (phosphate-buffered saline (PBS, 137 mM NaCl, 2.7 mM KCl, 1.8 mM KH_2PO_4, 10 mM Na_2HPO_4, pH 7.4) containing 4 mM EGTA) for 5 min at 37 °C. Subsequently, cytoskeleton buffer was replaced with fixation solution (4% (*w/v*) paraformaldehyde in cytoskeleton buffer). Fixation took place at room temperature for 10–15 min. After that, cells were rinsed three times with 1 M glycine in PBS and two times with PBS.

4.5. Imaging

For visualisation of fluorescent structures with spatial resolution of the order of 20–30 nm, a home-built SMLM microscope was used [21,37,38]. For SMLM imaging of EYFP-GABARAP and EYFP-LC3B, cells were kept in PBS (pH 7.4). Cells, stored at 4 °C after fixation, were accommodated to room temperature for about 30 min before imaging, because otherwise the recorded image showed lateral and focal drift of the order of several hundreds of nanometres. EYFP was excited with the 514 nm line of an Ar+ laser (Innova 70C, Coherent, Santa Clara, CA, USA). In single-color SMLM experiments with either EYFP-GABARAP or EYFP-LC3B containing structures, the fluorescent protein was first bleached for 10–60 s with 75% laser power until single fluorescent EYFP molecules could be observed in the field of view. The acquired number of single molecule images amounted to 4000–8000. The camera exposure time was set to 50 ms. Image analysis and super-resolution reconstruction were performed with the SNSMIL software, which has been described elsewhere [22]. In this study, the SNSMIL quality parameter was set to 1 to ensure maximum single molecule identification efficiency. The uncertainties of x- and y-position of single EYFP-GABARAP and EYFP-LC3B molecules in the image plane were determined as 38 nm and 27 nm, respectively. With such experimental conditions, the practical resolution of structures in the SMLM images is well below 50 nm.

4.6. Shape and Size Analysis

Evaluation of shape and size of EYFP-GABARAP and EYFP-LC3B containing cytoplasmic structures was performed with the use of ImageJ [39] in a semi-automated approach. The reconstructed

super-resolved image was first converted to a binary image containing only values of 0 or 1. A lower size cut-off must be applied in order to discard very small structures originating from isolated EYFP emitters not linked to EYFP-GABARAP or EYFP-LC3B containing structures, autofluorescence, or noise. We chose 50 nm, well above the positional uncertainty for single molecule emitters in our setup. In the case of asymmetric objects, the longest dimension of the structure had to fall in this size range. Shape classification of CS-EYFP-GABARAP and CS-EYFP-LC3B was performed by visual inspection by the experimenter based on three different geometrical patterns, named circles (c), ellipses (e), and U-shapes (u; see paragraph 2.2 and Figure 4; compare also [40]). The statistical significance of differences in relative abundances of shapes was assessed with the two-tailed t-test function of LibreOffice Calc (Version 5.2; The Document Foundation, Berlin, Germany).

4.7. Selection of Cytoplasmic EYFP-GABARAP and EYFP-LC3B Containing Structures

In order to identify the part of cytoplasmic EYFP-GABARAP and EYFP-LC3B containing structures, a contour around the nucleus was drawn in the transmission (bright field) image of the cell. This contour was transferred to the corresponding SMLM image and the structures within the contour were registered as nucleus-related structures. The remainder of the detected fluorescent structures in the super-resolution image was considered cytoplasmic (yielding the subsets CS-EYFP-GABARAP and CS-EYFP-LC3B) and further analysed.

Author Contributions: Conceptualisation, T.G., S.H. and O.H.W.; methodology, T.G. and J.H.; software, T.G. and J.H.; validation, T.G.; formal analysis, I.A. and T.G.; investigation, I.A., T.G., S.H. and O.H.W.; resources, T.G., S.H., J.L.S., I.M.S.; data curation, I.A., T.G., S.H. and O.H.W.; writing—original draft preparation, I.A., T.G., O.H.W.; writing—review and editing, I.A.,T.G., J.H., S.H., J.L.S., I.M.S., O.H.W. and D.W.; visualisation, I.A., T.G., S.H.; supervision, T.G., S.H. and O.H.W.; project administration, T.G., S.H., O.H.W and D.W.; funding acquisition, T.G., O.H.W. and D.W.

Conflicts of Interest: The authors declare no conflict of interest. The funders had no role in the design of the study; in the collection, analyses, or interpretation of data; in the writing of the manuscript, or in the decision to publish the results.

References

1. He, C.; Klionsky, D.J. Regulation mechanisms and signaling pathways of autophagy. *Annu. Rev. Genet.* **2009**, *43*, 67–93. [CrossRef] [PubMed]

2. Ravikumar, B.; Sarkar, S.; Davies, J.E.; Futter, M.; Garcia-Arencibia, M.; Green-Thompson, Z.W.; Jimenez-Sanchez, M.; Korolchuk, V.I.; Lichtenberg, M.; Luo, S.; et al. Regulation of mammalian autophagy in physiology and pathophysiology. *Physiol. Rev.* **2010**, *90*, 1383–1435. [CrossRef] [PubMed]

3. Nakatogawa, H.; Suzuki, K.; Kamada, Y.; Ohsumi, Y. Dynamics and diversity in autophagy mechanisms: Lessons from yeast. *Nat. Rev. Mol. Cell Biol.* **2009**, *10*, 458–467. [CrossRef] [PubMed]

4. Weiergräber, O.H.; Mohrlüder, J.; Willbold, D. Atg8 family proteins—Autophagy and beyond. In *Autophagy—A Double-Edged Sword–Cell Survival or Death?* Bailly, Y., Ed.; InTech: Rijeka, Croatia, 2013; pp. 13–45. ISBN 978-953-51-1062-0.

5. Schaaf, M.B.; Keulers, T.G.; Vooijs, M.A.; Rouschop, K.M. LC3/GABARAP family proteins: Autophagy-(un)related functions. *FASEB J.* **2016**, *30*, 3961–3978. [CrossRef]

6. Abdollahzadeh, I.; Schwarten, M.; Gensch, T.; Willbold, D.; Weiergräber, O.H. The Atg8 family of proteins–modulating shape and functionality of autophagic membranes. *Front. Genet.* **2017**, *8*, 109. [CrossRef]

7. Birgisdottir, Å.B.; Lamark, T.; Johansen, T. The LIR motif-crucial for selective autophagy. *J. Cell Sci.* **2013**, *126*, 3237–3247. [CrossRef]

8. Zaffagnini, G.; Martens, S. Mechanisms of selective autophagy. *J. Mol. Biol.* **2016**, *428*, 1714–1724. [CrossRef]

9. Weidberg, H.; Shvets, E.; Shpilka, T.; Shimron, F.; Shinder, V.; Elazar, Z. LC3 and GATE-16/GABARAP subfamilies are both essential yet act differently in autophagosome biogenesis. *EMBO J.* **2010**, *29*, 1792–1802. [CrossRef]

10. Alemu, E.A.; Lamark, T.; Torgersen, K.M.; Birgisdottir, A.B.; Larsen, K.B.; Jain, A.; Olsvik, H.; Øvervatn, A.; Kirkin, V.; Johansen, T. ATG8 family proteins act as scaffolds for assembly of the ULK complex: Sequence requirements for LC3-interacting region (LIR) motifs. *J. Biol. Chem.* **2012**, *287*, 39275–39290. [CrossRef]

11. Kriegenburg, F.; Ungermann, C.; Reggiori, F. Coordination of autophagosome-lysosome fusion by Atg8 family members. *Curr. Biol.* **2018**, *28*, R512–R518. [CrossRef] [PubMed]

12. Knorr, R.L.; Nakatogawa, H.; Ohsumi, Y.; Lipowsky, R.; Baumgart, T.; Dimova, R. Membrane morphology is actively transformed by covalent binding of the protein Atg8 to PE-lipids. *PLoS ONE* **2014**, *9*, e115357. [CrossRef] [PubMed]

13. Landajuela, A.; Hervás, J.H.; Antón, Z.; Montes, L.R.; Gil, D.; Valle, M.; Rodriguez, J.F.; Goñi, F.M.; Alonso, A. Lipid geometry and bilayer curvature modulate LC3/GABARAP-mediated model autophagosomal elongation. *Biophys. J.* **2016**, *110*, 411–422. [CrossRef]

14. Nguyen, T.N.; Padman, B.S.; Usher, J.; Oorschot, V.; Ramm, G.; Lazarou, M. Atg8 family LC3/GABARAP proteins are crucial for autophagosome-lysosome fusion but not autophagosome formation during PINK1/Parkin mitophagy and starvation. *J. Cell Biol.* **2016**, *215*, 857–874. [CrossRef]

15. Yoshii, S.R.; Mizushima, N. Monitoring and measuring autophagy. *Int. J. Mol. Sci.* **2017**, *18*, 1865. [CrossRef]

16. Huang, B.; Bates, M.; Zhuang, X. Super-resolution fluorescence microscopy. *Annu. Rev. Biochem.* **2009**, *78*, 993–1016. [CrossRef] [PubMed]

17. Sauer, M.; Heilemann, M. Single-molecule localization microscopy in eukaryotes. *Chem. Rev.* **2017**, *117*, 7478–7509. [CrossRef]

18. Dickson, R.M.; Cubitt, A.B.; Tsien, R.Y.; Moerner, W.E. On/off blinking and switching behaviour of single molecules of green fluorescent protein. *Nature* **1997**, *388*, 355–358. [CrossRef] [PubMed]

19. Biteen, J.S.; Thompson, M.A.; Tselentis, N.K.; Bowman, G.R.; Shapiro, L.; Moerner, W.E. Super-resolution imaging in live Caulobacter crescentus cells using photoswitchable EYFP. *Nat. Methods* **2008**, *5*, 947–949. [CrossRef]

20. Lee, S.F.; Thompson, M.A.; Schwartz, M.A.; Shapiro, L.; Moerner, W.E. Super-Resolution Imaging of the Nucleoid-Associated Protein HU in Caulobacter crescentus. *Biophys. J.* **2011**, *100*, L31–L33. [CrossRef] [PubMed]

21. Stölting, G.; Campos de Oliveira, R.; Guzman, R.E.; Miranda-Laferte, E.; Conrad, R.; Jordan, N.; Schmidt, S.; Hendriks, J.; Gensch, T.; Hidalgo, P. Direct Interaction of CaVβ with Actin Up-regulates L-type Calcium Currents in HL-1 Cardiomyocytes. *J. Biol. Chem.* **2015**, *290*, 4561–4572. [CrossRef]

22. Tang, Y.; Dai, L.; Zhang, X.; Li, J.; Hendriks, J.; Fan, X.; Gruteser, N.; Meisenberg, A.; Baumann, A.; Katranidis, A.; et al. SNSMIL, a real-time single molecule identification and localization algorithm for super-resolution fluorescence microscopy. *Sci. Rep.* **2015**, *5*, 11073. [CrossRef]

23. Huang, R.; Xu, Y.; Wan, W.; Shou, X.; Qian, J.; You, Z.; Liu, B.; Chang, C.; Zhou, T.; Lippincott-Schwartz, J.; Liu, W. Deacetylation of nuclear LC3 drives autophagy initiation under starvation. *Mol. Cell* **2015**, *57*, 456–466. [CrossRef]

24. Lassak, A.; Dean, M.; Wyczechowska, D.; Wilk, A.; Marrero, L.; Trillo-Tinoco, J.; Boulares, A.H.; Sarkaria, J.N.; Del Valle, L.; Peruzzi, F.; Ochoa, A.; Reiss, K. Molecular and Structural Traits of Insulin Receptor Substrate 1/LC3 Nuclear Structures and Their Role in Autophagy Control and Tumor Cell Survival. *Mol. Cell Biol.* **2018**, *38*, e00608-17. [CrossRef] [PubMed]

25. Joachim, J.; Jefferies, H.B.; Razi, M.; Frith, D.; Snijders, A.P.; Chakravarty, P.; Judith, D.; Tooze, S.A. Activation of ULK Kinase and Autophagy by GABARAP Trafficking from the Centrosome Is Regulated by WAC and GM130. *Mol. Cell* **2015**, *60*, 899–913. [CrossRef]

26. Shibutani, S.T.; Yoshimori, T. A current perspective of autophagosome biogenesis. *Cell Res.* **2014**, *24*, 58–68. [CrossRef]

27. Carlsson, S.R.; Simonsen, A. Membrane dynamics in autophagosome biogenesis. *J. Cell Sci.* **2015**, *128*, 193–205. [CrossRef] [PubMed]

28. Wollman, A.J.; Nudd, R.; Hedlund, E.G.; Leake, M.C. From Animaculum to single molecules: 300 years of the light microscope. *Open Biol.* **2015**, *5*, 150019. [CrossRef] [PubMed]

29. Wang, Y.; Li, Y.; Wei, F.; Duan, Y. Optical Imaging Paves the Way for Autophagy Research. *Trends Biotechnol.* **2017**, *35*, 1181–1193. [CrossRef] [PubMed]

30. Kumar, S.; Jain, A.; Farzam, F.; Jia, J.; Gu, Y.; Choi, S.W.; Mudd, M.H.; Claude-Taupin, A.; Wester, M.J.; Lidke, K.A.; Rusten, T.E.; Deretic, V. Mechanism of Stx17 recruitment to autophagosomes via IRGM and mammalian Atg8 proteins. *J. Cell Biol.* **2018**, *217*, 997–1013. [CrossRef]

31. Fazeli, G.; Wehman, A.M. Safely removing cell debris with LC3-associated phagocytosis. *Biol. Cell* **2017**, *109*, 355–363. [CrossRef] [PubMed]

32. Genau, H.M.; Huber, J.; Baschieri, F.; Akutsu, M.; Dötsch, V.; Farhan, H.; Rogov, V.; Behrends, C. CUL3-KBTBD6/KBTBD7 ubiquitin ligase cooperates with GABARAP proteins to spatially restrict TIAM1-RAC1 signaling. *Mol. Cell* **2015**, *57*, 995–1010. [CrossRef] [PubMed]

33. Ma, P.; Schwarten, M.; Schneider, L.; Boeske, A.; Henke, N.; Lisak, D.; Weber, S.; Mohrlüder, J.; Stoldt, M.; Strodel, B.; et al. Interaction of Bcl-2 with the autophagy-related $GABA_A$ receptor-associated protein (GABARAP): Biophysical characterization and functional implications. *J. Biol. Chem.* **2013**, *288*, 37204–37215. [CrossRef] [PubMed]

34. Simons, I.M.; Mohrküder, J.; Feederle, R.; Kremmer, E.; Zobel, T.; Dobner, J.; Bleffert, N.; Hoffmann, Si.; Willbold, D. The highly GABARAP specific rat momoclonal antibody 8H5 visualizes GABARAP in immunofluorescence imaging at endogeneous levels. *Sci. Rep.* **2019**, *9*, 526. [CrossRef]

35. Graham, F.L.; Smiley, J.; Russell, W.C.; Nairn, R. Characteristics of a human cell line transformed by DNA from human adenovirus type 5. *J. Gen. Virol.* **1977**, *36*, 59–74. [CrossRef] [PubMed]

36. Allen, J.R.; Ross, S.T.; Davidson, M.W. Sample preparation for single molecule localization microscopy. *Phys. Chem. Chem. Phys.* **2013**, *15*, 18771–18783. [CrossRef]

37. Baumgart, M.; Huber, I.; Abdollahzadeh, I.; Gensch, T.; Frunzke, J. Heterologous expression of the Halothiobacillus neapolitanus carboxysomal gene cluster in Corynebacterium glutamicum. *J. Biotechnol.* **2017**, *258*, 126–135. [CrossRef] [PubMed]

38. Conrad, R.; Stölting, G.; Hendriks, J.; Ruello, G.; Kortzak, D.; Jordan, N.; Gensch, T.; Hidalgo, P. Rapid turnover of the cardiac L- type CaV1.2 calcium channel by endocytic recycling regulates its cell surface availability. *iScience* **2018**, *1*, 1–15. [CrossRef] [PubMed]

39. Schneider, C.A.; Rasband, W.S.; Eliceiri, K.W. NIH Image to ImageJ: 25 years of image analysis. *Nat. Meth.* **2012**, *9*, 671–675. [CrossRef]

40. Karanasios, E.; Walker, S.A.; Okkenhaug, H.; Manifava, M.; Hummel, E.; Zimmermann, H.; Ahmed, Q.; Domart, M.-C.; Collinson, L.; Ktistakis, N.T. Autophagy initiation by ULK complex assembly on ER tubulovesicular regions marked by ATG9 vesicles. *Nat. Commun.* **2016**, *7*, 12420. [CrossRef]

Sample Availability: Samples of the EYFP-GABARAP and EYFP-LC3B constructs for overexpression in mammalian cells are available from the authors.

Chapter 4

Conclusions and Outlook

The ATG8 protein GABARAP is a well-studied protein particularly in current autophagy-related research. Yet, these are not the only functions of this multifaceted protein, having been discovered originally as receptor-associated protein. In this thesis, GABARAP was investigated for its participation in secretion (Figure 4.1A) and transport processes (Figure 4.1B), which are unrelated to classical, degradative autophagy (Figure 4.1C).

In the first part of the thesis, GABARAP was studied with respect to its unconventional secretion process. GABARAP is known to take part in vesicle-mediated secretion [59]. The secretion of GABARAP itself was first demonstrated by mass spectrometry of EV proteins obtained from cancer cell lines [131,132]; an in-depth analysis of the mechanisms underlying GABARAP's secretion, however, was still pending. Immunoblotting of EVs from cell culture supernatants enriched from the commonly used cell lines HEK293, Huh7, and SH-SY5Y, and from human blood plasma revealed the presence of predominantly lipidated GABARAP-II which is able to attach to autophagic and non-autophagic membranes [34]. Analysis of bovine blood plasma, which was used as supplement for cell culture media, revealed GABARAP's presence also in EVs originating from non-human material; here, however, mainly unlipidated GABARAP-I was detected extracellularly for unknown reasons. Still, this result supports the finding that lipidated GABARAP-II does in fact originate from EVs of the tested human cell lines. To subsequently study the mechanism(s) underlying GABARAP's secretion, the APEX2-mediated proximity labelling technique was applied. This method is based on the APEX2-catalysed oxidation of biotin-phenol which attaches to electron-rich amino acids of proteins in proximity to APEX2 in a confined cellular compartment [133]. At the beginning of this project, the APEX2-technique was well-established for application in intracellular compartments such as mitochondria [133] and also autophagosomes [134], but not for small, highly diluted, extracellular compartments like EVs. Within this thesis, the applicability of the APEX2-system to EVs was demonstrated for the

first time. By this strategy, solely proteins associated with (APEX2-)GABARAP-positive EVs are labelled, overcoming the lack of methods to isolate a cargo-specific EV-subpopulation in case the cargo is not surface-exposed. Labelled proteins were enriched via Streptavidin and applied to mass spectrometry, yielding the (APEX2-)GABARAP co-secretome. This co-secretome contained not only known GABARAP interaction partners like clathrin heavy chain 1 [40], but also proteins which are involved in exosomal secretion such as Alix, and KIF5B which facilitates vesicle-mediated secretion together with PRIP and GABARAP [59]. In an in-depth GO analysis of the GABARAP co-secretome, alongside control data sets, a significant overrepresentation of mitochondrion-annotated proteins was revealed. Additionally, when comparing the GABARAP co-secretome with a corresponding, independent autophagosomal proxitome [134], an overlap of the EV proxitome with the autophagosome proxitome was discovered, both findings pointing towards a biosynthetic/non-degradative autophagy-based branch or an autophagy-involving amphisome pathway (Figure 4.1A). Agreeing with GABARAP's involvement in autophagosome closure [35] and its association with autophagosomes [135], GABARAP was shown to co-localise with circular structures (Figure 4.1C) by super-resolution imaging. A block of autophagy by knocking down ATG5 and ATG7 or, alternatively, an inhibition of autophagosome formation by 3-Methyladenine might provide information on the relevance of functional autophagy during GABARAP's secretion. Alternatively, GABARAP might be secreted by a pathway distinct from classical autophagy but involving the ATG8-conjugation machinery. Shortly before submitting our study for publication, a proximity labelling approach based on an alternative enzyme to APEX2, namely the biotin ligase BirA*, was used to investigate the secretion of LC3 which is like GABARAP a member of the highly homologous ATG8 protein family. This study revealed by intracellular labelling that parts of the LC3-conjugation machinery are involved in the packaging of diverse RNA-binding proteins (RBPs) in MVB-contained ILVs as precursor of EVs that also contain lipidated LC3-II [136]. Also in the GABARAP co-secretome, as identified in frame of this work, various RBPs were detected, therefore suggesting a possible functional redundancy of GABARAP and LC3 in the process of RBP-loading into ILVs. In future experiments, the intracellular localisation of APEX2-GABARAP, determined by 3,3'-Diaminobenzidine (DAB) staining and subsequent electron microscopy, may enable a detailed assignment to secretion-related organelles such as MVBs or autophagosomes. Taken together, the here adapted proximity labelling method makes it possible to determine the co-secretome and thereby deliver hints for the underlying secretion mechanism(s) of specific EV proteins. Through analysis of the co-secretome of APEX2-GABARAP, two ways became obvious as possible mechanisms for GABARAP's secretion: an autophagosome-mediated pathway, which is distinct from classical, degradative autophagy, and/or an MVB-mediated pathway, which might include the ATG8-

conjugation machinery as recently described for LC3. These results may attract further attention to autophagy- and ATG8-related secretion mechanisms.

As second part of the thesis, the role of GABARAP during Golgi-related transport processes was investigated. Although GABARAP belongs to a subfamily of ATG8 proteins sharing high sequence homology, diverse functions have been assigned to the three members GABARAP, GABARAPL1, and GABARAPL2. While GABARAP and GABARAPL1 have been shown to be involved in receptor trafficking to the cell surface [39, 137], GABARAPL2 was initially identified as an intra-Golgi modulator [50] which is required for Golgi reassembly [138]. Within this work, all three members of the GABARAP subfamily were studied regarding their involvement in Golgi structure maintenance. By applying a panel of HEK293 knockout (KO) cell lines exhibiting either a single KO (SKO), a double KO (DKO) combination, or a triple KO (TKO) of the respective GABARAP subfamily member to immunolabelling of the *trans*-Golgi network marker protein TGN46 and subsequent confocal fluorescence microscopy, a change in Golgi morphology compared to WT cells was observed. GABARAP^{SKO} and GABARAPL2^{SKO}, respectively, resulted in a shift from a compact to a partly compact Golgi structure. Knocking out GABARAP and GABARAPL2 simultaneously, also in combination with GABARAPL1, led to a predominantly dispersed Golgi phenotype. GABARAPL1^{SKO} yielded a Golgi morphology similar to WT cells; however, because of a lower abundance of GABARAPL1 in HEK293 cells compared to GABARAP and GABARAPL2 [139], the effect of GABARAPL1^{SKO} on Golgi morphology might be not as prominent as for the other two GABARAPs. Staining with BODIPY FL-labelled C_5-ceramide, targeting the whole Golgi complex, led to a similar result as staining of the TGN. These results suggest that GABARAP and GABARAPL1 might be redundant to GABARAPL2 in establishing a compact Golgi structure, possibly during post-mitotic reassembly as already shown for GABARAPL2 [138]. A live-cell ceramide chase experiment with NBD-labelled C_6-ceramide demonstrated an increased accumulation of NBD-positive, vesicular structures in GABARAP/L1/L2^{TKO} cells compared to WT cells. The latter furthermore exhibited staining at the plasma membrane which was only faintly visible in GABARAP/L1/L2^{TKO} cells, indicating impaired anterograde lipid transport. The GABARAP/L1/L2^{TKO} phenotype could be mirrored in WT cells by Monensin which causes disruption of the *trans*-Golgi [140], hinting towards an involvement of the GABARAPs in *trans*-Golgi-mediated trafficking of ceramide and its metabolites. Future work will demonstrate whether these effects may be rescued by induction of expression of individual and/or a combination of GABARAP subfamily members, and which role their lipidation state plays in this process. It will also be interesting to determine whether the GABARAPs are directly, e.g. via interaction with NSF [138,141] or SNAREs [50,52], or indirectly, e.g. due to an altered lipid composition

of the Golgi, involved in Golgi structure maintenance. All in all, this work demonstrates an involvement of the GABARAPs in Golgi structure maintenance and lipid transport (Figure 4.1B). When working with systems deficient for members of the GABARAPs, attention should not only be given to the impact on the autophagic machinery, but also to general cellular integrity.
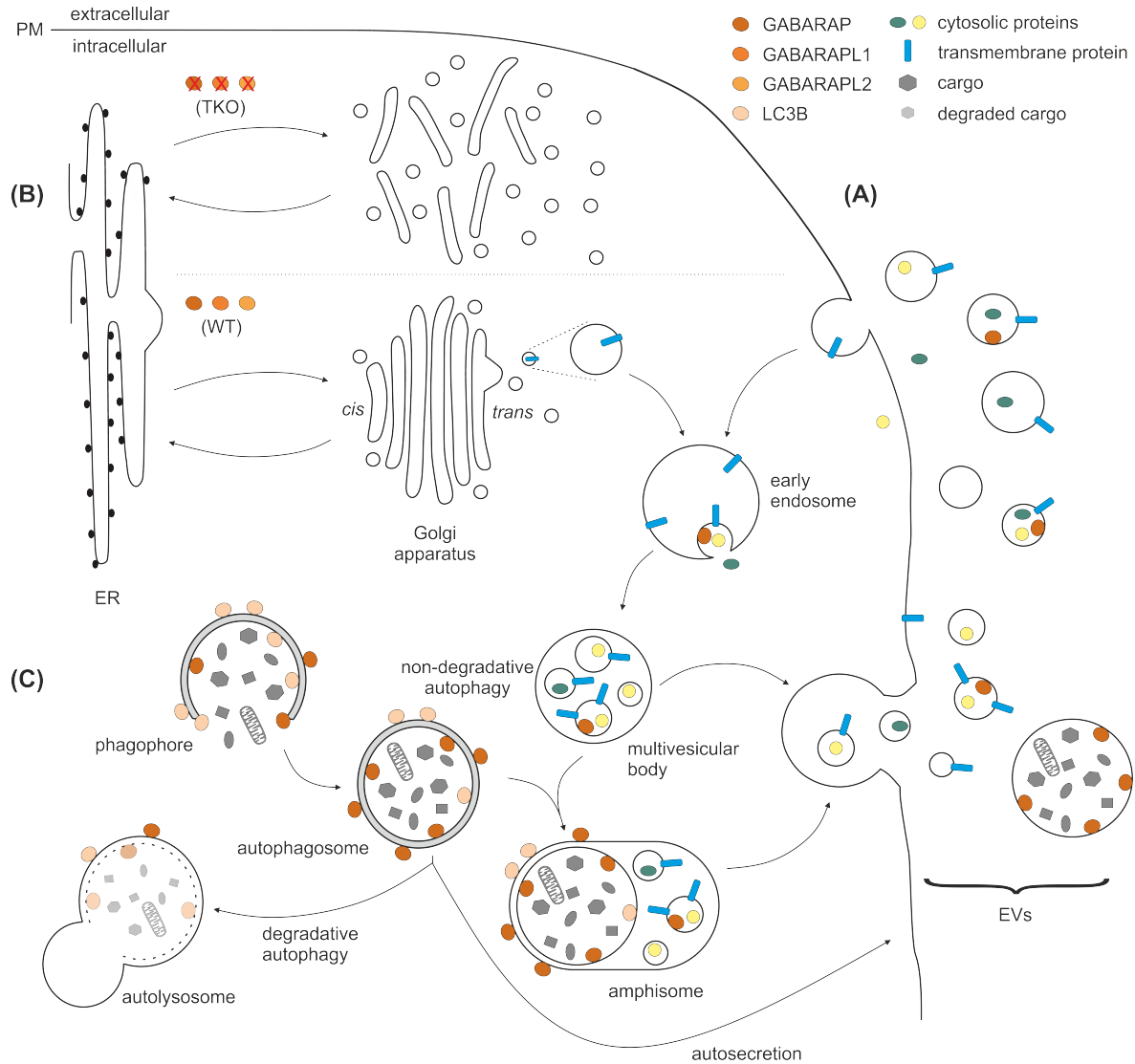
Figure 4.1:   Compilation of GABARAP's functions studied in this thesis. (A) GABARAP is secreted in EVs at least partly by an autophagosome-involving mechanism. (B) The GABARAPs were found to be necessary for establishing a compact Golgi structure, a simultaneous KO leading to Golgi fragmentation and an accumulation of vesicular structures. (C) By super-resolution imaging, LC3B was detected predominantly on U-shaped structures, while GABARAP was shown to locate to circular structures, agreeing with their specific roles during autophagy.

Appendix A

Material and Methods

A.1 Material

A.1.1 Antibodies

Table A.1: Overview of used primary antibodies.

Antibody	Cat. No.	Supplier
anti-Alix	sc-49268	Santa Cruz Biotechnology, Dallas, TX, USA
anti-Annexin V	ab14196	abcam, Cambridge, UK
anti-Calnexin	ab22595	abcam
anti-CD81	sc-23962	Santa Cruz Biotechnology
anti-GABARAP	8H5	in-house [142]
anti-GABARAP	13733	Cell Signaling Technology (CST), Danvers, MA, USA
anti-GABARAPL1	26632	CST
anti-GABARAPL2	14256	CST
anti-Hsc70	ab51052	abcam
anti-c-myc	A190-104A	Bethyl Laboratories, Montgomery, TX, USA
Streptavidin-HRP	S911	Invitrogen, Carlsbad, CA, USA
anti-TGN46	AHP500GT	Bio Rad Laboratories, Hercules, CA, USA

Table A.2: Overview of used secondary antibodies.

Antibody	Cat. No.	Supplier
anti-goat AlexaFluor488	ab150133	abcam
anti-goat HRP	sc-2354	Santa Cruz Biotechnology
anti-mouse HRP	P026002-2	Agilent Technologies, Santa Clara, CA, USA
anti-rabbit HRP	31460	Invitrogen
anti-rat Cy5	712-175-150	Jackson ImmunoResearch, Cambridgeshire, UK
anti-sheep AlexaFluor488	A-11015	Thermo Fisher Scientific, Waltham, MA, USA

A.1.2   Human Cell Lines

Human cell lines were obtained from the DSMZ – German Collection of Microorganisms and Cell Cultures, Braunschweig, Germany.

A.2   Methods

A.2.1   Microbiological Methods

A.2.1.1   Transformation and DNA preparation

To prepare DNA for transfection of eukaryotic cells, it was amplified by bacterial cell culture. Of the desired plasmid DNA, 100 ng were added to chemically competent *Escherichia coli* OmniMAX 2 T1 cells (Cat. No. C854003, Thermo Fisher Scientific) and incubated for 20 min on ice. After a heat shock for 45 s at 42 °C, the cells were cooled for another 5 min on ice, mixed with 1 mL LB medium, and incubated shaking for 1 h at 37 °C. Finally, the cells were plated on an LB agar dish containing an antibiotic selection factor and cultivated over night at 37 °C. Obtained colonies were used for inoculation of fluid cultures and subsequent DNA preparation using the innuPREP Plasmid Mini Kit (Cat. No. 845-KS-1041010, Analytik Jena, Jena, Germany) or the QIAGEN Plasmid Midi Kit (Cat. No. 12143, QIAGEN, Hilden, Germany) according to the manufacturer's instructions.

A.2.2 Cell Culture Methods

A.2.2.1 Thawing, Culturing, and Seeding of Cells

Eukaryotic cells were kept for long-term storage in liquid nitrogen in appropriate media containing 10 % dimethyl sulfoxide (DMSO) as cryoprotectant. For future usage, cells were thawed in a 37 °C water bath and transferred immediately into a previously prepared cell culture flask containing optimised media for the respective cell line according to the DSMZ - German Collection of Microorganisms and Cell Cultures, Braunschweig, Germany. For instance, HEK293 cells were cultured in Dulbecco's Modified Eagle's Medium (DMEM; Cat. No. D5796, Sigma-Aldrich, St. Louis, MO, USA) + 10 % FCS at 37 °C and 5 % CO_2.

For passaging, the cell culture supernatant was aspirated and the cells were washed once with pre-warmed 1x PBS. Then, the cells were detached by incubating in Trypsin/EDTA solution, resuspended in fresh media, and centrifuged for 5 min at 500 x g and RT. The supernatant was discarded, and the cells were carefully resuspended and transferred into an appropriate cell culture vessel (flasks or multi-well plates).

To seed a certain amount of cells, 20 µL of resuspended cells were mixed with 20 µL trypan blue solution and applied to a *Neubauer* chamber for counting the cells. The number of cells counted in the four $1\,mm^2$ squares, each subdivided into sixteen $0.0625\,mm^2$ squares, was subjected to the following formula to calculate the concentration of cells per µL in the original suspension:

$$cells/\mu L = \frac{(number\ of\ cells\ counted) \times (dilution\ factor)}{(area\ counted\ (4\,mm^2)) \times (chamber\ depth\ (0.1\,mm)}$$

A.2.2.2 Transfection

Transfection describes the process by which plasmid DNA is introduced into eukaryotic cells. Prior to transfection, 1×10^6 HEK293 cells were seeded into one well of a 6-well culture plate. On the following day, cells were transfected with 1-2 µg DNA using PolyFect (Cat. No. 301105, Qiagen, Hilden, Germany) as transfection reagent according to the manufacturer's instructions.

A.2.2.3 Stable Cell Line Generation

The generation of stable cell lines aimes towards the constant (over-)expression of a certain protein of interest (POI) due to a stable integration into the genome. Compared to transient transfections, this method has the advantage of a higher number of cells expressing the gene of interest, as successfully transfected cells are selected for an antibiotic resistance during the procedure.

To generate a stable HEK293 cell line, cells were seeded and transfected as described in section A.2.2.2. After 24 h incubation with plasmid DNA, the cells were washed to

remove residual PolyFect and fresh medium containing 1.0 mg/mL G418 as antibiotic selection factor was applied. Two days later, the G418 concentration was increased to 1.2 mg/mL for 48-96 h, followed by incubation at again 1.0 mg/mL G418 and daily change of the media throughout the selection procedure. In case the protein encoded by the transfected DNA was tagged to a fluorescent marker protein, the expression could be monitored in parallel by fluorescence microscopy. Fluorescent cell colonies were picked and transferred into one well of a 96-well plate each. As soon as the cells reached 80 % confluency, they were transferred into a larger vessel. In addition to fluorescence microscopy, the expression of the desired protein was confirmed by immunoblotting of the cell colonies (A.2.3.1). The colony showing the strongest POI expression was selected and stored in liquid nitrogen for future experiments which were conducted in absence of selection antibiotic.

A.2.2.4   The Flp-In T-REx System

The Flp-In T-REx system provides the opportunity to site-specifically integrate a gene of interest (GOI) into the cellular genome. Material needed for this technique is commercially available from Thermo Fisher Scientific (Cat. No. K650001). The corresponding host cell line HEK293 Flp-In T-REx was kindly provided by Prof. Dr. Christian Behrends and contains an integrated flippase (Flp) recombination target (FRT) recombination site. Here, the Flp-In T-REx system was used to inducibly express APEX2 constructs in HEK293 Flp-In T-REx cells.
Upon co-transfection with pOG44 as helper plasmid expressing the Flp recombinase and a pcDNA5/FRT/TO vector containing the GOI the latter is integrated into the FRT recombination site of the host cell line, in contrast to the transfection method described above (A.2.2.2) by which genomic integration occurs randomly. Furthermore, the Flp-In T-REx system enables the generation of stable cell lines in which GOI expression can be induced by incubation with 1 µg/mL tetracycline for 24 h, reducing the risk of off-target effects caused by constitutive POI overexpression. Selection of successfully transfected cells was achieved by incubation with 100 µg/mL Hygromycin B-containing media. Picked colonies were tested for POI expression after tetracycline induction by immunoblotting (A.2.3.1) and for lack of β-galactosidase activity, as integration of the GOI into the FRT site inactivates the *lac*Z gene.

A.2.2.5   APEX2-mediated proximity labelling

The APEX2 system is an emerging method for analysing the direct protein environment, the so-called proxitome, of a POI tagged to the engineered ascorbate peroxidase APEX2. The labelling procedure was conducted according to Hung *et al.* [143]. First, cells were seeded into an appropriate cell culture vessel. On the next day, expression of APEX2-POI was either induced with tetracycline (compare A.2.2.4) or by transient

transfection (A.2.2.2) and the cells were incubated for another 24 h. Then, 500 µM biotin-phenol was added to the media, followed by H_2O_2 after 30 min to induce the one-minute labelling step during which APEX2 catalyses the oxidation of biotin-phenol to a short-lived biotin-phenoxyl radical, thereby covalently tagging endogenous proteins in proximity to APEX2-POI. After 1 min, the reaction is quenched by a series of washing steps in freshly made quencher solution (10 mM sodium ascorbate, 5 mM Trolox, 10 mM sodium azide). Cells were then lysed in supplemented RIPA lysis buffer [143] and analysed by immunoblotting (A.2.3.1) or mass spectrometry (A.2.7).

For determining the APEX2-POI proxitome in EVs, these have to be enriched and precipitated as described below (A.2.2.6) before the labelling procedure; also see section 3.2.

A.2.2.6   Preparation of EVs

To isolate EVs from cell culture supernatants, cells were seeded into 175 cm² or 875 cm² cell culture flasks and incubated for 48-72 h at 37 °C and 5 % CO_2 in DMEM containing exosome-depleted FCS (Cat. No. A25904DG, Life Technologies). Conditioned cell culture media were depleted from cellular debris by differential centrifugation at 300 x g for 10 min and at 2,000 x g for 20 min. The supernatant was concentrated to one-tenth of the original volume using centricons with a molecular weight cutoff of 3,000 (VS0291 or VS2091, Sartorius, Göttingen, Germany) by centrifugation at 12 °C and 2,500 x g. EVs were then enriched by either ExoQuick-TC (EXOTC10A-1, System Biosciences, Palo Alto, CA, USA) according to the manufacturer's instructions or ultracentrifugation for two times 90 min at 4 °C and 100,000 x g including a washing step of the pellet in 1x PBS containing protease inhibitor cocktail.

A.2.3   Biochemical Methods

A.2.3.1   Immunoblot

Cellular and EV samples were analysed for the presence of proteins of interest by immunoblotting. After harvesting, pellets were lysed in RIPA lysis buffer following the protocol published by Hung *et al.* [143]. Lysates were either applied directly to subsequent analysis by immunoblotting or, if lipidation states of ATG8 proteins should be accessed, an additional protein precipitation step using methanol/chloroform (A.2.3.2) was employed. Protein concentrations were determined using the *DC* Protein Assay (Cat. No. 5000116, Bio Rad Laboratories, Hercules, CA, USA) according to the manufacturer's instructions. Per sample and lane, the volumes containing 25 µg total protein were mixed with 4x Lämmli sample buffer, incubated for 10 min at 45 °C, and subsequently applied to sodium dodecyl sulfate-polyacrylamide gel electrophoresis (SDS-PAGE) using Any kD Mini-PROTEAN TGX Stain-Free Protein Gels (Cat. No. 4568124

or 4568126, Bio Rad). Gels were run at const. 30 mA per gel. After recording a stainfree image at the ChemiDoc Imaging System (Bio-Rad), the proteins were transferred for 7 min at 1.3 A and 25 V to a polyvinylidene fluoride (PVDF) membrane using Trans-Blot Turbo Mini PVDF Transfer Packs (Cat. No. 1704156, Bio-Rad). Depending on the later used antibody, the membrane was either blocked in 5 % (w/v) milk powder or 3 % bovine serum albumin (BSA) in 0.05 % Tween-20 in tris-buffered saline (TBS-T) for 2 h at room temperature (RT). After one washing step with TBS-T, the membrane was incubated with primary antibody over night at 4 °C. On the next day, the membrane was washed three times for 5 min in TBS-T and incubated with horseradish peroxidase (HRP)-coupled secondary antibody. After three final washing steps, the HRP signal was visualised using Clarity Western ECL Substrate (Cat. No. 1705061, Bio-Rad) and the ChemiDoc Imaging System.

A.2.3.2   Methanol/Chloroform Protein Precipitation

To achieve access to the lipidation status of ATG8 proteins by immunoblotting, the proteins were separated from the lysate by Methanol/Chloroform precipitation [144]. To 150 µL sample, 400 µL methanol and 100 µL chloroform were added and homogenised on a shaker for 10 s. Then, 300 µL ddH$_2$O were added, the sample was homogenised once more and centrifuged for 5 min at 4 °C and 10,000 x g. The upper phase was carefully removed without disturbing the proteins in the interphase. After adding another 300 µL methanol and 1,000 µL ice-cold acetone, the sample was centrifuged again for 5 min at 4 °C and 10,000 x g. The supernatant was discarded. The pellet was air-dried at RT and resuspended in the smallest possible volume of 2 % SDS.

A.2.4   Confocal Laser Scanning Microscopy

Prior to microscopic measurements, 3-6 × 10^5 cells were seeded into either poly D-Lysine coated bottom dishes (Cat. No. P35GC-0-10-C, MatTek Corporation, MA, USA) or fibronectin coated 35 mm imaging dishes (Cat. No. 81158, ibidi, Gräfelfing, Germany) and cultured for 24 h in DMEM + 10 % FCS. For live cell fluorescence microscopy, the cells were then directly subjected to measurement, using Hoechst 33342 (Cat. No. R37605, Invitrogen) as nuclei staining dye. For immunofluorescence experiments, the cells were first fixed with 4 % (w/v) paraformaldehyde (PFA; pH 6.5) for 10 min at 37 °C, washed two times in phosphate-buffered saline (PBS; pH 7.4), and permeabilised in 0.2 % Triton-X-100 for 30 min at RT. After an over-night blocking step in 1 % BSA at 4 °C, the cells were incubated with primary antibody for 1 h shaking at RT, washed three times in PBS, and incubated with secondary antibody for 1 h shaking at RT under exclusion of light. Following two last washing steps in PBS, long storage buffer (0.05 % sodium azide in PBS) was applied and the cells were used for

image acquisition, using 4,6-diamidino-2-phenylindole (DAPI) for staining the nuclei. Images were acquired using an LSM 710 confocal microscope (Zeiss, Oberkochen, Germany) equipped with ZEN black 2009 software and a Plan-Apochromat 63x/1.40 Oil DIC M27 objective.

A.2.5   Transmission Electron Microscopy

For visualisation of EVs, transmission electron microscopy (TEM) was applied. The preparation of an EV sample was conducted following the protocol as published by Théry *et al.* [145] with the following modifications: The enriched and precipitated EVs were resuspended in 2 % (w/v) PFA (in PBS, pH 7.4) and 5 μL of this sample were absorbed on a formvar/carbon coated copper grid (Cat. No. S160-4-V, Plano, Wetzlar, Germany) for 20 min. Then, the specimen was fixed with 1 % glutaraldehyde for 5 min, followed by eight washing steps with ddH$_2$O, and a negative staining step with 4 % (v/v) uranyl acetate for 5 min. After embedding the sample in a freshly made 4:1 mixture of trehalose (10 %, in TBS) and uranyl acetate (2 %) for 10 min at RT, it was dried on a filter paper and finally subjected to TEM. Images were recorded using a Libra 120 transmission electron microscope (Zeiss) at 120 kV.

A.2.6   Nanoparticle Tracking Analysis

Nanoparticle tracking analyses were conducted at the laboratory and with the support of Prof. Dr. Payam Akhyari and Dr. Andreas Weber (*Universitätsklinikum Düsseldorf, Klinik für Kardiovaskuläre Chirurgie*). For details, see the method section of chapter 3.1.

A.2.7   Mass Spectrometry

Mass spectrometric analyses were performed in collaboration with Dr. Daniel Waldera-Lupa, Dr. Gereon Poschmann, and Prof. Dr. Kai Stühler at the Molecular Proteomics Laboratory (MPL; institution at the BMFZ (*Biologisch-Medizinisches Forschungszentrum*) of the Heinrich Heine University Düsseldorf). For details, see the method section of chapter 3.1.

List of Publications and Presentations

1   Publications

I. Abdollahzadeh, J. Hendriks, <u>J. L. Sanwald</u>, I. M. Simons, S. Hoffmann, O. H. Weiergräber, D. Willbold, and T. Gensch. Autophagy-Related Proteins GABARAP and LC3B Label Structures of Similar Size but Different Shape in Super-Resolution Imaging. *Molecules* 2019, 24(9), 1833.

<u>J. L. Sanwald</u>, G. Poschmann, K. Stühler, C. Behrends, S. Hoffmann, and D. Willbold. The GABARAP Co-Secretome Identified by APEX2-GABARAP Proximity Labelling of Extracellular Vesicles. *Cells* 2020, 9(6), 1468.

<u>J. L. Sanwald</u>, J. Dobner, I. M. Simons, G. Poschmann, K. Stühler, A. Üffing, S. Hoffmann, and D. Willbold. Lack of GABARAP-Type Proteins is Accompanied by Altered Golgi Morphology and Surfaceome Composition. *Int. J. Mol. Sci.* 2021, 22(1), 85.

2   Poster Presentations (only first authorships listed)

<u>J. L. Sanwald</u>, A. Boeske, S. Hoffmann, and D. Willbold.
Elucidation of the unconventional secretion pathways of HIV-1 Nef by investigating its W13A mutant.
Black Forest Winter Conference: "Autophagic Membrane Trafficking & Dynamics in Aging and Disease", 01/2016, Saig, Germany

<u>J. L. Sanwald</u>, A. Boeske, A. Weber, P. Akhyari, S. Hoffmann, and D. Willbold.
Characterization of extracellular vesicles purified from HIV-1 Nef overexpressing HEK293 cell supernatants.
68. Mosbacher Kolloquium - "Cell Organelles - Origin, Dynamics and Communication", 03-04/2017, Mosbach/Baden, Germany

J. L. Sanwald, A. Boeske, A. Weber, P. Akhyari, F. Le Guerroué, C. Behrends, S. Hoffmann, and D. Willbold.
Characterization of extracellular vesicles purified from HIV-1 Nef overexpressing HEK293 cell supernatants.
ISEV 2017 - Annual Meeting, 05/2017, Toronto, Canada

J. L. Sanwald, D. Waldera-Lupa, K. Stühler, F. Le Guerroué, C. Behrends, S. Hoffmann, and D. Willbold.
Investigation of GABARAP's secretion by proximity labeling of extracellular vesicles.
Keystone Symposia "Selective Autophagy", 04/2018, Kyoto, Japan

J. L. Sanwald, I. M. Simons, J. Dobner, S. Hoffmann, and D. Willbold.
Investigating the GABARAPs' impact on the intracellular localisation and secretion of HIV-1 Nef.
EMBO Workshop "Molecular mechanisms of unconventional protein secretion in eukaryotic cells", 09/2019, Assisi, Italy

J. L. Sanwald, I. M. Simons, J. Dobner, C. Behrends, S. Hoffmann, and D. Willbold.
Investigation of GABARAP's secretion by proximity labelling of extracellular vesicles.
GBM/DGZ Fall Conference 2019 "Age-Related Human Diseases - Special Focus Autophagy", 09/2019, Tübingen, Germany

Bibliography

[1] C. de Duve. The lysosome. *Scientific American*, 208(5):64–73, 1963.

[2] R. L. Deter, P. Baudhuin, and C. de Duve. Participation of lysosomes in cellular autophagy induced in rat liver by glucagon. *The Journal of Cell Biology*, 35(2):C11–C16, 1967.

[3] D. J. Klionsky. Autophagy revisited: A conversation with Christian de Duve. *Autophagy*, 4(6):740–743, 2008.

[4] T. Yorimitsu and D. J. Klionsky. Autophagy: molecular machinery for self-eating. *Cell Death & Differentiation*, 12(S2):1542–1552, 2005.

[5] M. Oku and Y. Sakai. Three distinct types of microautophagy based on membrane dynamics and molecular machineries. *BioEssays*, 40(6):1800008, 2018.

[6] A. Massey, R. Kiffin, and A. M. Cuervo. Pathophysiology of chaperone-mediated autophagy. *The International Journal of Biochemistry & Cell Biology*, 36(12):2420–2434, 2004.

[7] N. Mizushima, T. Yoshimori, and B. Levine. Methods in mammalian autophagy research. *Cell*, 140(3):313–326, 2010.

[8] B. Boland, A. Kumar, S. Lee, F. M. Platt, J. Wegiel, W. H. Yu, and R. A. Nixon. Autophagy induction and autophagosome clearance in neurons: relationship to autophagic pathology in Alzheimer's disease. *Journal of Neuroscience*, 28(27):6926–6937, 2008.

[9] A. Roscic, B. Baldo, C. Crochemore, D. Marcellin, and P. Paganetti. Induction of autophagy with catalytic mTOR inhibitors reduces huntingtin aggregates in a neuronal cell model. *Journal of Neurochemistry*, 119(2):398–407, 2011.

[10] A. Hermann, H. H. Kitzler, T. Pollack, S. Biskup, S. Krüger, C. Funke, C. Terille, and T. B. Haack. A case of beta-propeller protein-associated neurodegeneration due to a heterozygous deletion of WDR45. *Tremor and Other Hyperkinetic Movements (N Y)*, 7:465, 2017.

[11] M. M. Lipinski, B. Zheng, T. Lu, Z. Yan, B. F. Py, A. Ng, R. J. Xavier, C. Li, B. A. Yankner, C. R. Scherzer, and J. Yuan. Genome-wide analysis reveals mechanisms modulating autophagy in normal brain aging and in Alzheimer's disease. *Proceedings of the National Academy of Sciences*, 107(32):14164–14169, 2010.

[12] Q. Ma, J. Qiang, P. Gu, Y. Wang, Y. Geng, and M. Wang. Age-related autophagy alterations in the brain of senescence accelerated mouse prone 8 (SAMP8) mice. *Experimental Gerontology*, 46(7):533–541, 2011.

[13] X. Qu, J. Yu, G. Bhagat, N. Furuya, H. Hibshoosh, A. Troxel, J. Rosen, E.-L. Eskelinen, N. Mizushima, Y. Ohsumi, G. Cattoretti, and B. Levine. Promotion of tumorigenesis by heterozygous disruption of the beclin 1 autophagy gene. *Journal of Clinical Investigation*, 112(12):1809–1820, 2003.

[14] T. Wang, J. Hu, H. Luo, H. Li, J. Zhou, L. Zhou, and S. Wei. Photosensitizer and autophagy promoter coloaded ROS-responsive dendrimer-assembled carrier for synergistic enhancement of tumor growth suppression. *Small*, 14(38):1802337, 2018.

[15] I. Nakagawa, A. Amano, N. Mizushima, A. Yamamoto, H. Yamaguchi, T. Kamimoto, A. Nara, J. Funao, M. Nakata, K. Tsuda, S. Hamada, and T. Yoshimori. Autophagy defends cells against invading group A *Streptococcus*. *Science*, 306(5698):1037–1040, 2004.

[16] M. G. Gutierrez, S. S. Master, S. B. Singh, G. A. Taylor, M. I. Colombo, and V. Deretic. Autophagy is a defense mechanism inhibiting BCG and *Mycobacterium tuberculosis* survival in infected macrophages. *Cell*, 119(6):753–766, 2004.

[17] W. T. Jackson, T. H. Giddings, M. P. Taylor, S. Mulinyawe, M. Rabinovitch, R. R. Kopito, and K. Kirkegaard. Subversion of cellular autophagosomal machinery by RNA viruses. *PLoS Biology*, 3(5):e156, 2005.

[18] Y.-R. Lee, H.-Y. Lei, M.-T. Liu, J.-R. Wang, S.-H. Chen, Y.-F. Jiang-Shieh, Y.-S. Lin, T.-M-Yeh, C.-C. Liu, and H.-S. Liu. Autophagic machinery activated by dengue virus enhances virus replication. *Virology*, 374(2):240–248, 2008.

[19] J. E. McLean, A. Wudzinska, E. Datan, D. Quaglino, and Z. Zakeri. Flavivirus NS4A-induced autophagy protects cells against death and enhances virus replication. *Journal of Biological Chemistry*, 286(25):22147–22159, 2011.

[20] S. M. Robinson, G. Tsueng, J. Sin, V. Mangale, S. Rahawi, L. L. McIntyre, W. Williams, N. Kha, C. Cruz, B. M. Hancock, D. P. Nguyen, M. R. Sayen, B. J. Hilton, K. S. Doran, A. M. Segall, R. Wolkowicz, C. T. Cornell, J. L. Whitton,

R. A. Gottlieb, and R. Feuer. Coxsackievirus B exits the host cell in shed microvesicles displaying autophagosomal markers. *PLoS Pathogens*, 10(4):e1004045, 2014.

[21] M. Tsukada and Y. Ohsumi. Isolation and characterization of autophagy-defective mutants of *Saccharomyces cerevisiae*. *FEBS Letters*, 333(1-2):169–174, 1993.

[22] A. Matsuura, M. Tsukada, Y. Wada, and Y. Ohsumi. Apg1p, a novel protein kinase required for the autophagic process in *Saccharomyces cerevisiae*. *Gene*, 192(2):245–250, 1997.

[23] D. J. Klionsky. Autophagy: from phenomenology to molecular understanding in less than a decade. *Nature Reviews Molecular Cell Biology*, 8(11):931–937, 2007.

[24] I. G. Ganley, D. H. Lam, J. Wang, X. Ding, S. Chen, and X. Jiang. ULK1·ATG13·FIP200 complex mediates mTOR signaling and is essential for autophagy. *Journal of Biological Chemistry*, 284(18):12297–12305, 2009.

[25] N. Mizushima. The role of the Atg1/ULK1 complex in autophagy regulation. *Current Opinion in Cell Biology*, 22(2):132–139, 2010.

[26] S. Wesselborg and B. Stork. Autophagy signal transduction by ATG proteins: from hierarchies to networks. *Cellular and Molecular Life Sciences*, 72(24):4721–4757, 2015.

[27] K. Suzuki, T. Kirisako, Y. Kamada, N. Mizushima, T. Noda, and Y. Ohsumi. The pre-autophagosomal structure organized by concerted functions of APG genes is essential for autophagosome formation. *The EMBO Journal*, 20(21):5971–5981, 2001.

[28] E. L. Axe, S. A. Walker, M. Manifava, P. Chandra, H. L. Roderick, A. Habermann, G. Griffiths, and N. T. Ktistakis. Autophagosome formation from membrane compartments enriched in phosphatidylinositol 3-phosphate and dynamically connected to the endoplasmic reticulum. *The Journal of Cell Biology*, 182(4):685–701, 2008.

[29] C. Burman and N. T. Ktistakis. Autophagosome formation in mammalian cells. *Seminars in Immunopathology*, 32(4):397–413, 2010.

[30] S. A. Tooze and T. Yoshimori. The origin of the autophagosomal membrane. *Nature Cell Biology*, 12(9):831–835, 2010.

[31] A. C. Nascimbeni, F. Giordano, N. Dupont, D. Grasso, M. I. Vaccaro, P. Codogno, and E. Morel. ER-plasma membrane contact sites contribute to autophagosome biogenesis by regulation of local PI3P synthesis. *The EMBO Journal*, 36(14):2018–2033, 2017.

[32] R. Gómez-Sánchez, J. Rose, R. Guimarães, M. Mari, D. Papinski, E. Rieter, W. J. Geerts, R. Hardenberg, C. Kraft, C. Ungermann, and F. Reggiori. Atg9 establishes Atg2-dependent contact sites between the endoplasmic reticulum and phagophores. *The Journal of Cell Biology*, 217(8):2743–2763, 2018.

[33] J. Geng and D. J. Klionsky. The Atg8 and Atg12 ubiquitin-like conjugation systems in macroautophagy. 'Protein modifications: beyond the usual suspects' review series. *EMBO reports*, 9(9):859–864, 2008.

[34] Y. Kabeya, N. Mizushima, T. Ueno, A. Yamamoto, T. Kirisako, T. Noda, E. Kominami, Y. Ohsumi, and T. Yoshimori. LC3, a mammalian homologue of yeast Apg8p, is localized in autophagosome membranes after processing. *The EMBO Journal*, 19(21):5720–5728, 2000.

[35] H. Weidberg, E. Shvets, T. Shpilka, F. Shimron, V. Shinder, and Z. Elazar. LC3 and GATE-16/GABARAP subfamilies are both essential yet act differently in autophagosome biogenesis. *The EMBO Journal*, 29(11):1792–1802, 2010.

[36] N. Mizushima, A. Kuma, Y. Kobayashi, A. Yamamoto, M. Matsubae, T. Takao, T. Natsume, Y. Ohsumi, and T. Yoshimori. Mouse Apg16L, a novel WD-repeat protein, targets to the autophagic isolation membrane with the Apg12-Apg5 conjugate. *Journal of Cell Science*, 116(9):1679–1688, 2003.

[37] T. Shpilka, H. Weidberg, S. Pietrokovski, and Z. Elazar. Atg8: an autophagy-related ubiquitin-like protein family. *Genome Biology*, 12(7):226, 2011.

[38] T. Lang, E. Schaeffeler, D. Bernreuther, M. Bredschneider D. H. Wolf, and M. Thumm. Aut2p and Aut7p, two novel microtubule-associated proteins are essential for delivery of autophagic vesicles to the vacuole. *The EMBO Journal*, 17(13):3597–3607, 1998.

[39] H. Wang, F. K. Bedford, N. J. Brandon, S. J. Moss, and R. W. Olsen. GABA(A)-receptor-associated protein links GABA(A) receptors and the cytoskeleton. *Nature*, 397(6714):69–72, 1999.

[40] J. Mohrlüder, Y. Hoffmann, T. Stangler, K. Hänel, and D. Willbold. Identification of clathrin heavy chain as a direct interaction partner for the γ-aminobutyric acid type A receptor associated protein. *Biochemistry*, 46(50):14537–14543, 2007.

[41] D. S. Grunwald, N. M. Otto, J.-M. Park, D. Song, and D.-H. Kim. GABARAPs and LC3s have opposite roles in regulating ULK1 for autophagy induction. *Autophagy*, 28:1–15, 2019.

[42] Z. Xie, U. Nair, and D. J. Klionsky. Atg8 controls phagophore expansion during autophagosome formation. *Molecular Biology of the Cell*, 19(8):3290–3298, 2008.

[43] C. R. Bartholomew, T. Suzuki, Z. Du, S. K. Backues, M. Jin, M. A. Lynch-Day, M. Umekawa, A. Kamath, M. Zhao, Z. Xie, K. Inoki, and D. J. Klionsky. Ume6 transcription factor is part of a signaling cascade that regulates autophagy. *Proceedings of the National Academy of Sciences*, 109(28):11206–11210, 2012.

[44] S. K. Backues, D. Chen, J. Ruan, Z. Xie, and D. J. Klionsky. Estimating the size and number of autophagic bodies by electron microscopy. *Autophagy*, 10(1):155–164, 2013.

[45] R. L. Knorr, H. Nakatogawa, Y. Ohsumi, R. Lipowsky, T. Baumgart, and R. Dimova. Membrane morphology is actively transformed by covalent binding of the protein Atg8 to PE-lipids. *PLoS ONE*, 9(12):e115357, 2014.

[46] I. Abdollahzadeh, M. Schwarten, T. Gensch, D. Willbold, and O. H. Weiergräber. The Atg8 family of proteins—modulating shape and functionality of autophagic membranes. *Frontiers in Genetics*, 8:109, 2017.

[47] H. Abeliovich, W. A. Dunn, J. Kim, and D. J. Klionsky. Dissection of autophagosome biogenesis into distinct nucleation and expansion steps. *The Journal of Cell Biology*, 151(5):1025–1034, 2000.

[48] T. N. Nguyen, B. S. Padman, J. Usher, V. Oorschot, G. Ramm, and M. Lazarou. Atg8 family LC3/GABARAP proteins are crucial for autophagosome–lysosome fusion but not autophagosome formation during PINK1/Parkin mitophagy and starvation. *The Journal of Cell Biology*, 215(6):857–874, 2016.

[49] S. A. Kuznetsov and V. I. Gelfand. 18 kDa microtubule-associated protein: identification as a new light chain (LC-3) of microtubule-associated protein 1 (MAP-1). *FEBS Letters*, 212(1):145–148, 1987.

[50] A. Legesse-Miller, Y. Sagiv, A. Porat, and Z. Elazar. Isolation and characterization of a novel low molecular weight protein involved in intra-Golgi traffic. *Journal of Biological Chemistry*, 273(5):3105–3109, 1998.

[51] A. Legesse-Miller, Y. Sagiv, R. Glozman, and Z. Elazar. Aut7p, a soluble autophagic factor, participates in multiple membrane trafficking processes. *Journal of Biological Chemistry*, 275(42):32966–32973, 2000.

[52] Y. Sagiv, A. Legesse-Miller, A. Porat, and Z. Elazar. GATE-16, a membrane transport modulator, interacts with NSF and the Golgi v-SNARE GOS-28. *The EMBO Journal*, 19(7):1494–1504, 2000.

[53] T. A. Leil, Z.-W. Chen, C.-S. S. Chang, and R. W. Olsen. GABA$_A$ receptor-associated protein traffics GABA$_A$ receptors to the plasma membrane in neurons. *Journal of Neuroscience*, 24(50):11429–11438, 2004.

[54] Z.-W. Chen, C.-S. S. Chang, T. A. Leil, and R. W. Olsen. C-terminal modification is required for GABARAP-mediated GABA$_A$ receptor trafficking. *Journal of Neuroscience*, 27(25):6655–6663, 2007.

[55] Y. Thielmann, J. Mohrlüder, B. W. König, T. Stangler, R. Hartmann, K. Becker, H.-D. Höltje, and D. Willbold. An indole-binding site is a major determinant of the ligand specificity of the GABA type A receptor-associated protein GABARAP. *ChemBioChem*, 9(11):1767–1775, 2008.

[56] N. Okazaki, J. Yan, S. Yuasa, T. Ueno, E. Kominami, Y. Masuho, H. Koga, and M. Muramatsu. Interaction of the Unc-51-like kinase and microtubule-associated protein light chain 3 related proteins in the brain: possible role of vesicular transport in axonal elongation. *Molecular Brain Research*, 85(1-2):1–12, 2000.

[57] F. Green, T.O'Hare, A. Blackwell, and C. A. Enns. Association of human transferrin receptor with GABARAP. *FEBS Letters*, 518(1-3):101–106, 2002.

[58] J. Mohrlüder, T. Stangler, Y. Hoffmann, K. Wiesehan, A. Mataruga, and D. Willbold. Identification of calreticulin as a ligand of GABARAP by phage display screening of a peptide library. *FEBS Journal*, 274(21):5543–5555, 2007.

[59] S. Asano, T. Nemoto, T. Kitayama, K. Harada, J. Zhang, K. Harada, I. Tanida, M. Hirata, and T. Kanematsu. Phospholipase C-related catalytically inactive protein (PRIP) controls KIF5B-mediated insulin secretion. *Biology Open*, 3(6):463–474, 2014.

[60] S. Pankiv, T. H. Clausen, T. Lamark, A. Brech, J.-A. Bruun, H. Outzen, A. Øvervatn, G. Bjørkøy, and T. Johansen. p62/SQSTM1 binds directly to Atg8/LC3 to facilitate degradation of ubiquitinated protein aggregates by autophagy. *Journal of Biological Chemistry*, 282(33):24131–24145, 2007.

[61] Y. Ichimura, T. Kumanomidou, Y. Sou, T. Mizushima, J. Ezaki, T. Ueno, E. Kominami, T. Yamane, K. Tanaka, and M. Komatsu. Structural basis for sorting mechanism of p62 in selective autophagy. *Journal of Biological Chemistry*, 283(33):22847–22857, 2008.

[62] V. V. Rogov, A. Stolz, A. C. Ravichandran, D. O. Rios-Szwed, H. Suzuki, A. Kniss, F. Löhr, S. Wakatsuki, V. Dötsch, I. Dikic, R. C. J. Dobson, and D. G. McEwan. Structural and functional analysis of the GABARAP interaction motif (GIM). *EMBO reports*, 18(8):1382–1396, 2017.

[63] R. S. Marshall, Z. Hua, S. Mali, F. McLoughlin, and R. D. Vierstra. ATG8-binding UIM proteins define a new class of autophagy adaptors and receptors. *Cell*, 177(3):766–781, 2019.

[64] W. Nickel and C. Rabouille. Mechanisms of regulated unconventional protein secretion. *Nature Reviews Molecular Cell Biology*, 10(2):148–155, 2009.

[65] Y. Ding, J. Wang, J. Wang, Y.-D. Stierhof, D. G. Robinson, and L. Jiang. Unconventional protein secretion. *Trends in Plant Science*, 17(10):606–615, 2012.

[66] C. Milstein, G. G. Brownlee, T. M. Harrison, and M. B. Mathews. A possible precursor of immunoglobulin light chains. *Nature New Biology*, 239(91):117–120, 1972.

[67] P. Walter, I. Ibrahimi, and G. Blobel. Translocation of proteins across the endoplasmic reticulum. I. Signal recognition protein (SRP) binds to in-vitro-assembled polysomes synthesizing secretory protein. *The Journal of Cell Biology*, 91:545–550, 1981.

[68] P. Walter and G. Blobel. Translocation of proteins across the endoplasmic reticulum. II. Signal recognition protein (SRP) mediates the selective binding to microsomal membranes of in-vitro-assembled polysomes synthesizing secretory protein. *The Journal of Cell Biology*, 91:551–556, 1981.

[69] R. Beckmann, D. Bubeck, R. Grassucci, P. Penczek, A. Verschoor, G. Blobel, and J. Frank. Alignment of conduits for the nascent polypeptide chain in the ribosome-Sec61 complex. *Science*, 278(5346):2123–2126, 1997.

[70] R. J. Keenan, D. M. Freymann, R. M. Stroud, and P. Walter. The signal recognition particle. *Annual Review of Biochemistry*, 70(1):755–775, 2001.

[71] R. Friedlander, E. Jarosch, J. Urban, C. Volkwein, and T. Sommer. A regulatory link between ER-associated protein degradation and the unfolded-protein response. *Nature Cell Biology*, 2(7):379–384, 2000.

[72] K. Römisch. Endoplasmic reticulum–associated degradation. *Annual Review of Cell and Developmental Biology*, 21(1):435–456, 2005.

[73] A. Nakano and M. Muramatsu. A novel GTP-binding protein, Sar1p, is involved in transport from the endoplasmic reticulum to the Golgi apparatus. *The Journal of Cell Biology*, 109(6):2677–2691, 1989.

[74] C. Barlowe and R. Schekman. SEC12 encodes a guanine-nucleotide-exchange factor essential for transport vesicle budding from the ER. *Nature*, 365(6444):347–349, 1993.

[75] K. Matsuoka, L. Orci, M. Amherdt, S. Y. Bednarek, S. Hamamoto, R. Schekman, and T. Yeung. COPII-coated vesicle formation reconstituted with purified coat proteins and chemically defined liposomes. *Cell*, 93(2):263–275, 1998.

[76] B. Antonny, P. Gounon, R. Schekman, and L. Orci. Self-assembly of minimal COPII cages. *EMBO reports*, 4(4):419–424, 2003.

[77] H. P. Hauri, F. Kappeler, H. Andersson, and C. Appenzeller. ERGIC-53 and traffic in the secretory pathway. *Journal of Cell Science*, 113 (Pt 4):587–596, 2000.

[78] C. Rabouille and J. Klumperman. The maturing role of COPI vesicles in intra-Golgi transport. *Nature Reviews Molecular Cell Biology*, 6(10):812–817, 2005.

[79] B. S. Glick and A. Luini. Models for Golgi traffic: a critical assessment. *Cold Spring Harbor Perspectives in Biology*, 3(11):a005215, 2011.

[80] R. Kornfeld and S. Kornfeld. Assembly of asparagine-linked oligosaccharides. *Annual Review of Biochemistry*, 54(1):631–664, 1985.

[81] J. S. Bonifacino and B. S. Glick. The mechanisms of vesicle budding and fusion. *Cell*, 116(2):153–166, 2004.

[82] A. Rubartelli, F. Cozzolino, M. Talio, and R. Sitia. A novel secretory pathway for interleukin-1 beta, a protein lacking a signal sequence. *The EMBO Journal*, 9(5):1503–1510, 1990.

[83] C. Rabouille. Pathways of unconventional protein secretion. *Trends in Cell Biology*, 27(3):230–240, 2017.

[84] C. Rabouille, V. Malhotra, and W. Nickel. Diversity in unconventional protein secretion. *Journal of Cell Science*, 125:5251–5255, 2012.

[85] T. Schäfer, H. Zentgraf, C. Zehe, B. Brügger, J. Bernhagen, and W. Nickel. Unconventional secretion of fibroblast growth factor 2 is mediated by direct translocation across the plasma membrane of mammalian cells. *The Journal of Biological Chemistry*, 279:6244–6251, 2004.

[86] J. P. Steringer, S. Bleicken, H. Andreas, S. Zacherl, M. Laussmann, K. Temmerman, F. X. Contreras, T. A. M. Bharat, J. Lechner, H.-M. Müller, J. A. G. Briggs, A. J. García-Sáez, and W. Nickel. Phosphatidylinositol 4,5-bisphosphate (PI(4,5)P2)-dependent oligomerization of fibroblast growth factor 2 (FGF2) triggers the formation of a lipidic membrane pore implicated in unconventional secretion. *The Journal of Biological Chemistry*, 287:27659–27669, 2012.

[87] M. Zeitler, J. P. Steringer, H.-M. Müller, M. P. Mayer, and W. Nickel. HIV-Tat protein forms phosphoinositide-dependent membrane pores implicated in unconventional protein secretion. *The Journal of Biological Chemistry*, 290:21976–21984, 2015.

[88] F. Martín-Sánchez, C. Diamond, M. Zeitler, A. I. Gomez, A. Baroja-Mazo, J. Bagnall, D. Spiller, M. White, M. J. D. Daniels, A. Mortellaro, M. Peñalver, P. Paszek, J. P. Steringer, W. Nickel, D. Brough, and P. Pelegrín. Inflammasome-dependent IL-1β release depends upon membrane permeabilisation. *Cell Death & Differentiation*, 23(7):1219–1231, 2016.

[89] J. Ding, K. Wang, W. Liu, Y. She, Q. Sun, J. Shi, H. Sun, D.-C. Wang, and F. Shao. Pore-forming activity and structural autoinhibition of the gasdermin family. *Nature*, 535(7610):111–116, 2016.

[90] J. P. McGrath and A. Varshavsky. The yeast STE6 gene encodes a homologue of the mammalian multidrug resistance P-glycoprotein. *Nature*, 340(6232):400–404, 1989.

[91] L. M. MacLean, P. J. O'Toole, M. Stark, J. Marrison, C. Seelenmeyer, W. Nickel, and D. F. Smith. Trafficking and release of *Leishmania* metacyclic HASPB on macrophage invasion. *Cellular Microbiology*, 14(5):740–761, 2012.

[92] C. Möskes, P. A. Burghaus, B. Wernli, U. Sauder, M. Dürrenberger, and B. Kappes. Export of *Plasmodium falciparum* calcium-dependent protein kinase 1 to the parasitophorous vacuole is dependent on three N-terminal membrane anchor motifs. *Molecular Microbiology*, 54:676–691, 2004.

[93] L. Urbani and R. D. Simoni. Cholesterol and vesicular stomatitis virus G protein take separate routes from the endoplasmic reticulum to the plasma membrane. *The Journal of Biological Chemistry*, 265:1919–1923, 1990.

[94] H. Schotman, L. Karhinen, and C. Rabouille. dGRASP-mediated noncanonical integrin secretion is required for *Drosophila* epithelial remodeling. *Developmental Cell*, 14(2):171–182, 2008.

[95] J. Kim, S. H. Noh, H. Piao, D. H. Kim, K. Kim, J. S. Cha, W. Y. Chung, H.-S. Cho, J. Y. Kim, and M. G. Lee. Monomerization and ER relocalization of GRASP is a requisite for unconventional secretion of CFTR. *Traffic*, 17(7):733–753, 2016.

[96] H. Y. Gee, S. H. Noh, B. L. Tang, K. H. Kim, and M. G. Lee. Rescue of ΔF508-CFTR trafficking via a GRASP-dependent unconventional secretion pathway. *Cell*, 146(5):746–760, 2011.

[97] M. A. Kinseth, C. Anjard, D. Fuller, G. Guizzunti, W. F. Loomis, and V. Malhotra. The Golgi-associated protein GRASP is required for unconventional protein secretion during development. *Cell*, 130(3):524–534, 2007.

[98] E. Dimou and W. Nickel. Unconventional mechanisms of eukaryotic protein secretion. *Current Biology*, 28(8):R406–R410, 2018.

[99] J. M. Duran, C. Anjard, C. Stefan, W. F. Loomis, and V. Malhotra. Unconventional secretion of Acb1 is mediated by autophagosomes. *The Journal of Cell Biology*, 188(4):527–536, 2010.

[100] R. Manjithaya, C. Anjard, W. F. Loomis, and S. Subramani. Unconventional secretion of *Pichia pastoris* Acb1 is dependent on GRASP protein, peroxisomal functions, and autophagosome formation. *The Journal of Cell Biology*, 188(4):537–546, 2010.

[101] C. Bruns, J. M. McCaffery, A. J. Curwin, J. M. Duran, and V. Malhotra. Biogenesis of a novel compartment for autophagosome-mediated unconventional protein secretion. *The Journal of Cell Biology*, 195(6):979–992, 2011.

[102] V. Malhotra. Unconventional protein secretion: an evolving mechanism. *The EMBO Journal*, 32(12):1660–1664, 2013.

[103] D. Cruz-Garcia, A. J. Curwin, J.-F. Popoff, C. Bruns, J. M. Duran, and V. Malhotra. Remodeling of secretory compartments creates CUPS during nutrient starvation. *The Journal of Cell Biology*, 207(6):695–703, 2014.

[104] C. Andrei, C. Dazzi, L. Lotti, M. R. Torrisi, G. Chimini, and A. Rubartelli. The secretory route of the leaderless protein interleukin 1β involves exocytosis of endolysosome-related vesicles. *Molecular Biology of the Cell*, 10(5):1463–1475, 1999.

[105] N. Dupont, S. Jiang, M. Pilli, W. Ornatowski, D. Bhattacharya, and V. Deretic. Autophagy-based unconventional secretory pathway for extracellular delivery of IL-1β. *The EMBO Journal*, 30(23):4701–4711, 2011.

[106] J. Nüchel, S. Ghatak, A. V. Zuk, A. Illerhaus, M. Mörgelin, K. Schönborn, K. Blumbach, S. A. Wickström, T. Krieg, G. Sengle, M. Plomann, and B. Eckes. TGFB1 is secreted through an unconventional pathway dependent on the autophagic machinery and cytoskeletal regulators. *Autophagy*, 14(3):465–486, 2018.

[107] V. Deretic, S. Jiang, and N. Dupont. Autophagy intersections with conventional and unconventional secretion in tissue development, remodeling and inflammation. *Trends in Cell Biology*, 22(8):397–406, 2012.

[108] M. Ponpuak, M. A. Mandell, T. Kimura, S. Chauhan, C. Cleyrat, and V. Deretic. Secretory autophagy. *Current Opinion in Cell Biology*, 35:106–116, 2015.

[109] M. Zhang, S. J. Kenny, L. Ge, K. Xu, and R. Schekman. Translocation of interleukin-1β into a vesicle intermediate in autophagy-mediated secretion. *eLife*, 4:e11205, 2015.

[110] C. Théry, K. W. Witwer, E. Aikawa, M. J. Alcaraz, J. D. Aderson, R. Andriantsitohaina, A. Antoniou, T. Arab, F. Archer, G. K. Atkin-Smith, D. C. Ayre, and J.-M. *et al.* Minimal information for studies of extracellular vesicles 2018 (MISEV2018): a position statement of the international society for extracellular vesicles and update of the MISEV2014 guidelines. *Journal of Extracellular Vesicles*, 7:1535750, 2018.

[111] K. W. Witwer and C. Théry. Extracellular vesicles or exosomes? On primacy, precision, and popularity influencing a choice of nomenclature. *Journal of Extracellular Vesicles*, 8(1):1648167, 2019.

[112] G. Raposo and W. Stoorvogel. Extracellular vesicles: Exosomes, microvesicles, and friends. *The Journal of Cell Biology*, 200(4):373–383, 2013.

[113] B. T. Pan and R. M. Johnstone. Fate of the transferrin receptor during maturation of sheep reticulocytes in vitro: selective externalization of the receptor. *Cell*, 33(3):967–978, 1983.

[114] B. T. Pan, K. Teng, C. Wu, M. Adam, and R. M. Johnstone. Electron microscopic evidence for externalization of the transferrin receptor in vesicular form in sheep reticulocytes. *The Journal of Cell Biology*, 101(3):942–948, 1985.

[115] J. Kowal, M. Tkach, and C. Théry. Biogenesis and secretion of exosomes. *Current Opinion in Cell Biology*, 29:116–125, 2014.

[116] J. R. Edgar, P. T. Manna, S. Nishimura, G. Banting, and M. S. Robinson. Tetherin is an exosomal tether. *eLife*, 5:e17180, 2016.

[117] F. Baixauli, C. López-Otín, and M. Mittelbrunn. Exosomes and autophagy: coordinated mechanisms for the maintenance of cellular fitness. *Frontiers in Immunology*, 5:403, 2014.

[118] H. Guo, M. Chitiprolu, L. Roncevic, C. Javalet, F. J. Hemming, M. T. Trung, L. Meng, E. Latreille, C. Tanese de Souza, D. McCulloch, R. M. Baldwin, R. Auer, J. Côté, R. C. Russell, R. Sadoul, and D. Gibbings. Atg5 disassociates the V_1V_0-ATPase to promote exosome production and tumor metastasis independent of canonical macroautophagy. *Developmental Cell*, 43(6):716–730.e7, 2017.

[119] M. Zhang and R. Schekman. Unconventional secretion, unconventional solutions. *Science*, 340(6132):559–561, 2013.

[120] C. Muratori, L. E. Cavallin, K. Krätzel, A. Tinari, A. De Milito, S. Fais, P. D'Aloja, M. Federico, V. Vullo, A. Fomina, E. A. Mesri, F. Superti, and A. S. Baur. Massive secretion by T cells is caused by HIV Nef in infected cells and by Nef transfer to bystander cells. *Cell Host & Microbe*, 6(3):218–230, 2009.

[121] J. Ratajczak, K. Miekus, M. Kucia, J. Zhang, R. Reca, P. Dvorak, and M. Z. Ratajczak. Embryonic stem cell-derived microvesicles reprogram hematopoietic progenitors: evidence for horizontal transfer of mRNA and protein delivery. *Leukemia*, 20(5):847–856, 2006.

[122] H. Valadi, K. Ekström, A. Bossios, M. Sjöstrand, J. J. Lee, and J. O. Lötvall. Exosome-mediated transfer of mRNAs and microRNAs is a novel mechanism of genetic exchange between cells. *Nature Cell Biology*, 9(6):654–659, 2007.

[123] T. Malm, S. Loppi, and K. M. Kanninen. Exosomes in Alzheimer's disease. *Neurochemistry International*, 97:193–199, 2016.

[124] M. Tkach and C. Théry. Communication by extracellular vesicles: Where we are and where we need to go. *Cell*, 164(6):1226–1232, 2016.

[125] C. Théry, L. Zitvogel, and S. Amigorena. Exosomes: composition, biogenesis and function. *Nature Reviews Immunology*, 2(8):569–579, 2002.

[126] T. Lener, M. Gimona, L. Aigner, V. Börger, E. Buzas, G. Camussi, N. Chaput, D. Chatterjee, F. A. Court, H. A. Del Portillo, L. O'Driscoll, and S. Fais *et al.* Applying extracellular vesicles based therapeutics in clinical trials - an ISEV position paper. *Journal of Extracellular Vesicles*, 4:30087, 2015.

[127] M. F. Peterson, N. Otoc, J. K. Sethi, A. Gupta, and T. J. Antes. Integrated systems for exosome investigation. *Methods*, 87:31–45, 2015.

[128] A. Cvjetkovic, S. C. Jang, B. Konečná, J. L. Höög, C. Sihlbom, C. Lässer, and J. Lötvall. Detailed analysis of protein topology of extracellular vesicles - evidence of unconventional membrane protein orientation. *Scientific Reports*, 6:36338, 2016.

[129] H. Kalra, R. J. Simpson, H. Ji, E. Aikawa, P. Altevogt, P. Askenase, V. C. Bond, F. E. Borràs, X. Breakefield, V. Budnik, E. Buzas, and G. Camussi *et al.* Vesiclepedia: a compendium for extracellular vesicles with continuous community annotation. *PLoS Biology*, 10(12):e1001450, 2012.

[130] EV-TRACK Consortium, J. Van Deun, P. Mestdagh, P. Agostinis, Ö. Akay, S. Anand, J. Anckaert, Z. A. Martinez, T. Baetens, E. Beghein, L. Bertier, and G. Berx *et al.* EV-TRACK: transparent reporting and centralizing knowledge in extracellular vesicle research. *Nature Methods*, 14(3):228–232, 2017.

[131] A. Sinha, V. Ignatchenko, A. Ignatchenko, S. Mejia-Guerrero, and T. Kislinger. In-depth proteomic analyses of ovarian cancer cell line exosomes reveals differential enrichment of functional categories compared to the NCI 60 proteome. *Biochemical and Biophysical Research Communications*, 445(4):694–701, 2014.

[132] S. N. Hurwitz, M. A. Rider, J. L. Bundy, X. Liu, R. K. Singh, and D. G. Meckes. Proteomic profiling of NCI-60 extracellular vesicles uncovers common protein cargo and cancer type-specific biomarkers. *Oncotarget*, 7(52):86999–87015, 2016.

[133] H.-W. Rhee, P. Zou, N. D. Udeshi, J. D. Martell, V. K. Mootha, S. A. Carr, and A. Y. Ting. Proteomic mapping of mitochondria in living cells via spatially restricted enzymatic tagging. *Science*, 339(6125):1328–1331, 2013.

[134] F. Le Guerroué, F. Eck, J. Jung, T. Starzetz, M. Mittelbronn, M. Kaulich, and C. Behrends. Autophagosomal content profiling reveals an LC3C-dependent piecemeal mitophagy pathway. *Molecular Cell*, 68(4):786–796.e6, 2017.

[135] Y. Kabeya, N. Mizushima, A. Yamamoto, S. Oshitani-Okamoto, Y. Ohsumi, and T. Yoshimori. LC3, GABARAP and GATE16 localize to autophagosomal membrane depending on form-II formation. *Journal of Cell Science*, 117(13):2805–2812, 2004.

[136] A. M. Leidal, H. H. Huang, T. Marsh, T. Solvik, D. Zhang, J. Ye, F. Kai, J. Goldsmith, J. Y. Liu, Y.-H. Huang, T. Monkkonen, and A. Vlahakis *et al.* The LC3-conjugation machinery specifies the loading of RNA-binding proteins into extracellular vesicles. *Nature Cell Biology*, 22(2):187–199, 2020.

[137] C. Chen, J.-G. Li, Y. Chen, P. Huang, Y. Wang, and L.-Y. Liu-Chen. GEC1 interacts with the opioid receptor and enhances expression of the receptor. *Journal of Biological Chemistry*, 281(12):7983–7993, 2006.

[138] J. M. M. Müller, J. Shorter, R. Newman, K. Deinhardt, Y. Sagiv, Z. Elazar, G. Warren, and D. T. Shima. Sequential SNARE disassembly and GATE-16–GOS-28 complex assembly mediated by distinct NSF activities drives Golgi membrane fusion. *The Journal of Cell Biology*, 157(7):1161–1173, 2002.

[139] P. J. Thul, L. Åkesson, M. Wiking, D. Mahdessian, A. Geladaki, H. A. Blal, T. Alm, A. Asplund, L. Björk, L. M. Breckels, A. Bäckström, and F. Danielsson *et al.* A subcellular map of the human proteome. *Science*, 356(6340):eaal3321, 2017.

[140] H. H. Mollenhauer, D. J. Morré, and L. D. Rowe. Alteration of intracellular traffic by monensin mechanism, specificity and relationship to toxicity. *Biochimica et Biophysica Acta (BBA) - Reviews on Biomembranes*, 1031(2):225–246, 1990.

[141] J. T. Kittler, P. Rostaing, G. Schiavo, J.-M. Fritschy, R. Olsen, A. Triller, and S. J. Moss. The subcellular distribution of GABARAP and its ability to interact with NSF suggest a role for this protein in the intracellular transport of GABA(A) receptors. *Molecular and Cellular Neuroscience*, 18(1):13–25, 2001.

[142] I. M. Simons, J. Mohrlüder, R. Feederle, E. Kremmer, T. Zobel, J. Dobner, N. Bleffert, S. Hoffmann, and D. Willbold. The highly GABARAP specific rat monoclonal antibody 8H5 visualizes GABARAP in immunofluorescence imaging at endogenous levels. *Scientific Reports*, 9(1), 2019.

[143] V. Hung, N. D. Udeshi, S. S. Lam, K. H. Loh, K. J. Cox, K. Pedram, S. A. Carr, and A. Y. Ting. Spatially resolved proteomic mapping in living cells with the engineered peroxidase APEX2. *Nature Protocols*, 11(3):456–475, 2016.

[144] D. Wessel and U. I. Flügge. A method for the quantitative recovery of protein in dilute solution in the presence of detergents and lipids. *Analytical Biochemistry*, 138(1):141–143, 1984.

[145] C. Théry, S. Amigorena, G. Raposo, and A. Clayton. Isolation and characterization of exosomes from cell culture supernatants and biological fluids. *Current Protocols in Cell Biology*, 30(1):3221–32229, 2006.